U.S. Dept of Energy Award # DE-SC0005392

The University of Alabama, Box 870104, Tuscaloosa, Alabama, 35487-0104

TITLE: Single-Molecule Spectroelectrochemistry of Interfacial Charge Transfer in Hybrid Organic Solar Cell

Principle Investigator (PI): Prof. Shanlin Pan
Mailing Address of PI: Department of Chemistry, Box 870336, The University of Alabama, Tuscaloosa, AL 35487-0336
Telephone Number of PI: (205)348-6381
Email: span1@ua.edu

Date of the final report: 11/16/2014
Period covered by the report: 08/15/2010-11/16/2014

Table of Content

I. Brief Summary of Major Research Accomplishments

Our research under support of this DOE grant is focused on applied and fundamental aspects of model organic photovoltaic (OPV) systems. Major accomplishments are briefly summarized below:

First, we improved spectroelectorchemistry of single molecule single nanoparticle method to study charge transfer between conjugated polymers and TiO2 at the single molecule level. The fluorescence of individual molecules of the conjugated polymers such as poly[2-methoxy-5-(2-ethylhexyloxy)- 1,4-phenylenevinylene] (MEH-PPV) at TiO2 surfaces was shown to exhibit increased intermittent (on/off "blinking") behavior compared to molecules on glass substrates. Single molecule fluorescence excitation anisotropy measurements showed the conformation of the polymer molecules did not differ appreciably between glass and TiO2 substrates. The similarities in molecular conformation suggest that the observed differences in blinking activity are due to charge transfer between MEH-PPV and TiO2, which provides additional pathways between states of high and low fluorescence quantum efficiency. Similar spectroelectrochemistry work has been done for small organic dyes such as BODIPY dye for understand their charge transfer dynamics on various substrates and electrochemical environments.

Secondly, we developed a method of transferring TiO_2 nanoparticles (NPs) and graphene oxide (GO) nanosheets into organic solvent for a potential electron acceptor in bulk heterojunction organic solar cells which employed poly[3- hexylthiophene] (P3HT) as the electron donor. Electron transfer from P3HT to GO and TiO_2 in solutions and thin films was established through fluorescence spectroscopy and electrogenerated chemilumescence (ECL) measurements. Bulk heterojunction solar cells containing P3HT, P3HT:GO, P3HT:TiO_2, and P3HT:phenyl-C61- butyric acid methyl ester (PCBM, a prototypical elector acceptor employed in polymer solar cells) were constructed and evaluated using transient absorption spectroscopy and dynamic fluorescence techniques to understand the charge carrier generation and recombination events.

Lastly, we invented a spectroelectorchemistry technique using dark field scattering (DFS) and ECL for rapid size determination and reconstruction of cyclic voltammetry for single NPs in an electrochemical cell. For example, we are able to use this technique to track ECL of single Au NPs, and the electrodeposition of individual Ag nanoparticles (NPs) *in-situ*. These metallic NPs are useful to enhance light harvesting in organic photovoltaic systems. The scattering at the surface of an indium tin oxide (ITO) working electrode was measured during a potential sweep. Utilizing Mie scattering theory and high resolution scanning electron microscopy (SEM), the scattering data were used to calculate current-potential curves depicting the electrodeposition of individual Ag NPs. The oxidation of individual presynthesized and electrodeposited Ag NPs was also investigated using fluorescence and DFS microscopies.

Our work has produced 1 US provisional patent, 15 published manuscripts, 1 submitted article and two additional in-writing manuscripts. 5 graduate students, 1 postdoctoral student, 1 visiting professor, and two undergraduate students have received research training under support of this award.

II. List of Accepted and Submitted Publications

A. Patent with this DOE-EPSCoR award acknowledged

Caleb Hill, Shanlin Pan, A New Optical Method for Tracking the Electordeposition of Metallic nanaoparticles and Catalytic Redox Reactions at Single Nobel Nanoparticle electrodes via Dark Field Scattering and Electrogenerated Chemiluminescence, Disclosure filed in **2013**, provisional filed in February 2014.

B. Published articles as of 11/15/2014 with this DOE-EPSCoR award acknowledged

(* correspondence author)

1. J. Liu, C. M. Hill, H.Y. Liu, S.L. Pan*, "Interfacial charge transfer events of BODIPY molecules: single molecule spectroelectrochemistry and substrate effects", *Phys. Chem. Chem. Phys.*, **2014**, DOI: 10.1039/c4cp02950j.
2. C. M. Hill, S.L. Pan*, A Dark Field Scattering Spectroelectrochemistry Technique for Tracking the Electrodeposition of Single Ag Nanoparticles, *J. Am. Chem. Soc.* **2013**, 135(46),17250-17253.
3. C. M. Hill, D. Clayton, S.L. Pan*, Understanding Spatial and Temporal Heterogeneities Of Electrochemical Events Using Combined Optical And Electrochemical Methods: Recent Progress and Perspectives, *Phys. Chem. Chem. Phys.* DOI:10.1039/C3CP52756E, **2013**.
4. Z.C. Shan, S.L. Pan*, A. Gupta*, "Visible Light Driven Photoelectrochemical Properties of Ti Nanowire Electrodes Sensitized with CoreShell Ag_2S Nanoparticles", *J. Phys. Chem. B*, **2014**, July, DOI: 10.1021/jp504346k.
5. H.W. Geng, C. Hill, S.L. Pan*, H.Y., L.B. Huang, Photoelectrochemical Properties and Interfacial Charge Transfer Kinetics of BODIPY-Sensitized TiO_2 electrodes, *RSC Advances*, **2013**, ***3,*** 2306-2312. DOI: 10.1039/C2RA21656F
6. H.W. Geng, C. Hill, S.L. Pan,* Libai Huang, Electrogenerated Chemiluminescence and Interfacial Charge Transfer Dynamics of Poly (3-hexylthiophene-2, 5-diyl) (P3HT)-TiO_2 Nanoparticle Thin Film, *Phys. Chem. Chem. Phys*., **2013**, *15*, 3504-3509**.** DOI: 10.1039/C2CP43680A
7. Xu, C.L., Geng, H.W., Clayton, D.A., Bennett, R. Pan, S.L.* "Ti@TiO_2 NW electrode with polydisperse gold nanoparticles for electrogenerated chemiluminescence and surface enhanced Raman spectroelectrochemistry", *J. Phys. Chem. C*, **2013**, 117, 1849-1856.
8. Hill, C. M.; Pan, S.L. * "Efficient analysis of single molecule spectroscopic data via MATLAB". *MRS Proc.* **2013**, 1493, DOI: http://dx.doi.org/10.1557/opl.2012.1676.
9. Geng, H.W.; Pan, S.L.*; Hu, D.H. "Electrogenerated chemiluminescence and fluorescence lifetime spatial heterogeneity of poly (2-methoxy-5-(2-ethylhexyloxy)-1,4-phenylenevinylene) in presence of [6,6]-phenyl-C61-butyric Acid Methyl Ester", *MRS Proc.* **2013**, 1493, DOI: http://dx.doi.org/10.1557/opl.2013.19.
10. Clayton, D. A., McPherson, T.E., Pan, S.L. * Chen, M.Y., Dixon, D.A., Hu, D.H. "Spatial and temporal variation of surface-enhanced Raman scattering at Ag nanowires in aqueous solution", *Phys. Chem. Chem. Phys*., **2013**, 15, 850-859.
11. Fraser Mole, Jue Wang and Shanlin Pan, * New double heterojunction nanostructured electrode for electrochemical charge storage, *Langmuir*, **2012**, 28(28), 10610-10619.
12. C. M. Hill, Y. Zhu, S. L. Pan, * "Fluorescence and Electroluminescence Quenching Evidences of Interfacial Charge Transfer in Poly (3-hexylthiopene): Graphene oxide Bulk Heterojunction Organic Photovoltaic Device", *ACS Nano* **2011**, 5(2), 942-951.
13. Y. Zhu; C. M. Hill; S.L. Pan, * "Reductive-oxidation Electrogenerated Chemiluminescence (ECL) Generation at Ag Nanowire Electrode", *Langmuir*, 2011, 27(6), 3121-3127.
14. Caleb M. Hill, Shanlin Pan, * Single Molecule/Nanoparticle Spectroelectrochemistry for Understanding Interfacial Charge Transfer Dynamics and Renewable Energy Conversion at Namometer Scale, *Prepr. Pap.-Am. Chem. Soc., Div. Energy Fuels* **2012**, 57 (2), 387-388.

15. Daniel A. Clayton, Shanlin Pan, * Surface-enhanced Raman Scattering at Photoreduced Silver Nanoparticles at Single Crystal TiO_2 Particles for Studying Their Interfacial Charge Transfer Activities and Renewable Energy Conversion, *Prepr. Pap.-Am. Chem. Soc., Div. Energy Fuels* **2012**, 57 (2), 200-201.

C. Submitted articles as of 11/15/2014

16. Caleb M. Hill, Robert Bennett,Chen Zhou,Shane Street, Jie Zheng, and Shanlin Pan*, Single Ag NP Spectroelectrochemistry via Dark Field Scattering and Fluorescence Microscopies, Small, submitted as of **10/29/2014**

D. Manuscripts in preparation

17. Daniel A Clayton, Caleb M. Hill, and Shanlin Pan. Interfacial charge transfer heterogeneities at single crystal TiO_2 surfaces.
18. Jia Liu, Caleb M Hill, and Shanlin Pan. Electrogenerated chemiluminescence (ECL) at single au nanoparticles.

E. Doctoral Dissertations

1. Fundamental and applied studies of organic photovoltaic systems, **Caleb M. Hill**, a dissertation submitted in partial fulfillment of the requirements for the degree of Doctor of Philosophy in the Department of Chemistry in the graduate school of The University of Alabama, **2014**.
2. Nanostructured silver for applications in surface enhanced raman spectroscopy and photoelectrochemical reactions, **Daniel A. Clayton**, a dissertation submitted in partial fulfillment of the requirements for the degree of Doctor of Philosophy in the Department of Chemistry in the graduate school of The University of Alabama, **2014**.

III.Students and Postdoc Support and Their Progresses

Name	Title, Percentage of support, Project and progress
Caleb M. Hill	**08/16/2011-08/15/2014:** Caleb received 60% support from this DOE program. Mr. Hill has been extremely productive by successfully demonstrated detection of single fluorescent silver nanoparticles and conjugate polymers using combined electrochemical and spectroscopic tools. In collaboration with Notra Dame radiation national lab, Caleb studied transient absorption spectroscopy and dynamics fluorescence spectroscopy of conjugate polymers in the presence of single crystal TiO_2, TiO_2 nanoparticles and the BODiPY dye conjugated with TiO_2. These studies are compared with his single molecule studies for interesting interfacial charge transfer dynamics in an organic hybrid solar cell. Mr. Hill has been supported by 2012 Dissertation Graduate Council Fellowship and 2014 Alabama EPSCoR Graduate Research Scholar Fellowship. He was selected as one of our GAANN Fellows in 2011 because of his outstanding academic performance and research productivity. Caleb has published nine research papers and holds one patent under support of this DOE program. Mr. Hill was recently selected to work with one of the world's famous electrochemists Professor Allen J. Bard (UT-Austin).
Daniel A. Clayton	**08/16/2011-08/15/2014:** Mr. Clayton received 60% support from this DOE program. Mr. Clayton has been working on single molecule since the start of this project. He has demonstrated the complex dynamics photophysical processes of single molecule conjugate polymer on nanotextured silver and their spectral dependence on solvents. More recently, Daniel started looking at photoelectrochemical reaction at the nanometer scale using single crystal TiO_2 surface and surface enhanced Raman imaging technique. Daniel received two travel funds from the graduate school and the EPSCoR program, respectively, to

	present his single molecule work at two separate ACS meetings. His research is well aligned with our proposed goals to develop a single polymer molecule raman setup, to vary surface chemistry techniques optimize the surface enhancement effects and demonstrate single polymer Raman used in organic photovoltaic cells to gain a fundamental understanding of their electronic properties. Mr. Clayton published seven papers under support of this program. Currently he holds a teaching position as a visiting assistant professor in Minot State University.
HongWei Geng	**08/16/2011-3/15/2013**: Dr. Geng received 100% support from this program during his stay at UA. Dr. Geng has been extremely productive during this support period. Dr. Geng has used single molecule spectroscopy, electrochemistry tools and transient spectroscopy to reveal the complex charge separation and photophysical processes in an organic hybrid solar cell. He has published fours papers in the area of hybrid organic solar cells and systems including conjugate polymer and TiO_2 nanostructure. In order to help fulfill the group's research goals in the area of single molecule spectroelectrochemistry, the postdoc Dr. **Geng** visited the Pacific Northwest National Laboratory (PNNL) for conductive AFM measurements on hybrid thin film of organic solar cell and lifetime imaging research for conjugate polymers. Currently Dr. Geng is working with Seventstar's R&D department for developing efficient $InGaSe_2$ solar cells.
Jia Liu	**08/15/2011-11/15/2014:** Mr. Liu received 50% support in this period from the DOE grant. His major contribution to this project includes 1) developing single molecule spectroelectrochemistry method for understanding the redox potential and substrate effects on photophysical characteristics of 4, 4′-difluoro-4-bora-3a, 4a-diaza-s-indacene) BODIPY dye bearing two carboxylic acid groups at its 2 and 6 positions. Mr. Jia also invented a single nanoparticle imagining method for studying single nanoparticles using electrogenerated chemiluminescence (ECL). Mr. Liu discovered that ECL can be enhanced gold nanoparticles (Au NPs) with diameters from 30 to 400 nm. He investigated this ECL system using single nanoparticle spectroelectrochemistry method. Au NPs are found to be able to catalyze the oxidation of tripropylamine (TrPA) when deposited onto TrPA-oxidation-sluggish indium-tin-oxide (ITO) surface, enabling us to detect enhanced ECL of $Ru(bpy)_3^{2+}$ at single Au NPs in aqueous solution. ECL at individual Au NPs is correlated to their particle size for improved understanding the kinetics and heterogeneities in particle sizes and local charge transfer events.
Diane M. Benoist	**08/15/2010-10/01/2010:** 100% support. Michelle's contribution under a short support of this grant is on fabricating transparent conductive electrode for single molecule spectroelectrochemical studies. Michelle has demonstrated the formation of quality graphene electrode on quartz using hydrothermal reaction. This project has been picked up by our postdoc Dr. Geng and graduate student Mr. Jue Wang.
Jue Wang	**10/01/2010-05/15/2011: 100**% support under this DOE grant during this period. Mr. Jue Wang is under support of a government fellowship during his summer time. Mr. Jue Wang's contribution to this project so far is mainly on fabricating useful Plasmon antenna for single molecule Raman of conjugate polymers. Mr. Jue Wang used wet chemistry and seeding methods to prepare high yield gold nanorods. He has obtained good control over aspect ratio of gold nanorods. This method can be extended onto TiO_2 surface for single molecule Raman study as we proposed in the original proposal. Jue's work on enhanced hematite photoelectronchemistry has provided solid preliminary results for another

	successful NSF award with professor Arun Gupta (UA).
Karson Brooks	**05/15/2011-08/15/2011: Summer undergraduate researcher, freshman, 100% support.** Karson is one of the best students in our chemistry program. She has worked on single molecule Raman in the past two semesters. She will continue work on this project under support of this project for ten weeks in the coming summer. We have received permission from Dr. Jane Zhu for this support.
Robert Matroni	**08/15/2010-05/2011: Undergraduate researcher, senior. 0% support.** Mr. Matroni has prepared TiO_2 nanotubes for our single molecule transport studies.
Cailing Xu	**08/15/2011-05/2012: 0% support under this grant.** A visiting professor from Lanzhou University of China, has made great contribution to our research projects in many aspects. Dr. Xu and the postdoc Dr. Hognwei Geng have been working closely on a new nanostructured electrode and they demonstrated that strong plasmon coupling can be obtained by coating $Ti@TiO_2$ nanowires with gold nanoparticles using under potential deposition technique.

IV. Planned and Accomplished Activities (With First Granted No-cost Extension from 08/16/2013-08/15/2014).

Accomplished (√) and planned research activities are summarized in the table below. This table is consistent with the timeline in the original proposal in the sequence of the experiment.

Planned Projects	Year 1				Year 2				Year 3-4			
Ordered TiO_2 substrate preparation using block polymer characterization	√	√										
Single fluorescent polymer charge transfer and dynamics at the surface of ordered TiO_2 template. Solvent and substrate effects		√	√	√	√	√						
Transient spectroscopy measurement for the fluorescence polymer sensitized TiO_2					√	√	√	√				
TiO_2 nanotube fabrication using hydrothermal reaction, characterization and structure optimization for single molecule study, spectroelectrochemistry			√	√	√	√	√	√	√	√	√	√
Single molecule interfacial charge transfer activities in single TiO_2 nanotubes and single molecule tracking					√	√	√	√	√	√		
Photoreduction of silver ion on ordered TiO_2 substrate for enhanced Raman and fluorescence of single fluorescence polymer (UA)				√	√	√	√	√				
Transient spectroscopy measurement for conjugate polymer and small molecules systems									√	√	√	√

Our work has produced 1 US provisional patent, 15 published manuscripts, 1 submitted article and two additional in-writing articles.

V. Current and pending

Current

1. The NanoBio Science Partnership for the Alabama Black Belt Region, NSF, $ 152,125/year, Co-PI, 08/15/2011-08/15/16. Dr. Pan has built five education modules on energy, solar and nanomaterials relevant to this current DOE/EPSCoR project.
2. Surface-Enhanced Solar Energy Conversion System for Advancing Alternative Energy, $422,000, PI, 05/15/2012-05/14/15, NSF.
3. Collaborative Research: Geopolymeric Nanocomposite, A Next Generation Material for Infrastructure Sustainability, NSF, Co-PI, 05/01/2010-4/30/13, $50,000/year.
4. Building EPSCoR-State/DOE National Laboratory Partnerships: Single-Molecule Spectroelectrochemistry of Interfacial Charge Transfer Dynamics in Hybrid Organic Solar Cell, single PI. $ 542,115, 08/15/10 - 08/14/15. With non-cost extension granted.

Pending

1. Plasmon-Engineered Photocatalytic Systems with Well-Defined Nanostructures Toward Efficient Solar Water Splitting, PI(Pan), CoPI (Gupta), $532,920, NSF, 06/01/2015-05/31/2018.
2. Understanding Redox Reaction Mechanism and Dynamics at Single Nanoparticles Using ECL and Scanning Nanoelectrode with Improved Spatial and Spectral Resolution, NSF, $326,699.00, PI (Pan) 11/13/2014-10/31/2014.
3. Single-Molecule Spectroelectrochemistry of Conjugate Polymer Chromophores in Intimate Contact with Semiconductor Surfaces for Improved Interfacial Charge Transfer in Organic Photov, DOE, PI (Pan), $568,224, 05/01/15 - 04/30/18

Expired

1. Research Stimulation Program of the University of Alabama, synthesis of new dyes for organic photovoltaics, $45,000/ year, Co-PI. One postdoctoral researcher for two years. 05/01/2011-04/30/2013. The University of Alabama.
2. Research Stimulation Program of the University of Alabama, Understanding the organic/semiconductor interface: Modeling and characterization of functionalized titanium dioxide, $35,000/year, Co-PI. One postdoctoral researcher for two years. 08/01/2010-07/30/2012. The University of Alabama.
3. 100 hours access to AFM and microscope of EMSL of PNNL for Spectroscopic and ultrafast dynamics study of double heterojunction hybrid organic solar cell. 10/01/2011-9/30/2012.
4. Research Grants Committee (RGC) of the University of Alabama, $5,000 for two years (single PI). Surface enhanced photoelectrochemical system for water splitting using solar energy. 5/13/2010-5/14/2012.
5. Travel funds for Fall 2012 American Chemical Society National Conference on Materials for Health & Medicine between Aug. 19 and 23 of 2012 in Philadelphia. Two research reprints have been submitted to the Division of Energy Fuels and accepted. $ 1,770, The DOE implementation award.
6. Travel funds for 2014 Plasmonics Gordon Research Conference in Maine **(**July 6 and 11, 2014) to present plasmonic energy research presentation. $ 1,000, The DOE implementation award.
7. Environmental Molecular Sciences Laboratory of Pacific Northwest National Lab Microscope: Scanning Probe - AFM Compound user proposal, Spectroscopic and ultrafast dynamics study of poly (3-hexylthiophene) in organic solar cell doped with graphene oxide, for 150 hours (2 weeks every 6 months), 09/30/2010-03/31/2011. project. This is required in order to send our graduate students to use PNNL's facility.
8. 100 hours access to AFM and microscope of EMSL of PNNL for Spectroscopic and ultrafast dynamics study of double heterojunction hybrid organic solar cell. 10/01/2011-9/30/2012.
9. College Academy for Research, Scholarship and Creative Activity (CARSCA) $8,825, Co-PI, The Study of Enzyme Motions on a Single-Molecule Level, The University of Alabama, 05/01/2010-04/30/2011.

VI. Detailed Description of Major Research Accomplishments

1. Single-molecule spectroelectrochemistry at TiO_2 electrodes with ordered nanostructures.

We have applied single molecule fluorescence spectroscopy technique to the studies of organic-inorganic hybrid photovoltaic systems. At the single molecule level, fluorophores can exhibit long lived "on" and "off" states corresponding to high and low periods of fluorescence quantum efficiency on the ms to s time scale ("blinking"). This can be due to several effects, such as molecular movement/rotation,

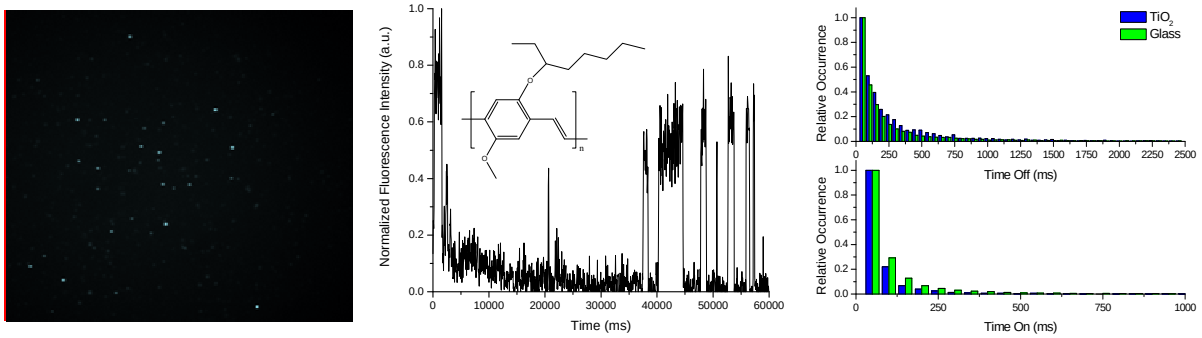

Figure 1. Single molecule MEH-PPV photoluminescence image (left), normalized fluorescence trajectory for a single MEH-PPV molecule (middle), and "On" and "Off" state distributions for MEH-PPV molecules on glass and TiO_2 substrates (Right).

triplet state crossover, spectrum shift, and electron transfer. This "blinking" behavior of a single organic molecule in contact with an inorganic acceptor material can provide insight into the charge transfer occurring between them without any interference from the other processes (most importantly, charge transfer) mentioned above. Our preliminary work in this support period was on two model systems: CdSe/ZnS core/shell quantum dots (QDs) and poly [2-methoxy-5-(2-ethylhexyloxy)-1,4-phenylenevinylene] (MEH-PPV) on well-characterized mesoporous TiO_2 films.

A typical fluorescence trajectory for a single MEH-PPV molecule on glass can be seen in Figure 1, along with its molecular structure. The blinking in this case is due to the reversible formation of

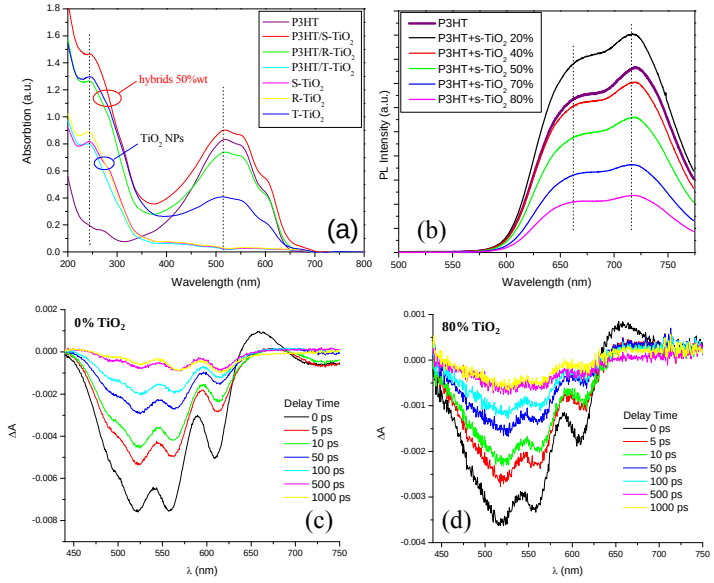

Figure 2. Transient absorption spectra for a P3HT film on TiO_2

polymer/O_2 complexes which quench the fluorescence of the fluorophores on the polymer chain due to intrachain energy transfer. Kinetically, this process is similar to a quantum case, where typical fluorescence trajectory for a CdSe/ZnS QD on a glass substrate shows on/off states can be seen, which

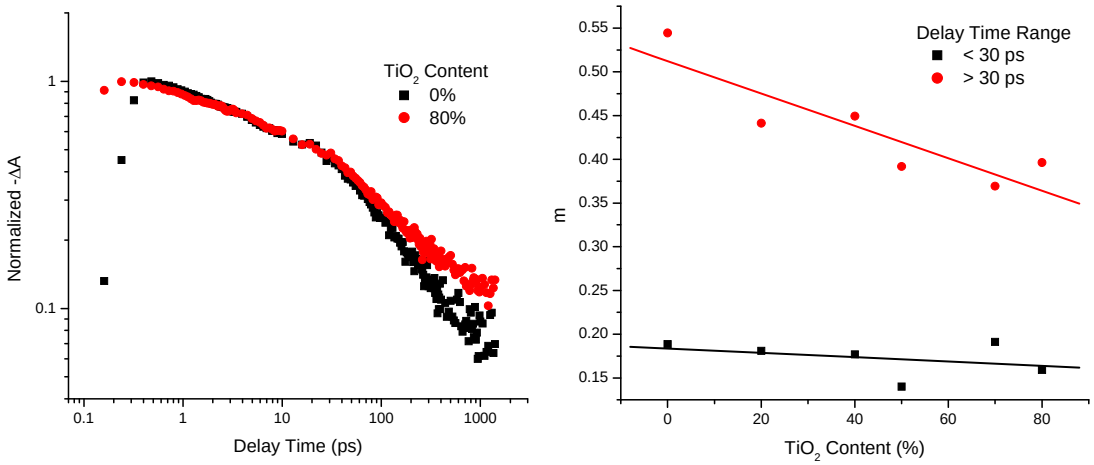

Figure 3. Ground state bleach kinetics of P3HT with various percentage of TiO_2.

have been explained previously to be due to Auger ionization/recombination. The distribution of the durations of these states typically follow a power law relationship ($P(t) \propto t^{-k}$); Shorter "On" times and longer "Off" times are observed for QDs on TiO_2 compared to those on glass. We attribute this difference to the presence of electron transfer from the QDs to TiO_2, which increases the rate of transfer to the non-fluorescent "Off" state and makes charge recombination less efficient.

2. ***Photophysical, spectroelectrochemistry and photovoltaic properties of conjugate polymer/ TiO_2 nanoparticles hybrid thin film with bulk heterojunctions***

To access dynamic photophysical processes of conjugate polymer/TiO_2 system at the nanometer scale, we have investigated the photophysical properties of previously synthesized TiO_2 nanoparticles of various

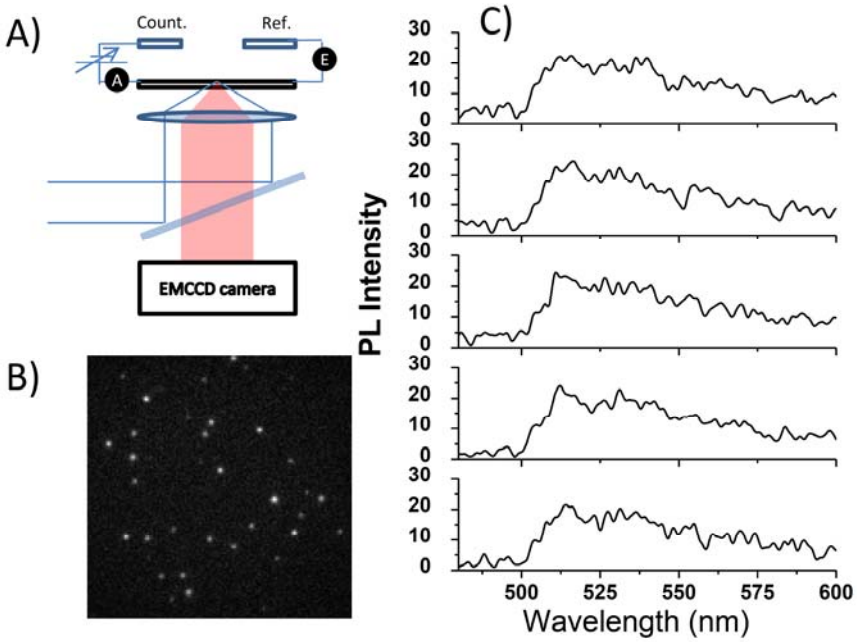

Figure 4. Single Schematic of spectroelectrochemistry setup (A), typical fluorescence image of single Ag nanoparticles (B), and fluorescence spectra of five selected silver nanoparticles (C).

shapes. The TiO_2 nanoparticles are about 10 nm in diameter and highly mono-dispersed. The photophysical properties of the blends of P3HT and TiO_2 nanoparticles were studied through a combination of steady state absorption (Figure 2a), fluorescence (Figure 2b), Raman, and transient absorption spectroscopies (Figure 2 c and d) and electrogenerated chemiluminescence. The photovoltaic properties these blends have been also characterized.

Transient absorption spectroscopy was employed to investigate the kinetics of photoinduced processes occurring in the P3HT/TiO_2 blends. Figure 2 c and d shows the transient absorption spectra of blends containing 0 and 80% TiO_2. The negative peaks at 520, 557, and 609 nm are due to the ground state bleach of P3HT. The positive peak at 660 nm visible in the 0 ps spectra is attributed to generation of polaron pairs in the P3HT. The corresponding ground state bleach decay kinetics are shown in Figure 3. The decay was fit to a power law ($-\Delta A = A_0 t^{-m}$) before and after a delay time of 30 ps. The prescence of TiO_2 does not have a significant effect in the region before 30 ps, while after TiO_2 causes slower decay rates. Qualitatively, this can be attributed to the need for photogenerated excitons to diffuse to the P3HT-TiO_2 interface, where subsequent electron injection into TiO_2 prevents regeneration of the ground state of P3HT. These results reinforce the conclusions made from our steady-state fluorescence results.

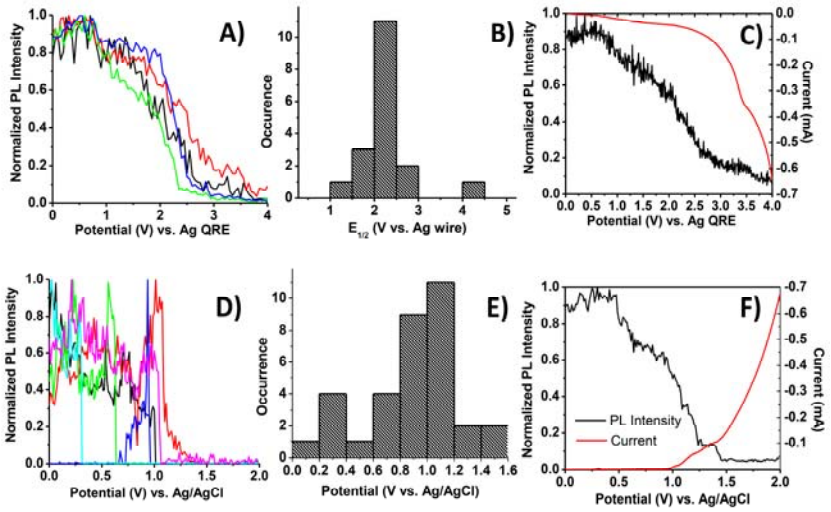

Figure 5. Single Ag nanoparticle spectroelectrochemistry. Single silver nanoparticle fluorescence trajectories and their dependences on substrate potential in acetonitrile containing 0.1 M $LiClO_4$ (A), statistical distribution of half potentials for single nanoparticles measured from the fluorescence trajectories (B), and averaged ensemble fluorescence trajectories in comparison to current dependence on substrate potential (C). Single nanoparticle fluorescence trajectories, half potential distribution, and averaged fluorescence dependence on substrate potential in aqueous 0.1 M NaOH are shown in (D), (E), and (F), respectively.

3. Spectroelectrochemistry of single fluorescent silver nanoparticles.

To compare single molecule spectroscopic behavior of MEH-PPV with another model system, we studied the spectroelectrochemical properties of individual luminescent plasmonic silver nanoparticles using the combined methods of electrochemistry and single nanoparticle spectroscopy (Figure 4). The luminescent plasmonic silver nanoparticles were synthesized via thermal reduction of silver nitrate in a glycine matrix. Individual nanoparticle fluorescence intensity is measured while the substrate electrochemical potential is controlled to oxidize the nanoparticles. Our studies show that the silver nanoparticles exhibit a range of redox potentials and their statistical distribution is dependent on the substrate material and electrolyte used. As shown in Figure 5, the spectroelectrochemical response of individual nanoparticles is used to reconstruct the bulk voltammetric properties of the silver nanoparticles without being obscured by high background signals present in direct electrochemical measurements. The observed distributions were more narrow in the aqueous phase. The fluorescence of these nanoparticles has been used to emulate voltammetric curves of single nanoparticles without being obscured by high nonfaradaic background currents. Also, no spectral shifts were observed during the oxidation of these nanoparticles, indicating that the individual emissive sites share the same energy levels.

4. Photophysical and electrochemical properties of BODIPY-sensitized TiO_2 electrode

We also studied electrochemistry, electrogenerated chemiluminescence, photoelectrochemistry and transient absorption spectroscopy of two new BODIPY (4, 4′-difluoro-4-bora-3a,4a-diaza-s-indacene) dye

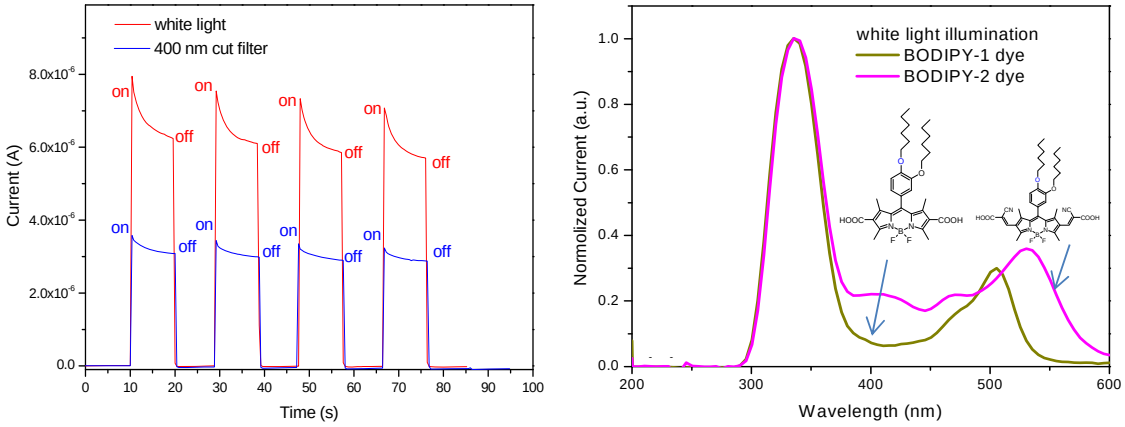

Figure 6. (Left) Photocurrent action spectra of ITO/TiO_2/BODIPY electrodes in an electrochemical cell under white light in 0.05 M LiI and 0.05 M I_2 in acetonitrile as electrolyte; and (right) short-circuit photocurrent responses of (a) ITO/TiO_2/BODIPY-1 Cell operated in short-circuit mode.

derivatives as these types of dyes have gained a great deal of attention recently because of their many desirable properties, such as high extinction coefficients, high quantum efficiencies of fluorescence, relative insensitivity to environmental perturbations, and resistance to photobleaching. We explored their

Parameter		DMF	TiO_2
BODIPY-1	τ_1 (ps)	35.68	6.94
	τ_2 (ps)	432.77	68.40
	k_{ct} (A.U. s^{-1})	7.36E+10	
BODIPY-2	τ_1 (ps)	9.08	4.29
	τ_2 (ps)	255.08	78.74
	k_{ct} (A.U. s^{-1})	9.20E+10	

Table 1. Fitting results for transient absorption decays.

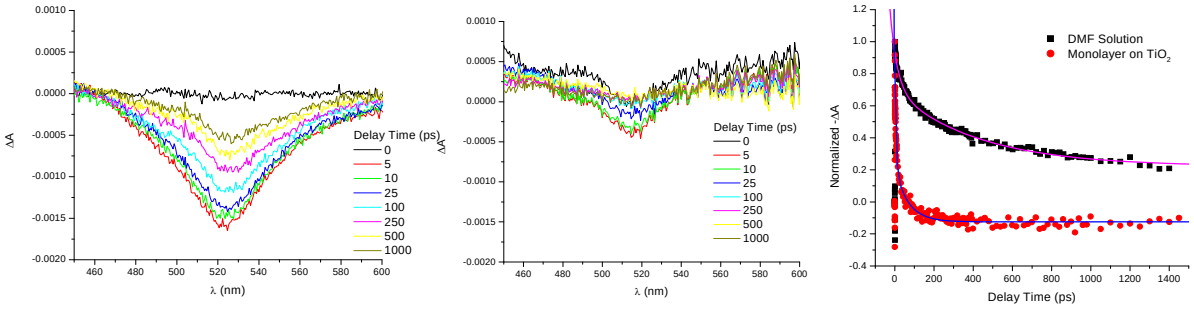

Figure 7. Transient absorption spectra of BODIPY-1 in DMF solution (a) and on TiO_2 (b) and the corresponding kinetic comparison (c).

possible application in sensitized organic hybrid solar cell. Figure 6 shows the selected photocurrent response of BODiPY dye sensitized TiO_2 electrode and corresponding action spectra.

Transient absorption spectroscopy was also to investigate the kinetics of charge transfer between the BODIPY dyes and TiO_2. Absorption, photoluminescence, photoelectrochemical action spectra and pulsed photocurrent generation have been studies. Figure 7 shows the transient absorption spectra for BODIPY-1 in DMF and on TiO_2 electrode surface, respectively. The only prominent feature is due to the ground state bleach of the dye molecule. The decay of this peak was fit to a double exponential; the results are given in Table 1. Significantly shorter lifetimes are observed on TiO_2 compared to in DMF, which can be attributed to fast forward electron transfer from the BODIPY dye molecule to TiO_2, followed by fast back electron transfer from the TiO_2 to the dye molecule which regenerates the ground state; this total charge transfer process can then be represented as $k_{ct} = (1/k_f+1/k_b)^{-1}$, where k_f and k_b are the rate constants for forward and back electron transfer, respectively. The initial charge transfer rates (calculated at 0 ps delay) were calculated assuming no significant differences in the other radiative and non-radiative decay rates between BODIPY molecules in DMF and on TiO_2. We find the charge transfer rate to be higher for the BODIPY-2 dye as compared to the BODIPY-1 dye, which is consistent with our photoelectrochemistry results discussed earlier.

5. ***Heterogeneous charge transfer activities of single polymer chain using SERS.***

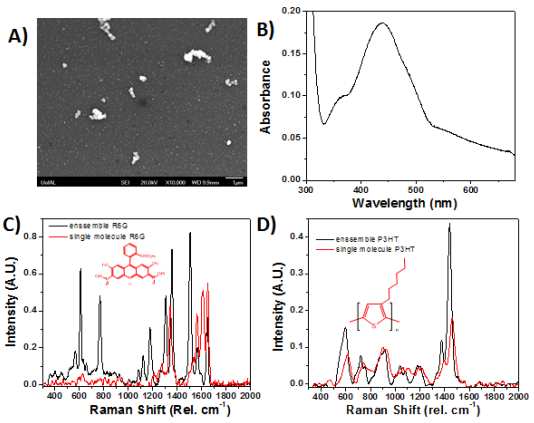

Figure 8. SEM image (A) of nanotextured silver surface for single molecule SERS, its absorption spectra (B), the comparison of SERS spectra of single R6G molecule and ensemble R6G molecules (C), and the SERS spectra of single P3HT molecule and ensemble P3HT molecules (D).

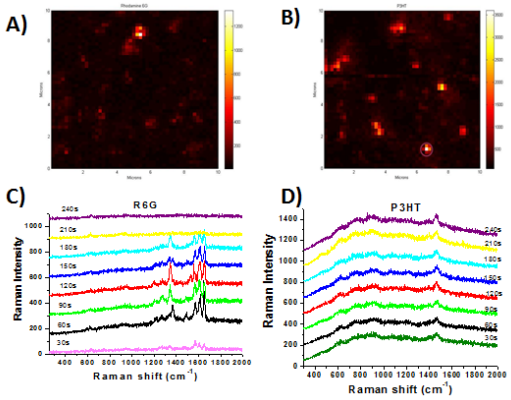

Figure 9. Panel A and B are scanning Raman image of Rhodamine 6G (R6G) and P3HT, respectively, on the Tollens silver mirror substrate shows multiple hotspots showing only a few spots contains an actual molecule. Panel C and D are the corresponding Raman spectra and time flow of the spectra of single molecule R6G and P3HT.

a. Single Molecule P3HT. This study is intended to increase the fundamental knowledge of structural and conformational dependence of single molecule Raman scattering one of the most common organic semiconductors, poly (3-hexylthiophene-2, 5-diyl) (P3HT) (Figure 8 and 9). Single molecule Raman spectra of P3HT are found to have extremely long lifetimes in comparison to the R6G single molecule trajectories due to the multiple chromophores nature contained in the conjugate polymer molecules. Single molecule spectra evolution and dynamic changes in its trajectories are recorded for polymer chains on SERS active silver substrate. Studies of the effects of four solvents, including Chlorobenzene, dichloromethane, toluene, and tetrahydrofuran, used to dissolve the polymer to spin coat the P3HT onto the Tollens silver mirror surface show good agreement with the ensemble measurements. Toluene showed the most Raman bands in its spectra but similar overall intensity was seen in the trajectories using all solvents, indicating that total photoluminescence is solvent independent while the solvent plays a critical role in defining the folding of the molecule on the surface. Time dependent Raman spectra were measured with 30 seconds per spectrum using a spectrometer. Polarization effects were confirmed by varying the

incident light polarization and help indicate the capability of local field for single molecule Raman detection and its sensitivity to incident light polarization.

A paper has been written and is undergoing internal group review. Further work needs to be performed regarding necessary experiments in order to fully clarify the results, but it is noted that single polymer Raman spectroscopy is obtained from these results on our instrumentation. Thus applications toward the TiO_2 and polymer dye interactions may be probed after further study into the electrical properties of TiO_2.

b.*SERS at single crystal TiO_2.* With single molecule and single polymer spectroscopic capabilities established, it was determined that further advancement needed to be made towards making a suitable substrate for these measurements that involved TiO_2. Anatase TiO_2 single crystals (Figure 10) have been shown to be favorable for light adsorption in solar cells, and have had a hydrothermal method developed for the controlled growth using HF. We started working on SERS at single anatase TiO_2 surface using our single molecule SERS capability in order to come to a better understanding of the charge transfer effects dependent upon the crystal shape, defects, and facial reactivity. In order to do this we start by preparing the single crystal TiO_2 using the hydrothermal reaction and HF. We then performed nitrogen doping on a portion of the TiO_2. Nitrogen doping is done because the presence of dopants, particularly nitrogen, has

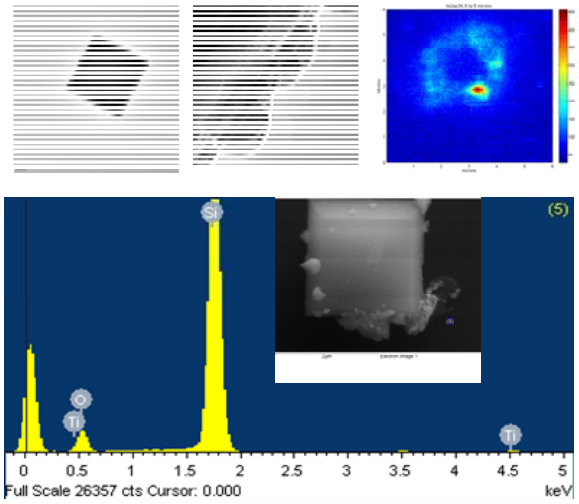

Figure 10. The TEM image shows bare TiO2 nanocrystal, (top left), clear silver growth on the nitrogen doped (top middle) sample and corresponding SERS image of r6G coated single Ag-TiO_2 crystal (top right). Bottom shows element analysis and SEM image of Ag nanoparticle coated single crystal TiO_2.

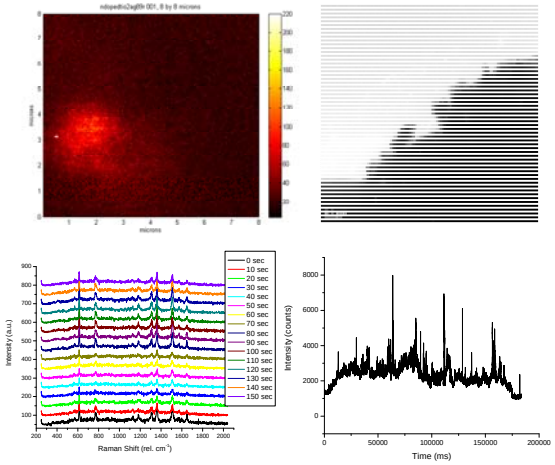

Figure 11. The optical image (top left) and the TEM image (top right) confirmed that silver did grow on the nitrogen doped TiO_2 single crystals. Once again the addition of R6G causes blinking effects to occur in the Raman spectrum (bottom left) shows the r6g Raman signature.and intensity trajectory (bottom right).

been noted to reduce the band gap making it possible for the TiO_2 to absorb visible light, not just ultraviolet light. The samples were then probed using a confocal microscope set-up, which allowed for imaging of the fluorescence of the samples, and allowed a direct probe of the silver growth sites. Further addition of rhodamine 6G (R6G) allowed Raman spectrums and images to be resolved, that when fully studied can provide details about the photoelectric effect dependent upon the crystal face **(**Figure 11**)**. Scanning electron microscopy (SEM) and transmission electron microscopy (TEM) where then used to confirm the structure, site specific x-ray diffraction to confirm the crystal and face structures, and x-ray photoelectron spectroscopy (XPS) is in the process of being performed to confirm elemental analysis.

6. Studying charge transfer between individual MEH-PPV molecules and TiO_2 via fluorescence microscopy.

Note: the following results are not published yet. A full detailed research description is included in this final report. This includes experimental and discussion.

Presented here in this report are fluorescence studies of individual MEH-PPV molecules at TiO_2 surfaces. Optical quality TiO_2 thin films were prepared which serve as both the sample substrate and an electron accepting material. The MEH-PPV: TiO_2 system constitutes a model interface for organic-inorganic hybrid solar cells. Time resolved transient absorption spectroscopy was carried out on MEH-PPV and P3HT thin films on the TiO_2 substrates in order to confirm the occurrence electron transfer at the ensemble level. Single molecule fluorescence measurements were then performed for molecules on glass and TiO_2 substrates, and an analysis of the molecules' transient "on"/"off" fluorescence switching behavior was carried out. Excitation polarization anisotropy studies are also presented which show the effects of the TiO_2 substrate morphology on the conformation of individual MEH-PPV molecules. These results are discussed within the context of previous single molecule studies, and possible directions for future single molecule studies of conjugated polymers at semiconductor substrates are discussed at the outset.

6.1 Experimental details

6.1.1 Chemicals. Titanium(IV) isopropoxide (98 %), Pluronic P123 (BASF), poly[3-hexylthiophene] (P3HT, MW = 45,000, American Dye Source), poly[2-methoxy-5-(2-ethylhexyloxy)-1,4-phenylenevinylene] (MEH-PPV, MW = 100,000, American Dye Source), poly[methyl methacrylate] (PMMA, MW = 15,000, Acros Organics), acetone (A.C.S. Spectrophotometric Grade, 99.5 %), and chloroform (A.C.S. Spectrophotometric Grade, 99.8 %, Sigma-Aldrich) were obtained from the indicated sources and used without further purification. Isopropanol, ethanol (200 proof), and concentrated HCl were standard laboratory grade and used without further purification. *The solvents used in the preparation of single molecule samples (chlorobenzene and chloroform) must be treated with extreme care to ensure they remain free from contamination.*

6.1.2 Synthesis and Characterization of TiO_2 Films. The syntheses of ordered mesoporous TiO_2 films for use in these studies were adapted from a surfactant-templated sol-gel method reported previously. In a typical synthesis, 620 µL of conc HCl was added dropwise to 1.04 g of Titanium(IV) isopropoxide under vigorous stirring. The solution was left stirring for 10 minutes. A solution of P123 in 3.7 mL of ethanol was then added dropwise under vigorous stirring and left to stir for 15 minutes. The resulting solution was used in the spin coating procedure described below. In the synthesis described above, the amount of P123 was varied to alter the resulting mesostructure of the film. 200 mg of P123 resulted in hexagonally ordered pores with a diameter of 8-9 nm. The concentration of P123 used in the synthesis of other films is given as a fraction of this concentration. P123 solutions were prepared by melting the P123 at 80 ^oC and pipetting the amount needed. Thin films were prepared by spin coating 150 µL of the TiO_2/P123 solution onto microscopic cover glass slides (Corning, 0.15 mm thick) at 7500 rpm for 60 s. The cover glass slides were cleaned via sonication for 15 min each in a mild detergent solution, 25 g L^{-1} KOH in EtOH, DI H_2O, i-PrOH, and DI H_2O, sequentially, followed by UV-O_3 cleaning (Bioforce Nanosciences Procleaner Plus) for 10 min. After spin coating, the TiO_2 films were left in a -10 ^oC freezer overnight. The films were then heated from room temperature to 400 ^oC at a ramp rate of 1 ^oC min^{-1} and were held at this temperature for 4 h. Scanning electron microscopy (SEM) images of the synthesized films were obtained using a JEOL 7000 FE-SEM with an accelerating voltage of 20 kV. Atomic force microscopy (AFM) images were obtained with a Digital Instruments Nanoscope IV AFM with bare Si AFM tips (325 kHz, 46 N m^{-1}, ~8 nm tip radius, MikroMasch). Steady-state absorption spectra were acquired with a Varian Cary 50 UV-Vis spectrophotometer.

6.1.3 Preparation and Characterization of Samples for Transient Absorption Measurements. P3HT and MEH-PPV films were prepared by spin coating from a solution in $CHCl_3$ onto clean plain cover glass and TiO_2 substrates at 1000 rpm under a N_2 atmosphere. The films were annealed by heating under an Ar atmosphere from room temperature to 140 ^oC at 10 ^oC min^{-1} and held at this temperature for 30 min. Absorption spectra of the films were acquired with a Varian Cary 50 UV-Vis spectrophotometer.

6.1.4 Transient Absorption Measurements. Transient absorption spectra were acquired with an instrument described previously. Samples were excited with a Ti-sapphire laser system (150 fs pulse width, 1 kHz

repetition rate, Clark MXR CPA-2010). The pump and probe beams were created by splitting the 775 nm fundamental output, with 95 % being frequency doubled to create 387 nm pump pulses while the other 5 % was used to generate continuum probe pulses in the visible region. A femtosecond transient absorption spectrometer (Ultrafast Systems Helios) was employed for data acquisition. In order to protect samples from oxygen and moisture, all measurements were performed in N_2-purged optical cells. The acquisition rate was 500 Hz, and the pulse fluence was 20 μJ cm^{-2}.

6.1.5 Preparation of Samples for Single Molecule Fluorescence Measurements. MEH-PPV solutions were prepared by carefully diluting a stock solution (1 μM in $CHCl_3$) with $CHCl_3$ to concentrations on the nM regime. Molecules were deposited on the substrate by spin coating 150 μL of these solutions at 1000 rpm. Where noted, an inert polymer layer was then deposited by spin coating 150 μL of a solution of PMMA in Acetone (10 mg mL^{-1}) at 1000 rpm.

6.1.6 Single Molecule Fluorescence Measurements. Single molecule fluorescence transients (fluorescence-time curves) were acquired using the instrument depicted in Figure 12.

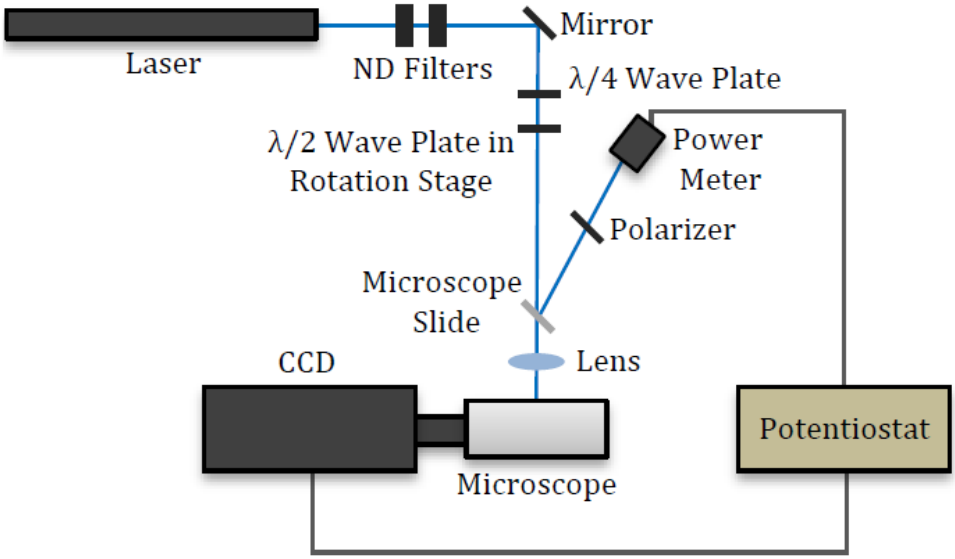

Figure 12. Optical setup for wide field fluorescence measurements. The optical path within the microscope is depicted in Figure 13.

Samples were mounted onto a standard inverted optical microscope (Olympus IX-71). Where noted, a custom flow cell was employed to allow measurements to be taken under N_2 purging. The excitation source for all measurements was a 488 nm laser (25 mW, Modu-Laser). The excitation light is directed through neutral density (ND) filters as necessary to reduce the power of the excitation beam. The beam (initially linearly polarized) can then be sent through quarter- or half-wave plates (denoted $\frac{\lambda}{4}$ and $\frac{\lambda}{2}$) to alter the polarization of the excitation beam. The $\frac{\lambda}{4}$ plate can be used to change from linear to circular polarization, while the $\frac{\lambda}{2}$ plate can be used to rotate the polarization angle of the linearly polarized excitation beam. If desired, the explicit polarization angle with the respect to the laboratory reference frame can be acquired by reflecting a small portion of the excitation beam (~4 %, using a microscope slide) through a polarizer and onto a Si photodiode. In this case, a potentiostat (CH Instruments 660C) is used to synchronize measurements at the CCD camera and Si photodiode. Before the excitation beam enters the microscope, it passes through a lens with a long focal length to slightly decollimate the excitation beam. The optical path within the microscope is depicted in Figure 13.

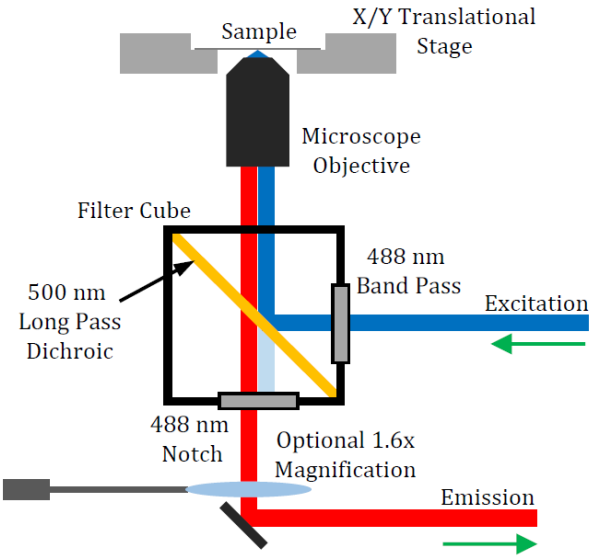

Figure 13. Optical path within the optical microscopes used for fluorescence measurements. The excitation and emission paths are offset for clarity.

The excitation beam first travels through a 488 nm band pass filter to eliminate any contributions from other fundamental lines of the laser source. The beam is then reflected off of a 500 nm long pass dichroic mirror into the microscope objective. The microscope objective, typically a 100x, NA = 1.3 oil-immersion lens, focuses the excitation light onto a small area of the sample. The resulting fluorescence is collected through the same objective and passes through the dichroic mirror, while reflected/scattering excitation light is reflected. The collected fluorescence signal is then passed through a 488 nm notch filter to remove any remaining excitation light and is directed into the detector. The fluorescence was detected using an electron multiplying charge coupled device (EM-CCD) camera (Andor iXon). The data was collected in the form of fluorescence "movies" (a stack of TIFF images) with time resolutions between 20 and 50 ms. The image dimensions were calibrated using a USAF test target (Thorlabs). Each pixel in the fluorescence images represent a 150 nm × 150 nm sample area. Single molecule fluorescence spectra were acquired using the optical setup depicted in Figure 14.

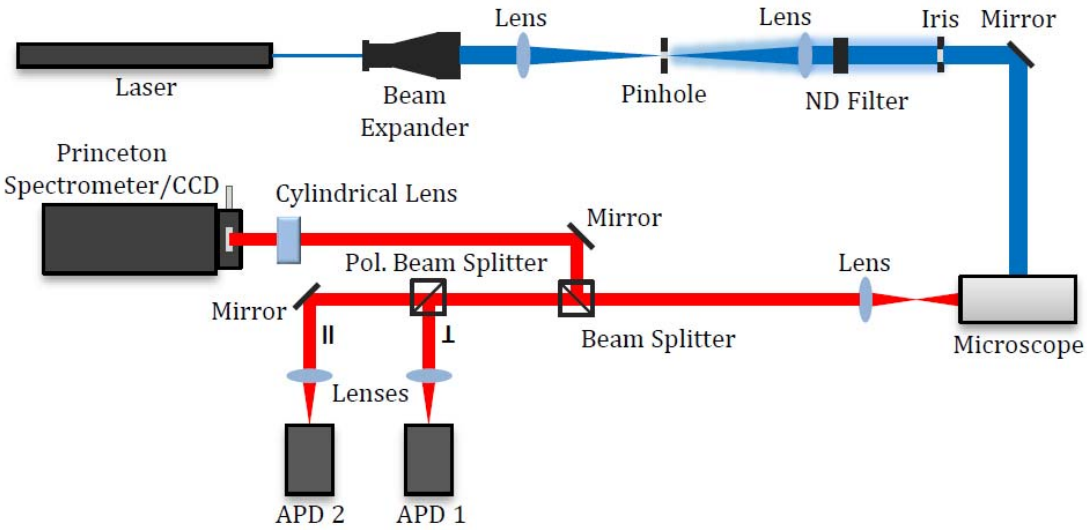

Figure 14. Optical setup used to acquire single molecule fluorescence spectra. The optical path within the microscope was identical to that given in Figure 13.

The excitation source here was the same 488 nm laser used in the wide field setup. The excitation beam was passed through a beam expander (10x, Thorlabs BE10M) before being focused through a 50 μm pinhole. After recollimation, the beam was passed through ND filters as needed to reduce the excitation power and an iris to eliminate diffracted light before passing into the microscope. The emitted fluorescence was collimated, then directed into a 50:50 beam splitter. Half of the beam was sent to a spectrometer/CCD (Princeton Instruments PI-200/Princeton Instruments Spec-10) for spectral acquisition and the other half was sent to a pair of avalanche photodiodes (APDs, PerkinElmer). A polarizing beam splitter was employed between the 50:50 beam splitter and the APDs to separate the orthogonal polarization components of the emission. The small active area (~180 μm in diameter) of the APDs and the pinhole provided a confocal optical configuration, which serves to reduce the detection of background light originating away from the focal plane. Images were first acquired by rastering the location of the excitation beam on the sample and detecting the emission intensity at the APDs. Single molecules appear as diffraction-limited ($d \cong \frac{\lambda}{2}$) spots in the image (as would any feature smaller than this limit). An area in the image which is believed to correspond to individual molecules is identified and the sample is moved so that the excitation beam resides in this area. It is at this point that spectra are acquired using the CCD camera.

6.1.7 Data Analysis. Custom MATLAB software was used to fit the transient absorption spectra, extract fluorescence transients from the raw TIFF data, acquire "on"/"off" blinking statistics, and perform polarization fitting.

6.2 Results and Discussion

6.2.1 Synthesis of TiO_2 Films. Mesoporous TiO_2 substrates for use in these studies were synthesized according to a reported literature procedure with slight modifications. Titanium (IV) isopropoxide was hydrolyzed by the addition of concentrated HCl. The resulting TiO_2 sol was mixed with a solution of the block copolymer Pluronic P123 in EtOH. This mixture was then spin coated onto to substrates to yield TiO_2-P123 thin films. During the aging process, phase separation within the films resulted in hexagonally packed cylindrical P123 micelles surrounded by TiO_2. The films were then heated to a high temperature (400 ^oC) in air to remove the P123 in the film, resulting in mesoporous TiO_2 films. The crystal structure of the films were investigated experimentally, but is predicted to be anatase based on the literature procedure that was followed. Typical SEM and AFM images of the synthesized films on Si and glass substrates, respectively, are given in Figure 15 and Figure 16, respectively.

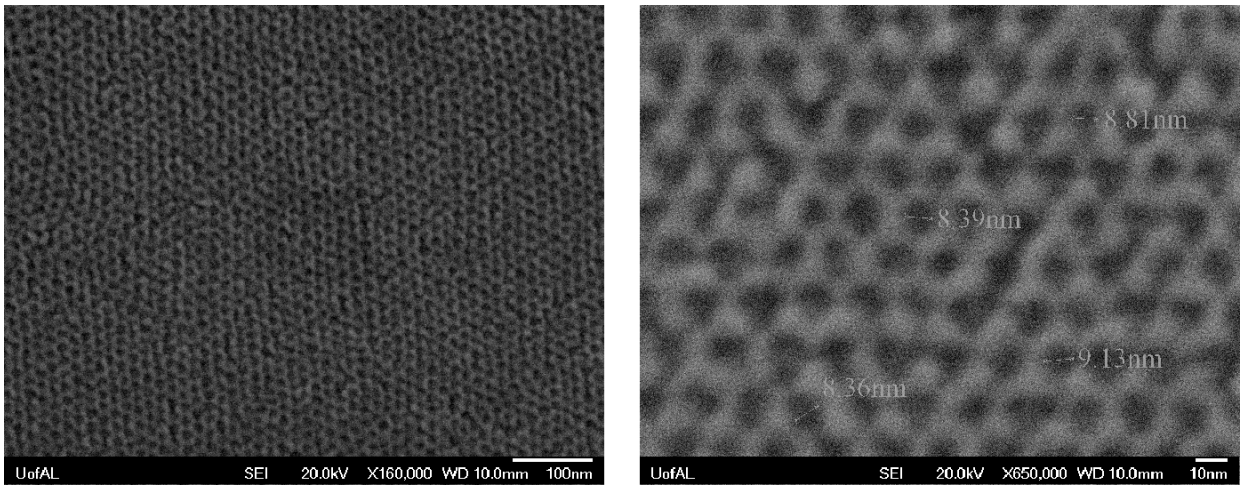

Figure 15. SEM images of a TiO_2 film prepared on Si with a P123 concentration of 54 mg mL^{-1}.

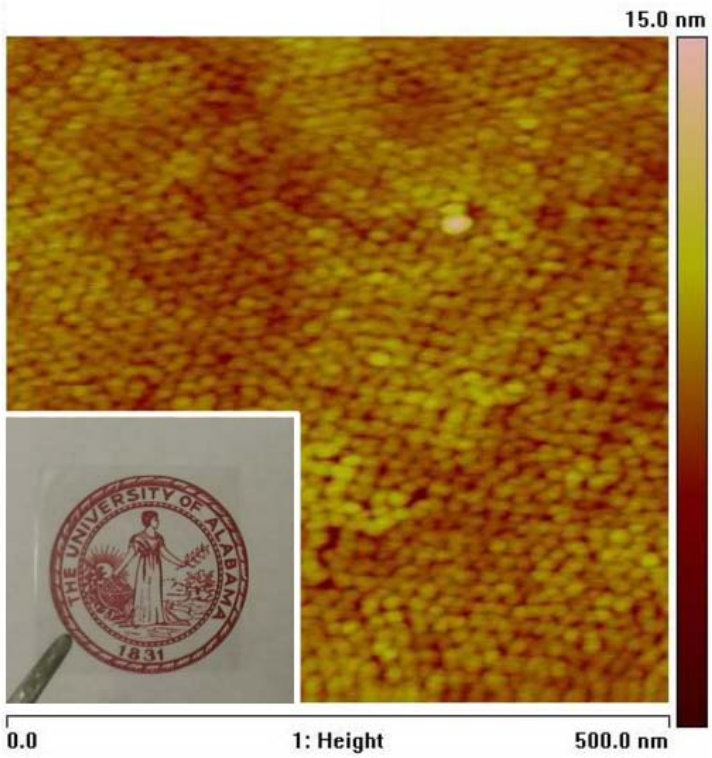

Figure 16. AFM height image of a TiO_2 film prepared on glass with a P123 concentration of 54 mg mL^{-1}. The inset is a photograph of a synthesized TiO_2 film on cover glass. Yellow and red coloring in the AFM image indicates areas of high and low height, respectively.

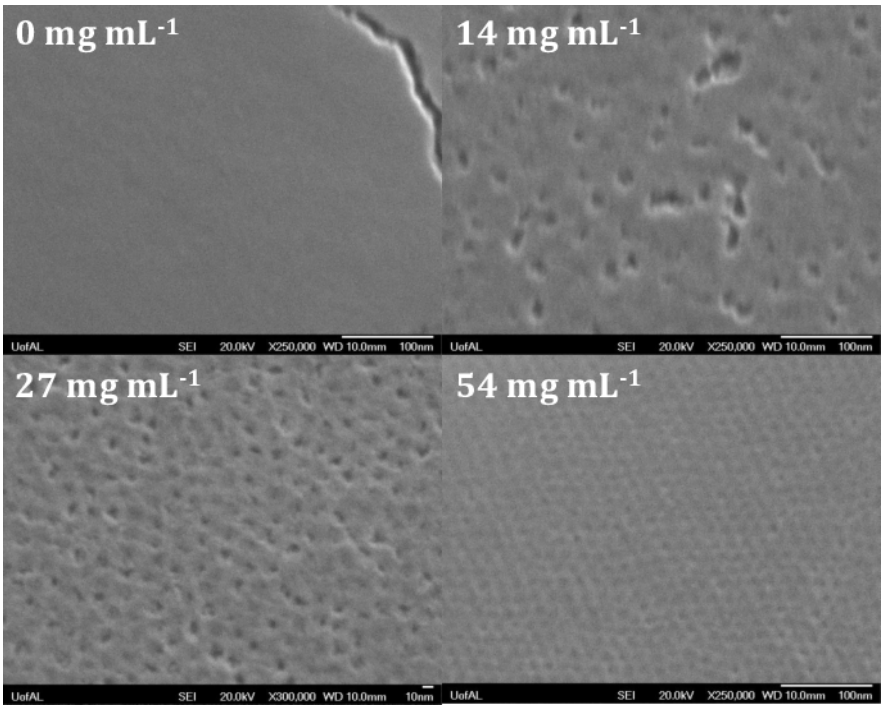

Figure 17. SEM images of TiO_2 films synthesized with the indicated concentrations of P123.

The resulting films on both substrates are highly ordered, with features between 8 and 9 nm in size. Films on Si substrates appear to consist of a continuous TiO_2 network with hexagonally arranged pores. A

closer inspection of the images, however, show that the pores are often not completely separated from one another and the true structure lies somewhere between a continuous TiO_2 network and isolated TiO_2 "nanopillars". The AFM images suggest that the TiO_2 films on glass are closer to the hexagonally packed TiO_2 nanopillar geometry. An OPV employing one of these mesoporous TiO_2 films as the electron acceptor would resemble the "ideal" device geometry. Provided the electron donor material could infiltrate the pores in the TiO_2 film, excitons generated within the light absorbing donor layer would only have to travel < 5 nm to reach a donor-acceptor heterojunction. The ability to use the same films for single molecule studies and the construction of functional devices is desirable, as it allows for more direct correlations between the fundamental studies described here and measured OPV efficiencies. In order to study the effects due to the films' mesostructure, TiO_2 films of varying porosity were synthesized. This was accomplished by simply varying the amount of P123 used in the film synthesis. This should alter the number of P123 micelles present in the TiO_2-P123 film after spin coating, but not the micelle (and therefore pore) size, which is determined by the polymer structure. SEM images of films synthesized with varying concentrations of P123 are given in Figure 17.

As predicted, reducing the concentration of P123 used in the film synthesis resulted in films with roughly the same pore diameter, but a lower pore density. At lower P123 concentrations, the pores are essentially randomly distributed across the film surface. It is also possible that the pores are oriented at random angles with respect to the substrate norm. The images provided here do not provide insight into this possibility, but it would not impact the utility of the films for use in these studies. As would be expected, TiO_2 films prepared without any surfactant were essentially flat.

6.2.2 Transient Absorption Studies. In order to confirm the synthesized TiO_2 substrates would perform well as electron accepting substrates for use in single molecule studies, transient absorption spectroscopy studies were carried out. Transient absorption spectroscopy is a time-resolved spectroscopic technique which can be used to track the evolution of photogenerated species within a sample. A "probe" pulse is first sent through the sample to obtain a baseline absorbance value, followed by a "pump" pulse to generate excite states within the sample. After a delay time, another probe pulse is used to measure the change in absorbance over time. Kinetic data is generated by varying this delay time. Results from transient absorption measurements for P3HT films on glass and TiO_2 substrates are given in Figure 18.

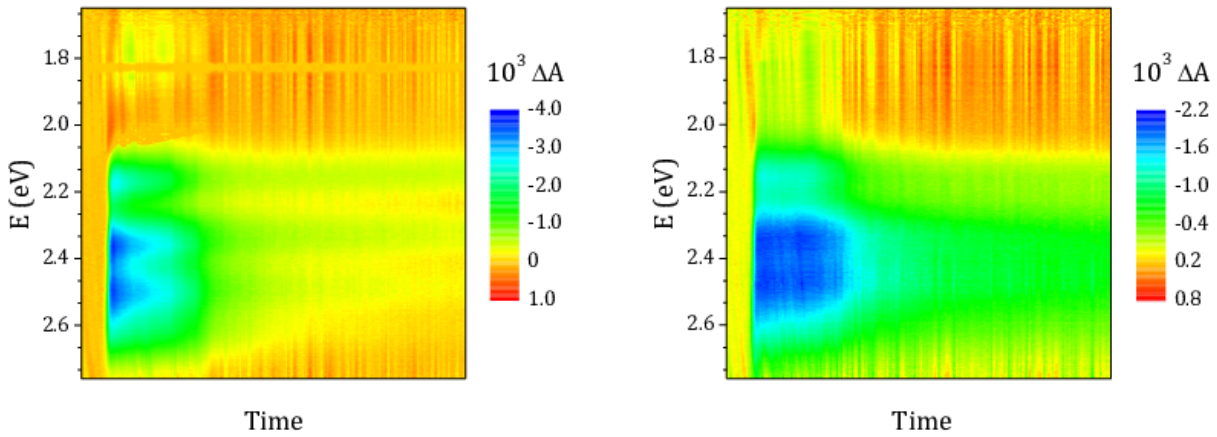

Figure 18. Transient absorption maps for annealed P3HT films on glass and TiO_2 substrates. Vertical slices represent individual spectra. Delay time increases from left to right.

These transient absorption "maps" give the change in absorbance (ΔA) as a function of photon energy (y-axis) and delay time (x-axis). The negative features at E > 2 eV are due to the "ground state bleaching" of P3HT. This arises simply from a lower number of ground state chromophores present in the film and resembles the ground state absorption spectra. Though difficult to see in Figure 18, there is a broad positive feature at E < 2 eV corresponding to the absorption of hole polarons within the film. The generation of polarons occurs at the interface as a result of exciton dissociation:

$$S_1 + CB \longrightarrow h^+ + CB^- \qquad 6.1$$

where S_1 denotes an exciton, h^+ a hole polaron localized on a P3HT chain, and CB the conduction band of TiO_2. The evolution of the polaron absorption signal therefore serves as a rather direct metric for charge transfer between P3HT and TiO_2. In order to extract useful kinetic data from the transient absorption spectra, each spectrum was fit to a combination of Gaussian functions. Example fits are given in Figure 19.

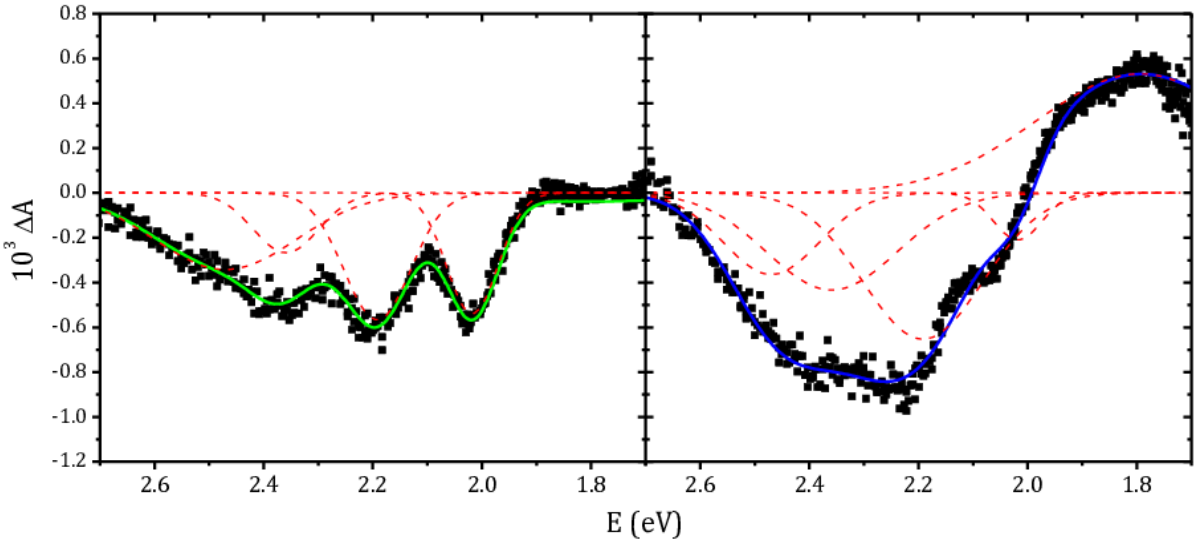

Figure 19. Transient absorption spectra at a 200 ps delay time for P3HT films on glass (left) and TiO_2 (right) substrates. Black squares are experimental data points, solid lines are fits, and red dashed lines represent contributions from individual peaks.

For the spectra of films on glass, the ground state bleaching signal was fit to a combination of 4 Gaussians (denoted B_1:B_4). The same peak positions were used to fit the spectra of films on TiO_2, along with a fifth to model the polaron absorption feature. The peak positions and widths are given in Table 2. The relative broadening of the peaks on TiO_2 is attributable to an increase in inhomogeneous broadening resulting from a higher distribution in polymer conformations induced by the mesostructured TiO_2 surface.

	Glass		TiO_2	
Peak	Position (eV)	FWHM (eV)	Position (eV)	FWHM (eV)
A_1	N/A	N/A	1.794 ± 0.006	0.450 ± 0.050
B_1	2.018 ± 0.001	0.111 ± 0.002	2.018	0.100 ± 0.010
B_2	2.192 ± 0.002	0.144 ± 0.007	2.192	0.260 ± 0.020
B_3	2.359 ± 0.005	0.140 ± 0.020	2.359	0.280 ± 0.050
B_4	2.270 ± 0.040	0.310 ± 0.050	2.470	0.210 ± 0.020

Table 2: Transient absorption peak positions and widths for P3HT films on glass and TiO_2 substrates. Errors given are standard errors from data fitting.

Ground state bleaching kinetics for films on glass and TiO_2 is given in Figure 20.

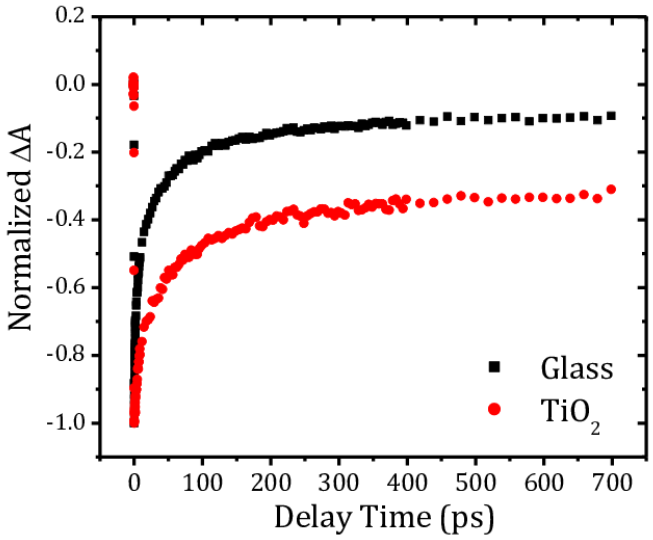

Figure 20. Normalized ground state bleaching signal for P3HT films on glass and TiO_2. Signal given was calculated from the total peak area ($B_1 + B_2 + B_3 + B_4$).

For films on both substrates, there is an essentially constant non-zero signal at long delay times. This indicates the formation of species whose lifetime is much longer than the experimental time window (< 1 ns) such as hole polarons, which have been shown to persist for up to several hundred ns in P3HT-PCBM blends. A significantly higher fraction of the original signal remains for films on TiO_2 than those on glass (~30 % vs. 10 %), which can qualitatively be attributed to exciton dissociation at the P3HT-TiO_2 interface. In order to extract quantitative information from the transient absorption data, a physical model used to derive expressions for peak areas (φ) in terms of the absorption cross-section (σ), exciton lifetime (τ_{ex}), diffusion constant (D_{ex}), film thickness (h), and initial exciton concentration (C^*_{ex}). The important expressions for the discussion here are:

$$\varphi = \frac{\Delta N(t)}{A}\left(\frac{1}{\ln 10}\int \sigma(E)dE\right) \tag{6.2}$$

$$\frac{\Delta N_{ss}(t)}{A} = -C^*_{ex}\left\{e^{-\frac{t}{\tau_{ex}}}\left[h\,\mathrm{erf}\left(\frac{h}{2(D_{ex}t)^{\frac{1}{2}}}\right)+2\left(\frac{D_{ex}t}{\pi}\right)^{\frac{1}{2}}\left(e^{-\frac{h^2}{4D_{ex}t}}-1\right)\right]+(D_{ex}\tau_{ex})^{\frac{1}{2}}\,\mathrm{erf}\left[\left(\frac{t}{\tau_{ex}}\right)^{\frac{1}{2}}\right]\right\} \tag{6.3}$$

$$\frac{\Delta N_{h^+}(t)}{A} = -C^*_{ex}(D_{ex}\tau_{ex})^{\frac{1}{2}}\,\mathrm{erf}\left[\left(\frac{t}{\tau_{ex}}\right)^{\frac{1}{2}}\right] \tag{6.4}$$

The model used assumes excitons dissociate at the polymer-TiO_2 interface much quicker than they can arrive via diffusion (i.e., exciton dissociation is a diffusion limited process). This assumption is commonly employed in the calculation of exciton diffusion lengths in conjugated polymers from fluorescence lifetime measurements. h was calculated from the optical absorption of the films at 540 nm, using a linear absorption coefficient of 1.6×10^5 cm^{-1} taken from the literature. Results of fitting the data presented in Figure 18 to this model are given in Figure 21. Fitting parameters are given in Table 3. The poor fit of the ground state bleaching signal is most likely due to the modeling of the natural exciton decay as a single exponential. This is overly optimistic, as heterogeneities in chromophore conjugation

lengths, interchain distances, etc. would result in a distribution of exciton lifetimes. The fit to the polaron absorption appears good, but the signal-to-noise ratio of the data is rather high.

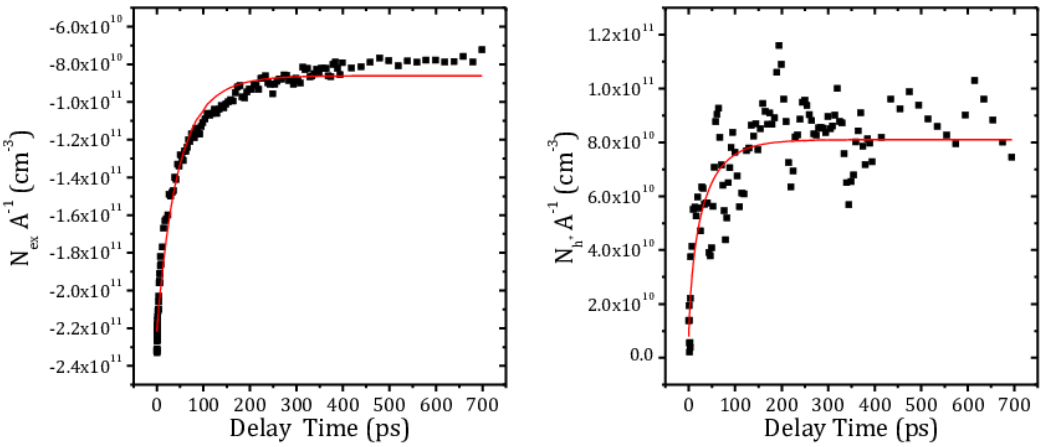

Figure 21. Fitting results for the ground state bleaching (left) and polaron absorption (right) for P3HT films on TiO_2.

	τ (ps)	D_{ex} (cm^2 s^{-1})	C^*_{ex} (cm^{-3})	R^2
P3HT GSB	67 ± 2	(4.0 ± 0.2) × 10^{-2}	(5.28 ± 0.03) × 10^{16}	0.986
P3HT Polaron	60 ± 10	N/A	N/A	0.642
MEH-PPV GSB	20 ± 1	(1.1 ± 0.1) × 10^{-3}	(8.8 ± 0.1) × 10^{16}	0.964

Table 3: Results of transient absorption kinetic fitting for P3HT and MEH-PPV films on TiO_2. GSB denotes the ground state bleaching signal. Values for D_{ex} and C^*_{ex} were not independently obtainable through fitting of the polaron absorption data (see Equation 6.4). The film thicknesses (h) of the P3HT and MEH-PPV films were estimated by optical absorption measurements to be 42 nm and 7.5 nm, respectively. Indicated errors are standard errors from data fitting.

The exciton lifetimes acquired from the ground state bleaching and polaron absorption features are the same within fitting error, which is required if the model is valid. It should be noted that this is on the lower end of the range of exciton lifetimes commonly reported. Most reported exciton lifetimes are obtained via fluorescence measurements, which are inherently skewed toward the relatively low fraction of fluorescent sites within a conjugated polymer film. In the case of P3HT, the fluorescence quantum efficiency can be well below 1 %. It would thus be expected for lifetimes obtained via transient absorption measurements to be significantly lower. The ~70 ps exciton lifetime reported here is close to those reported in the literature obtained using similar methods. An exciton diffusion length (L_{ex}) can be calculated from τ_{ex} and D_{ex} as:

$$L_{ex} = (D_{ex}\tau)^{\frac{1}{2}} \qquad 6.5$$

Using values of τ = 67 ps and D_{ex} = 0.040 cm^2 s^{-1} results in L_{ex}, which is significantly higher than the commonly accepted values. This results from an overestimation of the distance the excitons must diffuse to reach the P3HT: TiO_2 interface. Since infiltration of polymer into the TiO_2 film would reduce the "effective" film thickness, the value of D_{ex} extracted from the model employed should serve as an upper limit of the true value. As a result, L_{ex} would also serve as an upper limit, and in that sense is consistent with the reported literature. As will be seen below in the discussion of the transient absorption of MEH-PPV on TiO_2, the only substantial signal observed for MEH-PPV is due to ground state bleaching. However, the clear differences in this signal for films and glass and TiO_2 substrates can be used to demonstrate charge transfer occurs between MEH-PPV and TiO_2 at the ensemble level. Transient absorption maps for annealed MEH-PPV films on glass and TiO_2 substrates are given in Figure 22. No significant spectral signatures at energies lower than 2 eV were observed. This is to be expected, as the

highest energy absorption feature for hole polarons on MEH-PPV has been previously reported at ~1.4 eV, which is beyond the spectral window employed here. The ground state bleaching feature appears to persist for longer for films on TiO_2, consistent with electron transfer from MEH-PPV to TiO_2, preventing recover of the ground state.

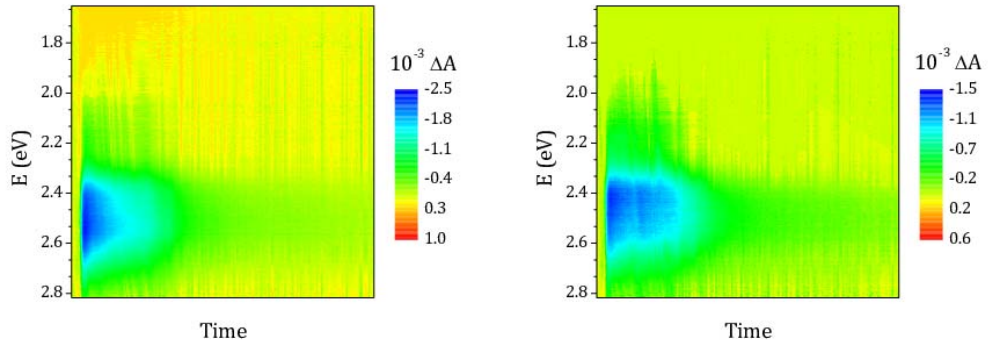

Figure 22. Transient absorption maps for annealed MEH-PPV films on glass and TiO_2 substrates. Vertical slices represent individual spectra. Delay time increases from left to right.

A kinetic analysis of the ground state bleaching feature was carried out in a similar fashion as in the P3HT case, fitting the ground state bleaching feature to a combination of Gaussian functions. The results of the kinetic analysis are given in Figure 23. There is a clear difference in the ground state bleaching dynamics for annealed MEH-PPV films on glass and TiO_2, attributable to exciton dissociation at the MEH-PPV: TiO_2 interface. The fact that no difference is seen for unannealed films supports this, as exciton diffusion in unannealed conjugated polymer films is severely limited.

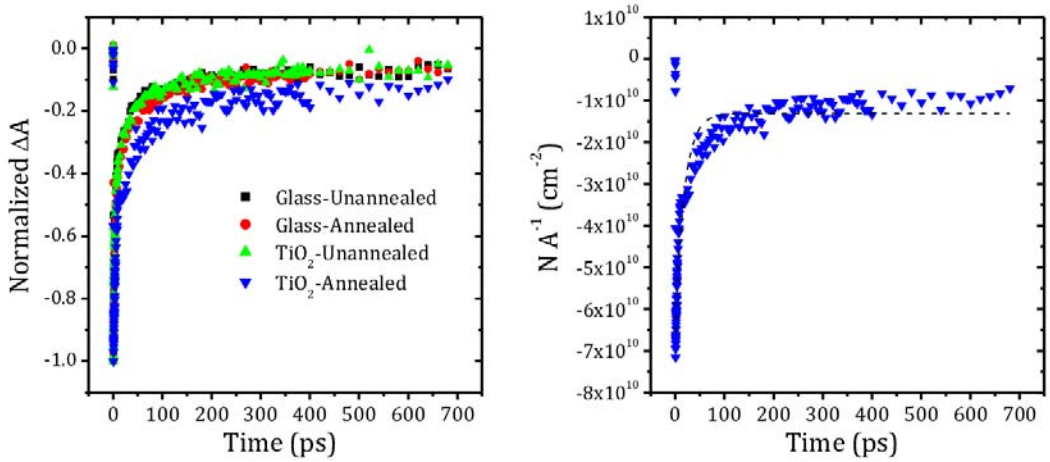

Figure 23. Comparison of normalized ground state bleaching kinetics for unannealed and annealed MEH-PPV films on glass and TiO_2 (left) and fit of ground state bleaching curve for the annealed film of TiO_2 to Equation 6.3 (right).

The kinetic data for the annealed MEH-PPV films on TiO_2 were fit to Equation 6.3 as before, and the results are given in Table 3. A linear absorption coefficient of 2×10^5 cm^{-1} at 2.45 eV was used to estimate the MEH-PPV film thickness from its optical absorption. The exciton lifetime of 20 ps is, as in the P3HT case, lower than that obtained via fluorescence measurements. In contrast to the results for P3HT, the value of D_{ex} obtained from the fit agrees well with previous reports for MEH-PPV. This may be due to a lower degree of polymer infiltration into the porous TiO_2 surface, making the geometry assumed in the derivation of Equation 6.3 more appropriate. The reconciliation of the transient absorption data for both P3HT and MEH-PPV with the model presented firmly supports that charge transfer between

conjugated polymers and the synthesized TiO_2 substrates readily occurs. Though these results are not particularly novel, they are a necessary foundation for the single molecule experiments discussed below.

6.2.3 Differences in Fluorescence Blinking Behavior on Glass and TiO_2 Substrates. Fluorescence microscopy was employed to study transient effects in charge transfer between single molecules of MEH-PPV and TiO_2. Typical single molecule fluorescence images acquired with the optical setup depicted in Figure 12 for MEH-PPV molecules on glass and TiO_2 substrates are given in Figure 24. Optical images are obtained in a wide field configuration, and contain no spectral information. Individual molecules appear in the images as diffraction limited spots, with widths of $\sim\frac{\lambda}{2}$. The samples are prepared by spin coating from a dilute (~ nM) solution in $CHCl_3$. The ideal concentration was determined by preparing samples from solutions with successively decreasing concentrations of MEH-PPV until the number of fluorophores visible on the sample was similar to that of a solvent blank.

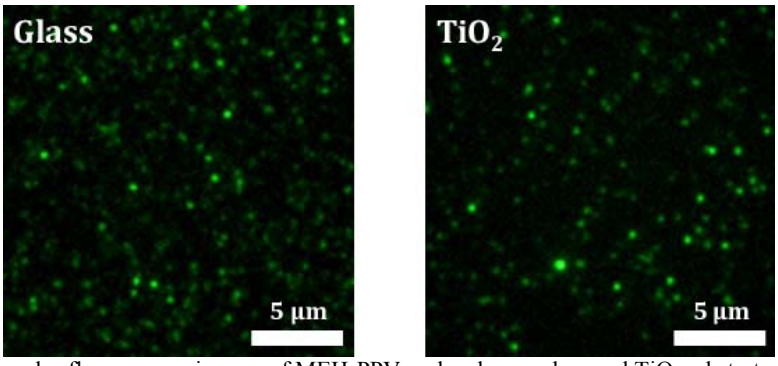

Figure 24. Example false color fluorescence images of MEH-PPV molecules on glass and TiO_2 substrates.

Though transient effects in the fluorescence of individual MEH-PPV molecules is the focus of this work, example fluorescence spectra for individual molecules and a thin film of MEH-PPV are provided in Figure 25. Immediately apparent is the differences in the spectral profile for individual molecules as compared to the bulk (thin film) sample: a portion of the single molecules exhibit peaks around 2.4 eV which are not present in the bulk spectrum. This can be attributed to an increase in the average effective conjugation length for chromophores via π-stacking interactions between adjacent polymer chains in the bulk sample. This increase in the number of low energy chromophores, or "red" sites results in rapid resonance energy transfer from "blue" chromophores within the film. Also apparent in Figure 25 is the considerable heterogeneity in peak positions and relative peak ratios from molecule to molecule. This relates directly to variations in molecular conformation, which affects the effective conjugation length of chromophores within each molecule.

Fluorescence transients for individual MEH-PPV molecules on glass and TiO_2 substrates are given in Figure 26. In total, more than 2,000 molecules on glass and 1,300 molecules on TiO_2 were analyzed. Though only 3 transients are given for molecules on each substrate in Figure 26, the differences between them are reflective of the general trends in the data.

Statistical analysis of the transients in which the on/off, or "blinking", behavior was apparent was carried out for molecules on glass and TiO_2. A threshold fluorescence intensity was set just above the background level, and the amount of time the molecule spent above or below this threshold was counted for each on/off event. The result of the statistical analysis is given in Table 4. Molecules on glass fluoresce longer before photobleaching, a higher proportion of molecules exhibit temporal fluctuations in fluorescence intensity, and these fluctuations are quicker for molecules on TiO_2.

	# Analyzed	% Blinking	$\langle t_{on} \rangle$ (s)	$\langle t_{off} \rangle$ (s)	m_{on}	m_{off}
Glass	2094	25	1.36	4.00	1.42 ± 0.04	1.23 ± 0.03
TiO_2	1345	55	0.82	3.56	1.64 ± 0.04	1.63 ± 0.03

Table 4: Statistical analysis of fluorescence blinking for MEH-PPV molecules on glass and TiO_2. $\langle \tau_{on} \rangle$ and $\langle \tau_{off} \rangle$ are the simple averages of on and off state durations. m_{on} and m_{off} are the power law fitting parameters ($P(t)=N_0 t^{-m}$). Errors given are standard errors from data fitting.

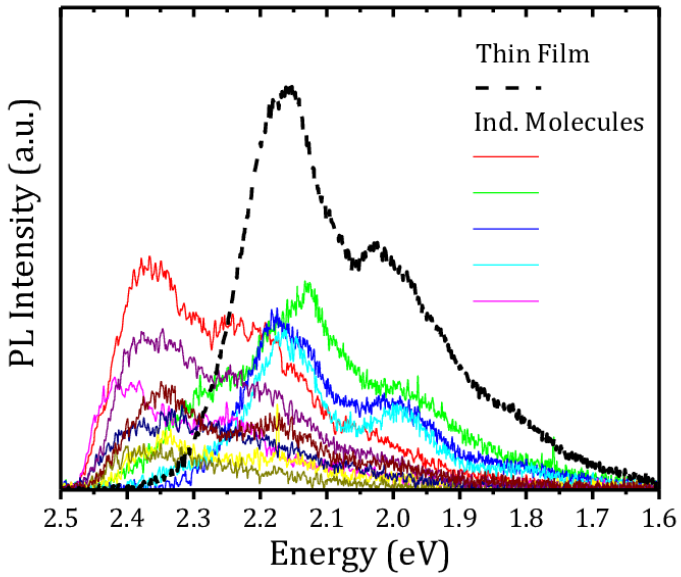

Figure 25. Example fluorescence spectra for individual MEH-PPV molecules on glass.

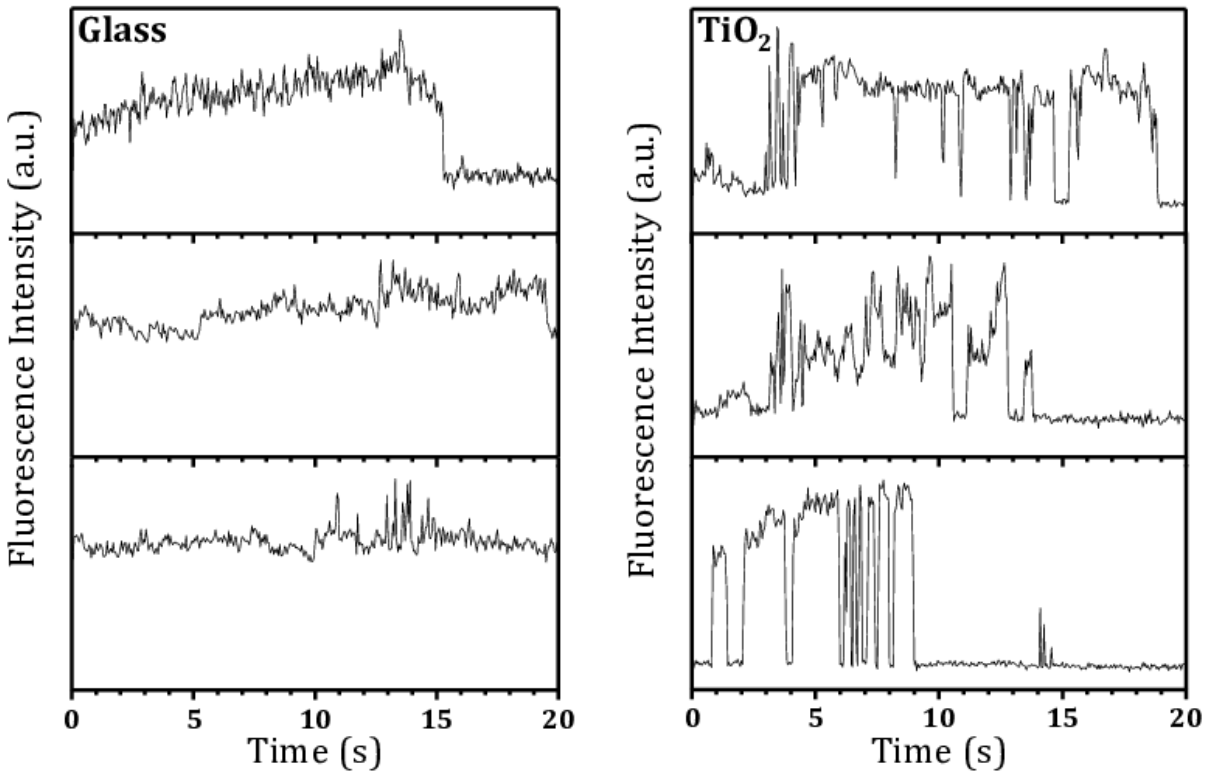

Figure 26. Example fluorescence transients for individual MEH-PPV molecules on glass and TiO_2 substrates. Excitation intensity was 130 W cm^{-2}.

Several things are striking about the results presented thus far. The fact that the fluorescence of individual MEH-PPV molecules on a TiO_2 substrate is detectable, much less comparable in intensity to that for molecules on glass, is surprising. Electron transfer between MEH-PPV and TiO_2 in thin films has occurs on ps timescales. Since exciton diffusion of nm distances is not required, one might expect (reasonably so) that electron transfer between individual MEH-PPV molecules and a TiO_2 surface would occur with essentially unit efficiency, constantly quenching their fluorescence. The data shown here contrasts with this situation, however. The quenching of individual molecules appears to be intermittent, "blinking" between "on" and "off" states on ms to s timescales. Before continuing in the discussion, one possible explanation for these observations must be addressed: that a small fraction of unquenched molecules on the surface are being probed. In this scenario, a large fraction of the molecules on the TiO_2 surface would be quenched and thus undetectable in the fluorescence measurements. Unfortunately, the optical measurements employed here can are of no use in testing this possibility; there will be no difference between the fluorescence from a region of the TiO_2 substrate with no molecules present and another with one or more efficiently quenched molecules. A physical microscopy method, such as AFM, would have to be employed in tandem with the optical measurements to provide a definitive conclusion about the presence of "dark" molecules on the substrate. Though this has not been done here, there is strong circumstantial evidence that the molecules probed on TiO_2 are representative of the entire population. If the visibility of molecules on TiO_2 was due to the occupation of inactive regions of the TiO_2, it would be expected for there to be minimal differences in their spectroscopic properties. The stark differences in blinking observed between molecules on the glass and TiO_2 strongly suggest that such a "defect occupation" scenario is invalid. Also, the images shown in Figure 24 show that the number of visible molecules on glass and TiO_2 are similar (certainly within an order of magnitude). A perfect agreement here is not to be expected, as differences in the substrate's structure and interaction with the spin coating solvent will affect the spin coating process used to deposit the molecules. So, assuming the molecules probed form a representative sample, why does this disparity between the thin film and single molecule measurements exist? The key difference in the underlying physics is the lack of intermolecular exciton/hole polaron transfer in the single molecule case. In the case of exciton dissociation at the interface of MEH-PPV and TiO_2 thin films, the resulting hole polaron can diffuse/migrate into the bulk of the film, making recombination less favorable. This would result in a longer lifetime for the h^+/CB^- state than that in the single molecule case, where the polaron is more or less confined close (within one polymer molecule) to the TiO_2 surface. Another possibility that would account for this discrepancy is that exciton dissociation might only be very favorable on localized regions of the TiO_2 surface. This would not have a profound effect for conjugated polymer films, as the lateral movement of excitons/holes parallel to the surface could ensure all generated excitons have a chance to reach an active area of the TiO_2 surface, provided a sufficient number of active sights per unit area exist. Such lateral movement of holes within organic films has been shown to impact photocatalytic processes in dye-sensitized TiO_2 systems. Whatever physical model is used to explain the visibility of individual MEH-PPV molecules on TiO_2 must also be able to explain their stark blinking behavior. The MEH-PPV polymer employed here had an average molecular weight of ~100,000, consisting of ~380 repeat units. Previous studies have shown that for MEH-PPV, the effective conjugation length for individual chromophores along the polymer chain varies within 10-20 repeat units. On average, the molecules employed here would thus consist of ~25 chromophores each. If such a large number of chromophores are behaving independently, one would expect for to any transient fluctuations in fluorescence intensity characteristic of single molecules to be "averaged out". In contrast to this expectation, the data shown in Figure 26 along with numerous previous literature reports concerning the single molecule spectroscopy of conjugated polymers show transient blinking behavior reminiscent of that for small dye molecules. This behavior can be explained by an exciton "funneling" process depicted graphically in Figure 27. In this model, excitons are transferred from high energy "blue" chromophores to successively lower energy "red" chromophores via intramolecular RET. Although all chromophores along the chain absorb incident radiation, only a small fraction emit as a result of the RET process.

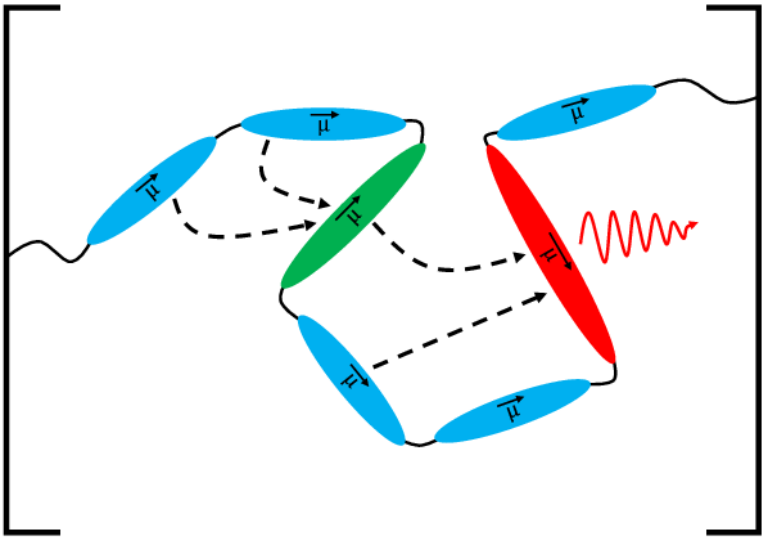

Figure 27. Depiction of the exciton "funneling" process within conjugated polymer molecules. Solid lines indicate linkages between adjacent chromophores. Dashed lines represent interchromophore RET.

For the MEH-PPV molecules on glass, the observed blinking behavior can be attributed to the formation of quenchers at "red" sites on the polymer chains. The quenchers result from photoinduced reactions with atmospheric O_2, likely through triplet states:

$$T_1 + O_2 \rightleftharpoons h^+/O_2^- \qquad 6.6$$

In these experiments, attempts to eliminate the presence of O_2 were made through the use of inert polymer (PMMA) capping layers. This was moderately successful, as only 25 % of the MEH-PPV molecules investigated on glass substrates displayed discernible blinking behavior (see Table 3). 55 % of MEH-PPV molecules on TiO_2 substrates demonstrated blinking behavior. If it is assumed that the same fraction of molecules on TiO_2 will show blinking behavior due to interactions with O_2, the fraction blinking due to the presence of TiO_2 can be estimated as:

$$f_{TiO_2} = 1 - \frac{1 - f_{tot}}{1 - f_{O_2}} = 1 - \frac{1 - 0.55}{1 - 0.25} = 40\ \% \qquad 6.7$$

A simple statistical analysis shows that of the 55 % of molecules which blink on TiO_2, only ~50 % of these are due solely to the presence of TiO_2, with ~30 % due solely to reactions with O_2 and the remainder a combination of these effects. These numbers should be kept in mind during the following discussion of blinking statistics. Blinking due to the presence of TiO_2 is presumably due to electron transfer from MEH-PPV to TiO_2:

$$S_1 + CB \underset{k_{bet}}{\overset{k_{fet}}{\rightleftharpoons}} h^+/CB^- \qquad (6.8)$$

The distribution of on and off state durations for MEH-PPV molecules on both glass and TiO_2 substrates were found to fit well to a power law distribution of the type:

$$P(t_{on}) = N_{0,on} t^{-m_{on}} \qquad P(t_{off}) = N_{0,off} t^{-m_{off}} \qquad (6.9)$$

The results of the fitting are given in Figure 28. Power law kinetics arise when a physical process cannot be described accurately by one (or even several) static exponential rate constants, instead requiring a broad distribution of such rate constants over the relevant time regime or dynamic changes in these rate constants. This type of power law dependent switching between on/off states has been previously reported for semiconductor quantum dots and small organic molecules. Several origins for this behavior have been proposed in the literature. A model which has been highly successful in explaining the blinking behavior

of semiconductor quantum dots is the formation of long lived (ms to s or longer) dark states via tunneling through a barrier whose width fluctuates over time. This blinking behavior has also been explained as the variation of non-radiative decay rates over time, which does not require the existence of long lived trap states. The agreement between the data presented here for MEH-PPV molecules on glass and TiO_2 and each of these possibilities will be discussed separately.

If the observed blinking behavior for MEH-PPV on glass were due to long lived (ms to s) dark states, the rate constants for on/off switching (k_{on} and k_{off}) would refer to:

$$T_1 + O_2 \xrightarrow{k_{off}} h^+/O_2^- \tag{6.10}$$

$$h^+/O_2^- \xrightarrow{k_{on}} S_0 + O_2 \tag{6.11}$$

The fluctuations on ms and longer times scales observed for MEH-PPV molecules on glass substrates have previously been attributed to the formation of quenchers along the polymer chain (On → Off) and the reversible elimination of these quenchers (Off → On). Intuitively, the formation of h^+/O_2^- at the dominant "red" emitter should be a well-defined process characterized by a single rate constant. To recover the power law behavior displayed in Figure 28, the barrier for h^+/O_2^- formation would have to exhibit large fluctuations over the experimental timescale. Considerable changes in this would require changes in the atmospheric concentration of O_2 and/or changes in the accessibility of the emitter to the atmosphere. Under the experimental conditions employed (ambient atmosphere, molecules embedded in a PMMA matrix), neither of these should change appreciably. For MEH-PPV on TiO_2, blinking due to discrete events could be represented as:

$$S_1 + CB \xrightarrow{k_{off}} h^+/CB^- \tag{6.12}$$

$$h^+/CB^- \xrightarrow{k_{on}} S_0 + CB \tag{6.13}$$

Some insights into this situation can be gained from reported ensemble experiments. Measurements on MEH-PPV *thin films* have shown that some charge separation persists after electron transfer for > 1 ms. This value should set an upper limit on the lifetime of the h^+/CB^- state for the single molecule case, since the resulting hole polaron is confined close (within a single molecule) to the TiO_2 surface. Considering the time resolution of these experiments (50 ms), it is unlikely that the blinking on TiO_2 could be due to the observation of individual charge transfer events. If the observation of discrete quencher formation/elimination events is not considered, the blinking process could conceptually be due to any process:

$$On \underset{k_{on}}{\overset{k_{off}}{\rightleftharpoons}} Off \tag{6.14}$$

which changes the effective non radiative decay rate(s) (k_{nr}) of the system. For a conjugated polymer molecule on TiO_2 undergoing resonance energy transfer to one emitter chromophore, the fluorescence observed from this chromophore can be modeled as:

$$I_{fl,r} = \frac{k_{rad}\tau_{1,r}}{[(1+N_d)k_{ex}]^{-1} + \tau_{1,r} + \Phi_{isc,r}\tau_t + \Phi_{fet}\tau_{h,r}} \tag{6.15}$$

where k_{rad} and k_{ex} are the radiative relaxation and excitation rates, $\tau_{1,r}$, τ_t, and $\tau_{h,r}$ are the lifetimes of the excited singlet, triplet, and h^+/CB^- states, Φ_{isc} and Φ_{fet} are the quantum efficiencies for intersystem crossing and forward electron transfer, and N_d is the number of "donor" chromophores. An exactly analogous equation could be derived for the formation of h^+/O_2^- states on glass substrates. Immediately apparent are the several variables (N_d, Φ_{fet}, $\tau_{h,r}$, etc.) which play a role in the observed fluorescence intensity. Of primary interest are changes in the forward and back electron transfer rates, which would be expected to be sensitive (presumably exponentially) to the distance between the chromophore and the TiO_2 surface. For the molecules here, which were embedded in a solid PMMA matrix, it is unlikely that a given chromophore's position would change drastically enough to account for the huge intensity fluctuations seen in Figure 26. The above discussion assumes the identity of the emitting chromophore

does not change over the course of the experiment. This is not necessarily true, however. Recent studies of model conjugated dimer molecules embedded in a PMMA matrix have shown that exciton flow (via RET) between chromophores can reverse directions over the timescale ms to s timescales considered here. This behavior is attributed to small, thermally activation molecular shifts which affect the conjugation lengths of the chromophores, switching the preferred direction for RET. So, while for the MEH-PPV molecules on TiO_2 discussed here it may be unlikely that a chromophore's position relative to the TiO_2 substrate could account for the observed blinking behavior, differences in chromophore-TiO_2 distances between chromophores could. Essentially, dynamic changes in RET pathways within the molecule would result in correlated changes in the proximity of excitons to the TiO_2 surface. Dynamic changes in RET within a molecule of this size would be a very complicated process, feasibly dependent on a multitude of rate constants for every bond rotation which would extend/decrease the conjugation for each chromophore within the molecule. It is certainly feasible for such a situation to result in power law-type kinetic behavior, but simulations are needed to confirm this. This scenario would also explain the power law blinking observed for molecules on glass substrates quite naturally, as it would be expected that these RET fluctuations would occur regardless of the substrate employed. Here, rather than chromophore-substrate distance, the blinking would be attributable to atmospheric accessibility. The differences in power law exponents for molecules on glass and TiO_2 would arise essentially from differences in the geometry of the situation. I.e., if chromophores were assumed to be lumped into "visible" and "dark" groups and the identity of the emitter switched randomly without prejudice, a 50:50 split would result in the highest frequency of switching events. One could imagine that *for the same molecular conformation*, the "dark" chromophores being those in close proximity to the substrate surface (TiO_2) or being the outermost chromophores on the molecule (glass) would result in different blinking frequencies. This naturally leads to the conclusion that if single molecule measurements of this type are going to be used to investigate charge transfer via comparison to an "inert" substrate, it is of paramount importance to ensure the observed differences are not due simply to differences in molecular conformation.

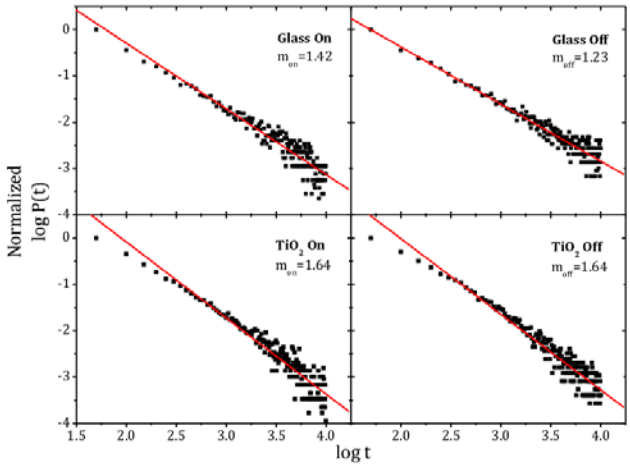

Figure 28. "On" and "off" state probability densities for MEH-PPV molecules on glass and TiO_2 substrates.

6.2.4 Effect of TiO_2 Film Morphology on Molecular Conformation. The TiO_2 substrates used in the blinking studies were of the type depicted in Figure 15. Though the electronic differences between the substrates are of interest, as these would give rise to differences in electron transfer, there are also stark geometric differences present. The glass substrates are planar, while the TiO_2 substrates are mesoporous with regular features smaller than 10 nm. It is therefore possible that the conformation of the MEH-PPV molecules is different on glass and TiO_2. Differences in polymer conformation (controlled by varying the spin coating solvent) have been shown to drastically affect the blinking behavior of conjugated polymer molecules. In order to address this possibility of differing molecular conformations due to the mesostructure of the TiO_2 substrates, excitation polarization anisotropy experiments were carried out. In these experiments, the fluorescence of individual MEH-PPV molecules was measured under low power excitation with linearly polarized light. The polarization angle was altered during the measurement,

resulting in fluorescence transients resembling the one given in Figure 29. These experiments were carried out for molecules on each of the substrates depicted in Figure 17.

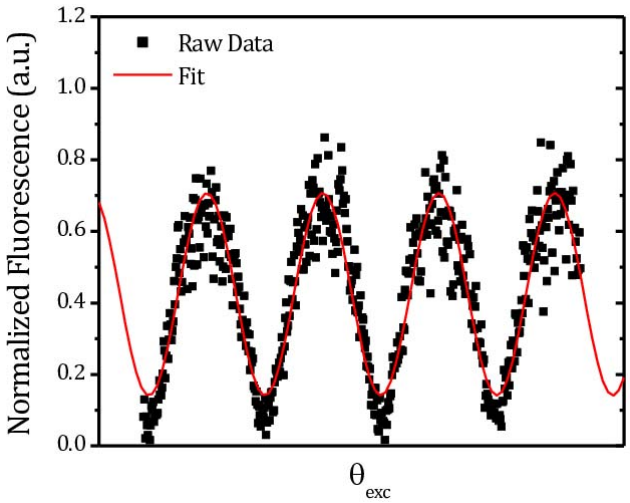

Figure 29. Example fluorescence transient obtained during a polarization anisotropy experiment. The polarization angle of the excitation light was rotated at 20^{o} s^{-1} and the time resolution was 0.5 s. The red line shows the fit to a $\cos^2$ function.

A typical polarization trajectory is given in Figure 29. As expected for a linear absorption process, the trajectory fits well to a $\cos^2$ relation:

$$I(\theta) = I_0 + (I_{max} - I_0)\cos^2\theta \tag{6.16}$$

where θ is the excitation angle. A polarization anisotropy, M, can be defined from these fitting parameters:

$$M = \frac{I_{max} - i_0}{I_{max} + i_0} \tag{6.17}$$

For the molecules considered, which are composed of ~25 individual chromophores, the measured intensity at any point in the polarization trajectory would be due to:

$$I(\theta) = I_{ex}\sum_{i=1}^{28}\sigma_i\cos^2(\theta - \phi_i) \tag{6.18}$$

where I_{ex} is the excitation intensity, σ_i is the absorption cross-section for the ith chromophore, and ϕ_i is the orientation angle of the *i*th chromophore's transition dipole. The distribution of ϕ_i will affect the observed polarization anisotropy, which provides insight into the conformation of the polymer molecule. For example, a high value of M implies high alignment of chromophores within the molecule. This is indicative of a straight, or "rod-like" conformation. If the chromophores were more or less randomly distributed, as in a totally disordered polymer molecule, a low value of M would be expected.

[P123] (mg mL^{-1})	# Analyzed	$\langle M \rangle$	$\frac{\langle I_{max} \rangle}{\langle I_{max,84} \rangle}$
54	93	0.8 ± 0.4	1.0 ± 1.7
27	78	0.7 ± 0.3	0.6 ± 0.8
14	73	0.7 ± 0.4	0.5 ± 0.8
0	49	0.7 ± 0.3	0.5 ± 0.9

Table 4: Average excitation polarization anisotropy ($\langle M \rangle$) and average relative maximum fluorescence intensity ($\langle I_{max} \rangle$) for MEH-PPV molecules on TiO_2 substrates prepared with different P123 concentrations. The fluorescence intensities are normalized to that for the 54 mg mL^{-1} film.

This fitting was carried out for a large number of molecules on TiO_2 substrates of varying porosity. The porosity was altered by controlling the amount of templating surfactant, P123, used in the film synthesis, with higher concentrations resulting in films with higher ordering and porosity. The results of these experiments are summarized in Table 4. There are no statistically significant differences in the excitation anisotropy (M) or maximum emission intensity (I_{max}) found between molecules prepared on the different substrates. This is consistent with previous reports, which show that conjugated polymer molecules exhibit significant "memory" of the solvent system from which they were cast. The obtained M values of around 0.7 is consistent with theoretical expectations for rod-like polymer conformations.

6.3 Conclusions

These experiments further demonstrate the power of using single molecule techniques to study interfacial processes. The fluorescence of individual MEH-PPV molecules on glass and mesoporous TiO_2 substrates was demonstrated to be detectable. The detection of single molecule fluorescence for MEH-PPV on TiO_2 is surprising due to the expectation of quenching due to ultrafast electron transfer to the conduction band of TiO_2. The transient absorption studies presented demonstrated that this occurs in thin films of P3HT and MEH-PPV films on the TiO_2 substrates. The visibility of individual MEH-PPV molecules TiO_2 on substrates is attributed to efficient intramolecular RET to a low energy chromophore located away from the TiO_2 surface.

The transient on/off blinking behavior of individual MEH-PPV molecules on glass and TiO_2 was analyzed statistically. The lifetime distributions of both the "on" and "off" states for molecules on glass and TiO_2 substrates were found to follow a power law relationship. Fluctuations in the intramolecular RET process are a feasible explanation for this transient on/off blinking behavior on both substrates. Differences in the geometric distribution of "dark" chromophores within the molecules on glass (outermost chromophores) and TiO_2 (chromophores closest to the TiO_2 surface) could possibly account for the differences in m_{on}/m_{off} values, but quantitative conclusions concerning the kinetics of these systems cannot be reached without detailed simulations and further experiments evaluating the temperature dependence of this process.

Excitation polarization anisotropy experiments were carried out to assess the impact of the mesostructure of the TiO_2 films on the conformation of the MEH-PPV molecules. No statistically significant differences were observed between molecules on TiO_2 films with varying porosities, ranging from films with close-packed hexagonal pores to planar films. The lack of observed differences in the polarization anisotropy measurements strongly suggest that the mesostructure of the TiO_2 films does not appreciably affect polymer conformation. This provides additional evidence that the observed differences in blinking behavior are due to electron transfer between the MEH-PPV molecules and TiO_2.

Though these initial studies demonstrate that electron transfer from individual conjugated polymer molecules and semiconductor surfaces results in detectable changes in the molecules' fluorescence intermittency, this carries no inherent utility or insights into the construction of OPV devices. Most desirably, there would be some quantity calculable from the single molecule data to evaluate how effectively a given molecule would operate in an OPV. In the language of the analysis presented, ideal molecules would display large m_{on} values and small m_{off} values (i.e., the duration of "off" states in which the molecule's fluorescence is quenched are much longer than the "on" states). An idealized molecule would funnel excitons very efficiently to the TiO_2 surface where they would be instantaneously dissociated with no possibility of recombination. The overall efficiency of this process will depend on several molecular parameters, including the position of the lowest energy chromophore with respect to the acceptor surface, the energy alignment between this chromophore the density of states of the acceptor, the stability of RET pathways within the molecule, etc.

The type of single molecule studies presented here have the potential to be applied to systematically study the effects of varying these parameters on forward/back electron transfer at the donor-acceptor interface. Several experiments can be carried out to evaluate the effects of different steps in device construction. Polymer conformation could be controlled via the spin coating solvent and/or annealing temperature. The minimum chromophore-acceptor distance could be altered by functionalizing the acceptor surface with a "molecular spacer." Such experiments hold the potential to produce useful insights into the construction of better OPV devices.

7. Electrogenerated chemiluminescence (ECL) spectroelectrochemistry of single Au nanoparticles for rapid determination of local electrocatalytic events.

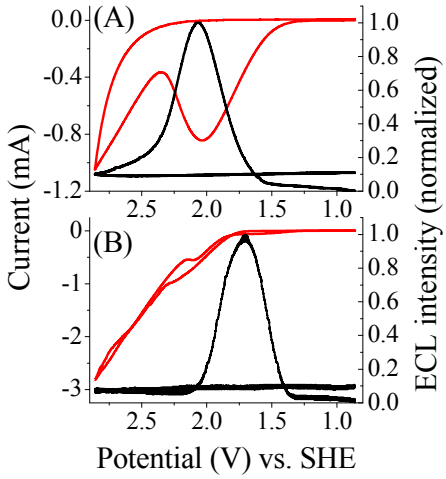

Figure 30. Current (red) and ECL (black) responses to electrode potential at bare ITO (A) and Au disc (B) electrodes in an ECL solution contains 0.1 M TrPA, 5 mM $Ru(bpy)_3Cl_2$ and 0.1 M PBS buffer at a pH of 7.4. Potential scan rate: 100 mV/sec. ECL was collected by a photomultiplier tube (PMT).

(Note: the following results are to be submitted soon. Full description of this work is included in this final report)

We developed a spectroelectrochemistry method for rapid determination of both nanoparticle (NP) size

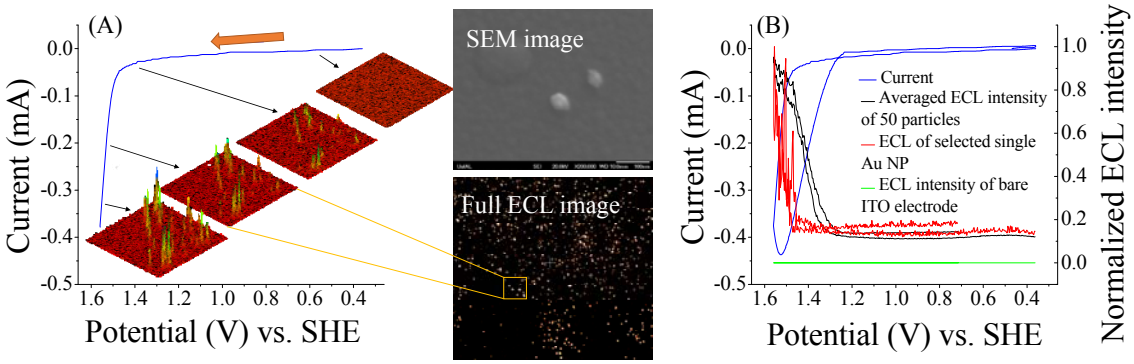

Figure 31. (A) The anodic current response of an Au NP modified ITO electrode to substrate potential linearly scanned in the indicated direction at 100 mV/sec, and corresponding 3D images (10 µm × 10 µm) of collected ECL from single Au NPs from selected region of the inset full ECL image (50 µm × 50 µm). Typical SEM image of electrodeposited Au NPs is shown in inset image above full ECL image. (B) ECL and current responses to electrode potential at an ITO electrode coated with Au NPs with average particle size of 29 nm; Spatial distribution of ECL at the ITO electrode was collected using an EM-CCD camera and analyzed to compare ECL response of one single Au NP, bare ITO surface, and average signal of 50 Au NPs.

and local ECL signal from single Au NPs electrodeposited on an ITO substrate. Correlation of particle size and ECL intensity for each individual Au NPs is obtained with the assistant of Au catalyzed ECL, dark field scattering, and aluminum (Al) indexing methods. In contrast to dark field light scattering spectroelectrochemistry technique, which would support rapid size determination of plasmonic active NPs and tracking redox activities of single metallic NP, the present ECL experiment provides a more efficient method for detecting catalyzed redox reactions on Au NPs.

A three electrode system was used to electrodeposit Au NPs on ITO glass and ECL generation was carried out in the same cell with a different solution. ECL was detected by an Electron Multiplying Charge-Coupled Device (EM-CCD) camera and analyzed using custom MATLAB programs as described in our previous publications. Brief ECL mechanism for $Ru(bpy)_3^{2+}$ and TrPA is described here. Both $Ru(bpy)_3^{2+}$ and TrPA are subject to be oxidized to produce $Ru(bpy)_3^{3+}$ and TrPA radicals, respectively, and these two energetic redox species will react to produce excited state of $Ru(bpy)_3^{2+}$ then emit light. Oxidation of TrPA is kinetically favorable at Au electrode than ITO electrode. As shown in Figure 1A, no appreciable ECL signal is detected at bare ITO electrode at a potential as low as 1.50 V (vs. SHE) unless the potential is scanned to 1.70 V vs. SHE. In contrast, efficient ECL can be produced at an Au electrode as shown in Figure 1B at a potential near 1.50 V (vs. SHE). Similar catalytic activity has also been observed on Au particles at TiO_2 substrate, CdS thin films and glassy carbon electrode. To obtain single NP detection sensitivity with ECL method, Au NPs were electrodeposited on an ITO electrode. The presence of Au NPs would enhance the oxidation of TrPA as suggested by the results of Figure 30 thus catalyze the ECL reaction for single particle imaging studies. Such metallic NP catalyzed ECL reactions have been reported before. For instance, platinum NPs as well as palladium NPs can catalyze the formation of excited state N-methylacridone that emits ECL.

Figure 31A shows current and selected ECL images of single Au NPs electrodeposited on ITO surface as we scanned the electrode potential. No pronounced redox features were observed at ITO after being coated with Au NPs because its current was dominated by ITO background charging current at low potential region and its sluggish redox reaction current at higher potential region. Individual Au NPs clearly produce ECL signals and the spatial distribution and intensity were found to be dependent on the location and sizes of Au NPs. The lower right insert of Figure 31A shows the full ECL image of Au NPs with lower resolution than the ones shown along the current curve. It should be noted that the ITO substrate can also generate ECL at high over potentials but the kinetics of the ECL reaction is very sluggish and would not generate appreciable ECL at 1.50 V (vs. SHE). After analyzing the ECL images carefully, we plot the overall current and ECL signals from single and averaged Au NPs in Figure 2B to compare with ITO electrode. Clearly ECL generated by Au NPs is much stronger than that generated by the ITO substrate (green curve in Figure 31B).

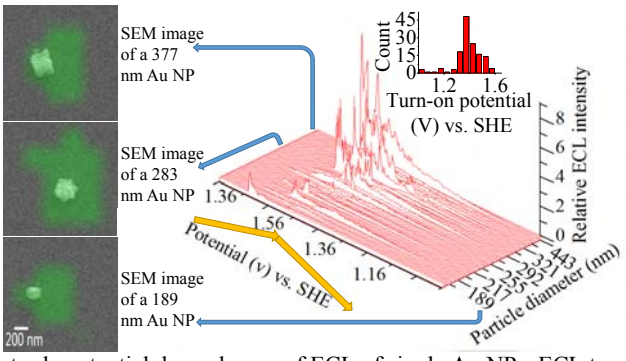

Figure 32. Particle size and electrode potential dependences of ECL of single Au NPs. ECL traces from 61 individual Au NPs are extracted from ECL image and plotted with their particle sizes size measured using SEM with the assistant of an indexed ITO electrode. Electrode potential was scanned 0.36 to 1.56 V (vs. SHE) and then reversed back to 0.36 V at a scan rate of 100 mV/sec (as indicated by yellow arrows). SEM images of three Au NPs are selected and overlapped with their ECL images in semi-transparent green color are shown on the left panel. The ECL image indicates the summed ECL of all electrode potential. The inset figure on the upper right panel is the statistical distribution of turn-on potentials of ECL from single Au NPs.

To further understand the structure-function relationship of single Au NP ECL, ECL signals of individual Au NPs were extracted using our custom MATLAB programs to examine their dependences on electrode potential and particle size with the assistance of Al indexed ITO glass. The Al indexed ITO

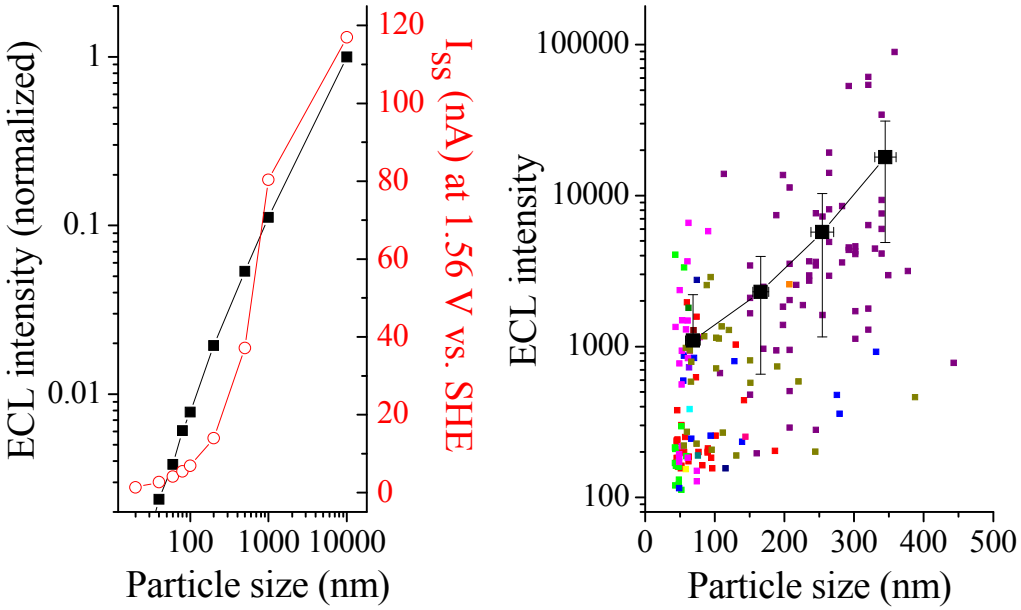

Figure 33. (A) Simulated ECL intensity versus Au NP diameter along with the steady state current at 1.56 V vs. SHE in 10 mM $Ru(bpy)_3^{2+}$ of 0.1 M TrPA buffered with PBS buffer with pH=7.5. (B) Measured ECL intensity versus particle diameter of each single Au NP. Data points of various colors are Au NP diameters measured by either dark field scattering or SEM. They are plotted in different colors because they are measured in different samples. Connected solid squares in black are the average ECL intensity of particles with indicated average Au NP sizes.

allowed us to perform ECL and SEM studies for Au NPs in the same area. With this capability, both SEM and ECL images were obtained and overlaid to determine the relationship between ECL and Au NP morphology at various electrode potentials. As shown in Figure 32, ECL responses of 61 Au NPs show strong particle size dependence as electrode substrate potential was scanned from 0.36 V up to 1.56 V and then reversed back to 0.36 V (vs. SHE) at a scan rate of 100 mV/sec. Clearly it shows a trend of increase in ECL intensity as the particle size increases. It should also be noted that NPs can give very different ECL intensity even they have similar size. This heterogeneity is due to shape and local conductivity variation as revealed by our dark field spectroelectrochemistry studies.[18] Three insert images on left panel are SEM overlaid with summed ECL from the entire potential range. The offset of the SEM and ECL images is expected simply because of the optical diffraction limit of ECL imaging and also the fact that we summed all ECL frames from the entire scanned potentials and projected them onto a two dimensional image while ignoring the detailed blinking events. Heterogeneity of the ECL signal on single NPs is also reflected in turn-on potentials as shown by the inset of Figure 32. An average turn-on potential of 1.39 V vs. SHE is obtained and the wide distribution is attributed to heterogeneities in Au NP shape, local conductivity variation of ITO electrode, and its contact with Au NPs.

Another interesting phenomenon shown in the ECL responses to electrode potential at Au NPs is that the ECL signal generated at individual NPs displays “blinking” (intermittent, on/off type behavior) if the gold particles are smaller than 100 nm. ECL signal of Au NPs larger than 100 nm also shows significant variation over the scanning potential as shown in Figure 32. To our knowledge, this is the first report of such ECL blinking phenomenon and further investigation is needed in order to fully understand its mechanism. A possible explanation is that Au NP surface has only a few active sites which can efficiently catalyze the ECL reactions at the studied overpotential. Each active site goes through a “deactivation” process while catalyzing ECL reactions. For instance, some species could occupy the catalytic site for a

long period of time, or the low coordination site may reversibly complex with amine species. Lack of enough active sites on small Au nanoparticles results in intermittency. Another possible explanation is that small Au NPs can be easily affected by ECL light around them and their change transfer ability is

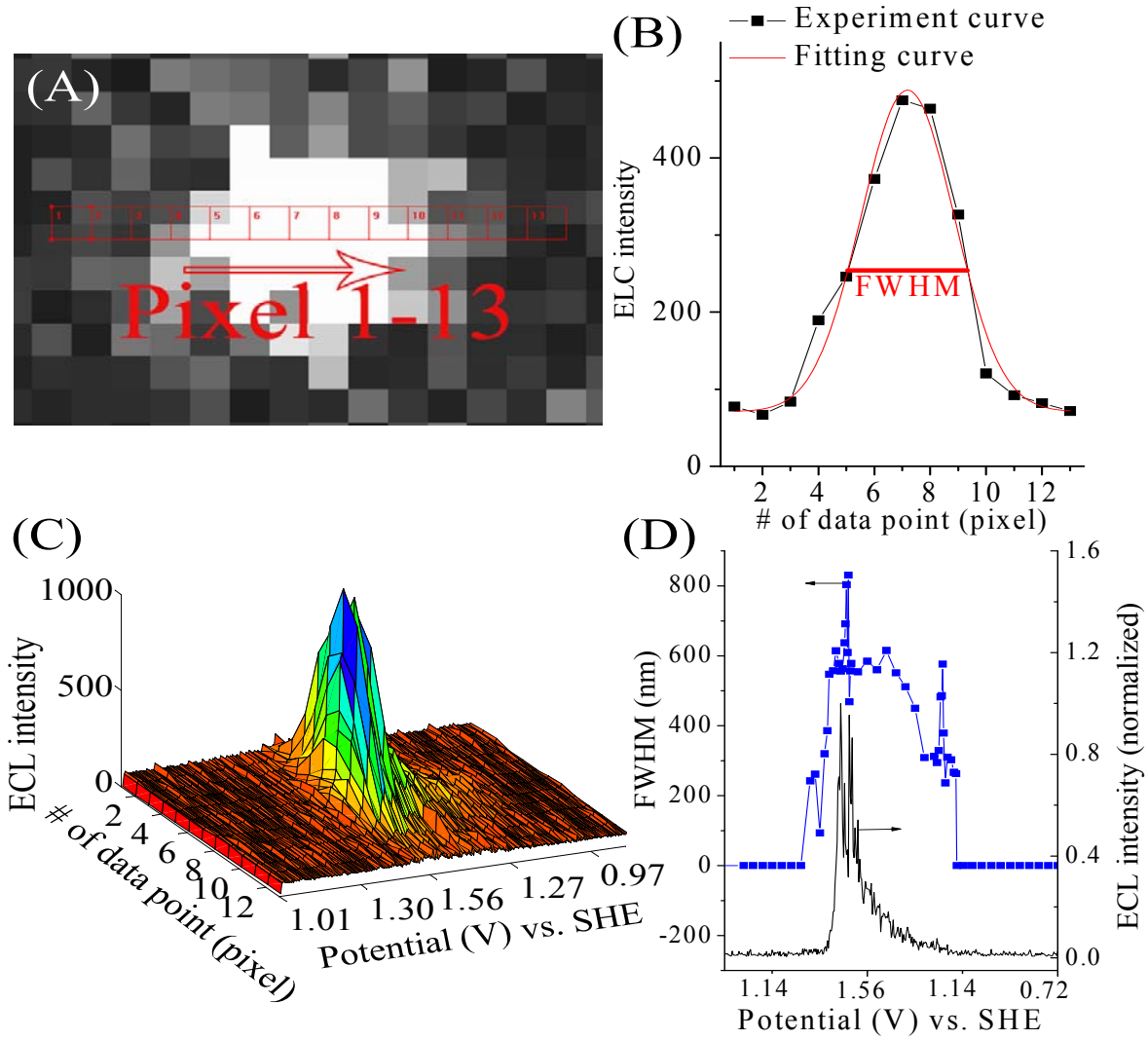

Figure 34. (A) 13 data points are selected (red squares) across the ECL image of a single Au NP (with a diameter of 80 nm) and numbered as 1 to 13 from left to right. Each data point represents a pixel of our EM-CCD camera with imaging size of 156.25 nm per pixel. (B) ECL intensity profile at 1.50 V vs. SHE is plotted against its position indicated in panel A. The experiment ECL intensity curve is fitted with Gaussian function (red curve) with its FWHM calculated and shown in panel D. (C) A 3D image of ECL intensity profile from panel B as the function of electrode potential canned from 1.01 V to 1.56 V and reversed to 0.97 V vs. SHE at scan rate of 100 mV/s. (D) FWHM values (in nm, blue curve) of ECL profile and ECL intensity (black) at different potentials scanned in the same rate and direction as panel C.

weaken, which leads to decreased ECL intensity. Then, the Au NPs can restore the change transfer ability and be observed to blink. The absorption peak of Au NPs smaller than 100 nm is between 500 and 600 nm, which largely overlaps with the ECL spectrum peak of $Ru(bpy)_3^{2+}$ at around 610 nm. This means that it's possible for Au NPs to absorb ECL light. It is also possible that charge transfer from ITO substrate to electrolyte in solution through Au NPs become discontinuous due to quantum size effect when particles are small enough.

We hypothesize that the total ECL intensity from single Au NPs will linearly increase with the particle diameter if the diameter of the particle is less than 1 μm. This is shown by our predicted trend in Figure 33A obtained by using finite difference methods with three charge transfer reactions, and nine other homogenous chemical reactions as discussed by Wightman and coworkers in their report. In this simulation, all redox and intermediates are assumed to have no absorption onto Au NPs, and the mass transfer coefficient remain the same as the one in bulk solution near the nanostructure electrode, and mass transfer and kinetics are similar to that for a bulk electrode. The ECL intensity simulation result generally agrees with experimental data: correlation of ECL peak intensity and corresponding particle size of more than a hundred Au NPs with particle size from 30 to 400 nm electrodeposited at different conditions are shown in Figure 33B. ECL intensities of single Au NPs were correlated directly with particle sizes as measured either by SEM directly or dark field scattering (DFS) method as we shown previously. DFS can be used to determine the size of an Au NP more rapidly with the assistant of SEM, thus it has been proved to be more effective to provide an effective means to measure Au NP sizes and compare directly their ECL. This instrument capability allowed us to obtain both particle size and ECL intensity of more than 100 Au NPs as shown in Figure 33.

The large spread in ECL intensity is mainly due to the heterogeneities in particle size, shape, and local contact resistance to ITO as well as variation in local conductivity of ITO. The calculated ECL and current increase as a function of diameter is slower for particles >1 μm (Figure 33A) due to the increase of the diffusion layer thickness and differences in the concentration profiles as well as the short lifetime of radical ions near the large electrode. We also predict the cyclic voltammetry (CV) and ECL response, and the corresponding concentration profiles of all intermediates involved in the ECL generation at a 60 nm Au NPs. The ECL images generated at Au NPs as big as 1 μm can block the central area of the ECL in our inverted ECL collection configuration to give a ring-like ECL pattern.

Figure 34 shows that ECL spot size dependence of a selected Au NP (80 nm) on electrode potential. Typical ECL frame of the selected Au NP is shown in Figure 34A with its measured and fitted ECL cross-sections shown in Figure 5B. Potential dependence of the measured ECL cross-section is shown in Figure 34C. The ECL intensity curve across highlighted in Figure 34A is fitted with a Gaussian function and its full wave at half maximum (FWHM) is calculated from the fitted curve to represent the size of the ECL spot (Figure 34B). Then FWHM values calculated from selected frames of the ECL image are plotted vs. potential in Figure 34D, which shows the FWHM start increasing from the optical diffraction limited spot size of 300 nm and expands with the increase of ECL intensity when the potential is scanned up to 1.56 V vs. SHE. Then, FWHM remains relatively stable than ECL intensity near around 600 nm accompanied with a sharp distribution of 800 nm FWHM until ECL becomes too weak at a lower potential level, indicating the ECL is a mass transfer controlled light emitting process with its light emitting species diffused as far as 800 nm region from the center of Au NPs. This is consistent with our calculated results of ECL profile for a 60 nm Au NP.

In addition to investigating the size dependence of the local ECL activities of electrodeposited Au NPs, our preliminary study shows that we are able to image pre-prepared single Au nanowires (Au NWs) and NPs using ECL. Our results also show that for Au NPs prepared using wet chemistry which have a narrower size distribution than electrodeposited particles, their ECL intensity distribution is much narrower.

To conclude, ECL generated at single Au NPs was observed and correlated with particle size and electrode potential. Simulations show that the ECL intensity should linearly increase with particle size if the diameter of the particle is less than 1 μm, which agrees with the experimental data quantitatively. This shows that this ECL system has promising potential to be used in rapidly measuring the size of individual NPs and studying electrocatalyzed local redox events essential for ultrasensitive electrochemical sensing, energy conversion and catalysts.

8. Interfacial Charge Transfer Events of BODIPY Dye Molecules: Single Molecule Spectroelectrochemistry and Substrate Effects

We present single molecule fluorescence and spectroelectrochemistry characteristics of 4, 4′-difluoro-4-bora-3a, 4a-diaza-s-indacene) BODIPY dye bearing two carboxylic acid groups at its 2 and 6 positions. Our study shows a heterogeneous half redox potential distribution of 1.78 (+/-0.19) V vs. NHE for the BODIPY molecules embedded in polystyrene film due to the heterogeneity in their charge transfer rates.

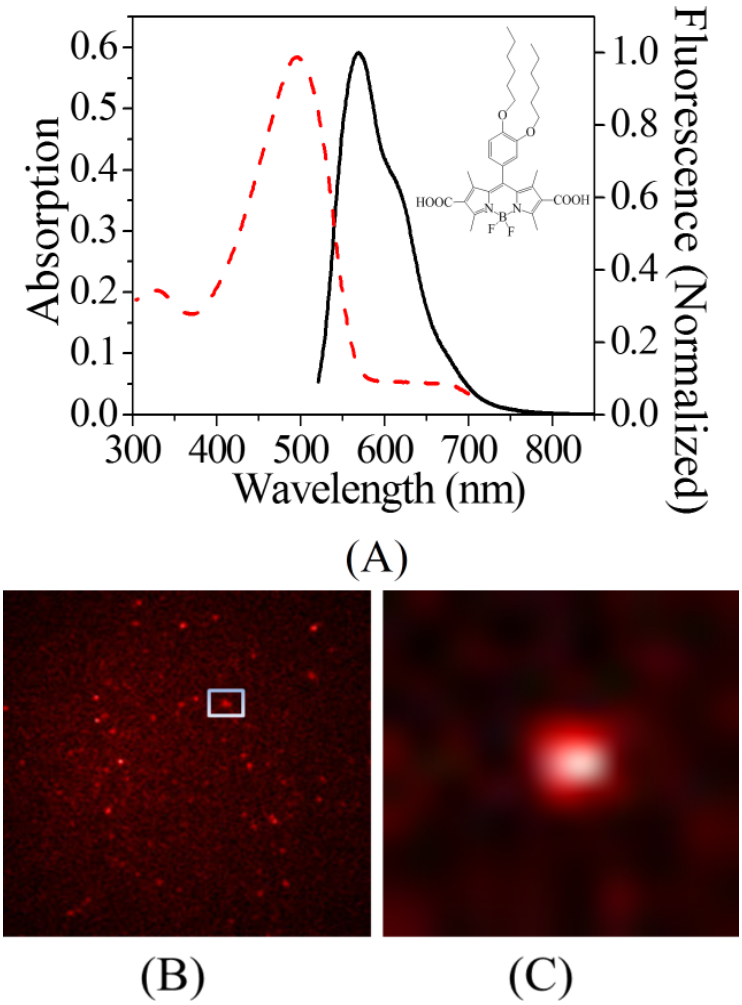

Figure 35. (A) Absorption and fluorescence spectra of the BODIPY dye and its molecular structure; (B) A typical single molecule BODIPY fluorescence image obtained on glass substrate; and (C) a zoom-in image of (B).

Single molecules adsorbed and self-assembled onto a TiO_2 surface with ordered nanostructures show the shortest ON duration time due to the efficient interfacial charge transfer events in comparison to bare glass and indium-tin oxide (ITO) surfaces. Single molecule stability tests show longer ON duration time and stable fluorescence feature when dispersed in polystyrene thin film than molecules exposed to air. Shorter ON times are observed for molecules coated onto ITO in comparison to glass substrate. Such fluorescence decrease in their stability or intensity is explained by charge transfer activity from the dye molecule to metal oxide surface. Electron transfer rate and back transfer rate are calculated by a well-established model.

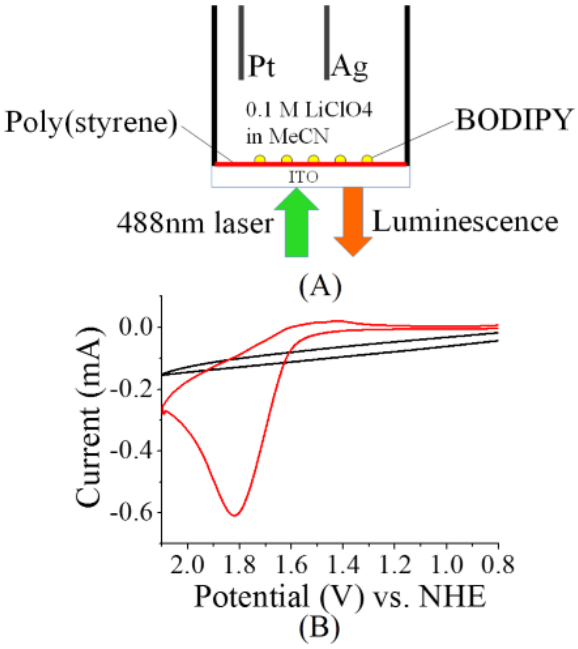

Figure 36. (A) Schematic of SMS-EC setup; (B) cyclic voltammogram of 1 nM BODIPY casted along with polystyrene

BODIPY dyes are of great interests for dye sensitized solar cells and can be used as molecule probe for sensing molecular recognition events because of their high extinction coefficients (> 80,000 $cm^{-1}M^{-1}$) and resistance to photobleaching. Yet their single molecule activities and redox activities at a bonded metal oxide and in an electrochemical cell are not tested at single molecule level. Recently, we studied the photoelectrochemical characteristics and interfacial charge transfer dynamics of two (4, 4′-difluoro-4-bora-3a, 4a-diaza-s-indacene) BODIPY dyes attached to nanostructured TiO_2 electrodes. Herein, we present single molecule fluorescence and spectroelectrochemistry studies of one of the BODIPY dyes bearing two carboxylic acid groups at its 2 and 6 positions on various substrates, including an ordered TiO_2 nanostructured surface onto which this dye can be covalently bonded. Their blinking dynamics on various surfaces in air and coated with polystyrene are studied, spectroelectrochemistry of this molecule is tested at single molecule level in a real electrochemical cell to illustrate their redox reaction characteristics.

8.1 Single molecule spectroelectrochemistry of BODIPY molecules

Figure 35A illustrates the absorption and fluorescence spectra of the BODIPY dye whose molecular structure is depicted as inset of the figure. This dye shows absorption maxima at 500 nm and fluorescence spectrum peaks at 580 nm. This typical BODIPY dye shows low fluorescence quantum yields of 28.1 % due to efficient photo-induced hole transfer from the excited BODIPY core to the electron-rich phenyl group at the meso position. The two carboxylic acid groups are designed for covalent attachment of the BODIPY onto a TiO_2 surfaces for characterizing the direct charge inject effect on single molecule blinking activities. Figure 35B shows a typical single molecule fluorescence image obtained for this BODIPY dye on glass substrate when 1 nM BODIPY molecule was spin-casted from chloroform solution containing 0.01% w/w polystyrene. Polystyrene is presumably to function as inert matrix to help maintain the stability of the single BODIPY molecules. Figure 35C shows a zoom-in image of one selected molecule from Figure 35B. It clearly shows good fluorescence contrast to the background signal. This high signal to noise contract would allow us to obtain the temporal response of single molecule with high accuracy. However, background subtraction was done using a custom MATLAB programs developed in our group to obtain images of single molecules coated onto metal oxide surfaces, such as ITO and TiO_2 due to their intrinsic fluorescence from defect emission.

To demonstrate redox characteristics of single BODIPY molecules and their difference from bulk counterparts, we used SMS-EC methods to study redox activity of single BODIPY molecules to compare with fluorescence stability at open circuit voltage (OCP). Figure 36A shows the schematic of single molecule spectroelectrochemistry. Florescence signals are collected using an EM-CCD camera, while a transparent electrode ITO is used as a working electrode along with a silver quasi-reference and Pt counter electrode arranged in a home-built electrochemical cell. Single molecules are spin-casted from polystyrene solution. The electrochemical cell contains acetonitrile and electrolytes to provide conductive media so that we can control and measure the redox reaction taking places at the working electrode using a potentiostat. Figure 36B shows the cyclic voltammogram (CV) of 1 nM BODIPY spin-casted along with polystyrene onto an ITO electrode in comparison to the CV of a dry-coated concentrated BODIPY sample. The bulk sample shows pronounced faradaic current due to the oxidation of this molecule while the single molecule sample shows only double layer charging current. Spectoelectrochemistry of the bulk

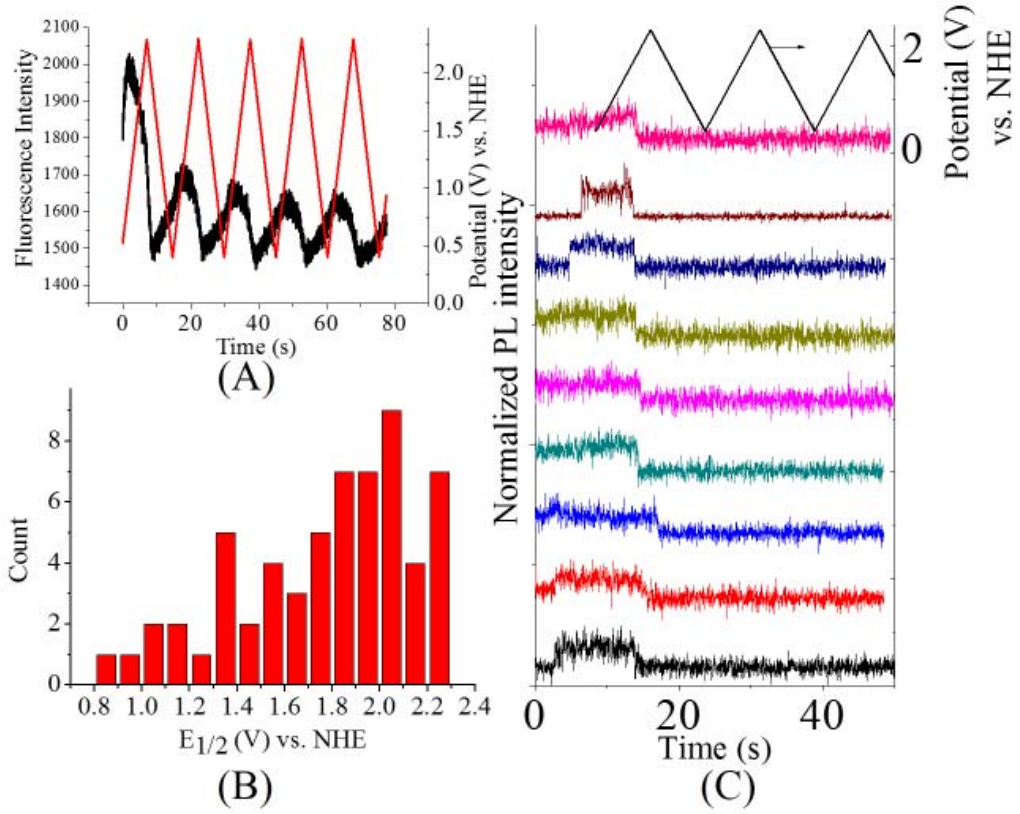

Figure 37. Spectoelectrochemistry of the bulk sample of BODIPY dye (A), histogram of measured single molecule

sample with high concentration of dye is shown in Figure 3A. It clearly shows that the PL of BODIPY dyes decreases upon the oxidation of the molecules and the total intensity decreases over the time when the electrode potential was cycled several times due to the irreversible electrochemical oxidation and photobleaching over the time. In comparison to bulk sample, single molecule PL signal only shows dramatic decrease with broad half potential $E_{1/2}$ distribution shown in Figure 3B. $E_{1/2}$ is defined by potential where the PL of single molecule decreases half of the initial intensity as shown by the selected PL traces in Figure 37C. There is around 50% of PL curves show instant decrease when applied with high potential, indicating the electron transfer to single BODIPY molecule (Figure 37C); others show slow fluorescence decrease upon applied electrode potential because of the presence of agglomerated BODIPY

molecules in the polymer matrix. Negative potential scan does not reverse the PL intensity because of the irreversible electrochemical reaction as clearly shown in the CV in Figure 36B. We then analyzed the PL responses of around a hundred single molecules and the measured average half oxidation potentials corresponding to 50% decrease in their PL intensity is around 1.78 (+/-0.19) V (vs. NHE). The heterogeneity in their half oxidation potential has to do with the heterogeneity in their charge transfer rates yielded by the heterogeneity in their spatial distribution inside the polymer layer. Measured redox potential of BODIPY dye in acetonitrile solution of 0.1 M $TBAPF_6$ is around 0.9 V, which is much less than above single molecule redox potential. This is because the polymer matrix can also increase the redox over potential due to their poor conductivity.

8.2 Single molecule fluorescence characteristics of BODIPY molecules and substrate effects

In order to understand redox activities and their stability of BODIPY molecules without using polymer matrix and electrolyte, single molecule fluorescence of BODIPY on different substrates (glass, ITO glass and ordered TiO_2) in air were studied at open circuit potential (OCP) and compared with molecules embedded in polystyrene. We also investigated whether molecules chemically bonded to TiO_2 would cause difference in their blinking dynamics in order to reveal the mechanism of charge transfer between substrates and BODIPY single molecules. As shown in Figure 38A and B, a typical single

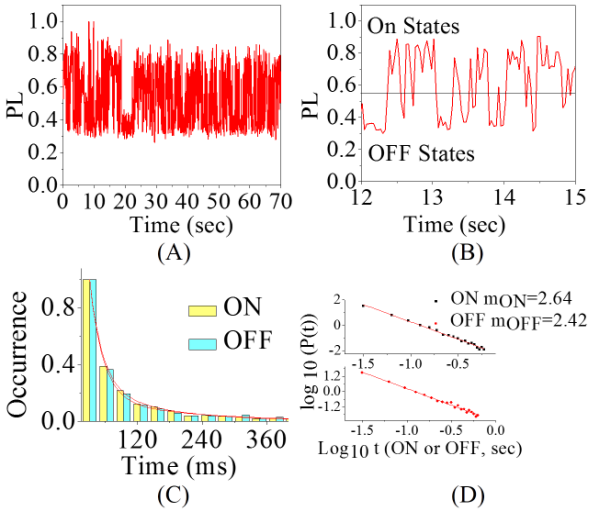

Figure 38. (A) Photoluminescence intensity curve vs. time showing the blinking behavior; (B) a zoom-in of (A); (C) the statistical distribution of occurrence of blinking and its corresponding time duration and fitting curves (red curves); and (D)

molecule on glass substrate show ON and OFF fluorescence blinking behaviour. Such single molecule blinking shows the duration distributions of the ON and OFF states, respectively. The duration of OFF states spans ranges from a few milliseconds to seconds, while the one of ON states is shorter than 50 milliseconds. The duration distributions of both ON and OFF states show no-Poisson behaviours because they show second-order exponential decay processes as shown in Figure 4C. All parameters obtained by second-order exponential data fitting are listed in Table 5. This phenomenon is similar to dynamic disorder fluctuation behavior of single molecule interfacial charge transfer activities.

To analyze such dynamic disordered blinking behavior, we constructed probability density distribution, P(t)=Occurrence(t)/Δt, for both ON and OFF states as shown in Figure 4D. The calculated probability density distributions P(t) show typical power-law behaviour, which can be described by a linear function of t^{-m}, m is a constant. We calculated the value of m by constructing a liner fitting of the log-log plot of P(t) and t^{-m} for both On and OFF states, and listed m values in Table 5. The power exponent m for BODIPY spin-casted on glass is found to be 2.64 for ON states, and 2.42 for the OFF state as shown in Figure 38D.

Direct charge transfer from photoexcited dye molecules to TiO_2 is of great interests to alternative energy conversion systems such as solar cells. To study single BODIPY molecules blinking dynamics and

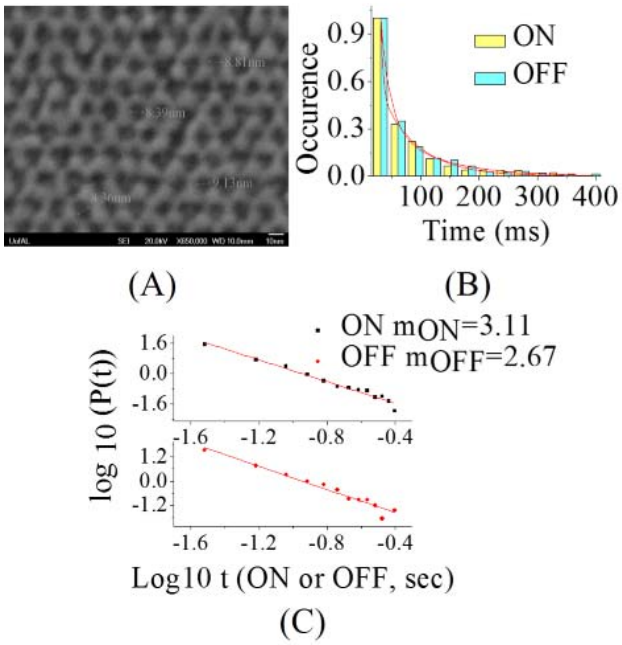

Figure 39. (A) SEM image of TiO_2 with ordered nanostructure; (B) statistical distribution of occurrence of blinking and its corresponding time duration and fitting curves (red curves) of self-assembled BODIPY molecules on ordered TiO_2 in air; and (C) log-log plot of P(t) and t^{-m} and fitting curves (red curves).

statistical analysis on their ON and OFF states on electron accepting semiconductor material TiO_2 as

Table 6. Fluorescence kinetic parameters of BODIPY molecules on various substrates.

Substrate	τ_{on} (s)	τ_{off} (s)	PL lifetime (ns)	k_{fluor} (s^{-1})	k_{et} (s^{-1})	k_{bet} (s^{-1})	k_{et}/k_{bet}
A	18	27.21	2.07	4.83E+09	984.33	3.68E-02	2.68E+04
C	20.06	21.88	1.60	6.25E+09	1142.70	4.57E-02	2.50E+04
D	16.23	26.65	1.44	6.94E+09	1569.29	3.75E-02	4.18E+04
F	24.4	13.41	1.44	6.94E+09	1043.84	7.46E-02	1.40E+04
G	15.88	38.16	2.21	4.52E+09	1045.06	2.62E-02	3.99E+04
I	25.96	20.3	1.58	6.33E+09	894.18	4.93E-02	1.82E+04
J	9.94	17.66	1.89	5.29E+09	1952.25	5.66E-02	3.45E+04
L	25.85	22.09	1.58	6.32E+09	896.05	4.53E-02	1.98E+04

Substrate labels A-L represent the same substrates as the ones in Table 5.

shown in Figure 39A. The TiO_2 substrate contains ordered nanopores with diameter of 10 nm that would presumably support high surface area for light absorption, efficient exciton diffusion and interfacial charge transfer for dye sensitized energy conversion system. Single molecule imaging in an inverted configuration is enabled because of the high optical transparency of the TiO_2 substrate. The duration distributions of both ON and OFF states for self-assembled BODIPY molecules show 2nd order exponential decay processes as shown in Figure 39B with shorter average ON duration time in comparison to bare glass substrate. Probability density distribution analysis shows m value is 3.11 for ON state, and 2.67 for OFF state, indicating faster blinking activity on TiO_2 than on glass. We attribute this enhanced blinking behavior to photo-induced charge transfer and back transfer that takes place when the dye is placed on the surface of a metal oxide semiconductor surface.

Blinking dynamics and occurrence population for ON and OFF states from several other control experiment results are further analyzed to show the stability and charge transfer dynamics of the BODIPY molecules. These control experiments include single BODIPY molecules casted along with polystyrene onto glass, ITO and TiO_2 surface in comparison with the results obtained in the absence of polystyrene. All occurrence data are fitted using a 2nd order exponential function $A_1\exp(-t/t_1)+A_2\exp(-t/t_2)$ process and obtained amplitudes and time constants are compared in the Table 5. Our data clearly shows that all molecules casted from polystyrene show longer ON time constants (t_1 value) and smaller m values than the ones without being embedded in the polymer matrix on matter what substrate being used for the measurements. This has to do with the improved photostability enabled by polystyrene matrix preventing photo-oxidation of BODIPY molecules by eliminating the abundant oxygen in atmosphere. Relatively longer distance from BODIPY single molecule to substrate surface is also ensured in the presence of polystyrene, to prevent interfacial charge transfer from single molecules to substrate. We also preformed fluorescence measurement of single BODIPY molecule in N_2. As shown in Table 5, in N_2 atmosphere, samples all show longer ON time constant than that in air, indicating N_2 can improve the photostability of BODIPY spin-casted on substrate. Our data also shows that, for spin-casted BODIPY samples without polystyrene, the ON time constant of ordered TiO_2 surface (15.88) is the smallest followed by ITO and glass, which is due to that ordered TiO_2 and ITO both have more favourable energy levels enabling fast

Table 5. Single molecule blinking dynamics and statistical analysis for BODIPY molecules on various substrates.

Substrate	ON					OFF					Lifetime
	m_{on}	A_1	t_1	A_2	t_2	m_{off}	A_1	t_1	A_2	t_2	(ns)
A	2.64	4.17	18.00	0.35	119.20	2.42	2.78	27.21	0.14	260.42	*2.07*
B	2.26	3.79	20.85	0.18	231.78	2.52	4.33	18.85	0.21	185.79	-
C	2.47	3.45	20.06	0.30	141.40	2.62	3.34	21.88	0.21	136.83	1.60
D	2.84	4.01	16.23	0.56	80.20	2.87	2.65	26.65	0.19	137.62	1.44
E	2.74	2.35	29.76	0.20	169.28	2.44	1.91	36.54	0.20	131.10	-
F	2.78	2.58	24.40	0.34	104.69	3.00	5.37	13.41	0.68	69.05	1.44
G	2.75	4.78	15.88	0.41	91.36	2.73	1.98	38.16	0.12	230.88	2.21
H	2.85	4.75	17.68	0.20	97.11	2.22	12.84	10.05	0.47	127.93	-
I	1.80	2.70	25.96	0.20	140.17	2.42	3.32	20.30	0.32	134.63	1.58
J	3.11	4.95	9.94	0.64	38.42	2.67	2.21	17.66	0.40	82.75	1.89
K	2.68	4.49	18.71	0.14	122.21	2.78	10.65	9.54	0.54	115.98	-
L	2.65	2.74	25.85	0.22	151.40	2.96	3.62	22.09	0.15	130.39	1.5834

** Data fitting was done using a formula with 2nd order exponential decays: $A_1\exp(-t/t_1) + A_2\exp(-t/t_2)$.*

A) glass in air; B) glass in N_2; C) glass, coated with polystyrene; D) ITO in air; E) ITO in N_2; F) ITO, coated with polystyrene; G) TiO_2 spin-casted BODIPY, in air; H) TiO_2 spin-casted BODIPY, in N_2; I) TiO_2 spin-casted BODIPY, coated with polystyrene; J) TiO_2, self-assembled BODIPY, in air; K) TiO_2, self-assembled BODIPY, in N_2; L) TiO_2, self-assembled BODIPY, coated with thick polystyrene.

charge transfer rate for BODIPY molecules than glass. The ON time constant at the ITO electrode is longer than bare glass in the presence of polystyrene. This is presumably due to the rough surface of our ITO electrode that would form more polystyrene loading than bare glass substrate to allow better substrate coating and improve molecule stability. The same reasoning can be used to explain the fact that ON time constant at the TiO_2 electrode with spin-casted BODIPY is also longer than glass in the presence of polystyrene. Our experiment also show weak background fluorescence from such TiO_2 films due to their defect emission that challenges the single molecule observation. Appropriate background subtraction is needed to extract useful information of single molecule on this substrate. We finally compare the occurrence dynamics for ON and OFF state of molecules spin-casted on TiO_2 surface with the ones self-assembled on TiO_2 via their carboxylic acid groups. The self-assembled molecules clearly show the lowest ON time constant (9.94) due to more efficient charge transfer rate when the molecules are approximated to the semiconductor surface. The calculated probability density distributions P(t) of all above substrates and sample preparation conditions show typical power-law behaviour that can be described as a liner function of t^{-m}, and the constant m for all samples are listed in Table 5 for both On and OFF states to be compared. It clearly shows that self-assembled BODIPY molecules on the ordered TiO_2 surface as the largest m followed by bare ITO and then glass in air.

8.3 BODIPY fluorescence lifetime and charge transfer kinetic parameters obtained from single molecule spectroscopy

We also measured the fluorescence lifetime of BODIPY dye thin film sample at the various substrate, and the measured lifetime for each of the substrates are listed in Table 5. The averaged fluorescence lifetime of all cases is around 1.7 (+/- 0.3) ns and the ground state recovering rate of 8.3 (+/-0.8) ps was obtained by our previous transient absorption spectroscopy study of BODIPY film on TiO_2. With the fluorescence lifetime data, we can calculate the interfacial electron transfer rate (k_{et}) from BODIPY to substrates and the back electron transfer rate (k_{bet}) with a well-established model. Following equations are used:

$$\frac{1}{\tau_{off}} = k_{bet} \quad (1)$$

$$\frac{1}{\tau_{on}} = k_{exc}\frac{k_{et}}{k_{et} + k_{fluor} + k_{isc} + k_{ic}} \quad (2)$$

$$k_{fluor} = \frac{1}{\tau_{fluor}} \quad (3)$$

$$\varphi_f = \frac{k_{fluor}}{k_{fluor} + k_{isc} + k_{ic}} \quad (4)$$

Where τ_{on} and τ_{off} are the time constants of ON and OFF distributions, respectively, obtained from Table 5. τ_{fluor} is the fluorescence lifetime. k_{isc} and k_{ic} are the rate constants of intersystem crossing to the triplet state and other nonradiative decay, respectively. The estimated photon absorption rate of single BODIPY molecules k_{exc} is 6.98×10^5 s^{-1} with the estimated light absorption cross section of 10^{-15} cm^2. We used fluorescence lifetime of ensemble samples to estimate other kinetics parameters in equation 1-4. This is because of the low fluorescence quantum yield of BODIPY, preventing us from measuring single molecule lifetime with our limited instrument capability. Calculated results of k_{et} and k_{bet} are collected in Table 6. The highest k_{et} value is observed for self-assembled BODIPY on TiO_2 without polystyrene (sample J), indicating very efficient charge transfer from BODIPY to TiO_2 because of their intimate contact with each other. For samples on ITO and TiO_2 coated with polystyrene, a smaller k_{et} than samples without polystyrene was obtained, indicating the impediment of polystyrene to the electron transfer from BODIPY to ITO or TiO_2. However, the same impediment is not observed for electron back transfer by analysing k_{bet} values. On the other hand, samples with polystyrene give smaller k_{et}/k_{bet} than samples coated with polystyrene; k_{et}/k_{bet} of glass substrate is smaller than ITO and TiO_2, which agrees with our previous conclusion that the enhanced blinking behaviour is due to photo-induced charge transfer and back transfer between BODIPY and substrate.

8.4 Conclusions

BODIPY dye bearing two carboxylic acid groups at its 2 and 6 positions shows excellent single molecule PL stability in polymer matrix and allows us to study its spectroelectrochemistry at single molecules level in inert polymer matrix. Our study shows a heterogeneous half redox potential distribution of 1.78(+/-0.19) V vs. NHE for single molecules embedded in polystyrene film due to the heterogeneity in their charge transfer rates. Redox events and photostability of single BODIPY molecules are investigated at open circuit potential. Molecules self-assembled onto a TiO_2 surface have the shortest ON time duration constant and highest interfacial electron charge transfer rate. Polystyrene helps reserve the stability of the individual molecules. Single molecule fluorescence decreases in their stability and intensity upon charge transfer activity and/or exposure to air.

VII. Patent , Submitted and unpublished papers are already in written are included in Appendix files below.

Appendix I. Single nanoparticle spectroelectrochemistry of Ag NPs

Appendix II. Single molecule P3HT SERS studies

Appendix III. Photoelectorchemistry at single crystal TiO_2 microparticles.

Appendix IV. Patent on single particle analysis using spectroelectrochemistry technique

WILEY-VCH

DOI: 10.1002/ ((please add manuscript number))
Article type: Full Paper

Single Ag NP Spectroelectrochemistry via Dark Field Scattering and Fluorescence Microscopies

Caleb M. Hill,[1] *Robert Bennett,*[1] *Chen Zhou,*[2] *Shane Street,*[1] *Jie Zheng,*[2] *and Shanlin Pan**[1]
[1]Department of Chemistry, The University of Alabama, Tuscaloosa, Alabama 35487
[2]Department of Chemistry, The University of Texas at Dallas, TX, 75080

*Corresponding Author. Email: span1@bama.ua.edu

Keywords: Nanoparticles, Electrochemistry, Spectroelectrochemistry, Dark Field Scattering, Photoluminescence

Abstract

The spectroelectrochemical properties of individual luminescent, plasmonic silver nanoparticles (Ag NPs) are investigated using the combined methods of dark field scattering (DFS) and photoluminescence (PL) spectroelectrochemistry. Individual NP light scattering and PL intensities are measured while the substrate's electrochemical potential is controlled to oxidize the NPs. The spectroelectrochemical responses of individual NPs are used to study heterogeneities not visible in bulk voltammetric measurements. Our studies show that the Ag NPs exhibit a range of redox potentials and their statistical distribution is dependent on the electrolyte system used. No variations in the spectral profile of bulk NP samples are observed, implying no correlation between the redox potentials of individual NPs and the energy of emitted photons from fluorescent sites on Ag NPs. This is due to a negligible difference in the redox potentials for individual emissive sites on a given Ag NP and/or the shrinking of the polarizable bulk of the Ag NP.

1. Introduction

Metallic nanoparticles (NPs) have emerged as a class of materials that have unique optical, electrical, catalytic, and mechanical properties. Due to the inherent heterogeneity in materials synthesized in this size regime, analytical methods capable of detecting individual

nanostructures are extremely valuable to provide insight into understanding their structure-function relationships. Few electrochemical methods thus far have been reported capable of analyzing single NPs. Single NPs have been detected via a current amplification scheme because of their catalytic capabilities as they collide at a microelectrode.[1] More recently, heterogeneities in the catalytic activity of single metal NPs[2,3,4] and the charge transfer performance of individual conjugated polymer molecules/NPs[5] have been studied using single molecule spectroelectrochemical (SMS-EC) methods.[6] Gold (Au) and silver (Ag) NPs are generally considered free-electron conductors due to their extremely large density of states. Their redox potentials have recently been shown to be size dependent using a dynamic potential control method.[7,8,9,10] Under visible light excitation, Au and Ag NPs exhibit strong light scattering and absorption because of their surface plasmon resonance properties, enabling large enhancements of optical spectroscopic signals (such as Raman scattering[11,12] and PL[13,14,15,16]), that can be used in trace analysis, high-resolution spatial and spectral imaging,[17,18] and, more recently, in solar cells and photoelectrochemical systems.[19,20,21] Ag nanostructures prepared by photoactivation processes [22,23,24,25] have been found to exhibit strong PL, which is highly dependent on the surrounding chemical environment.[26,27,28,29,30] These characteristics provide the opportunity to investigate the electrochemical characteristics of single Ag nanostructures via SMS-EC. Several issues need to be resolved in order to help fully understand these luminescent, plasmonic Ag nanostructures. First, it is unclear what the redox potentials of these Ag nanostructures are and how their redox activities are dependent on the surrounding environment. Further, it is unclear if the PL and light scattering characteristics of each individual Ag NP are identical, and how they can be measured for each selected silver NP. The spectroelectrochemical studies presented here address these issues. We recently demonstrated a dark field scattering (DFS) spectroelectrochemistry technique for analyzing the electrochemical formation of individual Ag NPs at the surface of an indium tin oxide (ITO) electrode.[31] This technique allows for the determination of heterogeneities in

redox potentials for Ag^+ reduction, and supports rapid particle size determination and the reconstruction of voltammetric curves of individual Ag NPs. This technique has yet to be applied to observe the subsequent oxidation of Ag particles. Here we present spectroelectrochemical studies of electrodeposited and pre-synthesized Ag NPs to help establish a firm relationship between their redox activities and PL/DFS signal at the single particle level.

2. Results and Discussion

2.1. Spectroelectrochemistry of electrodeposited single Ag NPs using DFS and PL methods.

2.1.1 DFS results. **Figure 1** shows schematics of the single Ag NP imaging systems employed in these studies. Single Ag NPs can be imaged by their strong light scattering in a DFS configuration in **Figure 1A**, which employs white light illumination through a dark field condenser for sample excitation and an objective lens for collection of the scattered light. The scattered light intensity is measured using an EM-CCD camera which can collect images with a temporal resolution down to a few milliseconds. A similar configuration is used for PL imaging by replacing the white light illuminator with a monochromatic laser as the excitation source and filtering the collected light to only pass emitted PL to the EM-CCD camera. An optically transparent working electrode made of indium-tin-oxide (ITO) is used to support Ag NPS for these spectroelectrochemical studies. Detailed imaging and electrochemical conditions are described in experimental section.

As shown in **Figure 2A**, Ag NPs can be synthesized electrochemically by reducing Ag^+ ions from an organic solvent (MeCN) containing a strong electrolyte. Ag NP formation and oxidation in an electrochemical cell is controlled by a potentiostat while DFS and PL signals originating from the ITO substrate are measured. **Figure 2B** shows a typical DFS image of electrodeposited Ag NPs.

Typical Cyclic voltammograms (CVs) of Ag^+ reduction and Ag NP oxidation are shown in **Figure 3A**. For Ag^+ reduction from MeCN, the onset potential is around -0.2 V (vs. SHE) and the higher current density in the reversed potential scan at -0.1 V (vs. SHE) indicates Ag deposition onto the ITO electrode, which lowers the required overpotential for further reduction of Ag^+. A small oxidation peak at 0.2 V is attributed to the oxidation of Ag to Ag_2O. This oxidation peak is virtually absent in dry MeCN due to the limited availability of water molecules which facilitate the formation of Ag_2O. The turn-on potential for Ag reduction is much more negative than the thermodynamic potential (0.591 V vs. SHE) calculated from Nernst equation ($E_{Ag+/Ag}=0.799V+0.059\log_{10}{}^{[Ag+]}$). This is because the reduction of Ag^+ at the ITO electrode is kinetically sluggish. The observed difference in the reduction turn-on potential for regular MeCN and dried MeCN is not clear, but may be due to variations in the quality of the ITO substrates employed. DFS images collected during the deposition and oxidation processes are shown in **Figure 3B**. An increase in the number and brightness of diffraction limited spots from image 1 to 2 is clearly visible and attributed to the deposition of Ag NPs. Most of these Ag NPs continue to scatter light intensely after applying a positive potential of 0.38 V or higher, suggesting few Ag NPs will be completely oxidized to form silver ions or oxide. Further analysis of the oxidation behavior of Ag NPs is presented in **Figure 4**. 16 individual Ag NP DSF intensity transients are selected as shown in **Figure 4** to illustrate their DFS responses during Ag^+ reduction and Ag oxidation. It clearly shows that all DFS transients increase instantaneously near the Ag^+ reduction potential of -0.1 V and only a small fraction of Ag NPs show decreases in their DFS intensity at the first oxidation potential at 0.2 V (vs. SHE). Further decreases in all DFS transients can be observed but there is no well-defined potential associated with this process. Our analysis of ~900 Ag NPs indicates that only ~30 % of electrodeposited NPs are oxidized on ITO. This apparent resistance to oxidation is not caused by the differences in the local conductivity of different sites on the ITO surface because of the lack of correlation between the observed deposition and oxidation

potentials. A more likely explanation may be differences in the electrical contact between the deposited NPs and the ITO surface, which would be expected due to heterogeneities in NP size/shape.

To better illustrate the insights these DFS measurements can provide into the stability of Ag NPs, the average DFS response of ~900 Ag NPs and the current signal of the entire substrate is given in **Figure 5A**. Two oxidation regions can be observed: a small peak located at 0.2 V vs. SHE (*cf.* **Figure 3A**) and another peak at 3.0 V vs. SHE. The second oxidation region starts at ~2.0 V vs. SHE. A 10 % decrease in DFS signal coincident with the first oxidation peak at 0.2 V clearly demonstrates that the Ag NPs are partially oxidized but not completely removed from the ITO surface. DFS intensities decrease gradually as we increase the electrode potential up to 4 V but there is no direct correlation found with the measured electrode current. This suggests DFS is incapable of directly measuring silver oxidation in this region, and instead it might only probe the change in the double layer charging of the electrode and/or other side reactions in this potential region.

To confirm the presence of Ag NPs and their morphological changes before and after oxidation, SEM images were taken of the Ag NPs (**Figure 6A** and **B**) after the deposition/oxidation process. Different sizes and shapes of Ag NPs are observed due to the roughness of ITO surface and the heterogeneities in nucleation and particle growth during electrochemical deposition. These heterogeneities in particle size and shape influence the observed heterogeneities in reduction and oxidation potentials of single Ag NPs. To estimate the Ag NP formation and oxidation potentials from the DFS transients of individual NPs, each transient was fitted to 2 sigmoid functions as shown in **Figure 7A** and the distributions of the fitted onset potentials (E_{on}, defined by extrapolating the slope at the sigmoid half potential to the initial intensity value) are given in **Figure 7B**. The average formation and oxidation potentials are comparable with the CV results shown in **Figure 3A** and **Figure 5B**. DFS

spectroelectrochemistry allows for the accurate analysis of redox properties of individual Ag NPs which otherwise are not possible using traditional voltammetric methods. DFS also confirms that Ag NPs remain on the ITO surface after partial oxidation around 0.2 V vs. SHE in MeCN. Further increases in electrode potential produce a gradual decrease in DFS signal but no complete oxidation of Ag NPs can be obtained. No correlation between the deposition and oxidation potentials of Ag NPs was observed based on our analysis as shown in **Figure 7C**, indicating that the observed heterogeneities are not likely to be due to local variations in substrate conductivity. No correlation between the oxidation potential and scattering intensity, which is directly related to NP size, was observed either as shown in **Figure 7D**, indicating that the NP size does not affect stability.

2.1.2 PL results. PL imaging is used as a complementary technique to DFS for probing the formation and oxidation of single Ag NPS in MeCN solution. Similar to the DFS experiments, Ag NPS were first deposited from a MeCN solution containing silver acetate and a strong electrolyte. The formation and subsequent oxidation of individual Ag NPs was then recorded using their PL signals instead of light scattering. **Figure 8A** shows a typical PL image of single Ag NPs electrodeposited onto an ITO surface. Only weak PL signals were obtained for such electrodeposited Ag NPs because they are freshly electrodeposited and only minimum surface activation steps have taken place, which are necessary for efficient PL emission. **Figure 8B** shows the PL transients of 16 selected Ag NPs when the electrode potential was scanned from 0.25 V to -0.25 V to form Ag NPs from MeCN solution, and then an anodic sweep was applied to oxidize the Ag NPs. It clearly indicates the presence of single Ag NPs upon Ag^+ reduction and the PL signal continues rising until the electrode potential becomes positive enough to oxidize Ag at 0.2 V (vs. SHE). This PL response is different from the DFS signal which remains constant after formation of Ag NPs and then decreases at 0.2 V. The absence of constant PL signal after formation of Ag NPs is due to the continual surface activation of the Ag NPs, forming more emissive Ag clusters which results in a stronger PL

signal. Another prominent feature of the PL transients is blinking effects which are superimposed onto the steady state PL. This is attributable to the activation and deactivation of PL active Ag clusters on the surface of each Ag NP. Another distinct feature of the PL transients in contrast to the DFS observations is that the PL of individual NPs continues to decrease after the first oxidation potential of 0.2 V. To illustrate this clearly, an average PL transient is plotted along with its DFS transient in **Figure 9**. When the second oxidation of Ag NPs takes place at 1.7 V (vs. SHE) (*cf.* **Figure 5B**), the PL signal decreases with increasing electrode potential until it is removed completely. The complete removal of PL at higher potentials provides evidence for the deep oxidation of Ag NPs to form a thick oxide layer which prevents PL emission. This makes the fluorescence based technique complementary, since such deep oxidation does not result in a pronounced change in scattering by the NPs. Utilizing both techniques, we are therefore able to estimate the redox potential of both oxidation peaks for each Ag NPs. It should be noted that not all Ag NPs visible via DFS exhibits a detectable PL signal, and not all PL transients show responses to oxidation. As shown in **Table 1**, all samples show a reproducible response to Ag NP formation in MeCN for both DFS and PL imaging techniques. Large populations of Ag NPS can be counted using DFS with more precise measurements of the formation turn-on potential. Only 30% of the Ag NPs exhibit a measurable decrease in scattering intensity in response to the first oxidation step. Comparatively fewer Ag NPs can be sampled via PL imaging and two distinct oxidation potentials are observed for some samples while others show no distinct difference. This might be due to issues with the local contact between the Ag NPs and ITO surface, as no DFS or PL responses can be obtained if a Ag NP losses its contact to ITO surface upon oxidation. Such poor PL efficiency and low yield of countable PL active Ag NPs limits these spectroelectrochemistry studies of single Ag NPs, although they already provide strong evidence that PL is a more sensitive technique than DFS for studying the oxidation of single

Ag NPs. To overcome this major issue, pre-synthesized strong PL emissive Ag NPs were investigated.

2.2. Pre-synthesized Ag NPs with efficient PL for spectroelectrochemical studies of single NPs

Figure 10A shows a typical transmission electron microscopy (TEM) image of Ag NPs synthesized using a thermal reduction method in a solid glycine matrix. Detailed synthesis procedures are described in the experimental section. Their size distribution is shown in **Figure 10B** and exhibits an average core diameter of 20.5 ± 2.4 nm. High-resolution TEM studies further confirmed that these NPs are highly polycrystalline with grain sizes down to 1 nm. The UV/Vis absorption and PL spectra are given in **Figure 10C**. While the peak at 420 nm in the absorption spectrum is attributed to surface plasmon resonance, strong green PL from 500 nm to 750 nm with a maximum at 540 nm was also observed from these polycrystalline Ag NPs. **Figure 10D** shows a typical PL image of these polycrystalline Ag NPs which exhibit a much higher PL efficiency than the electrodeposited Ag NPs. Surface enhanced Raman scattering of the glycine matrix can be observed in the spectra of the NPs drop coated onto Indium Tin Oxide (ITO), which disappears upon the addition of an organic electrolyte solution. For single particle PL imaging and spectroelectrochemistry studies, ITO substrates coated with these emissive Ag NPs were immersed in 0.1 M $LiClO_4$ in MeCN and PL spectra of single Ag NPs were obtained to confirm the monodispersity of the obtained Ag NPs.

Figure 11A shows the total PL intensity and electrode current density as the electrode potential was swept from 0 to 4 V at 100 mV/s. Clearly, the single particle PL shows a strong dependence on the substrate potential. **Figure 11B** shows four PL images of emissive Ag NPs acquired at four different electrode potentials as indicated in **Figure 11A** to illustate the PL decrease upon Ag NP oxidaiton. No distinct oxidaition peak was observed in the CV becasue

of the low coverage of Ag NPs on ITO surface resulting in the current being dominated by background processes. This is different from the experiments on electrodeposited Ag NPs where the surface coverage is much higher. PL transients for four individual Ag NPs are shown in **Figure 11C**, showing their respones to oxidation.

Figure 12B shows the histogram of oxidation onset potentials, E_{on}, which were defined as before, obtained by fitting each PL transient to a combination of two sigmoid functions as shown in **Figure 12A**. The average first and second onset potentials were found to be 0.9 ± 0.2 and 2.0 ± 0.5 V vs. SHE, respectively, where the errors given are 1 standard deviation. Similar experiments were also carried out using an aqueous electrolyte containing 0.1 M NaOH. The observed differences from acetonitrile are threefold: the signal to noise ratio is smaller in NaOH, the PL has exhbits marked blinking activities in NaOH, and the PL "switches off" much more abruptly. The blinking activity of Ag can be explained by photochemical reactions of Ag in aqueous solution containing oxygen. Such photochemical reactions can switch the PL on and off and the blinking frequency depends on the excitation intensity. The quicker „switching off" is due to the higher mass transfer rate and solvation of Ag^+ ions in aqueous solution. In addition, Ag^+ ion complexation with hydroxide ions can take place immediately in high pH environments when Ag is oxidized. In comparison, Ag NPs are much more stable in acetonitrile due to the slow kinetics of silver oxidation in organic solvents. In fact, these NPs in acetonitrile maintained ~20% of their PL after 4 oxidation cycles as shown in **Figure 13A**. The distribution of oxidation potentials for Ag NPs in 0.1 M NaOH is appreciably narrower than that observed in acetonitrile. Our preliminary studies suggests that the observed heterogeneities in oxidation potentials are attributable to the variation in size of the Ag NPs. Detailed studies of the effect of size and other parameters, such as surface modification and the electrode material are needed for a complete understanding of the electrochemical behavior of the Ag NPs.

The spectral evolution during the course of oxidation was also investigated. When no potential was applied (not shown), only a small decrease in PL intensity was observed. **Figure 13B** summarizes the effect of varying the substrate potential in terms of the peak wavelength and integrated spectral intensity. **Figure 13C** shows the spectral changes during the course of a substrate potential sweep. Dramatic decreases in intensity occur near the second half potential of the silver oxidation process established previously, though no spectral shift is apparent. The lack of spectral shifts suggests that there is no correlation between the redox potential of these NPs and the energy of emitted photons. If one assumes there is a static population of emissive species on a silver NP throughout the experiment, two possibilities logically follow: (1) there is a negligible difference in the $E_{1/2}$ values for individual emissive sites on a given NP or (2) the observed decrease in luminescence is due not to the direct oxidation of these individual fluorescent species, but instead to the shrinking of the polarizable bulk of the Ag NP which sustains the plasmon enhancement of the excitation field. Of course, due to the photoactive nature of Ag/Ag_2O surfaces, it is feasible that an equilibrium exists where new emissive sites are created through photochemical reactions while others are being oxidized electrochemically. In this case, the PL intensity could be representative of the ratio of k_{form} to k_{oxid}, the kinetic rates of site formation and oxidation, respectively. The spike in intensity at ~2V is an interesting effect which is also observed for individual NPs, albeit infrequently. We attribute this increase in intensity due to the initial oxidation of the Ag NPs, increasing the chance of producing photoactive luminescent silver clusters under laser excitation and/or shifting the plasmon frequency onto resonance with the excitation field prior to the complete oxidation of silver.

3. Conclusion

In this report, studies of the electrochemical formation and oxidation of individual Ag NPs via light scattering and fluorescence microscopies were presented. These optical

spectroelectrochemical measurements can be used to directly obtain heterogeneities in redox potentials between NPs or locations on the electrode surface not obtainable via standard electrochemical methods. DFS and PL transients for individual NPs can be used to infer the voltammetric responses of individual NPs without being obscured by high nonfaradaic background currents. For Ag NPs electrodeposited onto ITO, it is clear from our DFS and PL measurements that only a small fraction of NPs can be appreciably oxidized, which may be attributable to the destruction of electrical contact between the ITO surface and the Ag NPs.

4. Experimental Section

Chemicals: A solution of glycine-coated Ag NPs in H_2O was synthesized via the thermal reduction of Ag^+ in a solid glycine matrix.[32] Citrate-capped Ag NPs (20, 40, 60 and 80 nm in diameter) for size-dependence studies were purchased and used as received from Ted Pella, Inc. Silver Acetate (AgAc, 99 %, Acros Organics), $LiClO_4$ (99.99 %, Aldrich), and Acetonitrile (MeCN, HPLC Grade, EMD) were obtained from the indicated sources and used without further purification.

Sample Preparation: ITO-coated cover glass slides were cleaned via sonication for 15 min each in a mild detergent solution, 25 g L^{-1} KOH in EtOH, DI H_2O, i-PrOH, and DI H_2O, sequentially, followed by UV-O_3 cleaning (Bioforce Nanosciences Procleaner Plus) for 10 min. Pre-synthesized Ag NP samples were prepared by drop coating ~10 μL of a dilute solution of Ag NPs onto cleaned ITO substrates under ambient conditions.

Electrochemical Setup: All electrochemical experiments were carried out in a 3-electrode configuration using custom PTFE electrochemical cells designed to fit within the optical path of an Olympus IX-71 optical microscope. In all cases, cleaned ITO-coated cover glass slides served as the working electrode (WE) and a Pt wire as the counter electrode (CE). For experiments in aqueous electrolytes, a Ag/AgCl (sat'd KCl) reference electrode was employed. For experiments in organic electrolytes, a Ag wire was used as a quasireference electrode

(QRE). The electrolyte for experiments on presynthesized Ag NPs was either 0.1 M NaOH in H_2O or 0.1 $LiClO_4$ in MeCN. For the experiments on electrodeposited Ag NPs, the electrolyte solution contained 300 μM Ag Acetate and 0.1 M $LiClO_4$ in MeCN. All electrochemical measurements were obtained with a potentiostat (CH Instruments 760C).

PL Microscopy: Samples were mounted onto a standard inverted optical microscope (Olympus IX-71). The excitation source for all measurements was a 488 nm laser (25 mW, Modu-Laser). For wide field measurements, PL was excited/collected in an epifluorescence configuration and detected using an electron multiplying charge coupled device (EM-CCD) camera (Andor iXon). The data was collected in the form of PL "movies" (a stack of TIFF images). The image dimensions were calibrated using a USAF test target (Thorlabs). Each pixel in the PL images represent a 150 nm × 150 nm sample area. Excitation intensities were 20 W cm^{-2}.

For spectral acquisitions, a confocal optical geometry was employed. Emitted PL was collimated, then directed into a 50:50 beam splitter. Half of the beam was sent to a spectrometer/CCD (Princeton Instruments PI-200/Princeton Instruments Spec-10) for spectral acquisition and the other half was sent to a pair of avalanche photodiodes (APDs, PerkinElmer). Images were first acquired by rastering the location of the excitation beam on the sample and detecting the emission intensity at the APDs. Single NPs appeared as diffraction-limited (~λ/2) spots in the image. An area in the image which is believed to correspond to individual NP was identified and the sample was moved so that the excitation beam resided in this area. It is at this point that spectra were acquired using the CCD camera. Excitation intensities were 80 kW cm^{-2}.

Dark Field Scattering Microscopy: Samples were mounted onto an Olympus IX-71 inverted optical microscope. Light from a Hg arc lamp (X-Cite 120PC-Q) was focused onto the substrate surface by a dark field condenser (0.8-0.92 NA, Olympus). Scattered light was collected through a 40x, 0.75 NA objective and imaged using an EM-CCD camera (Andor

iXon). Each pixel of the CCD represented an actual sample area of ~380 nm × 380 nm. Scattering images of the substrate surface during electrodeposition were recorded at a time resolution of 50 ms. The start of data collection was controlled by a triggering pulse from the potentiostat.

Acknowledgements

This material is based upon work supported by the Department of Energy under Award Number (s) DE-SC0005392. C.Z. and J.Z. acknowledge the support of National Institute of Health (R21EB009853). S.P. and C.H. were partially supported by the National Science Foundation under award number CHE-1153120. We are very grateful to Research Stimulation Program the University of Alabama for supporting R.B., and The Center for Analytical Facility (CAF) of The University of Alabama for surface analysis instrument support.

Received: ((will be filled in by the editorial staff))
Revised: ((will be filled in by the editorial staff))
Published online: ((will be filled in by the editorial staff))

Figure 1. Experimental schematics for DFS (A) and PL (B) based single NP spectroelectrochemistry experiments.

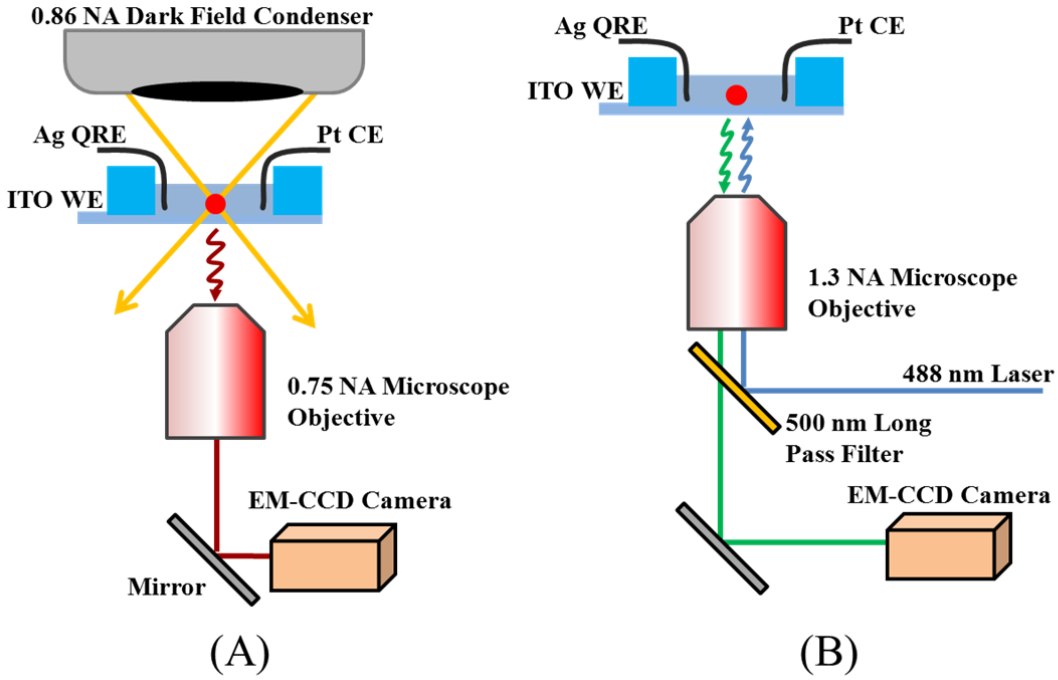

Figure 2. A: Schematic of light excitation and detection from a single Ag NP coated onto an ITO electrode for studying its redox behavior in an electrochemical cell; B: a typical DFS image of Ag NPs deposited onto an ITO surface via Ag^+ reduction.

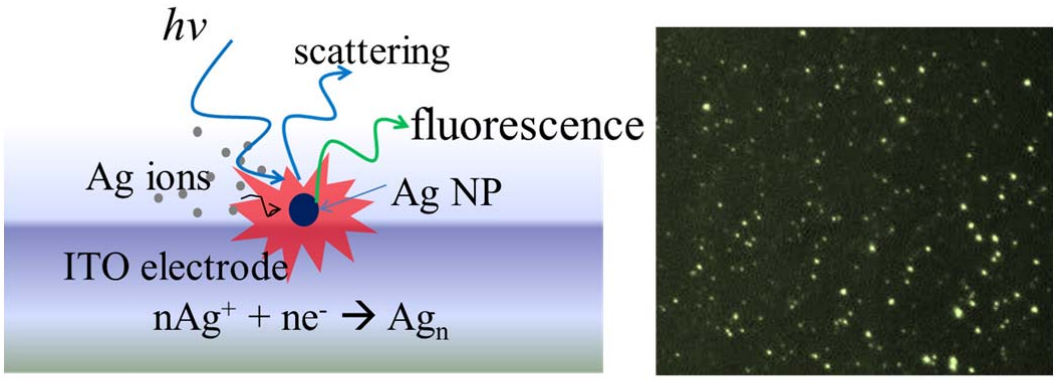

(A) (B)

Figure 3. Cyclic voltammograms of a bare ITO electrode in 300 μM Ag acetate and 0.1 M $LiClO_4$ in MeCN during Ag NP deposition/oxidation using regular and dry MeCN (A) and scattering images of the ITO electrode obtained during the deposition process (B). The potentials at which the given images in B were acquired are indicated by the blue points in the cyclic voltammogram of panel A.

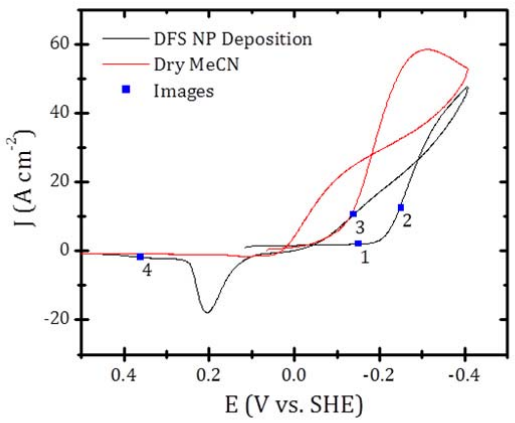

(A)

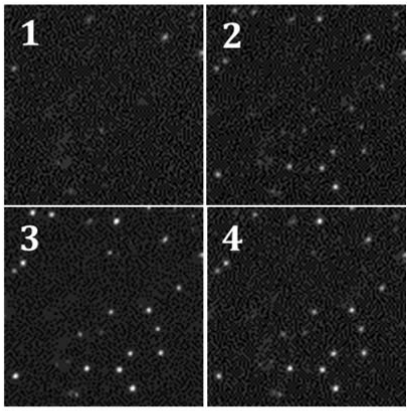

(B)

Figure 4. 16 individual Ag NP DSF intensity transients selected from DFS images of Figure 3B during Ag deposition and oxidation using CV at a scan rate of 100 mV/sec in a solution of 300 μM Ag acetate and 0.1 M $LiClO_4$ in MeCN. The electrode potential was scanned from 0.26 V (vs. SHE) to -0.26 V (vs. SHE), and then scanned to 4.24 V (vs. SHE) at a scan rate of 100 mV/sec as shown by the potential curve in the figure.

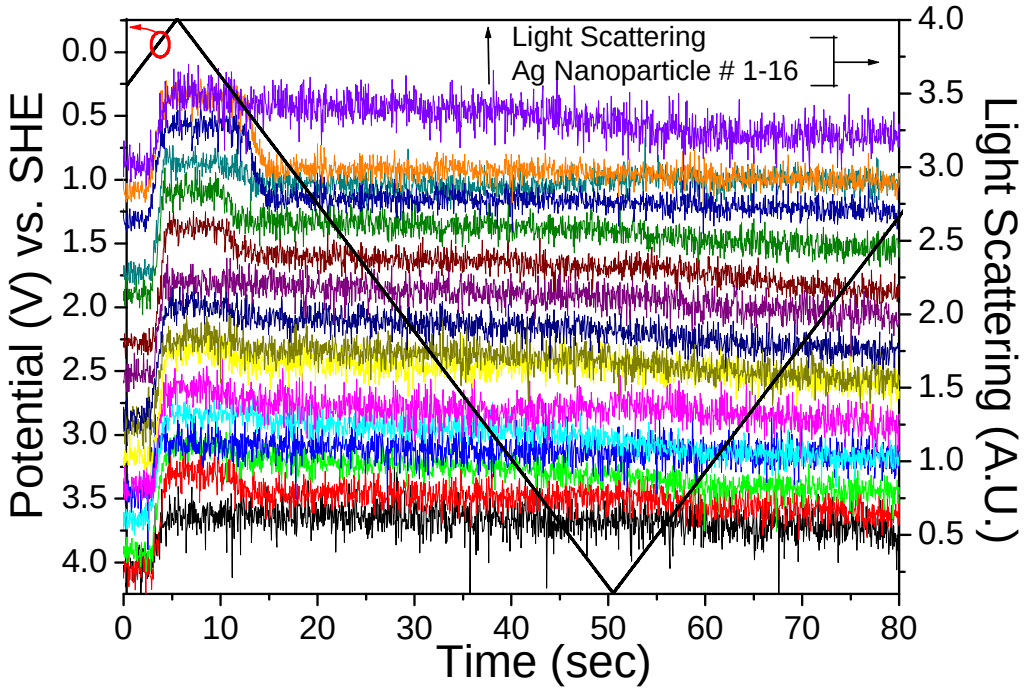

Figure 5. A: an averaged DSF intensity transient (in red) of 283 Ag NPs obtained from DFS images recorded during the course of Ag deposition. Current (in blue) and potential (black) transients are included to compare with the DSF intensity; B: CVs of a bare ITO electrode in 0.1 M $LiClO_4$ in MeCN with (red) and without (black) 300 μM Ag acetate present. The electrode potential was scanned from 0.26 V (vs. SHE) to -0.26 V (vs. SHE), and then scanned to 4.24 V (vs. SHE) at a scan rate of 100 mV/sec.

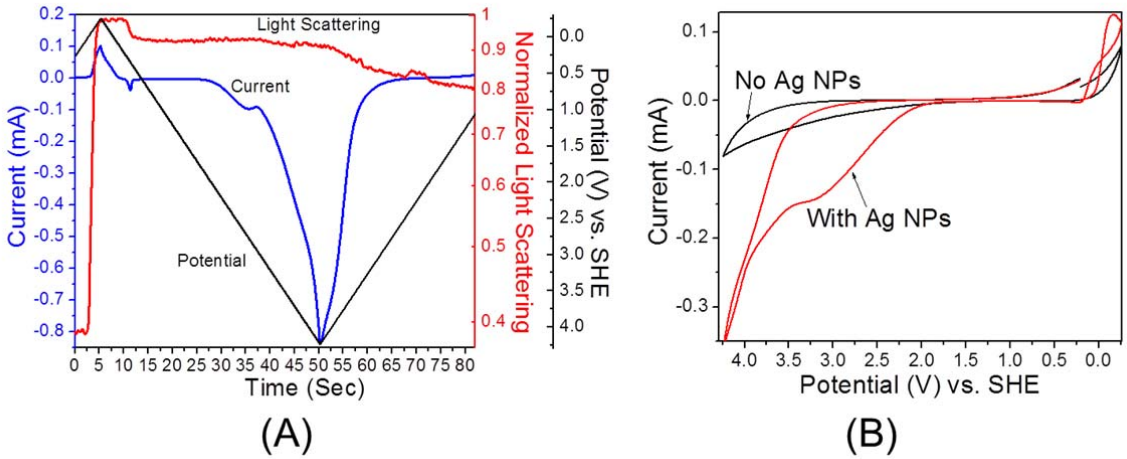

Figure 6. A and B are typical SEM images of Ag NPs prepared electrochemically on ITO surface from 300 μM Ag acetate and 0.1 M $LiClO_4$ in MeCN. These images were taken from a sample after DFS measurements demonstrating the presence of Ag NPs after applying a 4V (vs. SHE) electrode potential in 0.1 M $LiClO_4$ in MeCN.

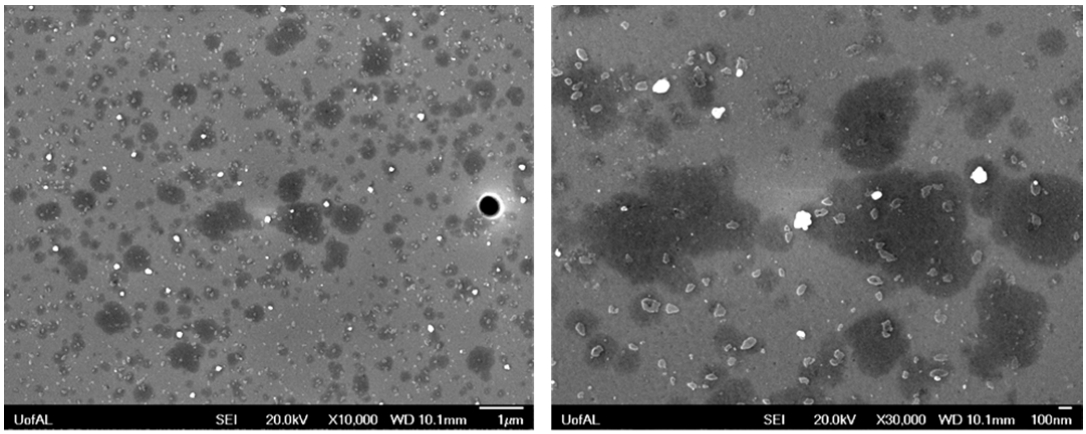

(A) (B)

Figure 7. Example fit of a single NP DFS scattering transient to 2 sigmoid functions (A), histogram of deposition and oxidation E_{on} values (B), correlation between deposition and oxidation E_{on} parameters (C), and correlation between oxidation E_{on} and A_{sig} parameters (D). The red points in the bottom panels represent binned averages. The errors bars represent 2 standard deviations.

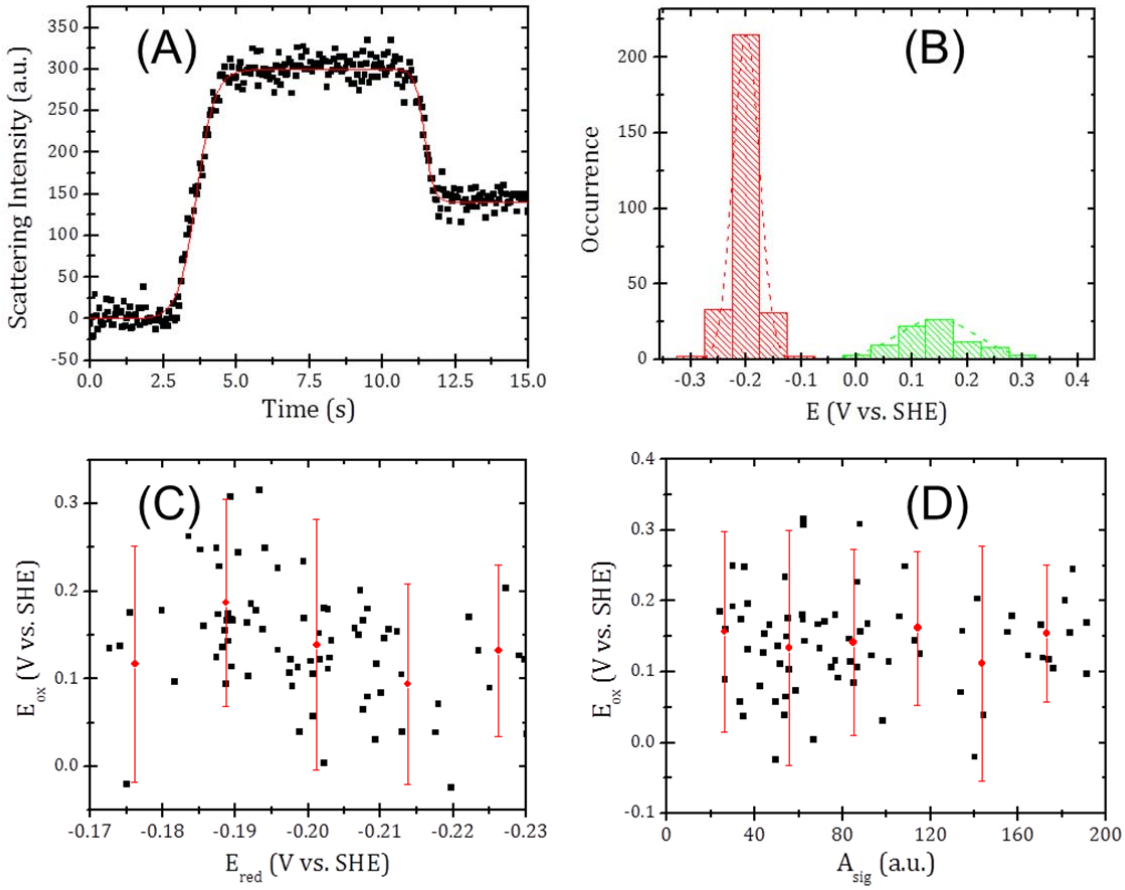

Figure 8. A: a typical PL image of electrodeposited Ag NPs on ITO electrode using CV at a scan rate of 100 mV/sec in 300 μM Ag acetate and 0.1 M $LiClO_4$ in MeCN; B: 16 individual Ag NP florescence intensity transients selected from PL during Ag deposition and oxidation. The electrode potential was scanned from 0.26 V (vs. SHE) to -0.26 V (vs. SHE), and then scanned to 2.5 V (vs. SHE) at a scan rate of 100 mV/sec as shown by the potential curve in the figure.

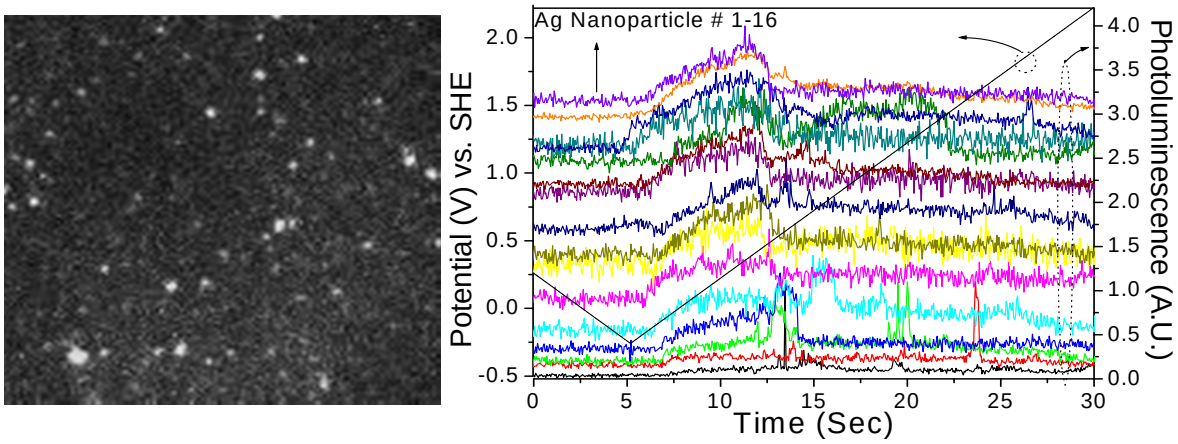

(A) (B)

Figure 9. A: an averaged PL intensity transient (in blue) of Ag NPs in comparison to the average DFS transient (in red) during the course of scanning the CV for Ag deposition and oxidation. The electrode potential (black) transient is included to compare with the PL and DSF intensity.

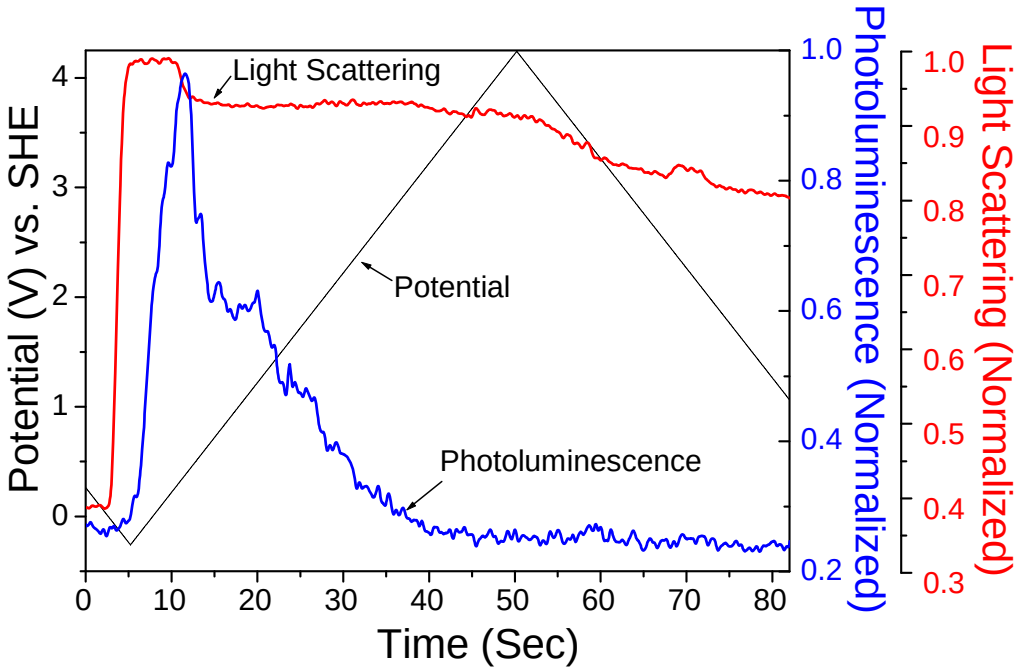

Figure 10. TEM image (scale bar is 50 nm) of fluorescent Ag NPs used for single particle PL spectroelectrochemistry studies (A), particle size statistics (B), absorption and PL spectra of the silver NPs ($\lambda_{exc.}$=488nm) (C), and a PL image of Ag NPs loaded onto an ITO electrode (D).

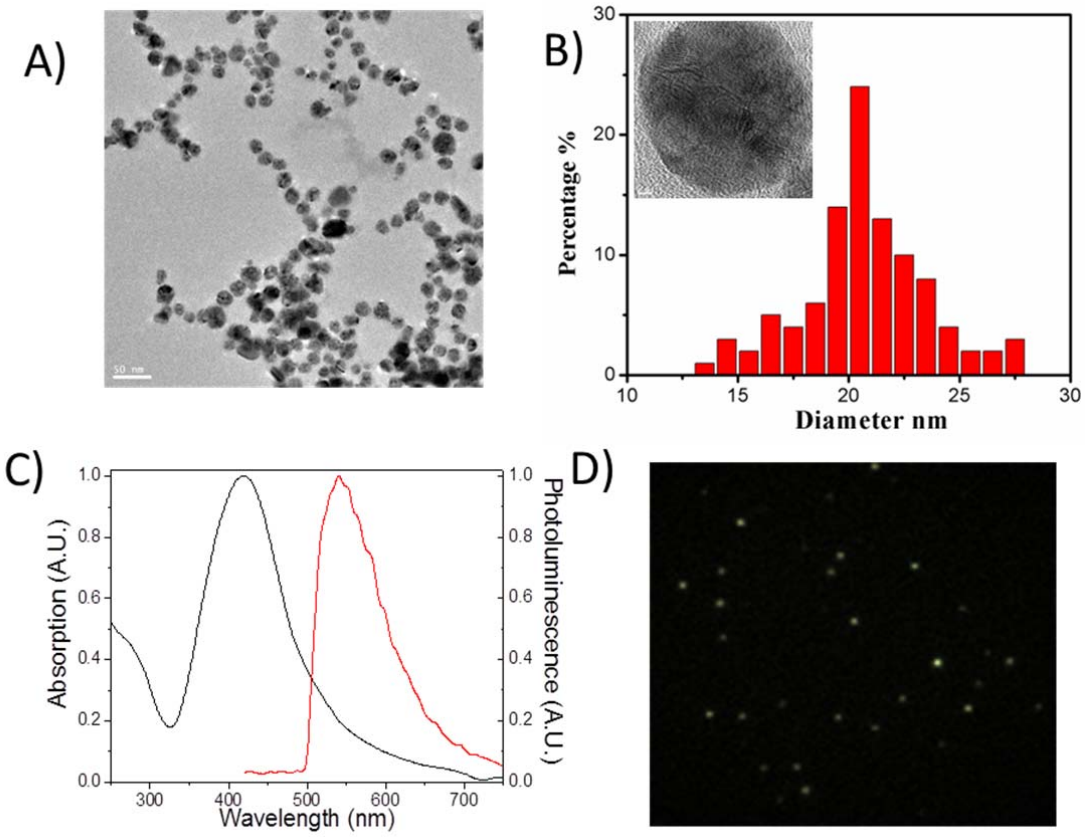

Figure 11. Total PL intensity and electrode current density during oxidation (A), PL images of the ITO electrode during oxidation (B), and PL transients for 4 selected individual plasmonic Ag NPs (C). The potentials at which the given images were acquired are indicated by the blue points in the CV.

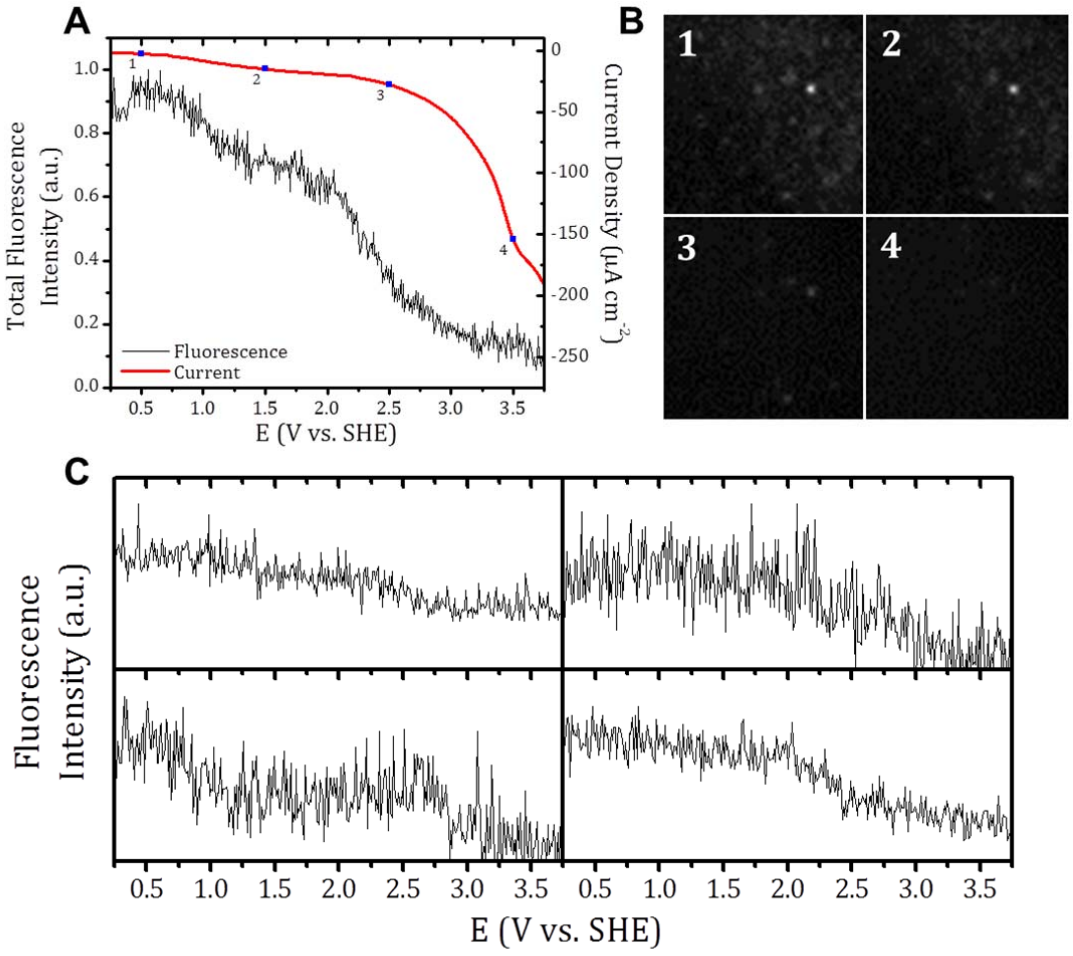

Figure 12. Example fit of a single NP PL transient to a combination of 2 sigmoid functions (A) and histograms of 1st and 2nd oxidation E_{on} values (B).

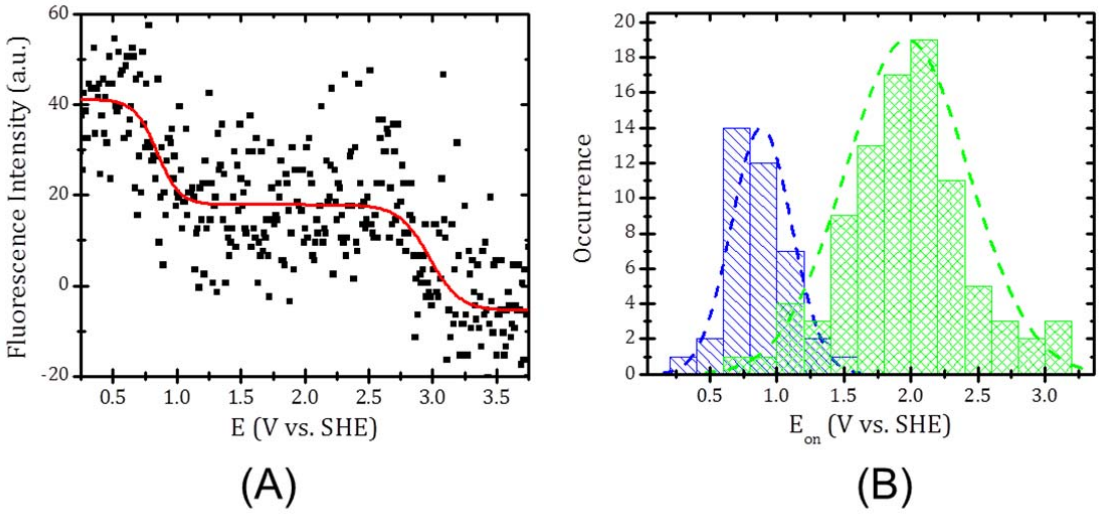

Figure 13. PL of the plasmonic Ag NPs under potential cycling (A), PL intensity and peak position during oxidation (B), and PL spectra during oxidation (C).

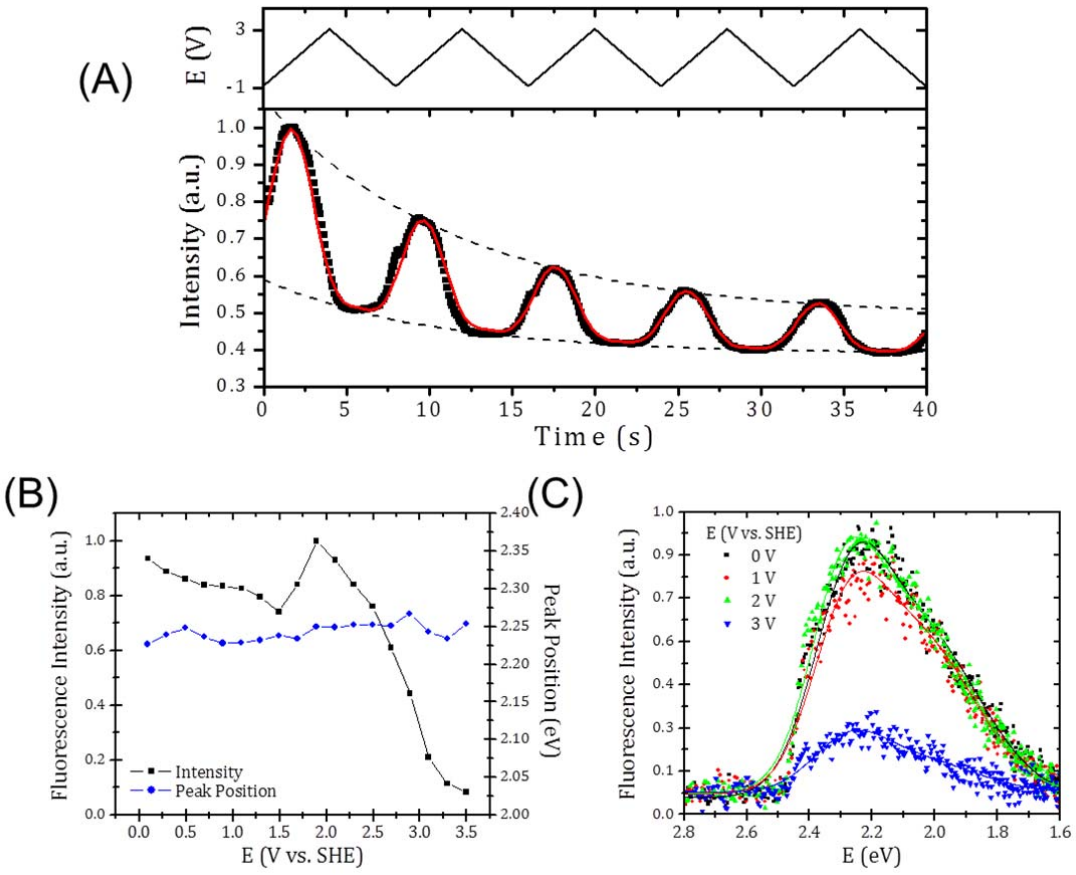

Table 1. Measured turn-on potentials for Ag reduction (Ec), first oxidation (Ea^1), and the second deep oxidation (Ea^2) for Ag NPs in 300 μM Ag acetate and 0.1 M $LiClO_4$ in MeCN using either single particle DFS or PL (PL) methods; Samples without turn-on potential data listed showed no DFS or PL signal response to oxidation.

Sample	# Analyzed	Ec_{on} vs. SHE	Ea^1 (V) vs. SHE	Ea^2 (V) vs. SHE	Method
1	283	-0.146(0.036)	0.354	-	DFS
2	784	-0.211(0.064)	0.573	-	DFS
3	40	-0.063(0.190)	-	-	DFS
4	618	-0.168(0.128)	-	-	DFS
5	15	-0.17(0.06)	0.36(0.06)	1.8(0.3)	PL
6	15	-0.21(0.04)	0.5(0.2)	1.9(0.7)	PL

TOC figure

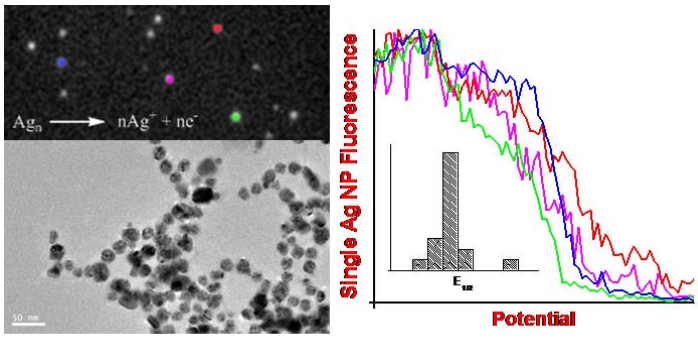

References:

[1] Xiao, X.; Bard, A. J. *J. Am. Chem. Soc.* **2007**, *129*, 9610-9612.

[2] Han, K. S.; Liu, G.; Zhou, X.; Medina, R. E.; Chen, P. *Nano Lett.* **2012**, *12*, 1253-1259.

[3] Zhou, X.; Xu, W.; Liu, G.; Panda, D.; Chen, P. *J. Am. Chem. Soc.* **2010**, *132*, 138-146.

[4] Xu, W.; Shen, H.; Liu, G.; Chen, P. *Nano Research* **2009**, *2*, 911-922.

[5] Palacios, R. E.; Fan, F. F.; Grey, J. K.; Suk, J.; Bard, A. J.; Barbara, P. F. *Nat Mater* **2007**, *6*, 680-685.

[6] Pan, S.; Wang, G. In *Single-molecule and single-nanoparticle electrochemistry at nanoelectrodes and spectroelectrochemistry;* Pierce, D., Ed.; Trace Analysis with Nanomaterials; Wiley-VCH: 2009;

[7]Ivanova, O. S.; Zamborini, F. P. *Anal. Chem.* **2010**, *82*, 5844-5850.

[8] Ivanova, O. S.; Zamborini, F. P. *J. Am. Chem. Soc.* **2010**, *132*, 70-72.

[9] Ward Jones, S. E.; Campbell, F. W.; Baron, R.; Xiao, L.; Compton, R. G. *J. Phys. Chem. C* **2008**, *112*, 17820-17827.

[10] Brainina, K.; Galperin, L.; Galperin, A. *Journal of Solid State Electrochemistry* **2010**, *14*, 981-988.

[11] Nie, S.; Emory, S. R. *Science* **1997**, *275*, 1102-1106.

[12] Fleischmann, M.; Hendra, P. J.; McQuillan, A. J. *Chemical Physics Letters* **1974**, *26*, 163-166.

[13] Glass, A. M.; Liao, P. F.; Bergman, J. G.; Olson, D. H. *Opt. Lett.* **1980**, *5*, 368-370.

[14] Ray, K.; Badugu, R.; Lakowicz, J. R. *J. Am. Chem. Soc.* **2006**, *128*, 8998-8999.

[15] Aslan, K.; Wu, M.; Lakowicz, J. R.; Geddes, C. D. *J. Am. Chem. Soc.* **2007**, *129*, 1524-1525.

[16] Pan, S.; Rothberg, L. J. *J. Am. Chem. Soc.* **2005**, *127*, 6087-6094.

[17] Futamata, M.; Bruckbauer, A. *Chemical Physics Letters* **2001**, *341*, 425-430.

[18] Jiang, Y.; Wang, A.; Ren, B.; Tian, Z. *Langmuir* **2008**, *24*, 12054-12061.

[19] Qi, J.; Dang, X.; Hammond, P. T.; Belcher, A. M. *ACS Nano* **2011**, *5*, 7108-7116.

[20] Kim, S.; Na, S.; Jo, J.; Kim, D.; Nah, Y. *Appl. Phys. Lett.* **2008**, *93*, 073307-3.

[21] Kim, K.; Carroll, D. L. *Appl. Phys. Lett.* **2005**, *87*, 203113-3.

[22] Chuang, C.; Wu, M.; Su, W.; Cheng, K.; Chen, Y. *Appl. Phys. Lett.* **2006**, *89*, 061912.

[23] Mihalcea, C.; Buechel, D.; Atoda, N.; Tominaga, J. *J. Am. Chem. Soc.* **2001**, *123*, 7172-7173.

[24] Peyser, L. A.; Vinson, A. E.; Bartko, A. P.; Dickson, R. M. *Science* **2001**, *291*, 103-106.

[25] Geddes, C. D.; Parfenov, A.; Gryczynski, I.; Lakowicz, J. R. *J Phys Chem B* **2003**, *107*, 9989-9993.

[26] Díez, I.; Pusa, M.; Kulmala, S.; Jiang, H.; Walther, A.; Goldmann, A. S.; Müller, A. H. E.; Ikkala, O.; Ras, R. H. A. *Angewandte Chemie International Edition* **2009**, *48*, 2122-2125.

[27]Zhou, Z.; Du, Y.; Dong, S. *Biosensors and Bioelectronics* **2011**, *28*, 33-37.

[28] Le Guevel, X.; Hotzer, B.; Jung, G.; Hollemeyer, K.; Trouillet, V.; Schneider, M. *J. Phys. Chem. C* **2011**, *115*, 10955-10963.

[29] Zheng, J.; Dickson, R. M. *J. Am. Chem. Soc.* **2002**, *124*, 13982-13983.

[30] Wu, W.; Zhou, T.; Zhou, S. *Chem. Mater.* **2009**, *21*, 2851-2861.

[31] Hill, C., Pan, S.L., A Dark Field Scattering Spectroelectrochemistry Technique for Tracking the Electrodeposition of Single Ag Nanoparticles, J. Am. Chem. Soc. 2013, 135(46),17250-17253.

[32] Zheng, J.; Ding, Y.; Tian, B.; Wang, Z. L.; Zhuang, X. *J. Am. Chem. Soc.* **2008**, *130*, 10472–10473.

Single Molecule Surface Enhanced Raman Spectroscopy of Region Regular poly (3-hexylthiophene-2, 5-diyl) on Nanostructured Silver Substrate

*Daniel A. Clayton, Karson S. Brooks, and Shanlin Pan**

The University of Alabama, Department of Chemistry, Tuscaloosa, AL 35487-0336

* **Corresponding Author: span1@bama.ua.edu**

Received Date (to be automatically inserted after your manuscript is accepted if required according to the journal that you are submitting your paper to)

ABSTRACT

This study is intended to increase the fundamental knowledge of structural and conformational dependence of single molecule Raman scattering characteristics of one of the most common organic semiconductors, region regular poly (3-hexylthiophene-2, 5-diyl) (P3HT). Single molecule Raman spectra of P3HT are found to have extremely long lifetimes in comparison to Rhodamine 6G (R6G) single molecule trajectories due to the multiple chromophoric nature of the conjugate polymer molecules. Single molecule spectra evolution and dynamic changes in its trajectories are recorded for polymer chains on SERS active silver substrate. Studies of the effects of four solvents, including chlorobenzene, dichloromethane,

toluene, and tetrahydrofuran (THF), used to dissolve the polymer to prepare single molecules on the nanotextured silver surface show good agreement with the ensemble measurements. The SERS spectrum of single P3HT in toluene shows the most Raman bands, indicating that the solvent plays a critical role in defining the folding of the molecule on the surface. Time dependent Raman spectra shows single P3HT polymer chains have very stable SERS spectra in comparison with R6G molecules. An incident light polarization effects study indicates only weak correlation of incident light polarization angle with plasmon enhanced photoluminescence of the silver nanostructure, and low sensitivity of single molecule SERS to incident light polarization because the molecules are excited along multiple different axes due to their poorly defined shapes on the nanotextured silver surface.

With the discovery of Surface Enhanced Raman Spectroscopy (SERS) by Jeanmarie and Van Duyne [1] as well as Albrecht and Creighton [2] in 1977, Raman spectroscopy has become a useful analytical tool for the development of ultrasensitive biosensors, [3-5] and helping understand the nature of kinds of interface problems such as charge transfer [6-8] and conformation of a molecule at a solid surface.[9-12] A major break-through in the area, specifically by Nie and Emory [13] and Kneipp et al.[14] in 1997, was able to reveal that strongly coupled silver nanoparticles under resonance conditions can enhance the local field intensity to a point where Single Molecule Surface Enhanced Raman Spectroscopy (SM-SERS) was possible. Yet most of the molecules studied have been small organic molecules, such as rhodamine 6g (R6G), [15-18] only a few reports have shown that this technique can be applied to larger molecules like polymers [19-26] and proteins. [27, 28] Conjugate polymers are a class of polymer molecules that have attractive optical and electrical properties for helping to understand the underlying photophysical properties of organic

semiconductors and real device applications such as organic solar cells[29], light emitting diodes[30], and transistors[31]. Past studies on conjugate polymers and their thin films have indicated that the processing conditions lead to variability [32, 33] in the morphology that can affect their photophysics and device performance.[34, 35] Recent studies have shown that SM-SERS is a powerful tool to help reveal the confirmation change and charge transfer of a conjugate polymer at a surface.[19,24] The present study intends to show the validity of using SM-SERS as a way of investigating polymer dyes, specifically poly(3-hexylthiophene-2,5-diyl) (P3HT), a common dye used in solar cells.[36] This molecule can adapt various conformations in different solvents and its conformation changes on a solid surface have yet to have been studied at the single molecule level.[37] Further the study intends to demonstrate the differences that can be gleaned from varying the solvent and incident field polarization angle.

Our SM-SERS experiment of P3HT will be performed on a nanostructured silver substrate prepared using the Tollens' silver mirror reaction[38] and the single molecule Raman performance of P3HT is compared with that of Rhodamine 6G. With the viability of the system proven, P3HT will be probed after coating from different solvents. Finally the surface enhanced Raman of single molecule P3HT and its dependence on the Tollens silver surface will be probed by varying the polarization angle of the incident light while performing SM-SERS.

The resulting nanotextured SERS slide is uniformly covered with silver and moderately brown in color. The slides were examined using a scanning electron microscope to discern the silver morphology (Figure 1A). The absorbance of the silver (Figure 1B) shows the optical density of the SERS substrate is around 1.18 at its plasmon absorption maxima of 445 nm. We found this would be the optimal silver coverage and resonance condition for our single molecule study. In order to confirm the viability of the Tollens silver mirror reaction substrate for SM-

SERS, we first exam the background SERS signal of bare silver substrate. Many “hot spots” were located on the sample emitting primarily silver fluorescence, but two Raman peaks at around 1258 and 1344 cm^{-1} were present. These peaks were attributed to nitric acid not being fully removed by the washing step. [39, 40] It should be noted that previous experiments have reported various contaminants, [41] such as atmospheric carbon, being present on single molecule substrates indicating that such contaminants are fairly common. R6G was used as the probe for confirming single molecule capability. As can be seen in Figure 1C, a single “hot spot” was chosen using the confocal microscopes scanning capabilities. Literature [42-44] confirms the correlation between “hot spots” and the luminescence/Raman intensity enhancement of a single R6G molecule. The Raman spectra signature is consistent with the SERS spectra of ensemble R6G molecule although some Raman peaks disappear from the single molecule spectra because the single molecule Raman is sensitive to the molecular orientation. We compare the ensemble SERS spectra of P3HT and single molecule P3HT from THF in Figure 1D; similar consistency can be observed for ensemble P3HT and single polymer chain SERS spectra. The C=C symmetric ring stretch of P3HT at 1459 cm^{-1} is reported in the literature [45] as being the most intense band, and appears in all measurements, though slightly blue shifted for SERS spectra. The blue shift might be due to the partial oxidation state of the polymer chain upon the photoinduced charge transfer at a hotspot and is consistent with previous report. [45] Also the C=C anti-symmetric ring stretch normally located at 1498 cm^{-1} appears to be absent. This band, which is normally used to help determine the conjugation length of the polymer, is thought to actually still be present but difficult to pick out from the broad symmetric ring stretch when combined with the background fluorescence. It should be noted that both panel C and D include no

fluorescence background from silver substrate. We made corrections to the SERS spectra by subtracting the fluorescence signature from the original spectra.

As shown in Figure 2 A and B, we recorded images of light scattering of the SERS substrate containing many hotspots but only a few spots were found to contain single molecule Raman signatures. The time evolution of single molecule R6G spectra (Figure 2 C) shows a high rate of intensity fluctuation indicative of single molecule behavior [43,46] as well as possible movement of the molecule. Differences in the peak intensity can be accounted for through variance in the angle of scattering, molecular orientation changes, and differences in the excited molecular motion.[47] The identifying peaks at 1392 and 1541 cm^{-1} are present confirming the presence of the R6G.[48-50] In comparing the various acquisitions in a single molecule of R6G over 4 minutes (Figure 2C), the intensity of the acquisition is first moderate for the first acquisition; however, after the first acquisition the intensity increases significantly. This remains relatively stable throughout many acquisitions, decreasing only slightly with each subsequent acquisition. However, after 150 s, the intensity decreases significantly, and the intensity further decreases at 210 s and remains low for the remainder of the collection period. On the other hand, the spectra of single P3HT molecules from chlorobenzene show that the molecule's Raman signal is much more stable throughout many acquisitions. As seen in Figure 2D, the relative intensity remained increasingly stable throughout the eight 30 s acquisitions. This lack of blinking in the molecule can also be seen in the molecule's trajectory, which shows a stable slightly downward sloping line. The trajectory does show several intense, short-lived peaks; however, these peaks are due to the minute variations of orientation of the molecule or charge transfers occurring in the sample. Unlike in R6G, these events in P3HT do not affect the overall stability of the molecule, and, therefore, P3HT is much more stable than R6G, which is contributed to P3HT being a

conjugated polymer. Additionally, the hydrophobic site chain may help minimize the photo-oxidation of the polymer backbone in air further increasing the stability.

Figure 3A shows the single molecule Raman spectra of P3HT cast from four different solvents onto SERS active silver substrate. The C=C symmetric ring stretch of P3HT around 1459 cm^{-1} appears for all solvents while dramatic differences for other Raman peaks exist. We think this is due to the conformation difference for P3HT when the molecules memorize the conformation in solution when they are transferred onto a nanotextured silver surface. Further studies are needed to confirm the conformation differences for all these solvents. For dichloromethane, the SM-SERS peaks match well with the ensemble confirming the identity of the P3HT. Importantly peaks such as the C-S-C bond at 683 cm^{-1} and the C-H bond at 1210 cm^{-1} are markedly absent in almost all the spectra, a common phenomenon in single molecule Raman studies where particular bands apparent in the ensemble are absent in the single molecule. Other peaks like the C=C bond at 1521 cm^{-1} are present in the shown spectra but absent in other measured spectra, indicating not only SM behavior but also implying that the orientation along the varied silver surface is not uniform when casting the single molecule. This should further indicate that local variability will occur with variances in the polarization angle of the incident light, with that aspect being further probed below. The peak at ~1498 cm^{-1} is related to the actual backbone of the polymer and can be used to indicate the conjugation of the polymer chain. In past cases, lower intensities and sharper peaks in this region have indicated more highly conjugated polymers with less overall flexibility along the backbone. Further the intensity ratio of the 1459 cm^{-1} over the 1498 cm^{-1} peak gives an inverse relationship with the conductivity of polythiophene films[46], and is a value worth noting in the single molecule systems. However, due to the high background fluorescence it is extremely difficult to find the antisymmetric stretch

band, without which the ratio cannot be calculated. The Raman signature of single P3HT molecule cast from the other three solvents (chlorobenzene, THF, and toluene) are shown in Figure 3 A. We found each single molecule run corresponds well with its ensemble measurements, showing some variance much as dichloromethane showed variance. Further, P3HT single molecules from each solvent demonstrate slightly different spectra. Peaks appear in some of the toluene and THF spectra at ~650 cm^{-1} that are not present in the other two solvents and which correspond closely with the distorted conformation around the inter-ring single bond also known as a kink in the polymer.[51, 52] This is thought to be due to the presence of chlorine causing solvent memory. In addition, dichloromethane does not exhibit a peak at 997 cm^{-1} which appears in each of the other solvents and is due to the C-C between the ring and alkyl chain. This is believed to be due to solvent memory influencing the side chains folding parameters upon the silver surface causing them to preferentially lay perpendicular with the surface and thus not be enhanced by the silver surface plasmon. Such solvent dependent conformation change of P3HT on the surface of TiO_2 and its effect on solar cell efficiency has been observed previously for ensemble system.[53] Good solvents such as xylene and chlorobenzene would lead to extended polymer chains which have sufficient contact with the substrate causing improved exciton dissociation and short circuit current for a solar cell.

The single molecule trajectories of P3HT were compared with the ones of R6G as shown in Figure 3 B. The intensity trajectories of P3HT from all kinds of solvent are fairly stable over the whole time period. Normally this would indicate several molecules being present with blinking behavior indicating a single molecule. However, previous studies [19, 54] done by SERS with polymers have suggested that the polymer can be thought of as having multiple specific chromophores. Other studies have indicated that it is possible to have both a system of non-

isolated chromophores that exhibit energy transfer to the lowest energy level chromophore [20, 21, 25] and isolated chromophores along the same polymer chain that fail to transfer energy.[22] The ability to energy transfer between these chromophores causes distinct broadening of the photoluminescence background that is overlaid on the Raman signal. The stair step nature of the intensity trajectory indicates that multiple chromophores are likely exhibiting Raman signals indicating a low level of intra-molecular conjugation. The majority of intensity trajectories for P3HT molecules from each solvent indicate similar low amounts of conjugation to that seen in dichloromethane. However, not all intensity trajectories showed the normal stair step decrease in intensity and thereby indicate the possibility that high levels of intra-molecular conjugation have occurred in some single molecule experiments. This appears to be largely solvent independent within the observed solvents, and may be more a function of the local surface. This is dramatically different from single molecule trajectories of R6G that show rapid stepwise changes in the trajectories due to changes in the molecular orientation and/or local heating before becoming photobleached. We found no such behavior for bare SERS substrate, except very short bursts in fluorescence background from small silver clusters that emit strong luminescence which can undergo dynamic changes because of the local photochemical reaction of silver oxide and silver as shown previously.[55]

The trajectories shown in Figure 3 include both Raman and the silver background fluorescence. To further demonstrate the solvent dependence and dynamic changing in the local field enhanced Raman spectra, time evolution Raman spectra are shown in Figure 4. Consistent with results of trajectories in Figure 3, Raman spectra of P3HT from all kinds of solvent are fairly stable over the whole time period in comparison to single molecule R6G. The appearance of particular bands also provides strong proof of actual single molecule activity, since it is a

common occurrence for some bands not visible in the ensemble to be visible in the SM spectra. For example, Raman bands in THF at 724 cm^{-1} of the C-S-C band appear initially but disappear over time, indicating that the local area is likely undergoing heating and thus the SM is undergoing conformational shifts over time, [19] with it being unlikely but possible that the silver surface is changing through photoreduction. [45] These findings hold for more than 20 molecules probed.

Stable single polymer Raman spectra would allow us to study the polarization dependence of the Raman intensity of a molecule. In order to fully confirm the single molecule nature, a polarization study is performed using P3HT, since the SERS enhancement is dependent upon the polarization of the incident light and its interactions with the orientation of the molecule and the local plasmonic field [56-58]. In order to accomplish this, a half plate is placed in the laser line attached to an electric motor with known acceleration and velocity. The plate is rotated from 0^o to 90^o then back 0^o with the cycle being repeated three times. This alters the polarization angle of the incident light so that its effects may be tracked. One of the major difficulties when performing this sort of experiment is that the dichroic mirror used in the microscope will not reflect all polarization angles equally. Therefore the first experiment is performed with a thin film of P3HT with no silver as shown in Figure 5 A to correct the actual light intensity in the laser focal volume. This leads to a situation where the P3HT is homogenous on the glass, and no differences in local geometry of the substrate should affect the overall output light. Figure 5 A shows the sinusoidal intensity traces taken of the P3HT thin film while the polarization angle is changed. The fluctuations in intensity is fairly uniform and despite some photo-bleaching due to the photoluminescence signal being largely fluorescence, lead us to believe that the dichroic mirror is having a standardized effect on the power of the incident light at the sample. The laser

intensity modulation by the dichroic is about 10% of the total laser intensity. With the nature of the dichroic's effect on the light intensity determined, it is now important to see if an uniform effect would occur on a nanostructured silver substrate. As such, Figure 5 A shows five traces taken of the silver scattering photoluminescence. The usual blinking phenomenon seen in silver is present and overlaid on a stronger background intensity modulation. The blinking phenomenon arises from the stochastic bursts of photoluminescence caused by the aggregation and formation of photoactive silver nanostructures.[55] These structures are extremely small, a few silver atoms in size, and thus produce a stochastic effect much like that of a set of single molecules. With the experiment being performed under air, one also expects that oxidation of the silver structures can cause bleaching, while the photoreduction occurs at other points causing reappearance of the silver photoluminescence. This modulation appears in all of the samples but is not uniform across the film in either time or intensity from spot to spot as shown in Figure 5A. The lack of uniformity in the modulation for some of the hotspots indicates that local field enhancement at some hotspots of the nanostructured silver substrate is strongly dependent on the geometry of the local silver nanostructure instead of the incident light intensity. Such local structural dependence of the surface enhancement is critical for single molecule Raman enhancement. Other spots we have probed show strong correlation between the background fluorescence of silver and incident light intensity modulation. This is not unexpected since the silver has been reported as enhancing the intensity several orders of magnitude due to the local field effect. Further the difference in intensity spectrums is further supported by the silver mirror process which leaves a poorly defined system. Thus one would expect to see multiple different intensity spectrums dependent upon the poorly defined, but strongly enhancing local field.

Finally single molecule P3HT samples are analyzed while the polarization angle of the incident laser is changed as shown in Figure 5 B. Overall, no large amount of uniformity is seen in the trajectory of single molecule Raman signal upon the change of polarization angle of the incident beam as the total collected light scattering signal of P3HT is overwhelmed by the background fluorescence signal of silver substrate as shown in Figure 2D and Figure 5A Most P3HT molecules we have spotted on the nanostructured silver surface show their light scattering seems to consistently follow the trend of the laser intensity as we change the polarization angle with local field effects appearing to have no effects. Because the silver substrate is poorly defined it cannot be ruled out that the local field may primarily be in resonance along the maximum polarizations of the incident laser, but is thought to be unlikely to continuously occur. Thus the polymer chains themselves are not laid out flat along the surface and instead are folded in many different directions. This leads to chromophores being excited along multiple different axes, and not just when the substrate's local field and incident laser are primarily interacting, and thus seeing the laser intensity modulation playing a large role in the excitement of the molecule. In addition, the polymer size is much smaller than the geometric size of the silver nanoparticles in the focus volume therefore the overall SERS of the molecule has to follow the field intensity of the nanostructure.

To conclude, this study successfully demonstrates single molecule characteristics of P3HT as a representative polymer dye commonly found in dye sensitized solar cells. Our results show that the multiple chromophores allow a higher stability and less overall blinking, but time resolved spectra do indicate differences in the excited Raman bands over time in comparison to single molecule Raman of R6G on a nanostructured silver surface. Further work indicated that solvent effects are apparent with particular bands being absent, and this data may possibly

provide better insight into the folding structure of the molecule dependent upon its solvent memory. Finally, the photoluminescence background of nanostructured silver substrate and single molecule Raman scattering show only weak polarization dependence. The collection of the polarization data is poor due to the undefined nature of the substrate causing a strong photoluminescence background. However, it was noted that it is likely that the polymer does form in a folded pattern with various chromophores showing preferential polarization on the nanostructured silver surface.

ASSOCIATED CONTENT

Supporting Information

Details of material, sample preparation, instrument and SERS measurement conditions. This material is available free of charge via the Internet at http://pubs.acs.org.

AUTHOR INFORMATION

Corresponding Author

*E-mail: span1@bama.ua.edu

Notes

The authors declare no competing financial interest

Funding Sources

Department of Energy under Award Number (s) DE-SC0005392.

ACKNOWLEDGMENTS

This material is supported by the Department of Energy under Award Number (s) DE-SC0005392.

REFERENCES

1. Jeanmarie, D.L.; Van Duyne, R.P. Surface Raman Spectroelectrochemistry: Part I. Heterocyclic, Aromatic, and Aliphatic Amines Adsorbed on the Anodized Silver Electrode. *J. Electroanal. Chem.* **1977**, *84*, 1-20.
2. Albrecht, M.G.; Creighton, J.A. Anomalously Intense Raman Spectra of Pyridine at a Silver Electrode. *J. Am. Chem. Soc.* **1977**, *99*, 5215-5217.
3. Bizzarri, A.R.; Cannistraro, S. SERS Detection of Thrombin by Protein Recognition using Functionalized Gold Nanoparticles. *Nanomedicine* **2007**, *3*, 306-310.
4. Cao, Y.C.; Jin, R.; Nam, J.M.; Thaxton, C.S.; Mirkin, C.A. Raman Dye-Labeled Nanoparticle Probes for Proteins. *J. Am. Chem. Soc.* **2003**, *125*, 14676-14677.
5. Culina, M.; Stokes, D.; Allain, L.R.; Vo-Dinh, T. Surface-Enhanced Raman Scattering Substrate Based on a Self-Assembled Monolayer for Use in Gene Diagnostics. *Anal. Chem.* **2003**, *75*, 6196-6201.
6. Milani, A.; Lucotti, A.; Russo, V.; Tommasini, M.; Cataldo, F.; Bassi, A.L.; Casari, C.S. Charge Transfer and Vibrational Structure of sp-Hybridized Carbon Atomic Wires Probed by Surface Enhanced Raman Spectroscopy. *J. Phys. Chem. C* **2011**, *115*, 12836-12843.
7. Wang, X.; Zhang, D.; Wang, Y.; Sevinc, P.; Lu, H.P.; Meixner, A.J. Interfacial Electron Transfer Energetics Studied by High Spatial Resolution Tip-Enhanced Raman Spectroscopic Imaging. *Angew. Chem. Int. Edit.* **2011**, *50*, A25-A29.
8. van Hal, P.A.; Christiaans, M.P.T.; Wienk, M.M.; Kroon, J.M.; Janssen, R.A.J. Photoinduced electron transfer from Conjugated Polymers to TiO_2. *J. Phys. Chem. B* **1999**, *103*, 4352-4359.

9. Li, D.; Borys, N.J.; Lupton, J.M. Probing the electrode-polymer interface in conjugated polymer devices with surface-enhanced Raman scattering. *Appl. Phys. Lett.* **2012**, *100*, 141907.
10. Podstawka, E. Structural Properties of Bombesin-Like Peptides Revealed by Surface-Enhanced Raman Scattering on Roughened Silver Electrodes. *Biopolymers* **2008**, *89*, 980-992.
11. Sun, L.; Song, Y.; Wang, L.; Guo, C.; Sun, Y.; Liu, Z.; Li, Z. Ethanol-Induced Formation of Silver Nanoparticle Aggregates for Highly Active SERS Substrates and Application in DNA Detection. *J. Phys. Chem. C* **2008**, *112*, 1415-1422.
12. Sambur, J.B.; Averill, C.M.; Bradley, C.; Schuttlefield, J.; Lee, S.H.; Reynolds, J.R.; Schanze, K.S.; Parkinson, B.A. Interfacial Morphology and Photoelectrochemistry of Conjugated Polyelectrolytes Adsorbed on Single Crystal TiO_2. *Langmuir* **2011**, *27*, 11906-11916.
13. Nie, S.; Emory, S.R. Probing Single Molecules and Single Nanoparticles by Surface-Enhanced Raman Scattering. *Science* **1997**, *275*, 1102-1106.
14. Kneipp, K.; Wang, Y.; Kneipp, H.; Perelman, L.T.; Itzkan, I.; Dasari, R.R.; Feld, M.S. Single Molecule Detection Using Surface-Enhanced Raman Scattering (SERS). *Phys. Rev. Lett.* **1997**, *78*, 1667-1670.
15. Michaels, A.M.; Jiang, J.; Brus, L. Ag Nanocrystal Junctions as the Site for Surface-Enhanced Raman Scattering of Single Rhodamine 6G Molecules. *J. Phys. Chem. B* **2000**, *104*, 11965-11971.

16. Dieringer, J.A.; Wustholz, K.L.; Masiello, D.J.; Camden, J.P.; Kleinman, S.L.; Schatz, G.C.; Van Duyne, R.P. Surface-Enhanced Raman Excitation Spectroscopy of a Single Rhodamine 6G Molecule. *J. Am. Chem. Soc.* **2009**, *131*, 849-854.
17. Constantino, C.J.L.; Lemma, T.; Antunes, P.A.; Aroca, R. Single-Molecule Detection Using Surface-Enhanced Resonance Raman Scattering and Langmuir-Blodgett Monolayers. *Anal. Chem.* **2001**, *73*, 3674-3678.
18. Kleinman, S.L.; Ringe, E.; Valley, N.; Wustholz, K.L.; Phillips, E.; Scheidt, K.A.; Schatz, G.C.; Van Duyne, R.P. Single-Molecule Surface-Enhanced Raman Spectroscopy of Crystal Violet Isotopologues: Theory and Experiment *J. Am. Chem. Soc.* **2011**, *133*, 4115-4122.
19. Wang, Z.; Rothberg, L.J. Structure and Dynamics of Single Conjugated Polymer Chromophores by Surface-Enhanced Raman Spectroscopy *ACS Nano*. **2007**, *1*, 299-306.
20. Yu, J.; Hu, D.; Barbara, P.F. Unmasking Electronic Energy Transfer of Conjugated Polymers by Suppression of O-2 Quenching. *Science* **2000**, *289*, 1327.
21. Hu, D.; Yu, J.; Wong, K.; Bagchi, B.; Rossky, P.J.; Barbara, P.F. Collapse of Stiff Conjugated Polymers with Chemical Defects into Ordered Cylindrical Conformations. *Nature* **2000**, *405*, 1030-1033
22. Huser, T.; Yan, M.; Rothberg, L.J. Single Chain Spectroscopy of Conformational Dependence of Conjugated Polymer Photophysics. *Proc. Natl. Acad. Sci. U.S.A.* **2000**, *97*, 11187-11191
23. White, J.D.; Hsu, J.H.; Yang, S.C.; Fann, W.S.; Pern, G.Y.; Chen, S.A. Deduction of the Conformation of Short Chain Luminescent Conjugated Polymers from Single Molecule Photophysics. *Chem. Phys. Lett.* **2001**, *338*, 263-268.

24. Schindler, F.; Lupton, J.M. Single Chromophore Spectroscopy of MEH-PPV: Homing-in on the Elementary Emissive Species in Conjugated Polymers. *Chem. Phys.* **2005**, *6*, 926-934.

25. Lee, Y.J.; Kim, D.Y.; Barbara, P.F. Single Conjugated Polymer Spectroscopy: Effect of Sample Preparation and Excitation Conditions. *J. Phys. Chem. B* **2006**, *110*, 9739-9742

26. Walker, M.J.; Lupton, J.M.; Becker, K.; Feldmann, J.; Gaefke, G.; Hoger, S. Simultaneous Raman and Fluorescence Spectroscopy of Single Conjugated Polymer Chains. *Phys. Rev. Lett.* **2007**, *98*, 137401.

27. Habuchi, S.; Cotlet, M.; Gronheid, R.; Dirix, G.; Michiels, J.; Vanderleyden, J.; De Schryver, F.C.; Hofkens, J. Single-Molecule Surface Enhanced Resonance Raman Spectroscopy of the Enhanced Green Fluorescent Protein. *J. Am. Chem. Soc.* **2003**, *125*, 8446-8447.

28. Bjerneld, E.J.; Foldes-Papp, Z.; Kall, M.; Rigler, R. Single-Molecule Surface-Enhanced Raman and Fluorescence Correlation Spectroscopy of Horseradish Peroxidase. *J. Phys. Chem. B* **2002**, *106*, 1213-1218.

29. Cowan, S.R.; Banerji, N.; Leong, W.L.; Heeger, A.J. Charge Formation, Recombination, and Sweep-out Dynamics in Organic Solar Cells. *Adv. Funct. Mater.* **2012**, *22*, 1116-1128.

30. Kulkarni, A.P.; Tonzola, C.J.; Babel, A.; Jenekhe, S.A. Electron Transport Materials for Organic Light-Emitting Diodes. *Chem. Mater.* **2004**, *16*, 4556-4573.

31. Yang, H.; Shin, T.J.; Yang, L.; Cho, K.; Ryu, C.Y.; Bao, Z. Effect of Mesoscale Crystalline Structure on the Field-Effect Mobility of Regioregular Poly(3-hexyl thiophene) in Thin-Film Transistors. *Adv. Funct. Mater.* **2005**, *15*, 671-676.

32. Schwartz, B.J. Conjugated Polymers as Molecular Materials: How Chain Conformation and Film Morphology Influence Energy Transfer and Interchain Interactions. *Annu. Rev. Phys. Chem.* **2003**, *54*, 141-172.

33. Peng, K.Y.; Chen, S.A.; Fann, W.S.; Chen, S.H.; Su, A.C. Well-Packed Chains and Aggregates in the Emission Mechanism of Conjugated Polymers. *J. Phys. Chem. B* **2005**, *109*, 9368-9373.

34. Collison, C.J.; Rothberg, L.J.; Treemaneekam, V.; Li, Y. Conformational Effects on the Photophysics of Conjugated Polymers: A Two Species Model for MEH-PPV Spectroscopy and Dynamics. *Macromolecules* **2001**, *34*, 2346-2352.

35. Spano, F.C. Modelling Disorder in Polymer Aggregates: The Optical Spectroscopy of Regioregular Poly(3-hexylthiophene) Thin Films. *J. Chem. Phys.* **2005,** *122*, 234701.

36. Li, G.; Zhu, R.; Yang, Y. Polymer solar cells. *Nature Photonics*. **2012**, *6*, 153-161.

37. Brinkmann, M.; Structure and Morphology Control in Thin Films of Regioregular Poly(3-hexylthiophene). *J. Polym. Sci. Pol. Lett.* **2011**, *49*, 1218-1233.

38. Saito, Y.; Wang, J.J.; Smith, D.A.; Batchelder, D.N. A Simple Chemical Method for the Preparation of Silver Surfaces for Efficient SERS. *Langmuir* **2002**, *18*, 2959-2961.

39. Grothe, H.; Myhre, C.E.L.; Nielsen, C.J. Low-Frequency Raman Spectra of Nitric Acid Hydrates. *J. Phys. Chem. A* **2006**, *110*, 171-176.

40. Lucas, H.; Petitet, J. High Pressure Raman Spectroscopy of Nitric Acid. *J. Phys. Chem. A* **1999**, *103*, 8952-8958.

41. Borys, N.J.; Lupton, J.M. Surface-Enhanced Light Emissions from Single Hot Spots in Tollens Reaction Silver Nanoparticle Films: Linear versus Nonlinear Optical Excitation. *J. Phys. Chem. C* **2011**, *115*, 13645-13659.

42. Moore, A.A.; Jacobson, M.L.; Belabas, N.; Rowlen, K.L.; Jonas, D.M. 2D Correlation Analysis of the Continuum in Single Molecule Surface Enhanced Raman Spectroscopy. *J. Am. Chem. Soc.* **2005**, *127*, 7292-7293.

43. Bizzarri, A.R.; Cannistraro, S. Statistical Analysis of Intensity Fluctuations in Single Molecule SERS Spectra. *Phys. Chem. Chem. Phys.* **2007**, *9*, 5315-5319.

44. Walter, M.J.; Borys, N.J.; Gaefke, G.; Hoger, S.; Lupton, J.M. Spatial Anticorrelation between Nonlinear White-Light Generation and Single Molecule Surface-Enhanced Raman Scattering. *J. Am. Chem. Soc.* **2008**, *130*, 16830-16831.

45. Bazzaoui, E.A.; Levi, G.; Aeiyach, S.; Aubard, J.; Marsault, J.P.; Lacaze, P.C. SERS Spectra of Polythiophene in Doped and Undoped States. *J. Phys. Chem.* **1995**, *99*, 6628-6634.

46. Weiss, A.; Haran, G. Time-Dependent Single-Molecule Raman Scattering as a Probe of Surface Dynamics. *J. Phys. Chem. B* **2001**, *105*, 12348-12354.

47. Wang, Z.J.; Rothberg, L.J. Origins of Blinking in Single-Molecule Raman Spectroscopy *J. Phys. Chem. B* **2005**, *109*, 3387-3391.

48. Guthmuller, J.; Champagne, B.; Resonance Raman Spectra and Raman Excitation Profiles of Rhodamine 6G from Time-Dependent Density Functional Theory. *ChemPhysChem* **2008**, *9*, 1667-1669.

49. Jensen, L.; Schatz, G.C. Resonance Raman Scattering of Rhodamine 6G as Calculated Using Time-Dependent Density Functional Theory. *J. Phys. Chem. A* **2006**, *110*, 5973-5977.

50. Watanabe, H.; Hayazawa, N.; Inouye, Y.; Kawate, S. DFT Vibrational Calculations of Rhodamine 6G Adsorbed on Silver: Analysis of Tip-Enhanced Raman Spectroscopy. *J. Phys. Chem. B* **2005**, *109*, 5012-5020.

51. Jakubiak, R.; Bao, Z.; Rothberg, L.J. Dendritic Sidegroups as Three-Dimensional Barriers to Aggregation Quenching of Conjugated Polymer Fluorescence. *Synth. Met.* **2000**, *114*, 61-64.

52. Akimoto, M.; Furukawa, Y.; Takeuchi, H.; Harada, I.; Soma, Y.; Soma, M. Correlation Between Vibrational Spectra and Electrical Conductivity of Polythiophene. *Synth. Met.* **1986**, *15*, 353-360.

53. Kwong, C.Y.; Djurisi, A.B.; Chui, P.C.; Cheng, K.W.; Chan, W.K. Influence of solvent on film morphology and device performance of poly(3-hexylthiophene):TiO_2 nanocomposite solar cells. *Chem. Phys. Lett.*, **2004**, *384*, 372-375.

54. Walter, M.J.; Lupton, J.M.; Becker, K.; Feldmann, J.; Gaefke, G.; Hoger, S. Simultaneous Raman and Fluorescence Spectroscopy of Single Conjugated Polymer Chains. *Phys. Rev. Lett.* **2007**, *98*, 137401.

55. Clayton, D.A.; Benoist, D.M.; Zhu, Y.; Pan, S. Photoluminescence and Spectroelectrochemistry of Single Ag Nanowires. *ACS Nano* **2010**, *4*, 2363-2373.

56. Furukawa, Y.; Akimoto, M.; Harada, I. Vibrational Key Bands and Electrical Conductivity of Polythiophene. *Synth. Met.* **1987**, *18*, 151-156.

57. Lyon, L. A.; Keating, C.D.; Fox, A.P.; Baker, B.E.; He, L.; Nicewarner, S.R.; Mulvaney, S.P.; Natan, M.J. Raman Spectroscopy. *Anal. Chem.* **1998**, *70*, 341R-361R

58. Yoon, D.; Moon, H.; Son, Y.; Samsonidze, G.; Park, B.H.; Kim, J.B.; Lee, Y.; Cheong, H. Strong Polarization Dependence of Double-Resonant Raman Intensities in Graphene. *Nano Lett.* **2008**, *8*, 4270-4274.

FIGURE CAPTIONS

Figure 1: SEM image (A) of nanotextured silver surface for single molecule SERS, its absorption spectra (B), the comparison of SERS spectra of single R6G molecule and ensemble R6G molecules (C), and the SERS spectra of single P3HT molecule and ensemble P3HT molecules (D).

Figure 2: Panel A and B are scanning Raman image of Rhodamine 6G (R6G) and P3HT, respectively, on the Tollens silver mirror substrate shows multiple hotspots showing only a few spots contains an actual molecule. Panel C and D are the corresponding Raman spectra and time flow of the spectra of single molecule R6G and P3HT.

Figure 3: Single molecule spectra P3HT coated from chlorobenzene, dichloromethane, toluene, and tetrahydrofuran (A), and corresponding typical single molecule Raman trajectories of P3HT from these four different solvent in comparison to single molecule R6G and SERS substrate (B).

Figure 4: The time evolution Raman spectra of a single molecule of P3HT coated from (A) Toluene, THF (B), dichloromethane (C), and chlorobenzene (D).

Figure 5: (A) photoluminescence intensity trajectories of several selected hotspots (1-5) on silver substrate in comparison to a P3HT thin film at various laser polarization angle. (B) single molecule P3HT intensity trajectory shows definite modulation due to the differences in laser intensity. Fluorescence modulation on ensemble P3HT intensity trajectory is shown in each figure to show changes in the laser intensity on the sample surface.

Figure 1

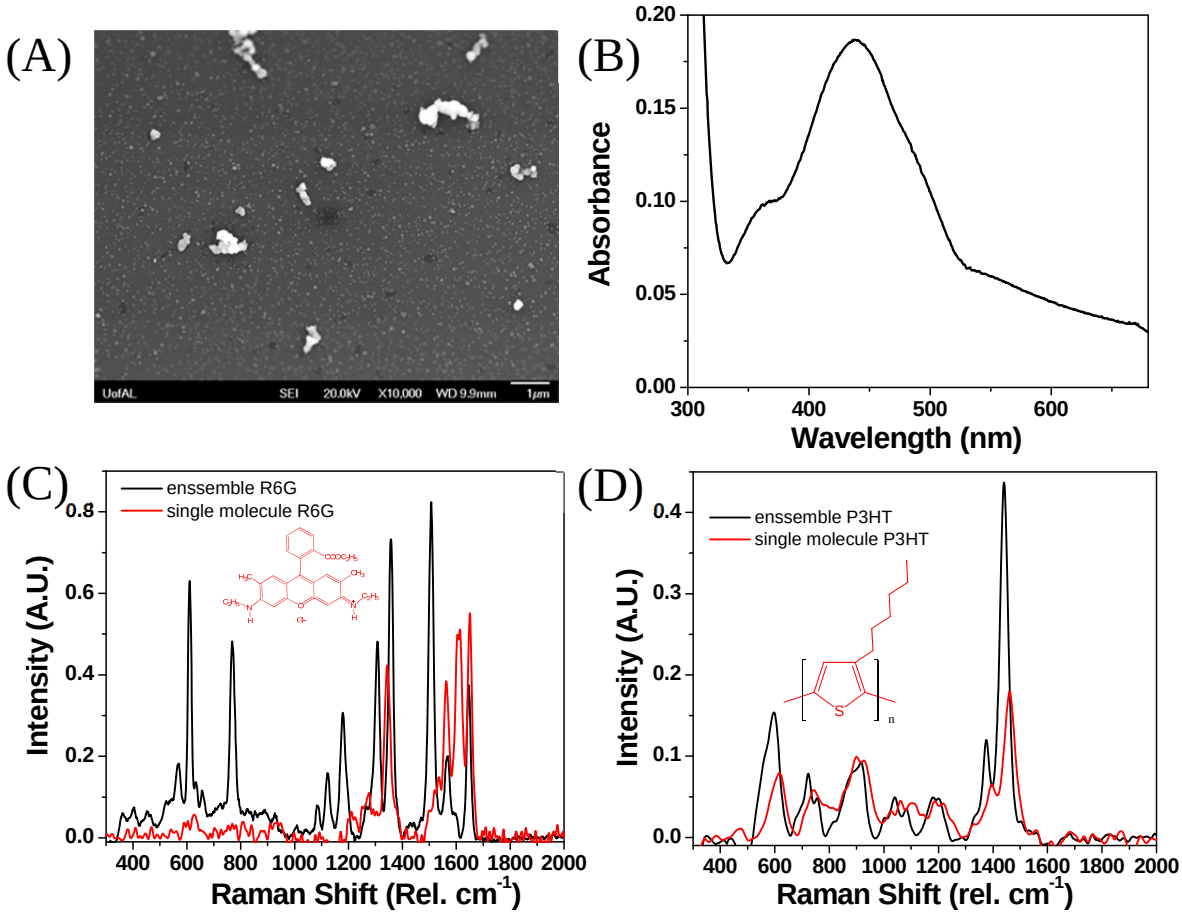
(A)
UofAL SEI 20.0kV X10,000 WD 9.9mm 1μm
(B)
Absorbance
Wavelength (nm)
(C)
enssemble R6G
single molecule R6G
Intensity (A.U.)
Raman Shift (Rel. cm-1)
(D)
enssemble P3HT
single molecule P3HT
Intensity (A.U.)
Raman Shift (rel. cm-1)

Figure 2

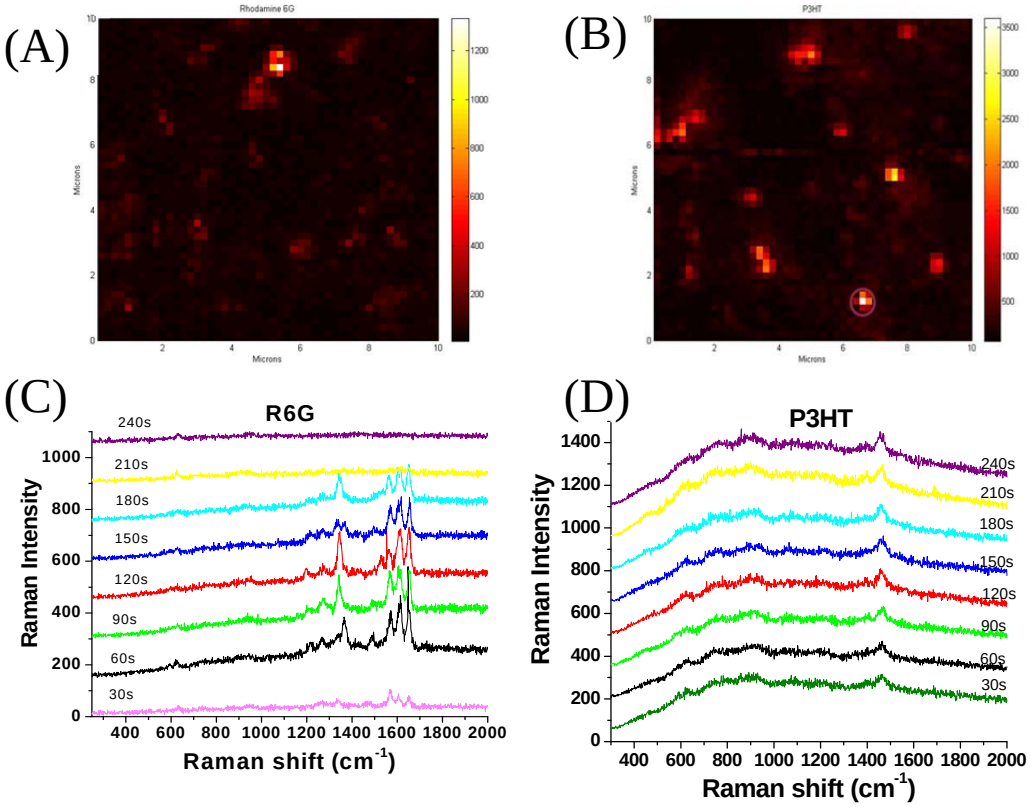
(A)
Rhodamine 6G
Microns
(B)
P3HT
Microns
(C)
R6G
240s
210s
180s
150s
120s
90s
60s
30s
Raman Intensity
Raman shift (cm-1)
(D)
P3HT
240s
210s
180s
150s
120s
90s
60s
30s
Raman Intensity
Raman shift (cm-1)

Figure 3

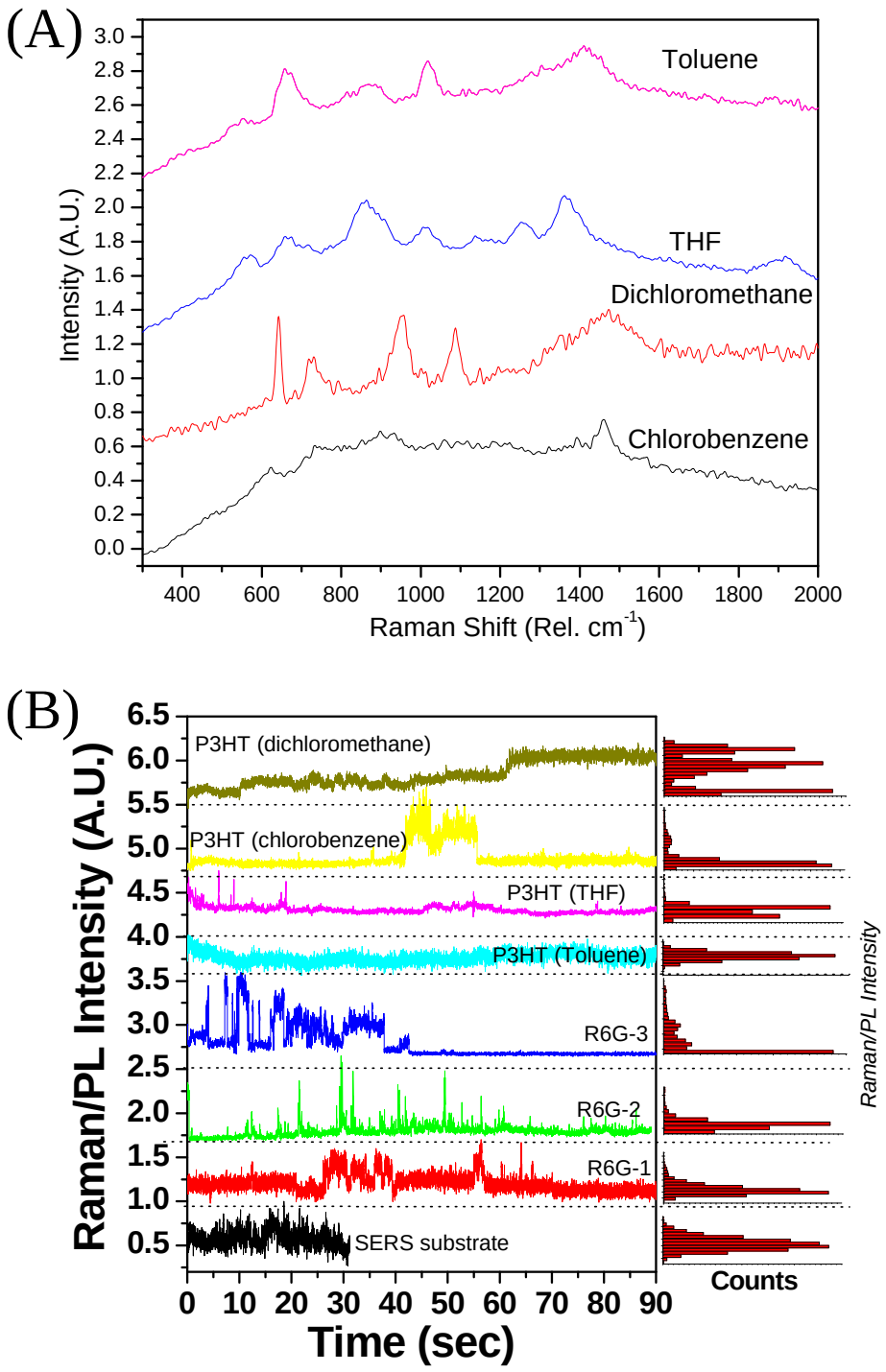
(A)
Toluene
THF
Dichloromethane
Chlorobenzene
Intensity (A.U.)
Raman Shift (Rel. cm-1)
(B)
P3HT (dichloromethane)
P3HT (chlorobenzene)
P3HT (THF)
P3HT (Toluene)
R6G-3
R6G-2
R6G-1
SERS substrate
Raman/PL Intensity (A.U.)
Time (sec)
Counts
Raman/PL Intensity

Figure 4

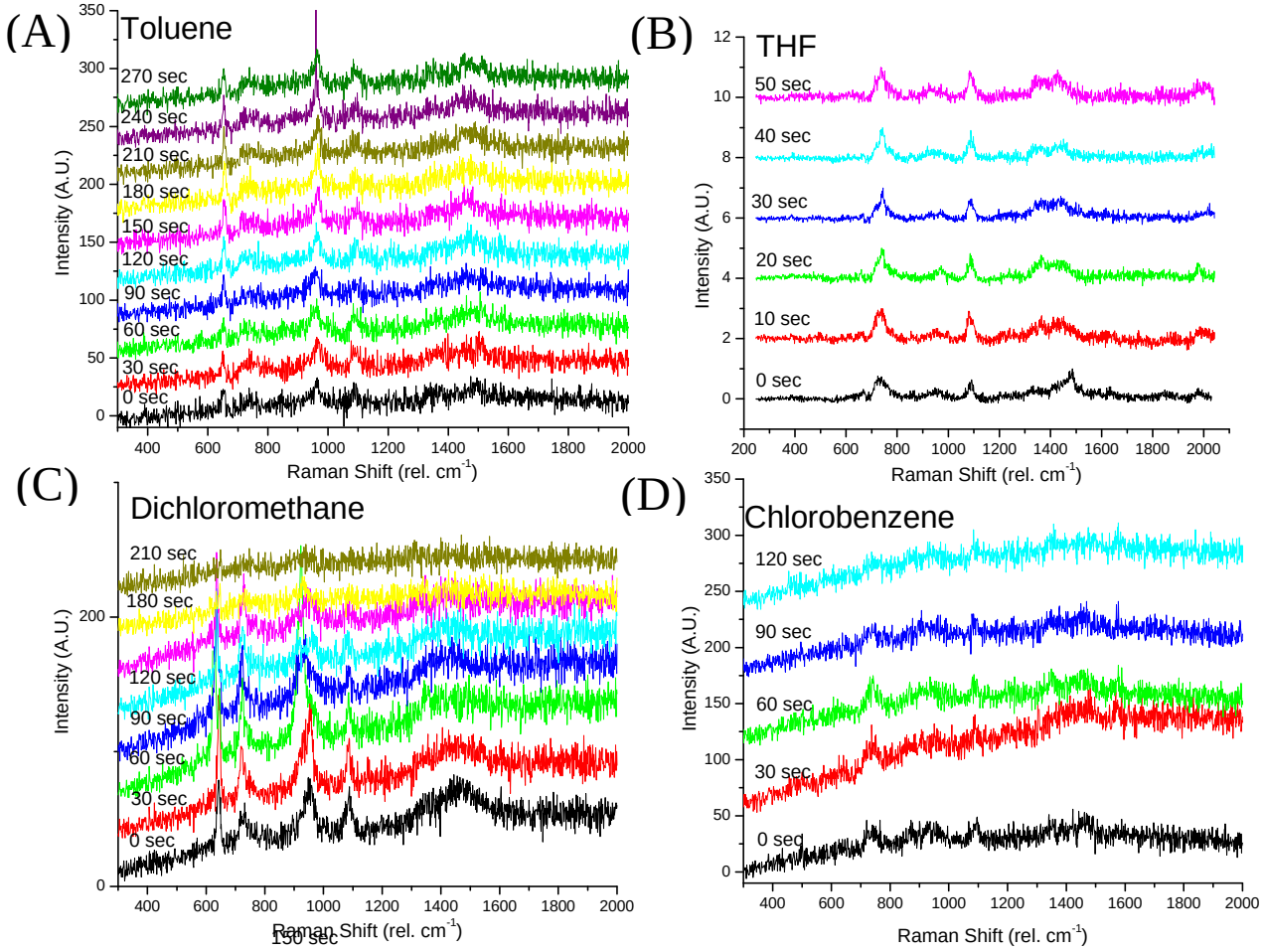
(A)
Toluene
270 sec
240 sec
210 sec
180 sec
150 sec
120 sec
90 sec
60 sec
30 sec
0 sec
Intensity (A.U.)
Raman Shift (rel. cm-1)
(B)
THF
50 sec
40 sec
30 sec
20 sec
10 sec
0 sec
Intensity (A.U.)
Raman Shift (rel. cm-1)
(C)
Dichloromethane
210 sec
180 sec
120 sec
90 sec
60 sec
30 sec
0 sec
Intensity (A.U.)
Raman Shift (rel. cm-1)
(D)
Chlorobenzene
120 sec
90 sec
60 sec
30 sec
0 sec
Intensity (A.U.)
Raman Shift (rel. cm-1)

Figure 5

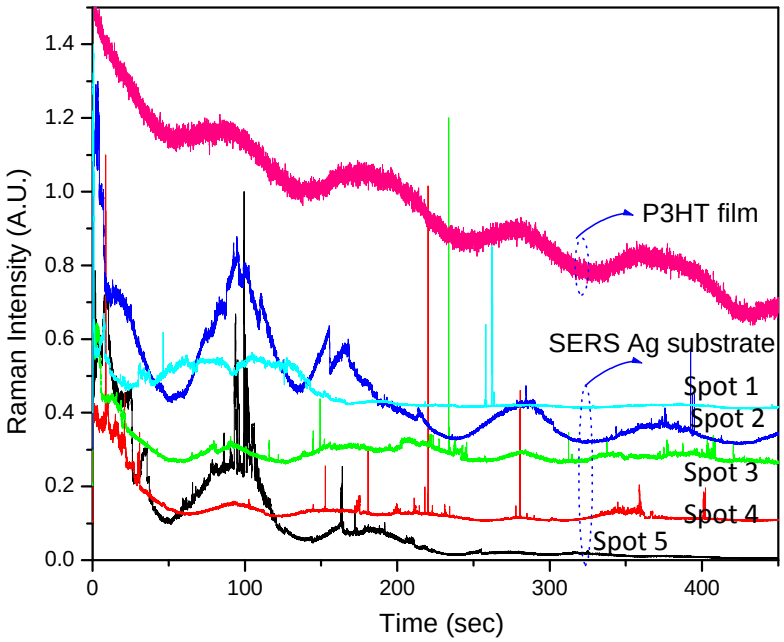
Raman Intensity (A.U.)
Time (sec)
P3HT film
SERS Ag substrate
Spot 1
Spot 2
Spot 3
Spot 4
Spot 5

(A)

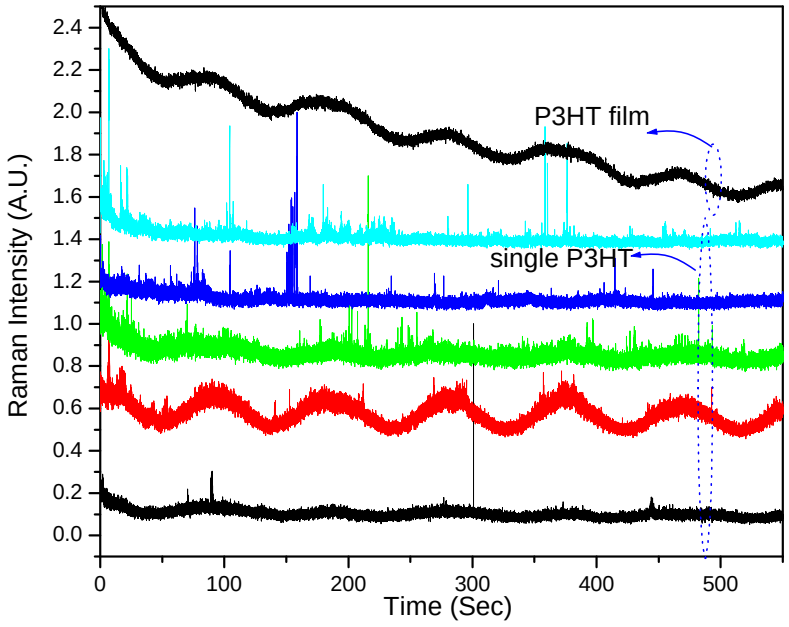
Raman Intensity (A.U.)
Time (Sec)
P3HT film
single P3HT

(B)

Supporting information

Single Molecule Surface Enhanced Raman Spectroscopy of poly (3-hexylthiophene-2, 5-diyl) on Nanostructured Silver Substrate

*Daniel A. Clayton, Karson S. Brooks, and Shanlin Pan**

The University of Alabama, Department of Chemistry, Tuscaloosa, AL 35487-0336

* **Corresponding Author: span1@bama.ua.edu**

Material: HPLC grade toluene, HPLC grade tetrahydrofuran (THF), silver nitrate, potassium hydroxide, strong ammonia solution, nitric acid and HPLC grade isopropanol were used as received from Fisher Chemicals. D-(+)-dextrose, poly (3-hexylthiophene-2, 5-diyl) and HPLC grade chlorobenzene were used as received from Sigma-Aldrich. Rhodamine 6G was obtained from Enzo Life Sciences and used as received.

Slide Cleaning: Cover glass (No. 1, 22 mm^2) was obtained from Corning. A standard cleaning procedure was performed by first placing the glass slides individually in a glass staining jar and filling the jar with 10% w/w potassium hydroxide in isopropanol. The jar was capped and sonicated for 10 minutes. The potassium hydroxide solution was removed and then the process was repeated with deionized water then isopropanol and then deionized water again. The slides

were then dried with nitrogen. Finally the slides were placed in a UV/Ozone Procleaner (BioForce Nanosciences, Ames, IA) and each side was exposed for 10 minutes.

SERS Surface Preparation. To prepare the two solutions of dextrose and silver diammine needed for the Tollens silver mirror reaction, 0.10M $AgNO_3$, 0.80 M KOH, and 0.25M dextrose ($C_6H_{12}O_6$) were prepared separately. To make the silver diammine, 30 mL of the 0.10M $AgNO_3$ solution was added to a 125 mL Erlenmeyer flask, and 15 mL of the 0.80M KOH solution was sequentially added to the flask. A brown precipitate immediately resulted from the mixture of the two solutions. Concentrated (15M) ammonia was then added drop-wise until the solution was clear and colorless. Both the solutions of dextrose and silver nitrate were stored in separate dark glass bottles and cooled until usage. Equal aliquots of the dextrose and silver diammine ion solutions at room temperature were placed in a disposable plastic vial and mixed thoroughly. This mixture was then pipetted onto a cleaned glass slide. This mixture was allowed to remain on the slide for three minutes. After three minutes, the mixture was rinsed with water and ethanol and allowed to dry. The resulting slide was uniformly covered with silver and moderately brown in color. The slides were examined using a scanning electron microscope (JEOL 7000, Tokyo, Japan) to discern the composition of the slides. The absorbance of the silver was also measured using an ultraviolet-visible spectrophotometer (Cary 50, Santa Clara, CA).

Sample Preparation. For the ensemble measurements, a 1×10^{-5} M solution of R6G in water and 1×10^{-5} M solutions of P3HT in each of toluene, THF, dichlorobenzene, and dichloromethane were prepared. Each one was independently spin coated onto a Tollens' silver mirror coated glass slide at 2,000 rpm for 60 seconds. For the single molecule measurements, a 1×10^{-9} M solution of R6G in water and 1×10^{-9} M solutions of P3HT in each of toluene, THF, dichlorobenzene, and dichloromethane were prepared and spin coated in the same way.

Instrumentation. Raman signals were obtained using a homemade confocal microscope set-up. A Nano-View 200-2/M nanopositioner (Mad City Laboratories, Madison, WI) was mounted to the top of an Olympus IX-71 Inverted Microscope for scanning. The sample was excited using a 633 nm self-contained HeNe laser (Thor Labs, Newton, NJ) at ~9.5 μW and imaged with a 100x numerical aperture oil-immersion objective (NA 1.3). The emission was collected with the same objective and passed through a 633 nm laser filter set with long pass emission (Z488LP, Chroma Technology, Brattleboro, VT) and a 633 nm Notch Filter (Edmund Optics Inc.). The photoluminescence signal was then split, sending one part into a spectrometer with a liquid-nitrogen cooled digital CCD spectroscopy system (Acton Spec-10:100B, Princeton instruments, Trenton, NJ) through a monochromator (Acton SP-2558, Princeton instruments, Trenton, NJ) and the other to an avalanche photodiode (APD, SPEM-AQRH-15, PerkinElmer). A PC 6602 card from National Instruments Inc. was used for data acquisition. Data collection and control of the photon counter and nanopositioner were done using labview 8.5 (National Instruments Inc.). Data analysis of the scanned images was done using MatLab (MathWorks, Natick, MA). The intensity trajectories and Raman spectra were analyzed using Origin 6.1 (OriginLab, Northampton, MA).

Probing Spatial Heterogeneities of Photo-induced Interfacial Charge Transfer at Surface of Single Crystal Anatase TiO_2 Particles

Daniel Clayton, Caleb Hill, Shanlin Pan

Department of Chemistry, The University of Alabama, Tuscaloosa, AL 35487-0336, United States

KEYWORDS: single crystal TiO_2, nanocrystals, photoreduction, photocatalyst

Abstract: We present photoreduction activities of silver ions and spatial heterogeneity of the photoreduction process at the surface of single crystal anatase TiO_2 particles synthesized using a hydrothermal process. Crystal facet dependence of the photoreduction process is revealed using surface enhanced Raman scanning (SERS) and strong light scattering of silver nanoparticles formed on the surface of the single crystal TiO_2 particles. High resolution electron microscopy (for morphology and element mapping) shows that {101} and {001} faces have similar activity, but that the introduction of surface defects leads to areas of more efficient silver ion reduction forming silver nanoparticles on the edges of the single crystals enabling strong SERS enhancement. Such spatial distribution and average photoactivities of silver ion reduction are compared for single crystal particles prepared under various conditions (e.g., thermal annealing, and chemical reduction in NH_3 gas) and we found that the majority of growth along the faces

occurs at defect sites. {not sure if this is formed by missing oxygen or Ti or physical defects of TiO_2}

TiO_2 has a wide band gap of around 3.2 eV with excellent ultraviolet (UV) light activity, [1,2,3] and has been used as low-cost photocatalytic material, [4,5,6,7] particularly for hydrogen generation from direct water splitting using solar energy, [8,9,10,11,12] The photocatalytic performance of TiO_2 can be improved using various types of doping methods (e.g., replacement of Ti [13,14,15,16,17] with another cation and/or replacement of O[18,19,20,21,22] with another anion). In particular the replacement of O has shown promise in reducing the bandgap by the introduction of localized bands just above the valence band[23,24,25] by producing oxygen vacancies which have better photocatalytic performance under visible light than pristine TiO_2.[26,27] Meanwhile the photocatalytic performance could actually be hampered by the additional defects introduced from the doping which can lead to efficient charge recombination that decreases the photocatalytic efficiency.[28,29,30] To improve its photocatalytic performance, the charge transfer rate in TiO_2 could be improved by producing TiO_2 with high crystalline domains, [31,32] which would serve as a substrate for optimal electron or hole transport.[33,34] Single crystal TiO_2 particles with size of several microns are particularly desirable for both practical application toward efficient water splitting and fundamental understanding of their structure-function relationship using electrochemical and optical methods. Multiple studies have revealed the impact of high crystalline TiO_2 on a photoelectrochemistry reaction. For example, Ohno et al were able to determine that electrons and holes were preferentially separated at the high crystalline face through Pt deposition and that rutile crystals tended to show more separation than the anatase crystals[34]. Majima and coworkers have developed a single molecule fluorescence photoreduction probe[35,36,37] that has confirmed a preferential electron transfer on the anatase

crystal for the {101} phase using spatially resolved calculations to determine the photon bursts at size less than the optical diffraction limit.[33] Further Majima and coworkers have gone on to determine that anatase TiO_2 shows no preference between the phases for the hole transport by designing a novel single molecule chemiluminescence probe[38] for use with their confocal measurement system. D'Arienzo et al [39] have shown similar effects for the anatase TiO_2 where the {001} facets show preferred photooxidation while the {101} facets act as photoreduction sites. In addition, Ahmed et al have shown that the rutile {001} face shows higher photocatalytic activity for the oxidation of methanol than the other rutile faces and the {101} anatase face[40]. Lu and coworkers showed that the fluorine terminated faces have similar photoreactivity while the cleaned phases show a preference for photoreactions on the {010} surface.[41,42] These highly crystalline TiO_2 particles are small enough to quickly grow and alter the dopants while maintaining the ideal crystal shape, providing great opportunity for thorough analysis of the dopant effects on photocatalytic activities and identification of preferred areas of charge separation at the surface of TiO_2. Here we provide a new method to investigate local photocatalytic activities and their preferred spatial distribution at single crystal TiO_2 particles using SERS and high resolution electron microscope imaging. Effects of thermal annealing and doping processes on their local photocatalytic activities are studied to reveal the structure-function relationship of TiO_2.

Micron sized anatase fluorine terminated TiO_2 crystals are obtained using a hydrothermal process according to a procedure outlined in the literature.[43,44] Figure 1A shows a typical SEM image of the TiO_2 crystal with an edge size of around 2 microns in a square shape and chemical composition being confirmed by the XPS data shown in Figure 1B. To understand the effect of surface composition on their photoelectrochemical performance, we performed an annealing

process under air to remove the surface adsorbed fluorine, which can be successfully confirmed by the XPS data in figure 1C. The annealing process was also carried out under an ammonia atmosphere (67% ammonia, balance argon at 500^{o} C for 1 hour). XPS data (cf. Figure 1D) confirms that a trace amount of nitrogen is present in both thermally annealed and as-synthesized crystals. A definite color change from white to yellow occurred in the crystals after ammonia treatment, indicating the hydrogen reduction of the crystal surface after ammonia decomposition into nitrogen and hydrogen at high temperature (500^{o}C).

Average photoelectrochemical performance of all three types of single crystal TiO_2 particles are assessed in a photoelectrochemical cell by coating TiO_2 particles in a gelatin matrix onto an ITO cover glass. Potential dependence of photocurrent and dark current responses of all three types of crystals are shown in Figure 2. Annealed single crystal samples show higher photocurrent than as-synthesized crystals, with it hypothesized to once again be due to the defect sites introduced through the annealing process for efficient charge separation and/or improved charge transport efficiency. The action spectra (cf. Figure 2d) of all three types of crystals show that the peak maximum essentially remains the same for all three different types of TiO_2. That means the average bandgap of the crystals has changed little due to the annealing processes. Therefore we conclude that the improved photocurrent and photocatalytic activities are attributed to the surface modification by removing fluorine and introduction of defect sites for efficient charge separation without making changes to the band gap of the material.

The enhanced UV and visible photocatalytic performance is further confirmed using photodecomposition of methylene blue (MB) in aqueous solution. as shown in Figure 3A, UV light shows much more efficient decomposition of MB than visible light with excitation wavelength longer than 420nm (intensity?? need to confirm with Greg and his student). Visible

light response to as-synthesized single crystal tio2 particles, and the ones annealed in air and in ammonia are shown in Figure 3B. Clearly improved efficiency was obtained on the thermmaled annealed sample and the one treated in ammonia. This is consistent with our electrochemical measurements in Figure 2.

Then show Figure 4 on XRD and Raman spectra in figures and discuss how they help understand figure 2-3. Ask Dr. Geng to help analyze the XRD

To reveal the local photoelectrochemical performance and its preferred facial growth, silver ions were photoreduced onto single crystal particles using a photoreduction scheme shown in Figure S1 of supporting information. Silver photoreduction was attempted on all three types of TiO_2 using both UV light (254 nm) and visible light (> 400 nm). Scanning electron microscopy (SEM) along with energy dispersive spectroscopy (EDS) mapping were used to study the morphology and spatial distribution of the silver on the surface of single crystals. As shown in Figure 5, UV illumination produces silver nanoparticles at the edges where single crystalline domains of TiO_2 meet, while small silver clusters grow on all the faces of three samples types with similar amounts as shown in table 1. More detailed electron microscope morphology and element mapping information is provided in Figure S2 of supporting information. On the other hand, only small amount of silver deposition occurs on all samples except as-synthesized TiO_2 under visible illumination with wavelength >400 nm, and silver growth does not occur primarily on the edges but equally on the faces. The as-synthesized single crystal TiO_2 particles do not show silver growth as much as the thermally annealed samples. We conclude that the ammonia treatment and thermal annealing processes introduce new defect sites by removing fluorine for efficient charge dissociation in contract to as-synthesized crystals. The enhanced visible light response has to do with the enhanced photocatalytic performance in the wavelength region which

falloffs near 400 nm. The new defect sites all over the crystal surface after ammonia treatment or thermally annealing in air are electron rich sites responsible for silver ion reduction, specifically the number of nucleation sites, whereas the growth process should be preferential based upon the deep electron transfer through the crystal.

To study the large silver nanoparticles at the edges of our single crystal samples, optical imaging was performed on a home-built inverted confocal microscope described fully in the supporting information and our previous work. [45] The laser beam can be focused on either the {101} or {001} face through a ×100 objective to resolve their light scattering features in the presence of silver nanoparticles as illustrated in Figure 6A and B. The optical imaging allowed us to identify the hot spots formed by silver nanoparticles on the single crystal TiO_2 sample, and these silver nanoparticles can localize the incident EM field for Raman scattering enhancement for any Raman active probing molecule such as rhodamine 6g (R6G). Further, the optical image can be compared directly to the SEM image as shown in Figure 6C, with the samples being very disperse on a gridded substrate. Our SERS study shows that very little SERS enhancement difference is obtained from hotspots located on the two faces, which can be seen in Figure 4. This is consistent with the results obtained from electron microscope and element mapping study. Most interesting to this study is the possibility of the TiO_2 face serving as a charge transfer enhancement route like that seen in nanoscale TiO_2 particles[46,47]. The essential idea is that excitons produced deep within the sample will separate and either the hole or electron will move preferentially along one the crystal axis towards the terminating face. If this holds true one would expect that additional SERs enhancement would occur preferentially along one of the faces further enhancing the SERs signal generated by the presence of silver. However, with the enhancement effects being similar between the faces and the silver growth being equal, which

would also indicate preferential deep electron transfer; it is reasonable to conclude that neither face exhibits preferential electron transfer. Future work using this well defined system with DFT calculations could better define the results.

We concluded that the silver growth and Raman imaging indicate that electron transfer occurs primarily at the edges where faces meet on anatase TiO_2. However, under visible light, absorption occurs primarily at defect sites that have a smaller band gap than the bulk sample. These sites are primarily generated on the faces by the removal of fluorine, not by the introduction of a dopant.

FIGURES:

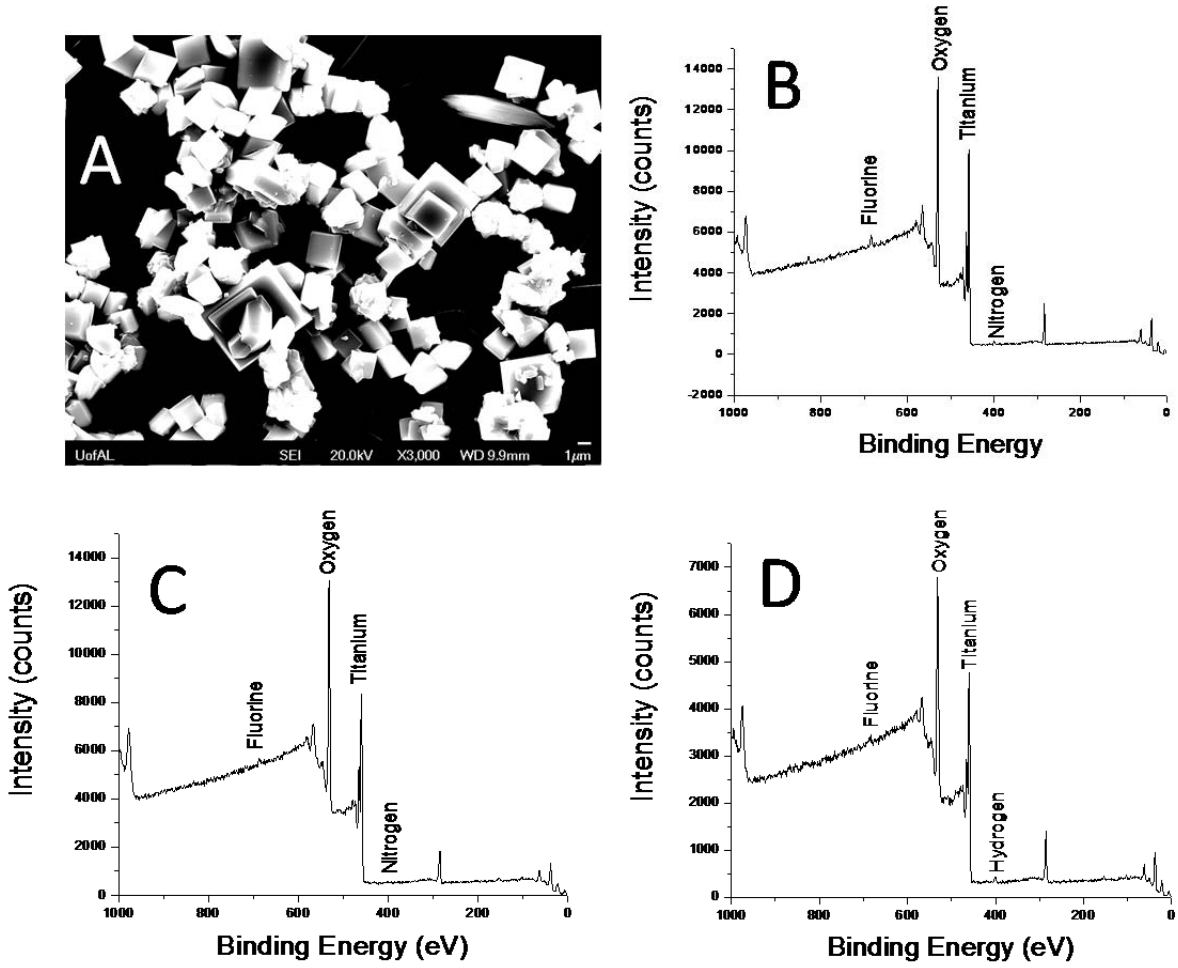

Figure 1. (A) A SEM image of the hydrothermally synthesized anatase TiO_2 confirms the anatase shape. XPS data confirms the composition of the (B) as synthesized sample, (C) annealed under air, and (D) annealed under nitrogen TiO_2 samples.

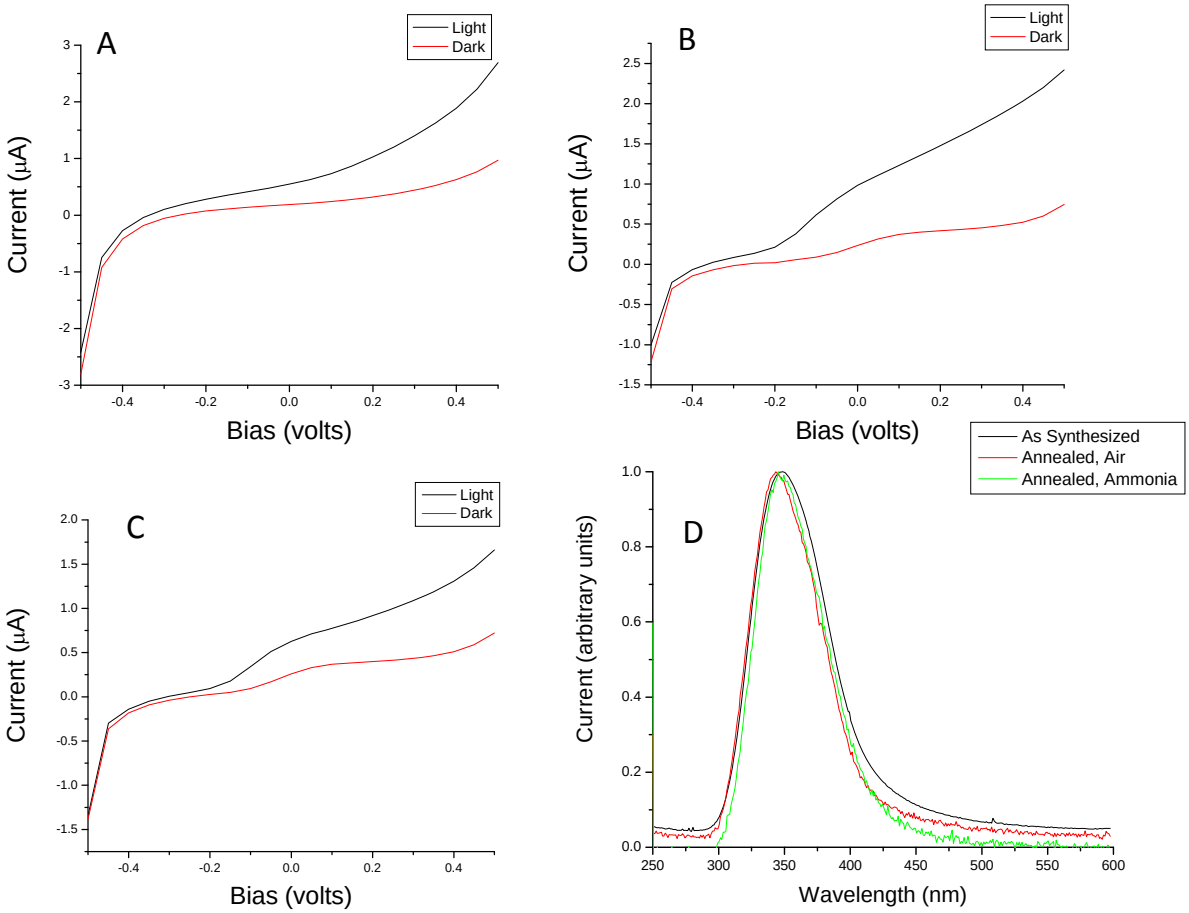

Figure 2. The IV curves for the (A) as synthesized sample shows less of an enhancement when the light is applied than the (B) annealed under air and (C) annealed ammonia samples. The (D) action spectra show no shift in the intensity peak.

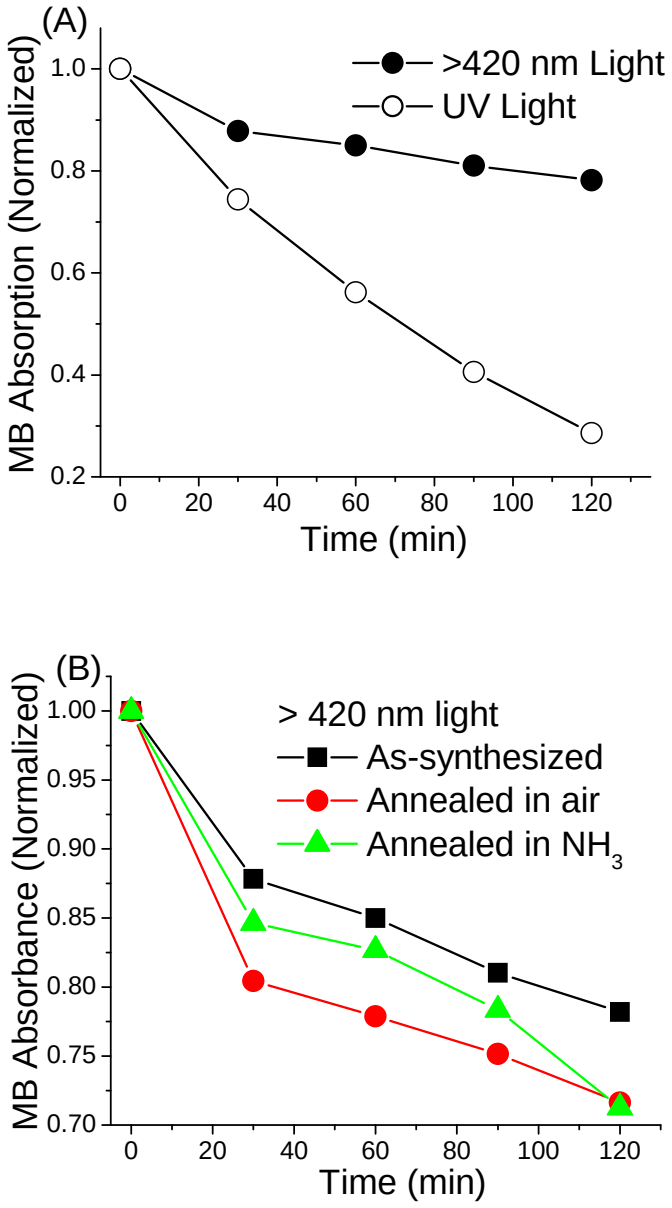

Figure 3. Photocatalytic decomposition of methylene blue (MB) at single crystal TiO2 nanoparticles under UV light irradiation. A: MB absorption response to visible and UV light irradiation. B: MB decomposition traces at as-synthesized single crystal TiO_2 particles, and single crystal TiO2 particles thermally annealed in air and annealed in ammonia, respectively.

Figure 4. XRD and Raman of the three samples

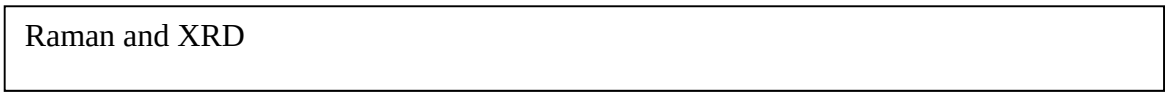

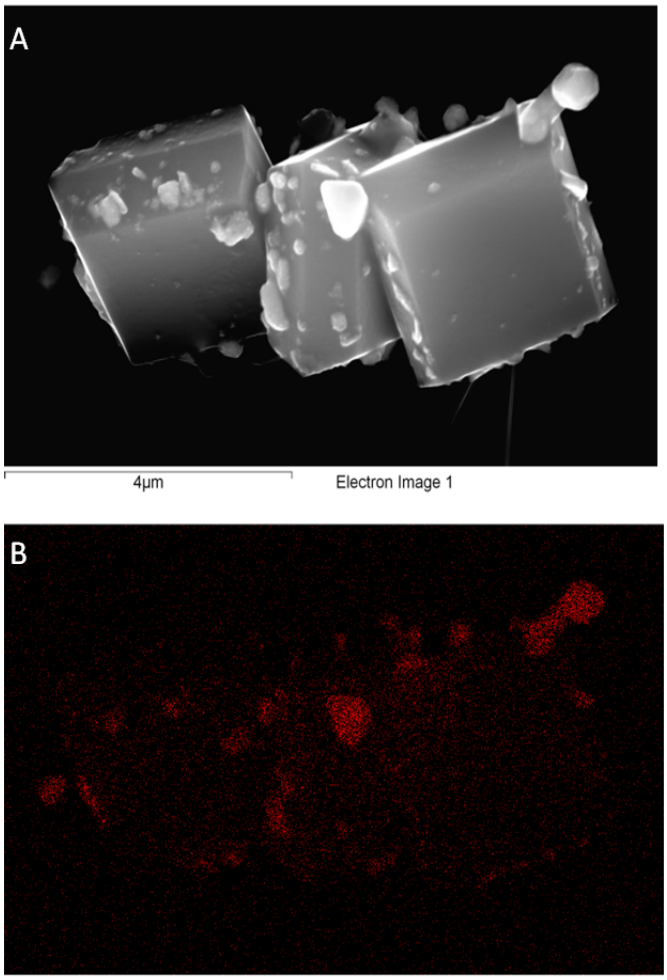

Figure 5. (A) SEM image of as synthesized TiO_2 with silver grown upon the sample using UV light. (B) The EDS mapping of silver on the sample. When the faces are manually identified the percent of coverage can be calculated.

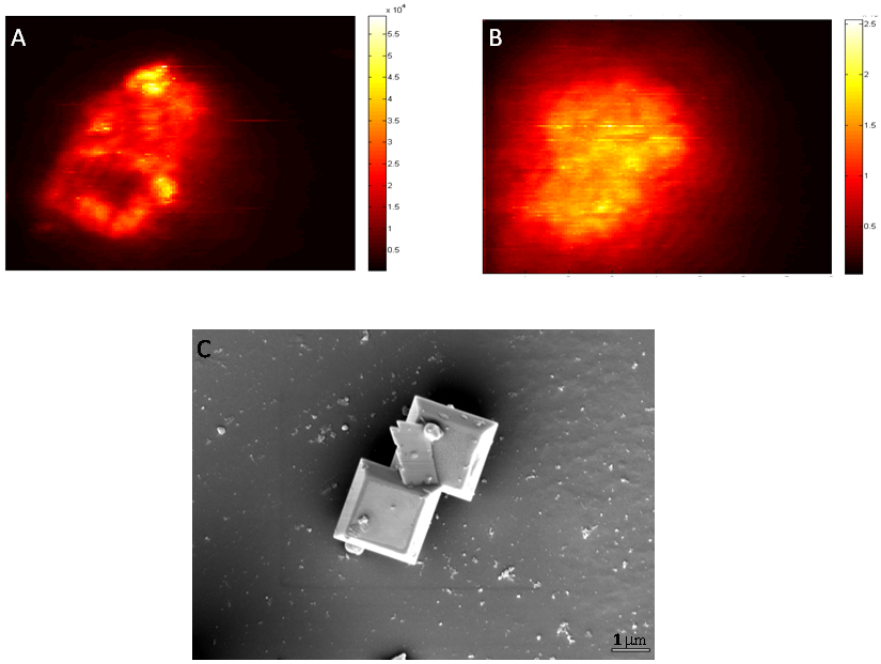

Figure 6. The scanning optical image focused on the (A) {101} face and the (B) {001) face allowed identification of hot spots and possible silver crystal formations on the TiO_2. (C) SEM images of the same crystal then allowed determination of the local area structures.
(can we added on the fluorescence image we took early as those two images show better contrast

of edge and top faces, I thin k they are in your poster and oral presentations??)

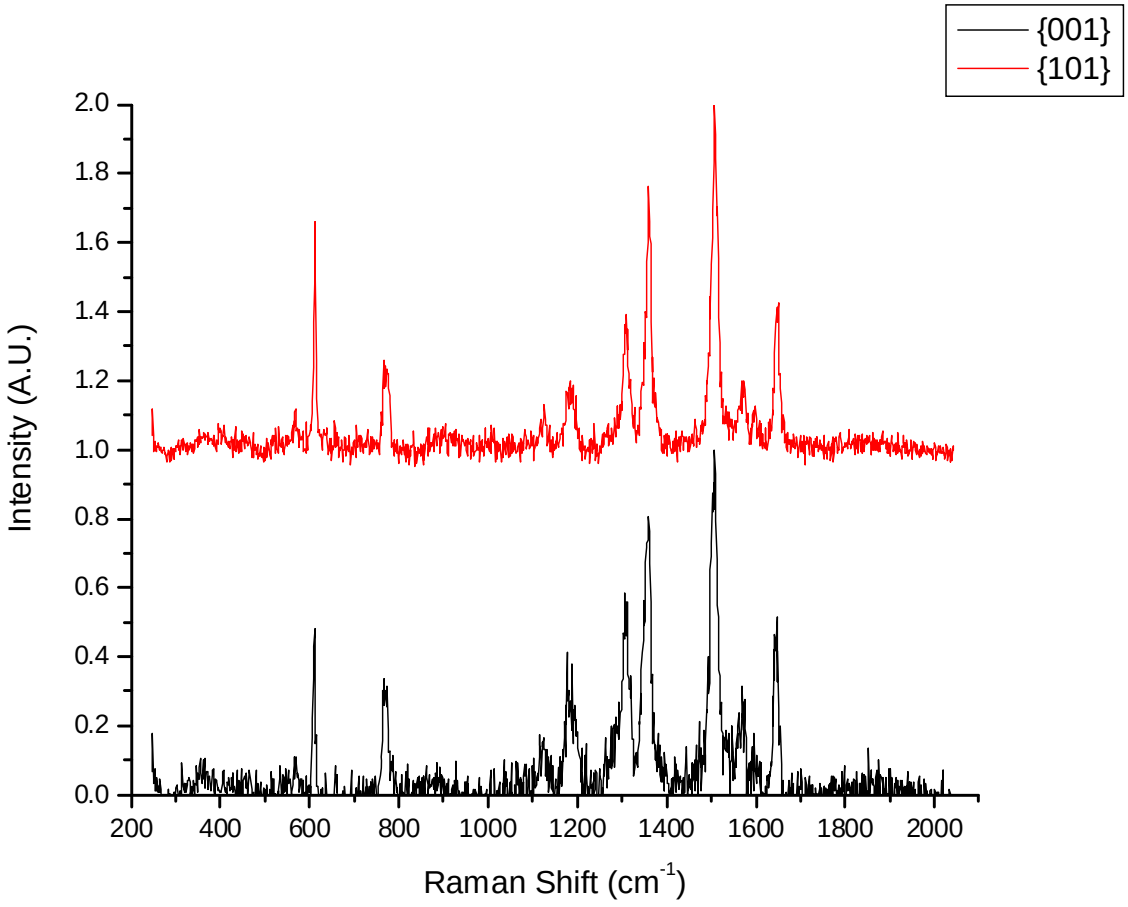

Figure 7. The normalized Raman spectra of rhodamine 6g on either the {001} (black) or {101} (red, offset of 1) face with silver attached. A 633 nm laser was used for excitation with the spectra being collected for 10 seconds. Add a spectrum from edge.

Combine this one with Figure 6. Only show one raman spectrum or delete this figure as I don't see difference of these two spectra}

Table 1. Percent coverage of TiO_2 faces by silver.

Sample	{001}	{101}
As Synthesized, UV[1]	0.067 (0.039)	0.090(0.037)
Annealed Air, UV[1]	0.032 (0.026)	0.031(0.018)
Annealed Air, Visible[2]	0.055 (0.019)	0.064(0.027)
Annealed Nitrogen, UV[1]	0.115 (0.074)	0.171(0.180)
Annealed Nitrogen, Visible[2]	0.032 (0.021)	0.030(0.017)

[1]284 nm illumination for 10 minutes. [2]>400 nm illumination for 10 minutes.

ASSOCIATED CONTENT

Supporting Information. Schematic of the photoreduction of silver on TiO_2, additional SEM images and EDS mapping of silver structures and detailed experimental details. This material is available free of charge via the Internet at http://pubs.acs.org.

AUTHOR INFORMATION

Corresponding Author

*E-mail: span1@bama.ua.edu

ACKNOWLEDGMENT

This material is supported by the Department of Energy under Award Number (s) DE-SC0005392. D. C. acknowledges the support of the Alabama EPSCoR Graduate Research Scholars Program.

Supporting Information

Detailed Experimental Section

Hydrothermal Synthesis of TiO_2. TiO_2 synthesis was carried out using a hydrothermal method. 64 mg of Titanium (IV) Oxysulfate Hydrate (Sigma-Aldrich) was weighed out and added to 40 mL of 120 mM hydrofluoric acid (VWR) in a Teflon lined acid digestion vessel (Parr Instrument Company). The acid digestion vessel was capped and placed in the oven for 12 hours at 180^{o}C. The samples were removed from the oven and allowed to cool. It was then centrifuged and the precipitate was collected and dispersed in deionized water. The centrifugation and dispersion process was repeated two more times in deionized water and then once in isopropanol. The precipitate was then dispersed in deionized water again and allowed to gravimetrically separate. The precipitate was then collected and filtered using vacuum filtration and a 1 size filter with rinsing by deionized water. The sample was allowed to dry and weighed.

TiO_2 Annealing Process. As synthesized TiO_2 was placed in a glass boat and into a tube furnace (Thermolyne, Thermo Scientific). For the annealing under air, the tube furnace was left open to atmosphere. The furnace was set to 500^{o}C for 1 hour with a ramp rate of 15^{o}C/minute. The sample was allowed to cool before being removed. For the annealing under nitrogen process, the tube furnace was purged by a series of vacuum and nitrogen purges. Ammonia gas (67% ammonia, balance argon, Airgas) was flowed through the tube furnace at 5 psi. The tube furnace was set to 500^{o}C for 1 hour with a ramp rate of 15^{o}C/minute. The tube furnace was allowed to cool, the ammonia flow was stopped, and the furnace was purged by nitrogen before the sample was removed from the furnace.

Silver Growth. Silver was deposited onto TiO_2 using a photoreduction process. The schematic can be seen in S1. To do so, 1 mg of TiO_2 (as synthesized, annealed under air, or annealed under

ammonia) was dispersed in 2 mL of a 0.1 M $AgNO_3$ (Fisher Scientific) solution with a 1/1 deionized water to methanol ratio. The sample was then illuminated by either UV (254 nm, UVP) or visible (>400 nm, Newport) light for ten minutes while stirring. The sample was then centrifuged and the precipitate was collected and rinsed.

TiO_2 Characterization. X-ray photoelectron spectroscopy (XPS) was performed using a Kratos Axis 165 XPS/Auger located in the Central Analytical Facility (CAF) at the University of Alabama in order to ascertain the differences in the make-up of our three types of TiO_2 crystals. Scanning electron microscopy (SEM) was performed using a JEOL 7000 FE scanning electron microscope located at the University of Alabama CAF. Energy dispersive x-ray spectroscopy maps were taken using the INCA system attached to the SEM. Samples were dispersed onto either gridded cover slips with a thin gold coating or on gridded holey carbon backed copper TEM grids.

Optical Imaging. TiO_2 samples were dispersed either upon gridded glass cover slips or upon gridded holey carbon backed copper TEM grids. Samples that were to be Raman imaged had 1 μM rhodamine 6g drop coated onto the sample. Images were scanned using a home built confocal system using an Olympus IX-71 Inverted Microscope with a 100x oil immersion objective and a Nano-View 200/2M nanopositioner (Mad City Laboratories) attached to the top for scanning. A 633 nm laser was used as the excitation source along with a 633 nm laser filter set with a long pass emission filter (Chroma Technology) and a 633 nm notch filter (Edmund Optics, Inc.). The inelastically scattered light was split and captured by avalanche photodiodes (APDs, SPEM-AQRH-15, Perkin Elmer) for photoluminescence images and collected by a liquid nitrogen cooled CCD (Acton Spec-10:100B, Princeton Instruments) attached to a monochromator (Acton SP-2558, Princeton Instruments) for Raman spectra collection.

Electrochemistry Measurements. For the electrochemistry measurements about 5 mg of the TiO_2 sample was added to 32 mg of gelatin () and 1.0 mL of water. The solution was shaken and then drop coated onto ITO glass. The coated slides were placed into the refrigerator and allowed to set for at least 1 hour. For the IV curves and wavelength scans, the sample was attached to an electrochemistry cell with the ITO serving as the working electrode, platinum as the counter electrode, and 0.01 M NaOH as the electrolyte. Measurements were performed using a potentiostat (CH Instruments) and a UV illumination source (Newport) with a monochromator. For the cyclic voltammetry measurements the ITO sample served as the working electrode with a counter electrode of platinum and a reference electrode of Ag/AgCl in a 0.01 M NaOH electrolyte. A potentiostat (CH Instruments) was used with the appropriate software package (CH Instruments).

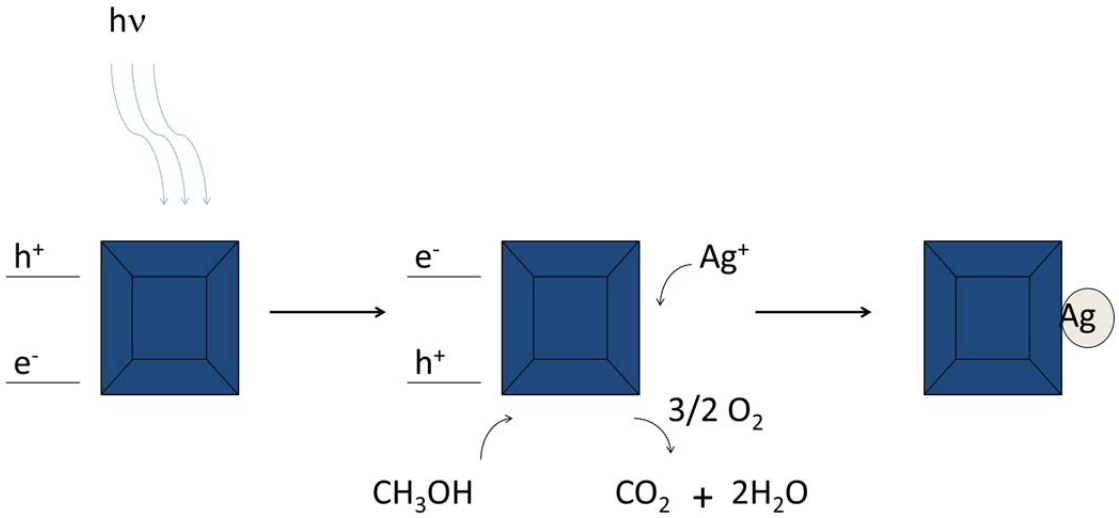

Figure S1. Schematic of the photoreduction of silver on the single crystal TiO_2.

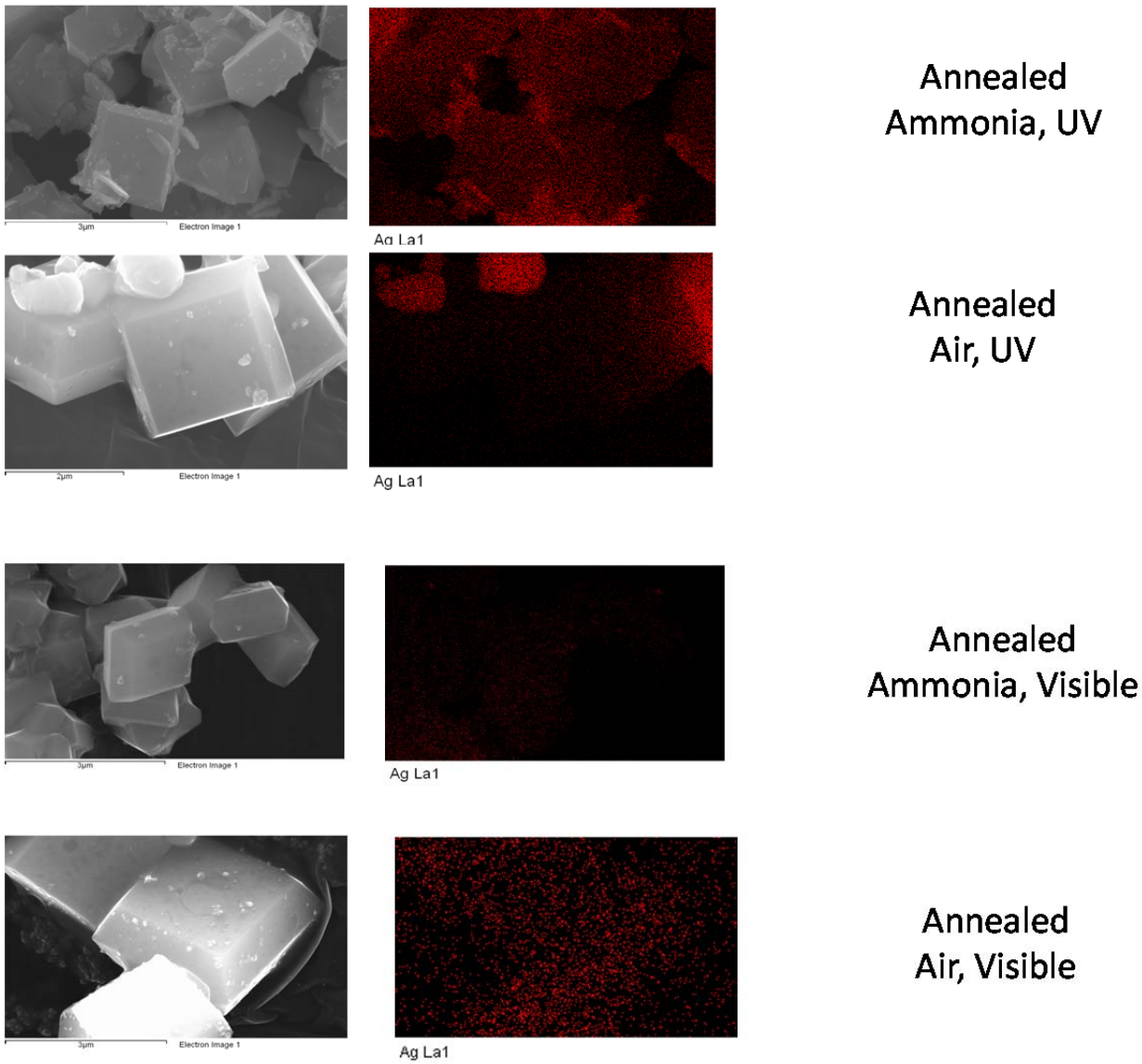

Figure S2. Additional SEM and EDS mapping images for the annealed under ammonia and annealed under air samples with silver grown using UV and visible light.

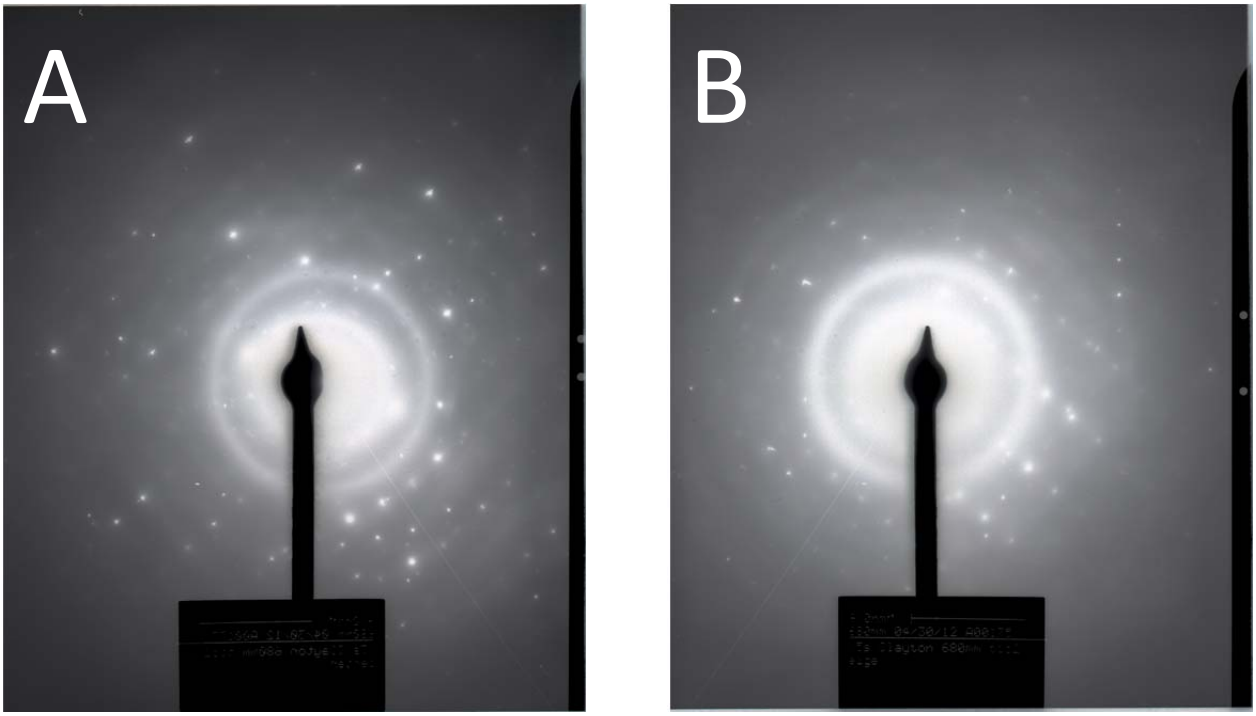

Figure S3. Site specific XRD images of the A.) {001} face and the B.) {101} face.

REFERENCES

[1] Fujishima, A.; Honda, K. Electrochemical Photolysis of Water at a Semiconductor Electrode. *Nature* **1972**, *238*, 37-38

[2] Bard, A.J. Design of Semiconductor Photoelectrochemical Systems for Solar Energy Conversion. *J. Phys. Chem.* **1982**, *86*, 172-177.

[3] Hagfeldt, A.; Gratzel, M. Light-Induced Redox Reactions in Nanocrystalline Systems. *Chem. Rev.* **1995**, *95*, 49-68.

[4] Grimes, C.A. Synthesis and application of highly ordered arrays of TiO_2 nanotubes. *J. Mater. Chem.* **2007**, *17*, 1451-1457.

[5] Zhang, Z.; Wang, C.; Zakaria, R.; Ying, J.Y. Role of Particle Size in Nanocrystalline TiO_2-Based Photocatalysts. *J. Phys. Chem. B* **1998**, *102*, 10871-10878.

[6] Ni, M.; Leung, M.K.H.; Leung, D.Y.C.; Sumathy, K. A review and recent developments in photocatalytic water-splitting using TiO_2 for hydrogen production. *Renew. Sust. Energ. Rev.* **2007**, *11*, 401-425.

[7] He, H; Liu, C.; Dubois, K.D.; Jin, T.; Louis, M.E.; Li, G. Enhanced Charge Separation in Nanostructured TiO_2 Materials for Photocatalytic and Photovoltaic Applications. *Ind. Eng. Chem. Res.*, **2012**, *51*, 11841-11849.

[8] Maeda, K.; Domen, K.; New Non-Oxide Photocatalysts Designed for Overall Water Splitting under Visible Light. *J. Phys. Chem. C* **2007**, *111*, 7851-7861

[9] Abe, R.; Sayama, K.; Domen, K.; Arakawa, H. A new type of water splitting system composed of two different TiO_2 photocatalysts (anatase, rutile) and a IO_3^-/I^- shuttle redox mediator. *Chem. Phys. Lett.* **2001**, *344*, 339-344.

[10] Youngblood, W.J.; Lee, S.A.; Kobayashi, Y.; Hernandez-Pagan, E.A.; Hoertz, P.G.; Moore, T.A.; Gust, D.; Mallouk, T.E. Photoassisted Overall Water Splitting in a Visible Light-Absorbing Dye-Sensitized Photoelectrochemical Cell. *J. Am. Chem. Soc.* **2009**, *131*, 926-927

[11] Choi, S.K.; Kim, S.; Lim, S.K.; Park, H. Photocatalytic Comparison of TiO_2 Nanoparticles and Electrospun TiO_2 Nanofibers: Effects of Mesoporosity and Interparticle Charge Transfer. *J. Phys. Chem. C* **2010**, *114*, 16475-16480

[12] Kamat, P.V.; Meeting the Clean Energy Demand: Nanostructure Architectures for Solar Energy Conversion. *J. Phys. Chem. C* **2007**, *111*, 2834-2860.

[13] Long, R.; English, N.J.; Dai, Y. First-Principles Study of S Doping at the Rutile TiO_2 (110) Surface. *J. Phys. Chem. C* **2009**, *113*, 17464-17470.

[14] Dvoranova, D.; Brezova, V.; Mazur, M.; Malatim M.A. Investigations of metal-doped titanium dioxide Photocatalysts. *Appl. Catal. B-Environ.* **2002**, *37*, 91-105

[15] Chen, Y.; Franzreb, M.; Lin, R.; Chen, L.; Chang, C.; Yu, Y.; Chiang, P. Platinum-Doped TiO_2/Magnetic Poly(methyl methacrylate) Microspheres as a Novel Photocatalyst. *Ind. Eng. Chem. Res.* **2009**, *48*, 7616-7623.

[16] Serpone, N.; Lawless, D.; Disdier, J.; Herrmann, J. Spectroscopic, Photoconductivity, and Photocatalytic Studies of TiO_2 Colloids: Naked and with the Lattice Doped with Cr^{3+}, Fe^{3+}, and V^{5+} Cations. *Langmuir* **1994**, *10*, 643-652.

[17] Choi, J.; Park, H.; Hoffmann, M.R. Effects of Single Metal-Ion Doping on the Visible-Light Photoreactivity of TiO_2. *J. Phys. Chem. C* **2010**, *114*, 783-792.

[18] Li, D.; Haneda, H.; Labhsetwar, N.K.; Hishita, S.; Ohashi, N. Visible-light-driven photocatalysis on fluorine-doped TiO_2 powders by the creation of the surface oxygen vacancies. *Chem. Phys. Lett.* **2005**, *401*, 579-584.

[19] Tafen, D. N.; Wang, J.; Wu, N.; Lewis, J.P. Visible light photocatalytic activity in nitrogen-doped TiO_2 nanobelts. *Appl. Phys. Lett.* **2009**, *94*, 093101

[20] Asahi, R.; Morikawa, T.; Ohwaki, T.; Aoki, K.; Taga, Y. Visible-Light Photocatalysis in Nitrogen-Doped Titanium Oxides. *Science* **2001**, *293*, 269-271

[21] Pan, H.; Zhang, Y.; Shenoy, V.B.; Gao, H. Effects of H-, N-, and (H, N)-Doping on the Photocatalytic Activity of TiO_2. *J. Phys. Chem. C* **2011**, *115*, 12224-12231.

[22] Chen, D.; Jiang, Z.; Geng, J.; Wang, Q.; Yang, D. Carbon and Nitrogen Co-doped TiO_2 with Enhanced Visible-Light Photocatalytic Activity. *Ind. Eng. Chem. Res.* **2007**, *46*, 2741-2746.

[23] Valentin, C.D.; Pacchioni, G.; Selloni, A. Origin of the different photoactivity of N-doped anatase and rutile TiO_2. *Phys. Rev. B* **2004**, *70*, 085116

[24] Batzill, M.; Morales, E.H.; Diebold, U. Influence of Nitrogen Doping on the Defect Formation and Surface Properties of TiO_2 Rutile and Anatase. *Phys. Rev. Lett.* **2006**, *96*, 026103

[25] Chen, X.; Burda, C. The Electronic Origin of the Visible-Light Absorption Properties of C-, N- and S-Doped TiO_2 Nanomaterials. *J. Am. Chem. Soc.* **2007**, *130*, 5018-5019.

[26] Serpone, N.; Is the Band Gap of Pristine TiO_2 Narrowed by Anion- and Cation-Doping of Titanium Dioxide in Second-Generation Photocatalysts? *J. Phys. Chem. B* **2006**, *110*, 24287-24293.

[27] Pan, H.; Gu, B.; Zhang, Z. Phase-Dependent Photocatalytic Ability of TiO_2: A First-Principles Study. *J. Chem. Theory Comput.* **2009**, *5*, 3074-3078.

[28] Chen, D.; Jiang, Z.; Geng, J.; Wang, Q.; Yang, D. Carbon and Nitrogen Co-doped TiO_2 with Enhanced Visible-Light Photocatalytic Activity. *Ind. Eng. Chem. Res.* **2007**, *46*, 2741-2746.

[29] D'Arienzo, M.; Siedl, N.; Sternig, A.; Scotti, R.; Morazzoni, F.; Bernardi, J.; Diwald, O. Solar Light and Dopant-Induced Recombination Effects: Photoactive Nitrogen in TiO_2 as a Case Study. *J. Phys. Chem. C* **2010**, *114*, 18067-18072.

[30] Torres, G.R.; Lindgren, T.; Lu, J.; Granvist, C.; Lindquist, S. Photoelectrochemical Study of Nitrogen-Doped Titanium Dioxide for Water Oxidation. *J. Phys. Chem. B* **2004**, *108*, 5995-6003.

[31] Wang, G.; Wang, Q.; Lu, W.; Li, J. Photoelectrochemical Study on Charge Transfer Properties of TiO_2-B Nanowires with an Application as Humidity Sensors. *J. Phys. Chem. B* **2006**, *110*, 22029-22034.

[32] Choi, S.K.; Kim, S.; Lim, S.K.; Park, H. Photocatalytic Comparison of TiO_2 Nanoparticles and Electrospun TiO_2 Nanofibers: Effects of Mesoporosity and Interparticle Charge Transfer. *J. Phys. Chem. C* **2010**, *114*, 16475-16480.

[33] Tachikawa, T.; Yamashita, S.; Majima, T. Evidence for Crystal-Face-Dependent TiO_2 Photocatalysis from Single-Molecule Imaging and Kinetic Analysis. *J. Am. Chem. Soc.* **2011**, *133*, 7197-7204

[34] Ohno, T.; Sarukawa, K.; Matsumura, M. Crystal Faces of rutile and anatase TiO_2 particles and their roles in photocatalytic reactions. *New J. Chem.* **2002**, *26*, 1167-1170.

[35] Tachikawa, T.; Wang, N.; Yamashita, S.; Cui, S.; Majima, T. Design of a Highly Sensitive Fluorescence Probe for Interfacial Electron Transfer on a TiO_2 Surface. *Angew. Chem. Int. Ed.* **2010**, *49*, 8593-8597

[36] Wang, N.; Tachikawa, T.; Majima, T. Single-molecule, single-particle observation of size-dependent photocatalytic activity in Au/TiO_2 nanocomposites. *Chem. Sci.* **2011**, *2*, 891-900.

[37] Tachikawa, T.; Majima, T. Single-molecule, single-particle fluorescence imaging of TiO2-based photocatalytic reactions. *Chem. Soc. Rev.* **2010**, *39*, 4802-4819

[38] Tachikawa, T.; Majima, T. Photocatalytic oxidation surfaces on anatase TiO_2 crystals revealed by single-particle chemiluminescence imaging. *Chem. Commun.* **2012**, *48*, 3300-3302.

[39] D'Arienzo, M.; Carbajo, J.; Bahamonde, A.; Crippa, M.; Polizzi, S.; Scotti, R.; Wahba, L. Photogenerated Defects in Shape-Controlled TiO_2 Anatase Nanocrystals: A Probe to Evaluate the Role of Crystal Facets in Photocatalytic Processes. *J. Am. Chem. Soc.* **2011**, *133*, 17652-17661.

[40] Ahmed, A. Y.; Kandiel, T.A.; Oekermann, T.; Bahnemann, D. Photocatalytic Activities of Different Well-Defined Single Crystal TiO_2 Surfaces: Anatase versus Rutile. *J. Phys. Chem. Lett.* **2011**, *2*, 2461-2465.

[41] Yang, H.G.; Sun, C.H.; Qiao, S.Z.; Zou, J.; Smith, Sean Campbell, Cheng, H.M.; Lu, G.Q. Anatase TiO_2 single crystals with a large percentage of reactive facets. *Nature* **2008**, *453*, 638-641.

[42] Pan, J.; Gang, L.; Lu, G.Q.; Cheng, H. On the True Photoreactivity Order of {001}, {010}, and {101} Facets of Anatase TiO_2 Crystals. *Angew. Chem. Int. Ed.* **2011**, *50*, 2133-2137.

[43] Tian, N.; Zhou, Z.; Sun, S.; Ding, Y.; Wang, Z.L. Synthesis of Tetrahexahedral Platinum Nanocrystals with High-Index Facets and High Electro-Oxidation Activity. *Science* **2007**, *316*, 732-735.

[44] Zhang, H.; Wang, Y.; Liu, P.; Han, Y.; Yao, X.; Zou, J.; Cheng, H.; Zhao, H. Anatase TiO_2 Crystal Facet Growth: Mechanistic Role of Hydrofluoric Acid and Photoelectrocatalytic Activity. *ACS Appl. Mater. Interfaces* **2011**, *3*, 2472-2478.

[45] Clayton, D.A.; Benoist, D.M.; Zhu, Y.; Pan, S. Photoluminescence and Spectroelectrochemistry of Single Ag Nanowires. *ACS Nano* **2010**, *4*, 2363-2373.

[46] Yang, L.; Jiang, X.; Ruan, W.; Zhao, B.; Xu, W.; Lombardi, J.R. Observation of Enhanced Raman Scattering for Molecules Adsorbed on TiO_2 Nanoparticles: Charge-Transfer Contribution. *J. Phys. Chem. C* **2008**, *112*, 20095-20098.

[47] Jiang, X.; Li, X.; Jia, X.; Li, G.; Wang, X.; Wang, G.; Li, Z.; Yang, L.; Zhao, B. Surface-Enhanced Raman Scattering from Synergistic Contribution of Metal and Semiconductor in TiO_2/MBA/Ag(au) and Ag(Au)/MBA/TiO_2 Assemblies. *J. Phys. Chem. C* **2012**, *116*, 14650-14655.

Appendix IV

METHODS AND SYSTEMS FOR ANALYSIS

STATEMENT OF GOVERNMENT SUPPORT

This invention was made with government support under Grant No. DE-SC0005392 awarded by the Department of Energy. The government has certain rights in this invention.

BACKGROUND

Metallic nanostructures have been thoroughly studied over the past several decades due to their unrivaled ability to catalyze redox reactions that are relevant to alternative energy storage and conversion systems. Some metallic nanoparticles, such as silver and gold nanoparticles, also have interesting optical properties (*e.g.*, surface plasmon resonance (SPR)) in the visible region of the electromagnetic spectrum. These properties have been most notably exploited to enhance detection for a litany of optical spectroscopies (Raman, scattering, fluorescence, sum frequency generation, etc.) and to improve the efficiency of photovoltaic devices. Given the importance of such structures, method for characterizing them, especially *in situ* methods, are valuable for studying structure-property relationships. Even better are methods capable of resolving individual structures, dispelling the broadening of peaks inherent in ensemble measurements. The methods and compositions disclosed herein address these and other needs.

SUMMARY

Disclosed herein are systems and method for the detection, quantification, and/or monitoring of analytes, including nanoparticles, in samples. The disclosed systems and methods can be used, for example, to track the deposition of individual nanoparticles and nanoparticle clusters *in situ* with high spatial and temporal resolution. The disclosed systems and methods can even be used to track the deposition of several hundreds to thousands of nanoparticles simultaneously and reconstruct their voltammetric curves at the single nanoparticle level, feats not possible through existing electrochemical techniques.

Also, disclosed herein are systems that comprise an electrochemical cell, a light source configured to illuminate the electrochemical cell, and an instrument configured to capture an optical signal from the electrochemical cell. The disclosed electrochemical cell can comprise a working electrode in electrochemical contact with a liquid sample comprising an analyte, one or more additional electrodes in electrochemical contact with the liquid sample, a sample containment vessel, and a power supply. The sample containment vessel can comprise a top end, a bottom end, an exterior surface, and an interior void

defined by an interior surface. The sample containment vessel can be configured such that the bottom end forms a liquid tight seal with the working electrode, and the liquid sample is contained in the volume defined by the interior void of the sample containment vessel and the working electrode.

Optionally, the sample containment vessel can further comprise a channel that punctuates the interior surface and leads through the sample containment vessel to the exterior surface or top end of the sample containment vessel. The one or more additional electrodes can be inserted through the channel such that the one or more additional electrodes are in electrochemical contact with the liquid sample and the one or more additional electrodes form a liquid tight seal with the channel.

In some examples, the system can further comprise a first lens. In some examples, the first lens can be configured such that the light source and instrument are below the first lens and the electrochemical cell is above the first lens. In some examples, the system can further comprise a second lens. In some examples, the system further comprising the first lens and the second lens can be aligned such that the first lens is above the instrument; the electrochemical cell is above the first lens; the second lens is above the electrochemical cell; and the light source is above the second lens.

In certain examples, the system can further comprise a computing device configured to receive an electrochemical signal from the power supply; receive an optical signal from the instrument; process the electrochemical signal to obtain an electrochemical parameter; process the optical signal to obtain an optical parameter; optionally correlate the electrochemical parameter to the optical parameter to obtain an optoelectrochemical parameter; and output the electrochemical parameter, the optical parameter, the optoelectrochemical parameter, or combinations thereof.

Methods for the detection, quantification, and/or monitoring of analytes, including nanoparticles, in liquid samples are also disclosed herein. The methods can involve the use of optical signal and/or electrochemical signal analysis to detect, quantify and/or monitor analytes, including nanoparticles, in a liquid sample. The methods can be performed using the systems described herein. Methods for the detection, quantification, and/or monitoring of analytes can comprise providing an electrochemical cell comprising a working electrode in electrochemical contact with a liquid sample comprising an analyte, a sample containment vessel, one or more additional electrodes in electrochemical contact with the liquid sample and a power supply electrically coupled to the working electrode and the one or more additional electrodes. The sample containment vessel can comprise a top end, a

bottom end, an exterior surface and an interior void defined by an interior surface, wherein the bottom end forms a liquid tight seal with the working electrode and the liquid sample is contained in the volume defined by the interior void of the sample containment vessel and the working electrode. The disclosed methods can further comprise capturing an electrochemical signal from the power supply, capturing an optical signal from the electrochemical cell, processing the electrochemical signal to obtain an electrochemical parameter, processing the optical signal to obtain an optical parameter, and optionally correlating the optical parameter to the electrochemical parameter to obtain an optoelectrochemical parameter.

Also disclosed herein are sample containment vessels. The sample containment vessel can comprise a top end, a bottom end, an exterior surface and an interior void defined by an interior surface. In some examples, the sample containment vessel is configured to receive a working electrode such that the bottom end forms a liquid tight seal with the working electrode. In some examples, the volume defined by the interior void of the sample containment vessel and the working electrode is configured to contain a liquid sample, and the working electrode can be in electrochemical contact with the liquid sample. In some examples, the sample containment vessel further comprises a channel that punctuates the interior surface of the sample containment vessel and leads through the sample containment vessel to the top end or exterior surface of the sample containment vessel. In some examples, the channel is configured to receive one or more additional electrodes such that the one or more additional electrodes are in electrochemical contact with the liquid sample and the one or more additional electrodes form a liquid tight seal with the channel.

In some examples, the sample containment vessel can further comprise a channel that punctuates the interior surface and leads through the sample containment vessel to the exterior surface or the top end of the sample containment vessel. The one or more additional electrodes can be inserted through the channel such that the one or more additional electrodes are in electrochemical contact with the liquid sample and the one or more additional electrodes form a liquid tight seal with the channel. In some examples, the sample containment vessel comprises multiple channels through which multiple electrodes or other probes can be inserted.

Additional advantages will be set forth in part in the description that follows, and in part will be obvious from the description, or may be learned by practice of the aspects described below. The advantages described below will be realized and attained by means of the elements and combinations particularly pointed out in the appended claims. It is to be

understood that both the foregoing general description and the following detailed description are exemplary and explanatory only and are not restrictive.

DESCRIPTION OF FIGURES

Figure 1 is a schematic of an exemplary system as disclosed herein for the detection, quantification and/or monitoring of samples.

Figure 2 is a schematic of an exemplary computing device.

Figure 3 is a schematic of an exemplary system as disclosed herein for the detection, quantification and/or monitoring of samples with a channel punctuating an interior surface and exterior surface of a sample containment device.

Figure 4 is a schematic of an exemplary system as disclosed herein for the detection, quantification and/or monitoring of samples with a channel punctuating an interior surface and a top end of a sample containment device.

Figure 5A is a bottom view of an exemplary sample containment vessel for an electrochemical cell as disclosed herein. Figure 5B is a side perspective of the sample containment vessel shown in Figure 5A.

Figure 6A is a bottom view of an exemplary sample containment vessel for an electrochemical cell as disclosed herein. Figure 6B is a side perspective of the sample containment vessel shown in Figure 6A.

Figure 7 is a schematic of an exemplary system as disclosed herein that includes a light source and a camera below an electrochemical cell with a lens between the electrochemical cell and the instrument.

Figure 8 is a schematic of an exemplary system as disclosed herein that includes a light source above an electrochemical cell, with a lens between the light source and the electrochemical cell, and a camera below the electrochemical cell with another lens between the electrochemical cell and the camera to focus and magnify an optical signal from a sample.

Figure 9 is a schematic of an exemplary system as disclosed herein that combines the systems shown in Figure 7 and Figure 8.

Figure 10 is a photograph of a working set up of the system described in Figure 7.

Figure 11 is a graph showing a theoretical scattering cross-section as a function of particle size.

Figure 12 is a graphical depiction of a turn-on potential calculation.

Figure 13 shows the calculated single nanoparticles deposition current and scattering intensity, A_{eff} = 20 μm^2, 100 mV s^{-1} sweep rate.

Figure 14 shows histograms of (A) $E_{1/2}$ and (B) A_{eff} values obtained from data fitting according to the theoretical model with and without the ΔE_{size} term following the Plieth equation.

Figure 15 is a schematic of the experimental setup for the dark field scattering spectroelectrochemistry experiments.

Figure 16 is a graph showing the total measured scattering intensity and bulk current density during a potential sweep. The insets are scattering images (~40 μm x 40 μm) at the indicated points along the sweep.

Figure 17 shows linear sweep voltammograms and total substrate scattering intensities for different potential sweep rates.

Figure 18 shows example individual particle scattering transients (A), histograms of the final light scattering intensity ("A_{sig}", inset of A), and "turn-on" potential obtained from the data fitting (B).

Figure 19 is a plot of final particle radius (determined from A_{sig} values) as a function of E_{on}. The circles indicate binned (10 mV) averages and the squares represent single particles. Error bars are two standard deviations.

Figure 20 contains a low magnification SEM image of deposited Ag particles (A), high magnification SEM image of the indicated particle (B), histogram of particle sizes obtained through SEM analysis (C), and results of single particle scattering-size correlations (D). The overlay in (A) is generated from the corresponding dark field scattering image (Figure 21).

Figure 21 is a dark field scattering image of the deposited Ag particles depicted in Figure 20.

Figure 22 shows an example reconstructed voltammetric curves for single particles (A), histogram of peak potentials (inset of A), and a comparison of measured and calculated bulk current densities obtained through the scattering calculations for all 753 particles (B).

Figure 23 shows the bulk current density and total scattering intensity at the ITO surface during potential cycling.

Figure 24 shows the scattering transients for individual particles deposited and subsequently oxidized during potential cycling.

Figure 25 is a flowchart depicting program flow.

Figure 26 contains fluorescence images displaying the effects of background removal.

Figure 27 is a screenshot of the MATLAB program used for trajectory extraction.

DETAILED DESCRIPTION

The systems, methods, articles, and devices described herein may be understood more readily by reference to the following detailed description of specific aspects of the disclosed subject matter, figures and the examples included therein.

Before the present systems, methods, articles, and devices are disclosed and described, it is to be understood that the aspects described below are not intended to be limited in scope by the specific systems, methods, articles, and devices described herein, which are intended as illustrations. Various modifications of the systems, methods, articles, and devices in addition to those shown and described herein are intended to fall within the scope of that described herein. Further, while only certain representative systems and method steps disclosed herein are specifically described, other combinations of the systems and method steps also are intended to fall within the scope of that described herein, even if not specifically recited. Thus, a combination of steps, elements, components, or constituents may be explicitly mentioned herein or less, however, other combinations of steps, elements, components, and constituents are included, even though not explicitly stated.

The term "comprising" and variations thereof as used herein is used synonymously with the term "including" and variations thereof and are open, non-limiting terms. Although the terms "comprising" and "including" have been used herein to describe various examples, the terms "consisting essentially of" and "consisting of" can be used in place of "comprising" and "including" to provide for more specific examples of the invention and are also disclosed. Other than in the examples, or where otherwise noted, all numbers expressing quantities of ingredients, reaction conditions, and so forth used in the specification and claims are to be understood at the very least, and not as an attempt to limit the application of the doctrine of equivalents to the scope of the claims, to be construed in light of the number of significant digits and ordinary rounding approaches.

As used in the description and the appended claims, the singular forms "a," "an," and "the" include plural referents unless the context clearly dictates otherwise. Thus, for example, reference to "a composition" includes mixtures of two or more such compositions, reference to "an agent" includes mixtures of two or more such agents, reference to "the component" includes mixtures of two or more such components, and the like.

"Optional" or "optionally" means that the subsequently described event or circumstance can or cannot occur, and that the description includes instances where the event or circumstance occurs and instances where it does not.

It is understood that throughout this specification the identifiers "first" and "second"

are used solely to aid in distinguishing the various components and steps of the disclosed subject matter. The identifiers "first" and "second" are not intended to imply any particular order, amount, preference, or importance to the components or steps modified by these terms.

Also, throughout this specification, various publications are referenced. The disclosures of these publications in their entireties are hereby incorporated by reference into this application in order to more fully describe the state of the art to which the disclosed matter pertains. The references disclosed are also individually and specifically incorporated by reference herein for the material contained in them that is discussed in the sentence in which the reference is relied upon.

Reference will now be made in detail to specific aspects of the disclosed materials, compounds, compositions, articles, and methods, examples of which are illustrated in the accompanying examples and figures.

For any quantitative analytical technique, a single analyte or single chemical reaction event represents the ultimate attainable limit of detection. This may come in the form of an atom, a molecule, a nanoparticle (NP), a defect site on a crystal surface, or a single molecule undergoing a redox reaction at a bulk electrode. There are inherent advantages to measurements at this limit, a primary one being the ability to thoroughly characterize heterogeneities in structure or reactivity that would only manifest in ensemble measurements as the broadening of peaks. In the electrodeposition of NPs, for example, traditional electrochemical measurements can be used to calculate the total quantity of material deposited through Faraday's law. If the number and shape of particles are known, an average size can be obtained easily. However, information on the resulting size distribution cannot be directly obtained through such measurements.

Methods capable of resolving electrochemical reactions occurring at individual nanostructures are critical to accurately determining their structure-function relationships. The direct electrochemical detection of single NPs has been demonstrated via a current amplification scheme as they collide at a microelectrode. More recently, heterogeneities in the catalytic activity of single metal NPs and the charge transfer performance of individual conjugated polymer molecules/NPs have been studied using fluorescence-based single molecule spectroelectrochemical (SMSEC) methods. Tao *et al.* have developed a surface plasmon resonance (SPR)-based imaging technique capable of measuring local electrochemical currents down to the single nanoparticle level by exploiting the sensitivity of SPR to the local dielectric environment. However, disclosed herein is a method that uses

dark field scattering (DFS) spectroelectrochemistry to analyze the electrochemical formation of individual nanoparticles (NPs) at the surface of an electrode. Heterogeneities in redox potentials among NPs not visible in the bulk electrochemical measurements are also disclosed. Through correlated electron microscopy, single nanoparticle light scattering intensity can be correlated to particle size according to Mie theory, permitting the rapid particle size determination and the construction of voltammetric curves of individual nanoparticles.

In the disclosed methods, the change in signal is dominated by the modification of the metal nanostructure geometry rather than changes in dielectric environment, which is the case in SPR. Neither the reported SPR imaging techniques nor the other aforementioned SMS-EC methods have been employed to directly observe the synthesis of individual NPs.

Provided herein are systems and method for the detection, quantification, and/or monitoring of analytes, including nanoparticles, in samples. The disclosed systems and methods utilize a spectroelectrochemical method employing dark field scattering microscopy and can be used, for example, to track the deposition of individual nanoparticles and nanoparticles clusters *in situ* with high spatial (~350 nm) and temporal (ms) resolution. The systems and methods can be used to track the deposition of several hundreds to thousands of NPs simultaneously and reconstruct their voltammetric curves at the single nanoparticle level, feats not possible through existing electrochemical techniques.

Referring now to Figure 1, example system (**100**) can comprise an electrochemical cell (**110**), a light source (**140**) configured to illuminate the electrochemical cell and liquid sample comprising an analyte (**114**) contained therein, and an instrument (**150**) configured to capture an optical signal from the liquid sample in the electrochemical cell. The electrochemical cell (**110**) comprises, a working electrode (**112**) in electrochemical contact with a liquid sample (**114**), an additional electrode (**130**) in electrochemical contact with the liquid sample (**114**)(though more can be present, only one is shown for clarity), a sample containment vessel (**116**), and a power supply (**180**). The sample containment vessel (**116**) comprises a top end (**118**), a bottom end (**120**), an exterior surface (**122**), and an interior void (**124**) defined by an interior surface (**126**). The sample containment vessel (**116**) can be configured such that the bottom end (**120**) forms a liquid tight seal with the working electrode (**112**), and the liquid sample (**114**) is contained in the volume defined by the interior surface (**126**) of the sample containment vessel (**116**) and the working electrode (**112**).

The system (**100**) can further comprise a computing device (**160**) configured to receive and process the optical signals from the instrument (**150**), as well as receive and process signals from the electrochemical cell (**110**), as discussed in more detail below.

Optionally, the sample containment vessel can further comprise a channel. Referring now to Figure 3, the sample containment device (**116**) can further comprise a channel (**128**) that punctuates the interior surface (**126**) and leads through the sample containment vessel (**116**) to the exterior surface (**122**) of the sample containment vessel (**116**). The one or more additional electrodes (**130**) can be inserted through the channel (**128**) such that the one or more additional electrodes (**130**) are in electrochemical contact with the liquid sample (**114**) and the one or more additional electrodes (**130**) form a liquid tight seal with the channel (**128**).

Referring now to Figure 4, the sample containment device (**116**) can further comprise a channel (**128**) that punctuates the interior surface (**126**) and leads through the sample containment vessel (**116**) to the top end (**118**) of the sample containment vessel (**116**), as shown in and, respectively. The one or more additional electrodes (**130**) can be inserted through the channel (**128**) such that the one or more additional electrodes (**130**) are in electrochemical contact with the liquid sample (**114**) and, optionally in this configuration, the one or more additional electrodes (**130**) form a liquid tight seal with the channel (**128**).

In some examples, the sample containment vessel comprises multiple channels through which multiple electrodes or other probes can be inserted.

The sample containment vessel, as well as the components thereof, can be fabricated form any suitable material or combination of materials compatible with the methods described herein. Examples of suitable materials include polymers, silicones, glasses, ceramics, inorganic materials and combinations thereof. In some examples, the interior surface of the sample containment vessel is substantially non-conducting. In some examples, the sample containment vessel comprises a cylindrical piece of a nonconducting material, as shown in Figure 5 and Figure 6. In some examples, the nonconducting material is Teflon.

The working electrode and one or more additional electrodes can be fabricated from any suitable material or combination of materials compatible with the methods described herein. In some examples, the working electrode is substantially optically transparent. In some examples, the working electrode comprises an indium tin oxide (ITO) coated microscope coverslip.

The power supply (**180**) can comprise any additional features suitable for an electrochemical cell. Examples of additional features include, but are not limited to, a voltmeter, an ammeter, a multimeter, an ohmmeter, a signal generator, a pulse generator, an oscilloscope, a frequency counter, a potentiostat, or a capacitance meter. In some examples the power supply (**180**) is configured to apply a potential to the liquid sample (**114)**.

In some examples, the system further comprises a first lens. In some examples, the system further comprises a second lens. The lenses may independently be any type of lens, such as a simple lens, a compound lens, a spherical lens, a toric lens, a biconvex lens, a plano-convex lens, a plano-concave lens, a negative meniscus lens, a positive meniscus lens, a biconcave lens, a converging lens, a diverging lens, a cylindrical lens, a Fresnel lens, a lenticular lens, or a gradient index lens.

In some examples, the system further comprising a first lens can be configured as shown schematically in Figure 7. Referring now to Figure 7, the system (**100**) is configured such that the light source (**140**) and instrument (**170**) are below the first lens (**195**) and the electrochemical cell (**110**) is above the first lens (**195**). In some examples, the first lens is a microscope objective.

In some examples, the system further comprising a first lens and a second lens can be configured as shown schematically in Figure 8. Referring now to Figure 8, the system (**100**) is aligned such that the first lens (**195**) is above the instrument (**150**); the electrochemical cell (**110**) is above the first lens (**195**); the second lens (**190**) is above the electrochemical cell (**110**); and the light source (**140**) is above the second lens (**190**). In some examples, the first lens is a dark field microscope objective and the second lens is a dark field microscope condenser.

The system can further comprise any other suitable optical components. Examples of additional optical components include, but are not limited to, mirrors, beam splitters, filters, lenses, optical fibers, beam expanders, or collimators.

The working electrode can comprise any suitable material. In some examples, the working electrode is substantially optically transparent. In some examples, the working electrode comprises an indium tin oxide (ITO) coated coverslip.

The system (**100**) can further comprise a first computing device (**160**) configured to receive and process electrochemical signals from the electrochemical cell, as well as receive and process optical signals from the instrument (**150**).

Figure 2 illustrates an example computing device upon which examples disclosed herein may be implemented. The computing device (**160**) can include a bus or other

communication mechanism for communicating information among various components of the computing device (**160**). In its most basic configuration, computing device (**160**) typically includes at least one processing unit (**212**) (a processor) and system memory (**214**). Depending on the exact configuration and type of computing device, system memory (**214**) may be volatile (such as random access memory (RAM)), non-volatile (such as read-only memory (ROM), flash memory, etc.), or some combination of the two. This most basic configuration is illustrated in Figure 2 by a dashed line (**210**). The processing unit (**212)** may be a standard programmable processor that performs arithmetic and logic operations necessary for operation of the computing device (**160**).

The computing device (**160**) can have additional features/functionality. For example, computing device (**160**) may include additional storage such as removable storage (**216**) and non-removable storage (**218**) including, but not limited to, magnetic or optical disks or tapes. The computing device (**160**) can also contain network connection(s) (**224**) that allow the device to communicate with other devices. The computing device (**160**) can also have input device(s) (**222**) such as a keyboard, mouse, touch screen, antenna or other systems configured to communicate with the camera in the system described above, etc. Output device(s) (**220**) such as a display, speakers, printer, etc. may also be included. The additional devices can be connected to the bus in order to facilitate communication of data among the components of the computing device (**160**).

The processing unit (**212**) can be configured to execute program code encoded in tangible, computer-readable media. Computer-readable media refers to any media that is capable of providing data that causes the computing device (**160**) (*i.e.*, a machine) to operate in a particular fashion. Various computer-readable media can be utilized to provide instructions to the processing unit (**212**) for execution. Common forms of computer-readable media include, for example, magnetic media, optical media, physical media, memory chips or cartridges, a carrier wave, or any other medium from which a computer can read. Example computer-readable media can include, but is not limited to, volatile media, non-volatile media and transmission media. Volatile and non-volatile media can be implemented in any method or technology for storage of information such as computer readable instructions, data structures, program modules or other data and common forms are discussed in detail below. Transmission media can include coaxial cables, copper wires and/or fiber optic cables, as well as acoustic or light waves, such as those generated during radio-wave and infra-red data communication. Example tangible, computer-readable recording media include, but are not limited to, an integrated circuit (*e.g.*, field-

programmable gate array or application-specific IC), a hard disk, an optical disk, a magneto-optical disk, a floppy disk, a magnetic tape, a holographic storage medium, a solid-state device, RAM, ROM, electrically erasable program read-only memory (EEPROM), flash memory or other memory technology, CD-ROM, digital versatile disks (DVD) or other optical storage, magnetic cassettes, magnetic tape, magnetic disk storage or other magnetic storage devices.

In an example implementation, the processing unit (**212)** can execute program code stored in the system memory (**214**). For example, the bus can carry data to the system memory (**214**), from which the processing unit (**212**) receives and executes instructions. The data received by the system memory (**214**) can optionally be stored on the removable storage (**216**) or the non-removable storage (**218**) before or after execution by the processing unit (**212**).

The computing device (**160**) typically includes a variety of computer-readable media. Computer-readable media can be any available media that can be accessed by device (**160**) and includes both volatile and non-volatile media, removable and non-removable media. Computer storage media include volatile and non-volatile, and removable and non-removable media implemented in any method or technology for storage of information such as computer readable instructions, data structures, program modules or other data. System memory (**214**), removable storage (**216**), and non-removable storage (**218**) are all examples of computer storage media. Computer storage media include, but are not limited to, RAM, ROM, electrically erasable program read-only memory (EEPROM), flash memory or other memory technology, CD-ROM, digital versatile disks (DVD) or other optical storage, magnetic cassettes, magnetic tape, magnetic disk storage or other magnetic storage devices, or any other medium which can be used to store the desired information and which can be accessed by computing device (**160**). Any such computer storage media can be part of computing device (**160**).

It should be understood that the various techniques described herein can be implemented in connection with hardware or software or, where appropriate, with a combination thereof. Thus, the methods, systems, and associated signal processing of the presently disclosed subject matter, or certain aspects or portions thereof, can take the form of program code (*i.e.*, instructions) embodied in tangible media, such as floppy diskettes, CD-ROMs, hard drives, or any other machine-readable storage medium wherein, when the program code is loaded into and executed by a machine, such as a computing device, the machine becomes an apparatus for practicing the presently disclosed subject matter. In the

case of program code execution on programmable computers, the computing device generally includes a processor, a storage medium readable by the processor (including volatile and non-volatile memory and/or storage elements), at least one input device, and at least one output device. One or more programs can implement or utilize the processes described in connection with the presently disclosed subject matter, *e.g.*, through the use of an application programming interface (API), reusable controls, or the like. Such programs can be implemented in a high level procedural or object-oriented programming language to communicate with a computer system. However, the program(s) can be implemented in assembly or machine language, if desired. In any case, the language can be a compiled or interpreted language and it may be combined with hardware implementations.

In certain examples, system memory (**214**) comprises computer-executable instructions stored thereon that, when executed by the processor (**212**), provide for analysis of signals captured by the instrument (**150**) and the power supply (**180**) to obtain information about the liquid sample and/or one or more analytes present in the liquid sample (i.e., one or more sample characteristics, as discussed in more detail below). To implement analysis of this type, system memory **(214)** can comprise computer-executable instructions stored thereon that, when executed by the processor (**212**), cause the processor to: receive an electrochemical signal from the power supply; receive an optical signal from the instrument; process the electrochemical signal to obtain an electrochemical parameter; process the optical signal to obtain an optical parameter; optionally correlate the electrochemical parameter to the optical parameter to obtain an optoelectrochemical parameter; and output the electrochemical parameter, the optical parameter, the optoelectrochemical parameter, or combinations thereof.

The electrochemical parameter can be, for example, how the electrochemical signal progresses over time. For example, if the electrochemical signal comprises voltage or current, the electrochemical parameter can be voltage over time or current over time. Similarly, the optical parameter can be, for example, how the optical signal progresses overtime. The optical signal can be, for example, intensity, brightness, scattering, fluorescence, or electrogenerated chemiluminescence. Then, the optical parameter can be, for example, intensity over time, brightness over time, scattering over time, fluorescence over time, or electrogenerated chemiluminescence over time. The optoelectrochemical parameter is a correlation between the optical parameter and the electrochemical parameter. For example, the optoelectrochemical parameter instead of being of a signal progresses over time, can be an expression of how one signal or parameter progresses with relation to the

other. For example, how the optical signal or optical parameter progresses in terms of the electrochemical signal or parameter, or vice-versa. For example, the optoelectrochemical parameter can be scattering over voltage, scattering over current, fluorescence over voltage, or fluorescence over current.

The analysis of signals captured by the instrument and power supply can be carried out in whole or in part on one or more computing device. For example, the system may comprise one or more additional computing device.

In certain examples, the instrument comprises a camera. In certain examples, the optical signal comprises an image.

In certain examples, system memory (**214**) comprises computer-executable instructions stored thereon that, when executed by the processor (**212**), provide for analysis of images captured by the camera (**150**) to obtain information about the liquid sample and/or one or more analytes present in the liquid sample. Image analysis can involve fluorescence image analysis, dark field scattering image analysis, electrogenerated chemiluminescence image analysis, or combinations thereof. For example, the analysis can be dark field scattering image analysis. The data can be saved as a series of image files, or "frames". The first frame can be subtracted from each subsequent frame to correct for any static defects. Next, all the frames can be summed together to yield an image depicting total scattering intensity throughout the experiment. Gradient filtering methods can be used to enhance the contrast within the image. A threshold can be set to differentiate between "active" (scattering) and "inactive" (not scattering) pixels. Adjacent pixels can be grouped together to form "spots". The scattering intensity can then be extracted on a frame-by-frame basis by taking the maximum of the individual pixel intensities for each spot. In some examples, the scattering intensity can be further processed to obtain a different characteristic from the sample. For example, if the liquid sample comprises metal ions that can form nanoparticles upon the application of sufficient voltage, the scattering intensity from the particles can be processed using appropriate theoretical models (*i.e.* Mie theory) to ultimately give nanoparticle size.

The light source present in the systems described above can be any type of light source. In some examples, the system can include a single light source. In other examples, more than one light source can be included in the system. Examples of suitable light sources include natural light sources (*e.g.*, sunlight) and artificial light sources (*e.g.*, incandescent light bulbs, light emitting diodes, gas discharge lamps, arc lamps, lasers etc.). In some examples, the light source is an arc lamp. In some examples, the light source is a laser.

Methods for the detection, quantification, and/or monitoring of analytes, including nanoparticles, in liquid samples are also provided. The methods can involve the use of optical signal and/or electrochemical signal analysis to detect, quantify and/or monitor analytes, including nanoparticles, in a liquid sample. The methods can be performed using the systems described above. Methods for the detection, quantification, and/or monitoring of analytes can comprise providing an electrochemical cell comprising a working electrode in electrochemical contact with a liquid sample comprising an analyte, a sample containment vessel, one or more additional electrodes in electrochemical contact with the liquid sample and a power supply electrically coupled to the working electrode and the one or more additional electrodes. The sample containment vessel can comprise a top end, a bottom end, an exterior surface and an interior void defined by an interior surface, wherein the bottom end forms a liquid tight seal with the working electrode and the liquid sample is contained in the volume defined by the interior void of the sample containment vessel and the working electrode. Methods can further comprise capturing an electrochemical signal from the power supply, capturing an optical signal from the electrochemical cell, processing the electrochemical signal to obtain an electrochemical parameter, processing the optical signal to obtain an optical parameter, and optionally correlating the optical parameter to the electrochemical parameter to obtain an optoelectrochemical parameter.

In some examples, the sample containment vessel can further comprise a channel that punctuates the interior surface and leads through the sample containment vessel to the exterior surface or the top end of the sample containment vessel. The one or more additional electrodes can be inserted through the channel such that the one or more additional electrodes are in electrochemical contact with the liquid sample and the one or more additional electrodes form a liquid tight seal with the channel. In some examples, the sample containment vessel comprises multiple channels through which multiple electrodes or other probes may be inserted.

The sample containment vessel, as well as the components thereof, can be fabricated form any suitable material or combination of materials compatible with the methods described herein. Examples of suitable materials include polymers, silicones, glasses, ceramics, inorganic materials and combinations thereof. In some examples, the interior surface of the sample containment vessel is substantially non-conducting. In some examples, the sample containment vessel comprises a cylindrical piece of a nonconducting material, as shown in Figure 5 and Figure 6. In some examples, the nonconducting material is Teflon.

The working electrode and second electrode can be fabricated from any suitable material or combination of materials compatible with the methods described herein. In some examples, the working electrode is substantially optically transparent. In some examples, the working electrode comprises an indium tin oxide (ITO) coated microscope coverslip.

In certain examples, the optical signal can comprise dark field scattering images. Methods for processing the dark field scattering images can comprise saving the images as a series of image files, or "frames". The first frame is subtracted from each subsequent frame to correct for any static defects. Next, all the frames are summed together to yield an image depicting total scattering intensity throughout the experiment. Gradient filtering methods can be used to enhance the contrast within the image. A threshold can be set to differentiate between "active" (scattering) and "inactive" (not scattering) pixels. Adjacent pixels can be grouped together to form "spots". The scattering intensity can then be extracted on a frame-by-frame basis by taking the maximum of the individual pixel intensities for each spot. In some examples, the scattering intensity can be further processed to obtain a different characteristic from the sample. For example, if the liquid sample comprises metal ions that can form nanoparticles upon the application of sufficient voltage, the scattering intensity from the particles can be processed using appropriate theoretical models (*i.e.* Mie theory) to ultimately give nanoparticle size.

In some examples, the analyte can include nanoparticles. In some examples, the optical signal comprises dark field scattering, which can be processed using theoretical methods (*i.e.*, Mie theory) to determine nanoparticles size. In some examples, the optoelectrochemical parameter comprises the potential at which individual nanoparticles, clusters of nanoparticles, or a combination thereof, of a specific size are formed.

Also disclosed herein are sample containment vessels. The sample containment vessel can comprise a top end, a bottom end, an exterior surface and an interior void defined by an interior surface. In some examples, the sample containment vessel is configured to receive a working electrode such that the bottom end forms a liquid tight seal with the working electrode. In some examples, the volume defined by the interior void of the sample containment vessel and the working electrode is configured to contain a liquid sample, and the working electrode can be in electrochemical contact with the liquid sample. In some examples, the sample containment vessel further comprises a channel that punctuates the interior surface of the sample containment vessel and leads through the sample containment vessel to the top end or exterior surface of the sample containment vessel. In some examples, the channel is configured to receive one or more additional electrodes such that

the one or more additional electrodes are in electrochemical contact with the liquid sample and the one or more additional electrodes form a liquid tight seal with the channel.

In some examples, the sample containment vessel can further comprise a channel that punctuates the interior surface and leads through the sample containment vessel to the exterior surface or the top end of the sample containment vessel. The one or more additional electrodes can be inserted through the channel such that the one or more additional electrodes are in electrochemical contact with the liquid sample and the one or more additional electrodes form a liquid tight seal with the channel. In some examples, the sample containment vessel comprises multiple channels through which multiple electrodes or other probes may be inserted.

The sample containment vessel, as well as the components thereof, can be fabricated form any suitable material or combination of materials compatible with the methods described herein. Examples of suitable materials include polymers, silicones, glasses, ceramics, inorganic materials and combinations thereof. In some examples, the interior surface of the sample containment vessel is substantially non-conducting. In some examples, the sample containment vessel comprises a cylindrical piece of a nonconducting material, as shown in Figure 5 and Figure 6. In some examples, the nonconducting material is Teflon.

In some examples, the volume defined by the interior void of the sample containment vessel is 5 mL or less. For example, the volume can be 4 mL or less, 3 mL or less, 2 mL or less or 1 mL or less. For example, the volume can be from 5 mL to 1 μL, from 3 mL to 1 μL, from 1 mL to 1 μL, from 500 μL to 1 μL from 300 μL to 1 μL, and the like.

In some examples, the sample containment vessel is configured to reside in a microscope.

EXAMPLES

The following examples are set forth below to illustrate the methods and results according to the disclosed subject matter. These examples are not intended to be inclusive of all aspects of the subject matter disclosed herein, but rather to illustrate representative methods and results. These examples are not intended to exclude equivalents and variations of the present invention which are apparent to one skilled in the art.

Efforts have been made to ensure accuracy with respect to numbers (*e.g.*, amounts, temperature, etc.) but some errors and deviations should be accounted for. Unless indicated otherwise, parts are parts by weight, temperature is in °C or is at ambient temperature, and pressure is at or near atmospheric. There are numerous variations and combinations of

reaction conditions, *e.g.*, component concentrations, temperatures, pressures and other reaction ranges and conditions that can be used to optimize the product purity and yield obtained from the described process. Only reasonable and routine experimentation will be required to optimize such process conditions.

Example 1

Indium-Tin-Oxide (ITO)-coated coverglass substrates (0.15 mm thick, 15-30 Ω/sq, SPI) were cleaned by sequential sonication for 10 min each in a mild detergent solution, DI H_2O, isopropanol, and DI H_2O followed by drying under a stream of N_2. A Ni TEM grid (SPI) was attached to the substrate using standard laboratory labeling tape. Al (~100 nm) was then thermally deposited through the TEM grid at a pressure of ~10^{-6} torr. The tape and TEM grid were carefully taken off and the substrates were swabbed with $CHCl_3$ to remove the residual adhesive. The sonication procedure was repeated before using the substrates for the electrodeposition experiments.

The electrochemical cell used for these experiments was machined from Teflon. It was designed to use a 0.15 mm thick working electrode and wire counter/reference electrodes while being thin enough to fit within the optical path of our dark field microscope. The previously described ITO substrates were used as working electrodes, along with a Pt wire and Ag wire as counter and quasi-reference electrodes, respectively. The electrolyte solution for depositions comprised 300 μM Ag Acetate (99%, Acros Organics) and 0.1 M $LiClO_4$ (99.99%, Aldrich) in MeCN (HPLC Grade, EMD). An electrolyte solution containing 1 mM Ferrocene MeOH (97%, Aldrich) and 0.1 M $LiClO_4$ was used for calibration of the QRE.

Light from an Hg arc lamp (X-Cite 120 PC Q) was focused onto the substrate surface by a dark field condenser (0.8-0.92 NA, Olympus). Scattered light was collected through a 40x, 0.75 NA objective and imaged using an electron multiplying charge coupled device (EM-CCD) camera (Andor iXon). No EM Gain was used for these measurements. Each pixel of the CCD represented an actual sample area of about 380 x 380 nm. Scattering images of the substrate surface during electrodeposition were recorded at a time resolution of 50 ms. The start of data collection was controlled by a triggering pulse from the potentiostat.

The electrode current was measured as the potential of the ITO electrode was swept at 100 mV/s from 0 V to -0.3 V vs. the Ag QRE using a potentiostat (760C, CH Instruments). The Ag QRE electrode was calibrated by cyclic voltammetry in the Ferrocene MeOH reference solution described previously. All potentials were subsequently reported

against the standard hydrogen electrode (SHE). For the cyclic voltammetry experiment, the potential was ramped from ~0V to -0.5 V to ~ 1 V vs. the Ag QRE at 100 mV/s.

SEM analysis was carried out at a 20 keV accelerating voltage on a JEOL 7000 FE-SEM. The area imaged optically via electrodeposition was first located with the aid of the deposited Al index and imaged at low magnification. After correlating individual spots in the SEM and scattering images, the sample was imaged again at high magnifications to obtain particle sizes for about 40 scattering centers on the substrate.

Custom MATLAB software was used to extract particle scattering transients. An outline of the process is given below.

- The data is initially saved as a TIFF stack (serried of tagged image file format images, or "frames").
- The first frame is subtracted from each subsequent frame. This corrects for any static defects/particles on the sample surface that may scatter light.
- All frames are summed together to yield an image depicting total scattering intensity throughout the experiments.
- Simple gradient filtering methods are used to enhance contrast within the image, if necessary.
- A threshold is set to differentiate between "active" (scattering) and "inactive" (no scattering) pixels.
- Adjacent pixels are grouped together to form "spots".
- Scattering intensity is then extracted on a frame-by-frame basis by taking the maximum of the individual pixel intensities for each spot, resulting in single particle "transients".

Calculations for theoretical scattering-size curves were carried out according to the Mie solution for scattering from a homogeneous sphere. The cross-section representing the scattered light between polar angles $\theta_i \pm \frac{1}{2} \Delta\theta$ was calculated as:

$$\sigma_i(k, r, \theta_i, \Delta\theta) = \frac{2\pi}{k^2} \int_{\theta_i - \frac{1}{2}\Delta\theta}^{\theta_i + \frac{1}{2}\Delta\theta} S_{11}(k, r, \theta) d\theta \quad (1)$$

where k is the wavenumber of the scattered radiation and r the particle radius. The scattering matrix element S_{11} was calculated via MATLAB programs, which followed a well-established algorithm (Bohren, CF; Huffman, DR. *Absorption and Scattering of Light by Small particles*. 1983). Values for the complex refractive index of Ag (*Handbook of Optical Constants of Solids,* Palik, 1985), MeCN (n = 1.3442, *CRC Handbook of Chemistry and Physics*, Lide, 2008), and ITO (Sopra Materials Database) were obtained from the

indicated sources. The Ag and ITO refractive indices were functions of scattering wavelength, which were interpolated as necessary to yield values at wavelengths matching those at which the lamp intensity was measured. The medium refractive index used for these calculations was taken to be an average of the MeCN and ITO values, and an angular resolution of 1 degree was used. The observed scattering intensity at the detector was modeled as:

$$I_i(r,\theta_i,\Delta\theta) = \chi \int \sigma_i(k,r,\theta_i,\Delta\theta) I_{lamp}(k)\eta_{CCD}(k)\eta_{coll}(\theta_i)\, dk$$
$$I_{obs}(r) = \sum_i I_i(r,\theta_i,\Delta\theta) \quad (2)$$

where I_{lamp} is the lamp intensity, η_{CCD} is the detector quantum efficiency, and η_{coll} is the optical collection efficiency. χ is an empirical factor used to account for variations in lamp intensity/optical collection efficiency; this is the factor allowed to vary in the data fitting process. The lamp intensity/CCD efficiency factors are straightforward to obtain. The collection efficiency term was defined as:

$$\eta_{coll}(\theta_i) = \frac{1}{2\pi}\int_0^{2\pi} M_{coll}(\theta_i,\varphi)d\varphi$$
$$M_{coll}(\theta,\varphi) = \begin{cases} 1 \; if \; \theta_{obj} < 48.6^o \\ 0 \quad otherwise \end{cases} \quad (3)$$
$$\theta_{obj} = arcsin\left(\frac{n_{med}\sin\left(arccos(\sin\theta\cos\varphi\sin\theta' + \cos\theta\cos\theta')\right)}{n_{air}}\right)$$

where θ' is the angle between the incident light path and the objective axis (59.3^o). This expression makes the geometric assumption that all scattered light which leaves the sample at an angle smaller than the acceptance defined by the objective lens (NA = 0.75) will be collected. Here, again, n_{med} was taken to be an average of ITO and MeCN values. This resulting scattering cross section-size curve for the calculations presented here is given in Figure 11.

All data fitting was carried out using the "fminsearch" function (which follows the Nelder-Mead algorithm) in MATLAB. First, the extracted single particle transients were fit to sigmoidal functions:

$$I(E) = I_{bg} + \frac{A_{sig}}{1+e^{k\left(E-E_{1/2}\right)}} \quad (4)$$

The average R^2 value for single NP transient fits was about 0.994. The amplitudes (A_{sig}) were used as the values for the final particle scattering intensity. The "turn-on" potential, E_{on}, was defined as:

$$E_{on} = E_{1/2} + 2k^{-1} \tag{5}$$

E_{on} is illustrated graphically in Figure 12. Fitting of the experimental single particle scattering-size curve (generated by plotting sigmoid amplitude, A_{sig}, as a function of particle size obtained via SEM) to the theoretical curve was used to generate a value for χ which effectively correlated the observed scattering intensity with particle size. From this point, the scattering intensity for individual particles was interpolated to obtain radius-potential curves. Single particle currents were generated according to:

$$i(t) = \frac{dQ_{dep}(t)}{dt} \qquad Q_{dep}(t) = \frac{\rho_{Ag}F}{M_{Ag}}V_{NP}(t)$$

$$i(t) = \frac{\rho_{Ag}F}{M_{Ag}}\frac{dV_{NP}(t)}{dt} = \frac{\rho_{Ag}F}{M_{Ag}}\frac{d}{dt}\left(\frac{4}{3}\pi r(t)^3\right) \tag{6}$$

$$i(t) = \left(\frac{4\pi\rho_{Ag}F}{M_{Ag}}\right)r(t)^2\frac{dr(t)}{dt}$$

These relations make the assumption of uniform spherical growth of the particles. Here, Q_{dep} represents the total charge passed due to the reduction of Ag^+. ρ_{Ag}, F, and M_{Ag} are the density of silver, Faraday's constant, and atomic weight of Ag, respectively. r is the nanoparticle's radius.

The model employed to calculate the profile of scattering intensity transients for the deposition of single NPs makes the following assumptions: (1) linear diffusion is established quickly, (2) each NP effectively "controls" a geometric area of the electrode surface, (3) the kinetics of Ag^+ reduction are much faster (reversible) at the surface of deposited Ag than at the bare ITO surface, and (4) the diffusion constant of Ag^+ ions in MeCN is not appreciably different than that for in H_2O ($D = 1.65 \times 10^{-5}$ cm^2 s^{-1}). Assumption 1 is justified by considering the short time necessary for the diffusion layer thickness to grow to the average particle-particle distance observed in the DFS images. Once the initially spherical diffusion layers from nearby NPs collide, diffusion of Ag^+ parallel to the substrate ceases as it consumed, resulting in the shift from spherical to linear diffusion behaviors. The geometric area of the ITO electrode covered by the diffusion layer for a single NP once linear diffusion is established will be referred to as the "effective" area, or A_{eff}. Only Ag^+ ions approaching the electrode within the effective area for a given NP will be reduced at the nanoparticles surface and contribute to its growth. It is reasonable to assume that the kinetics of Ag^+ reduction will be sufficiently quicker at the surface of the deposited Ag NPs. Working within these assumptions, the deposition current for the individual Ag NPs can be effectively modeled as the current at an electrode of area A_{eff} undergoing strictly linear diffusion.

The nanoparticles current is then:

$$i_{NP}(E) = nFA_{eff}\left(C^*_{Ag^+}\right)\left(\upsilon D_{Ag^+}\right)^{\frac{1}{2}}\Pi\left(E - E_{\frac{1}{2}}(E)\right)$$

$$E_{\frac{1}{2}}(E) = E_{\frac{1}{2},bulk} + \Delta E_{size}(E) = E_{\frac{1}{2},bulk} - \left(\frac{2\gamma_{Ag}V_m}{nF}\right)\frac{1}{r(E)+R_0} \quad (7)$$

where n is the number of electrons transferred in the redox reaction, F is Faraday's constant, C^* is the bulk concentration of Ag^+, D is the diffusion constant of Ag^+, υ is the scan rate, and Π is the function which accounts for the shape of the i-E curve. As reversible electrode kinetics and linear diffusion are assumed here, the values for this function are well known and were taken directly from the literature (Bard, AJ; Faulkner, LR. *Electrochemical Methods: Fundamentals and Applications*; John Wiley & Sons, Inc.: 2001). It has been long-proposed theoretically (Plieth, WJ. *J. Phys. Chem.* 1982, *86*, 3166-3170; Henglein, A. *J. Phys. Chem.* 1993, *97*, 5457-5471) and confirmed experimentally (Ivanova, O; Zamborini, FP. *JACS*. 2010, *132*, 70-72; Masitas, RA; Zamborini, FP. *JACS*. 2012, *134*, 5014-5017) that the reduction potential of metal nanoparticles shifts positively with increasing particle size. This is accounted for in this analysis by including a size dependent potential shift based on the Plieth equation (Plieth, WJ. *J. Phys. Chem.* 1982, *86*, 3166-3170). This shift is the ΔE_{size} term in equation (7), where γ_{Ag} and V_m are the surface tension and molar volume for Ag, respectively. Since the standard form of the Plieth equation predicts an infinitely large negative reduction potential shift at r = 0 (theoretically forbidding NP formation), a phenomenological term, R_0, was included. This parameter was set so that $\Delta E_{size(r=0)}$ was equal to the experimental shift of smallest NPs reported in the literature ($\Delta E \cong$ -107 mV for about 4 nm particles, R_0 = 3.17 nm) (Ivanova, O; Zamborini, FP. *JACS*. 2010, *132*, 70-72). Example calculated i-E and scattering-E curves calculated with and without a size dependent $E_{1/2}$ value are given in Figure 13. The scattering-E curve was generated by using the relations in equation 6 to calculate a particle size as a function of electrode potential and then interpolating the σ_{obs} curve to obtain scattering intensities from these particle sizes. The single NP scattering trajectories were then fit numerically by varying the values of A_{eff} and $E_{1/2}$. Distributions of the fitted parameters are given in Figure 14. The theoretical form including the ΔE_{size} term more closely fit the experimental scattering data; average R^2 values for single NP transient fits were 0.97 and 0.93 with and without this correction.

The experimental setup can be seen in Figure 15. Ag particles were deposited from MeCN containing Ag acetate and $LiClO_4$ by ramping the ITO electrode potential cathodically (~0.1 V to -0.2 V vs. SHE). Simultaneously, light scattering at the electrode

surface was imaged over a ~100 × 100 μm sample area. Upon the application of sufficiently cathodic potentials, light scattering due to the presence of deposited AgNPs on the ITO electrode becomes detectable. This can be seen visually in the inset images in Figure 16, given at the indicated points along the sweep. The total measured scattering intensity and measured electrode current are included for reference. This total scattering intensity across the electrode surface exhibits shifts towards more negative potentials as one would expect with increasing sweep rates (Figure 17), due to the slow kinetics of Ag^+ reduction at ITO.

Individual diffraction limited spots (FWHM = ~350 nm) were resolved in the scattering images. For data analysis, spot location was carried out through custom MATLAB programs and resulted in several hundreds to thousands being detected per sample. For the sample depicted in Figure 16, 770 spots were detected, resulting in an apparent surface density of 7.55×10^6 spots • cm^{-2}. The average distance between a given spot and its nearest neighbor is about 2.8 μm. This resulting density can be rationalized by considering the growth of spherical diffusion layers originating from nucleation sites on the electrode surface; the diffusion layer overlapping resulting from the deposition of individual particles would control the effective final particle sizes and density. Due to this well documented behavior, and the scanning electron microscopy (SEM) data to be discussed later, the diffraction limited spots in the final scattering images correspond to either "lone" or a few closely "grouped" particles, though it's likely the observed particles result from several nucleation sites early in the deposition process.

Some example scattering-potential transients for individual spots are given in Figure 18A. The individual scattering transients were fit to obtain distributions of final scattering intensities (A_{sig}), as shown as inset of Figure 18, and light scattering "turn-on" potentials (E_{on}) as shown in Figure 18. Detailed data fitting procedures are described above. The distribution of final scattering intensities is correlated with the final shape and size of the particles. E_{on} physically represents the electrode potential at which the scattering of light by the particle becomes detectable, which is dependent on the experimental configuration. For the configuration employed herein, the limit of detection in terms of particle diameter is about 46 nm (using a definition of 3 times the detection noise). The distribution in E_{on} values reflects a combination of several factors, including (1) variations in the required overpotential to drive Ag^+ reduction at different sites on the ITO surface, (2) the proximity/overpotential of neighboring sites on the surface, and (3) variations in particle geometry and/or orientation with respect to the substrate. The observed E_{on} values span a 60 mV range. Variations in the local overpotential could be due to inherent variations in the

defect sites on the ITO surface at which deposition occurs or to local variations in contact area with or conductivity of the ITO electrode. The E_{on} and A_{sig} parameter values for individual NPs were found to be weakly correlated, with a more negative turn-on potential corresponding to a smaller final scattering intensity (Figure 19). The observed weak correlation can be due to several competing factors that affect the final deposited particle size: variations in the local ITO conductivity, distance from neighboring particles, and the potential at which those particles began to grow.

While these results provide qualitative insight into the heterogeneity in the reduction of Ag^+ at ITO, quantitative information on fundamental electrochemical parameters (reaction half potentials, kinetic parameters, etc.), rather than the empirical analysis discussed thus far, can also be provided. This can be done by correlating the observed scattering signal with the actual particle size.

The measured scattering intensity can be expressed as Equation 2, as discussed above. χ is a factor which accounts for the absolute lamp intensity at the sample surface, and is the quantity varied to perform the data fitting. Calculation of σ_i for spherical, homogeneous metal particles can be carried out directly using Mie theory; not knowing explicit values for all of the other quantities prevents one from obtaining a direct relationship between scattering intensity and particle size. To address this issue, correlated SEM measurements were carried out on the deposited particles. The particles corresponding to spots in the scattering image were identified via SEM and sized. Example SEM images can be seen in Figure 20A and B. The image in Figure 20A is overlaid with the scattering image obtained during the deposition process (Figure 21). Immediately evident is that there are particles on the ITO surface not visible in the scattering image. These particles are a combination of stray Al particles created during the deposition of the Al index and deposited Ag particles too small to be detected via scattering. The Al particles (and any other static defect) are ignored in the scattering analysis through a background correction procedure. The SEM analysis made it possible to unambiguously attribute the spots in the scattering image to scattering from lone or closely grouped particles. Of the ~40 correlated areas for the sample discussed here, roughly one-third could be unambiguously assigned to individual particles. More careful control over deposition parameters (*e.g.*, employing a dual potential step instead of a sweep) can eliminate this issue by lowering the particle surface density further. The morphology of the deposited particles was found to be roughly spherical in nature. A histogram of obtained particle sizes is given in Figure 20C. The relationship between the scattering intensity and particle size for the lone particles can be

observed in Figure 20D (squares). The proper value of χ is obtained by a numerical fitting procedure using the scattering intensity values for the lone particles. The result of this fitting procedure is given as the curve in Figure 20D. For the spots found to correspond to small groups of particles, individual particle intensities can be extracted from the measured intensity according to the theoretical curve profile. The result of this process for the "grouped" spots in the SEM analysis is the triangles in Figure 20D. This illustrates that even in cases where a given diffraction limited spot does not correlate to an individual particle, the Mie theory approximation used in this analysis can still accurately agree with the measured intensity.

Once the final scattering intensities have been "calibrated" against the SEM data, it becomes possible to convert single NP scattering transients into corresponding size transients. This process was carried out blindly for all 770 spots imaged optically. Once radius potential curves are in hand, it is then possible to estimate the Faradaic current for Ag^+ reduction contributing to a given particle's growth according to equation 6. Example single particle voltammograms can be seen in Figure 22A along with the distribution of peak potentials. Using the resulting single particle currents and the observed particle surface density, the bulk faradaic current density was then estimated from the scattering data and compared to the current density measured by the potentiostat (Figure 22B). The agreement between the calculated and measured current densities is impressive and supports the validity of the single NP scattering analysis. The discrepancy at more cathodic potentials can be due to the presence of undetected Ag particles, differing particle size distributions between the entire working electrode (~2 cm^2) and 100 × 100 μm imaged area, or to non-Faradaic processes occurring at the working electrode which are effectively ignored in the scattering analysis. Disagreement due to non-Faradaic processes actually highlights an important inherent advantage to this technique: the only processes which contribute to scattering signal are those considerably altering either the morphology of the nanoparticle or its surrounding dielectric environment.

In order to obtain single particle i-E curves such as those given in Figure 22, no assumptions about the electrochemical behavior of the system (diffusion behavior, electrode kinetics, etc.) is required. This is due to the direct correlation between particle size and scattering intensity established through the SEM measurements. However, because the scattering analysis provides no information about the NPs' growth until it reaches a detectable size, fitting the data to a theoretical model has value because it can help infer information about the behavior before this point. To this end, a model is disclosed for fitting

the single NP scattering data in terms of the local Ag^+ reduction potential and effective electrode area the NP occupies.

This technique has also been applied to observe the subsequent oxidation of the electrodeposited Ag particles. The results are given in Figure 23 and Figure 24. Oxidation of the Ag NPs is visible in the cyclic voltammagram at ~0.2 V vs. SHE. This correlates with a drop in total scattering intensity for the ensemble of deposited particles of about 10%. The relative reduction in scattering intensity for single particles upon oxidation varies from particle to particle, not being visible at all in some cases (*e.g.*, Figure 24).

Example 2

A MATLAB program was developed to help analyze single silver nanoparticle spectroscopic data obtained with a standard inverted optical microscope. The described software has provisions to mitigate the effects of high background signals present in such data sets and greatly streamlines their analysis. Efficient single nanoparticle image analysis is provided with these programs to support single nanoparticle imaging in an inverted configuration.

Dark field scattering was collected through an X40 objective using a CCD camera (Andor iXon). Light scattering movies were recorded as a function of working electrode potential, as described earlier, at 50 ms resolution and saved as a Tagged Image File Format (TIFF) image stack.

Single molecule video files were analyzed using a MATLAB program that follows the process outlined in Figure 25. Typically, the data was input as TIFF image stack.

Every frame of the image stack was first summed to create a "raw" image. This can be seen in Figure 26. Due to the relatively low signal-to-noise ratio for these measurements, a large, inhomogeneous background signal was often present. This made locating active sites within the image by setting a simple intensity threshold difficult. To combat this, the discrete gradient norm (G_{ij}) and Laplacian (L_{ij}) for the image were then computed from the RAW image as:

$$G_{ij} = \sqrt{\left[\left(f_{i+1,j} - f_{ij}\right) + \left(f_{ij} - f_{i-1,j}\right)\right]^2 + \left[\left(f_{i,j+1} - f_{ij}\right) + \left(f_{ij} - f_{i,j-1}\right)\right]^2}$$

$$L_{ij} = \frac{1}{4}\left(f_{i+1,j} + f_{i-1,j} + f_{i,j+1} + f_{i,j-1}\right) - f_{ij} \qquad (12)$$

The Raw, Gradient, and Laplacian images were visually mixed to generate a composite image which best resolves individual molecules and effectively "flattens" the background. Upon setting an appropriate intensity threshold, the active pixels adjacent to one another

were grouped together into "spots", each representing a single nanoparticle. Dark field scattering trajectories for single nanoparticles were then extracted by adding the intensities for each pixel in a given spot and subtracting a background value on a frame-by-frame basis.

For a given spot, the bordering pixels' intensities were averaged together to generate a suitable background value and subtracted according to:

$$S = \sum f_a - \frac{N_a}{N_b} \sum f_b \tag{13}$$

where S is the molecule's fluorescence intensity, f_a are the intensities for the active pixels, and f_b are the intensities for the background pixels. The effects of the background separation can be seen in Figure 26. A screenshot of this programs' interface can be seen in Figure 27.

Other advantages which are obvious and which are inherent to the invention will be evident to one skilled in the art. It will be understood that certain features and sub-combinations are of utility and may be employed without reference to other features and sub-combinations. This is contemplated by and is within the scope of the claims. Since many possible examples may be made of the invention without departing from the scope thereof, it is to be understood that all matter herein set forth or shown in the accompanying drawings is to be interpreted as illustrative and not in a limiting sense.

CLAIMS

What is claimed is:

1. A system comprising:

    a) an electrochemical cell comprising

        i. a working electrode in electrochemical contact with a liquid sample comprising an analyte;

        ii. a sample containment vessel comprising a top end, a bottom end, an exterior surface, and an interior void defined by an interior surface;

            wherein the bottom end forms a liquid tight seal with the working electrode;

            wherein the liquid sample is contained in the volume defined by the interior void of the sample containment vessel and the working electrode;

        iii. one or more additional electrodes in electrochemical contact with the liquid sample; and

        iv. a power supply electrically coupled to the working electrode and the one or more additional electrodes;

    b) a light source configured to illuminate the liquid sample; and

    c) an instrument configured to capture an optical signal from the liquid sample.

2. The system of claim 1, wherein the sample containment vessel further comprises a channel that punctuates the interior surface and leads through the sample containment vessel to the top end or exterior surface of the sample containment vessel,

    wherein the one or more additional electrodes can be inserted through the channel such that the one or more additional electrodes are in electrochemical contact with the liquid sample; and

    wherein the one or more additional electrodes form a liquid tight seal with the channel.

3. The system of any of claims 1-2, further comprising a first lens.

4. The system of claim 3, wherein the system is configured such that the light source and the instrument are below the first lens, and the electrochemical cell is above the first lens.

5. The system of claim 4, where in the first lens is a microscope objective.

6. The system of claim 3, further comprising a second lens.

7. The system of claim 6, wherein the system is aligned such that:

the first lens is above the instrument;

the electrochemical cell is above the first lens;

the second lens is above the electrochemical cell; and

the light source is above the second lens.

8. The system of claim 7, wherein the first lens is a dark field microscope objective and the second lens is a dark field microscope condenser.

9. The system of any of the claims 1-8, further comprising a computing device comprising a processor and a memory operably coupled to the processor, the memory having further computer-executable instructions stored thereon that, when executed by the processor, cause the processor to:

receive an electrochemical signal from the power supply;

receive an optical signal from the instrument;

process the electrochemical signal to obtain an electrochemical parameter;

process the optical signal to obtain an optical parameter;

optionally correlate the electrochemical parameter to the optical parameter to obtain an optoelectrochemical parameter; and

output the electrochemical parameter, the optical parameter, the optoelectrochemical parameter, or combinations thereof.

10. The system of any of the claims 1-9, wherein the interior surface of the sample containment vessel is substantially non-conductive.

11. The system of any of the claims 1-10, wherein the working electrode is substantially optically transparent.

12. The system of any of the claims 1-11, wherein the working electrode comprises an indium tin oxide (ITO) coated coverslip.

13. The system of any of the claims 1-12, wherein the instrument is a camera.

14. The system of any of the claims 1-13, wherein the light source comprises an artificial light source.

15. The system of claim 14, wherein the artificial light source comprises an arc lamp.

16. The system of claim 14, wherein the artificial light source comprises a laser.

17. A method comprising

a) providing an electrochemical cell comprising

i. a working electrode in electrochemical contact with a liquid sample comprising an analyte;

ii. a sample containment vessel comprising a top end, a bottom end, an exterior surface, and an interior void defined by an interior surface;

wherein the bottom end forms a liquid tight seal with the working electrode;

wherein the liquid sample is contained in the volume defined by the interior void of the sample containment vessel and the working electrode;

iii. one or more additional electrodes in electrochemical contact with the liquid sample; and

iv. a power supply electrically coupled to the working electrode and the one or more additional electrodes;

b) capturing an electrochemical signal from the liquid sample;

c) capturing an optical signal from the liquid sample;

d) processing the electrochemical signal to obtain an electrochemical parameter;

e) processing the optical signal to obtain an optical parameter;

f) optionally, correlating the optical parameter to the electrochemical parameter to obtain an optoelectrochemical parameter.

18. The method of claim 17, wherein the optical signal comprises dark field scattering, electrogenerated chemiluminescence, fluorescence or a combination thereof.

19. The method of any of the claims 17-18, wherein the optical parameter comprises nanoparticle size.

20. The method of any of the claims 17-19, wherein the optoelectrochemical parameter comprises the potential at which individual nanoparticles, clusters of nanoparticles, or a combination thereof of a specific size are formed.

21. A sample containment vessel, comprising a top end, a bottom end, an exterior surface, and an interior void defined by an interior surface

wherein the sample containment vessel is configured to receive a working electrode;

wherein the bottom end forms a liquid tight seal with the working electrode;

wherein the volume defined by the interior void of the sample containment vessel and the working electrode is configured to contain a liquid sample; and

wherein the working electrode can be in electrochemical contact with the liquid sample.

22. The sample containment vessel of claim 21, further comprising a channel that punctuates the interior surface of the sample containment vessel and leads through the sample containment vessel to the top end or exterior surface of the sample containment vessel,

wherein the channel is configured to receive one or more additional electrodes such that the one or more additional electrodes are in electrochemical contact with the liquid sample; and

wherein the one or more additional electrodes form a liquid tight seal with the channel.

23. The sample containment vessel of any of the claims 21-22, wherein the volume defined by the interior void is from 5 mL to 1 μL.

24. The sample containment vessel of any of the claims 21-23, wherein the sample containment vessel is configured to reside in a microscope.

ABSTRACT

Provided herein are systems and methods for the detection, quantification, and/or monitoring of analytes in samples. The systems and methods can be used, for example, to track the deposition of individual nanoparticles and nanoparticles clusters clusters *in situ* with high spatial and temporal resolution. The systems and methods can be used to track the deposition of several hundreds to thousands of nanoparticles simultaneously and reconstruct their voltammetric curves at the single nanoparticle level.

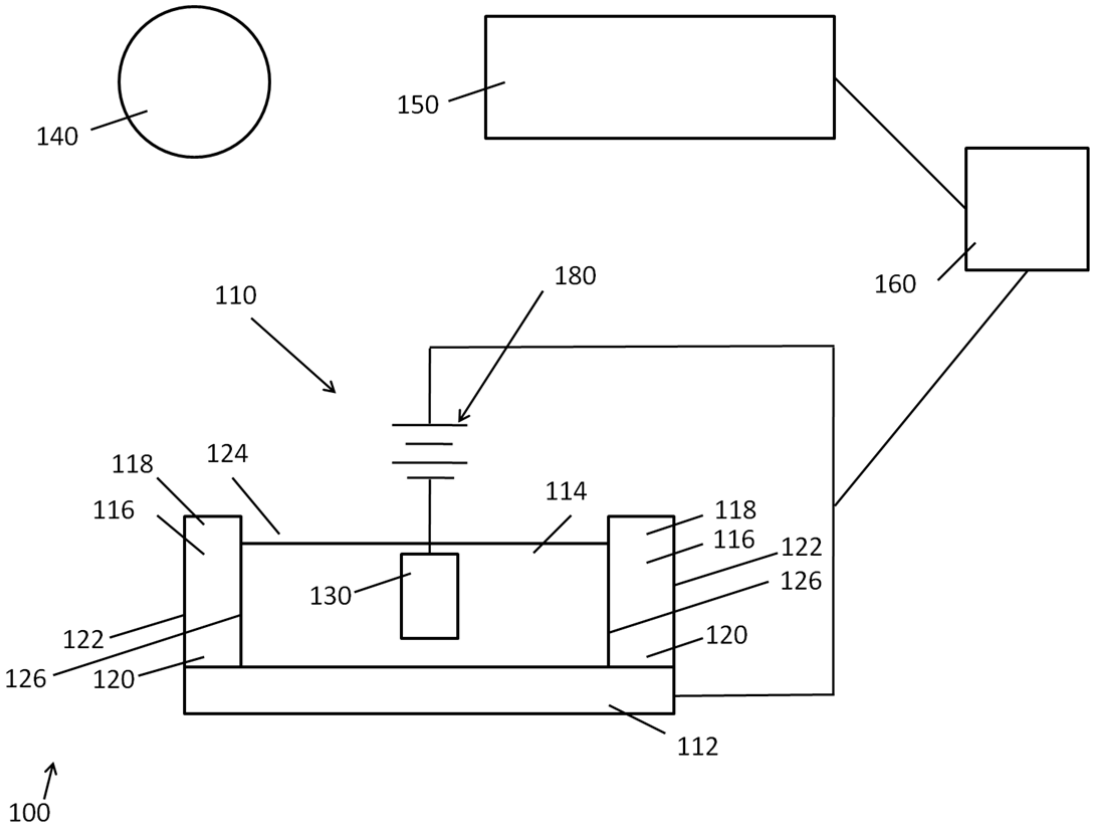
140
150
160
110
180
118
124
116
114
118
116
122
126
130
122
126
120
120
112
100

Figure 1

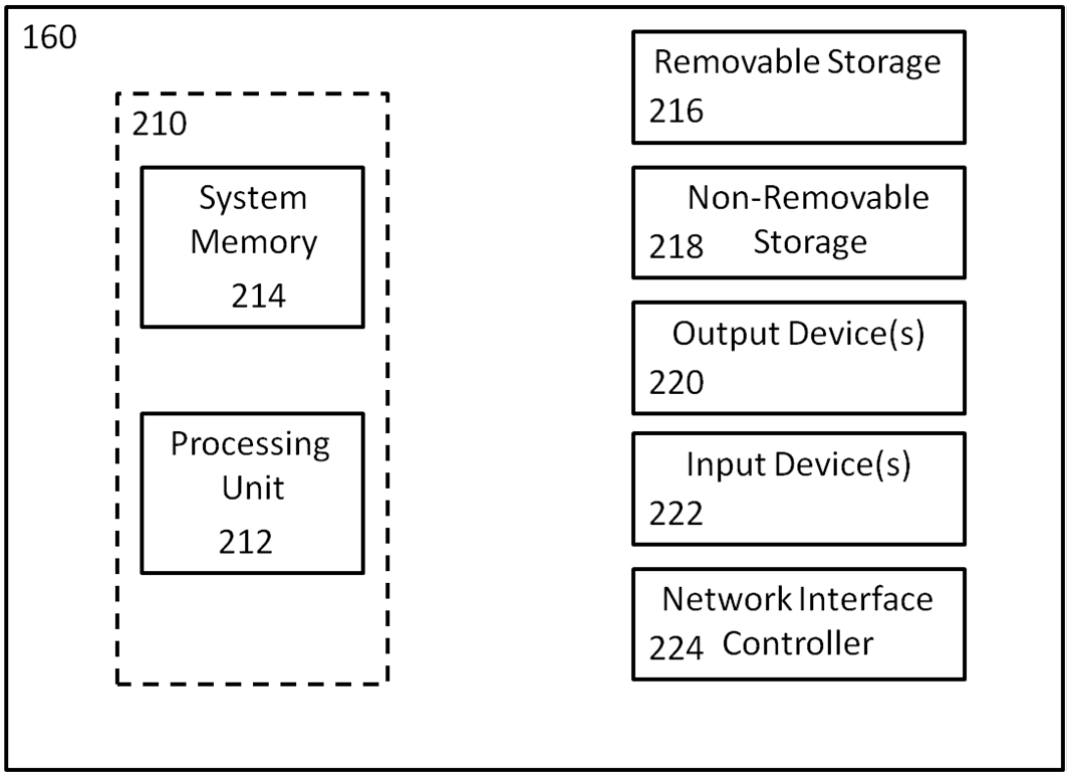
160
210
System Memory 214
Processing Unit 212
Removable Storage 216
Non-Removable Storage 218
Output Device(s) 220
Input Device(s) 222
Network Interface Controller 224

Figure 2

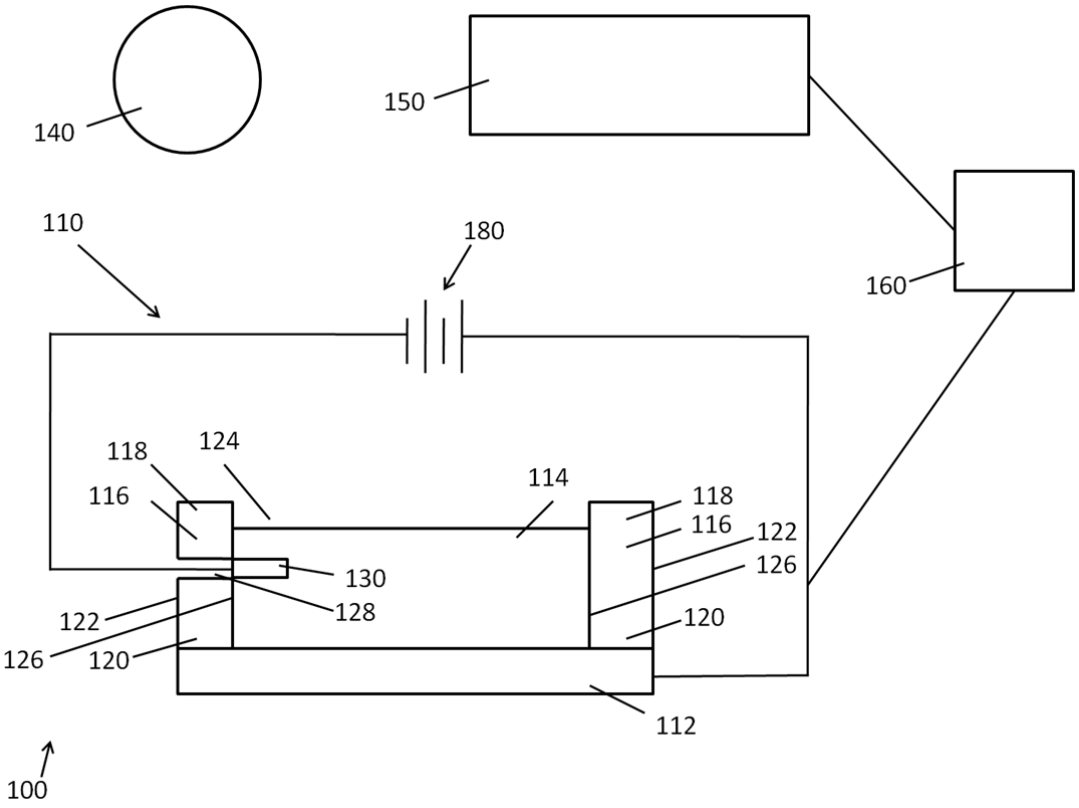
140
150
160
110
180
118
124
116
114
118
116
122
126
130
128
122
126
120
120
112
100

Figure 3

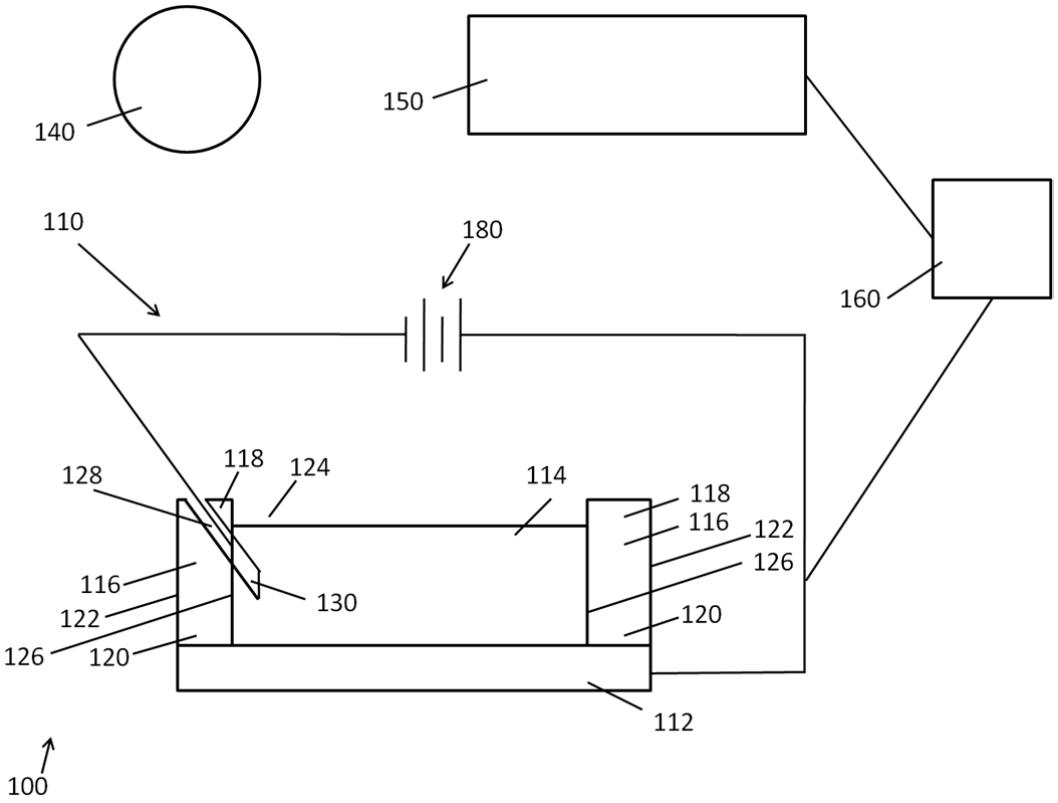
140
150
110
180
160
128
118
124
114
118
116
122
126
116
122
126
130
120
120
112
100

Figure 4

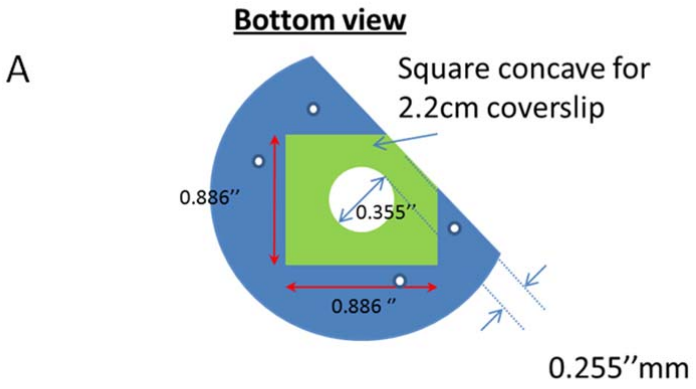
Bottom view
A
Square concave for
2.2cm coverslip
0.886''
0.355''
0.886 ''
0.255''mm

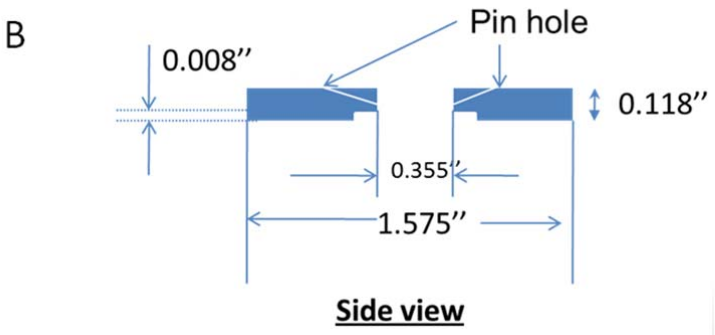
B
Pin hole
0.008''
0.118''
0.355''
1.575''
Side view

Figure 5

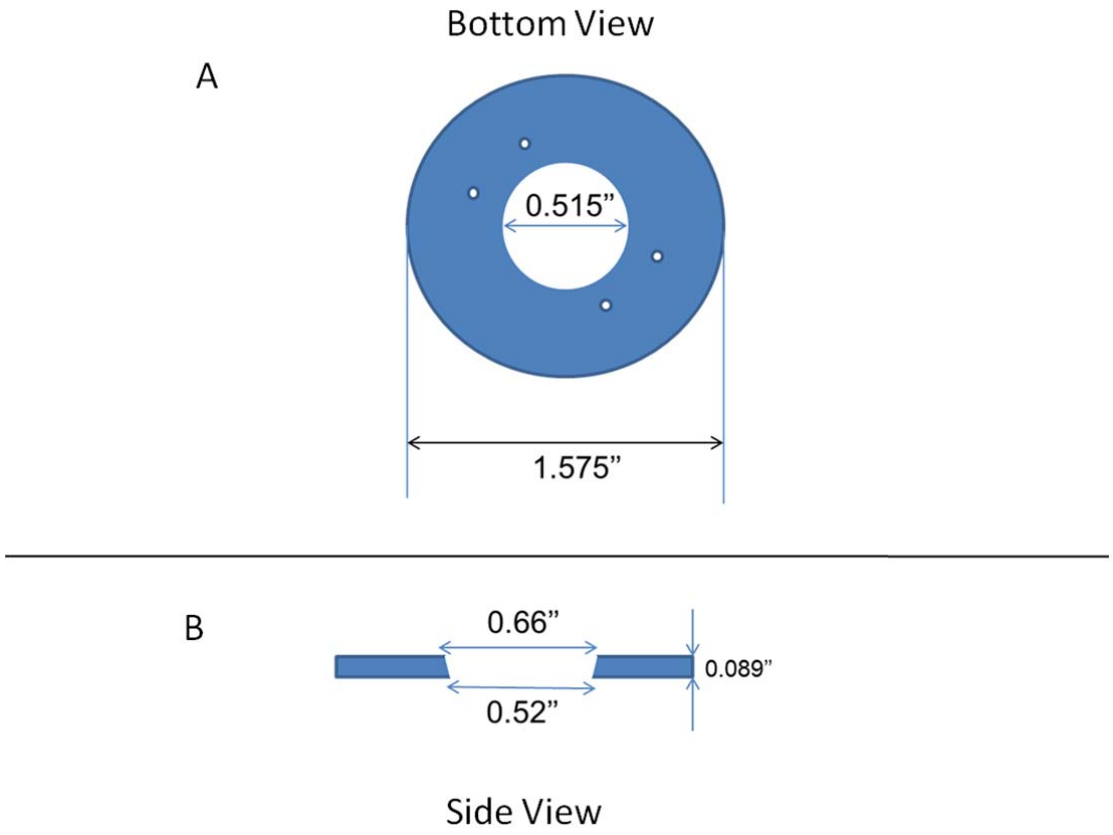

Figure 6

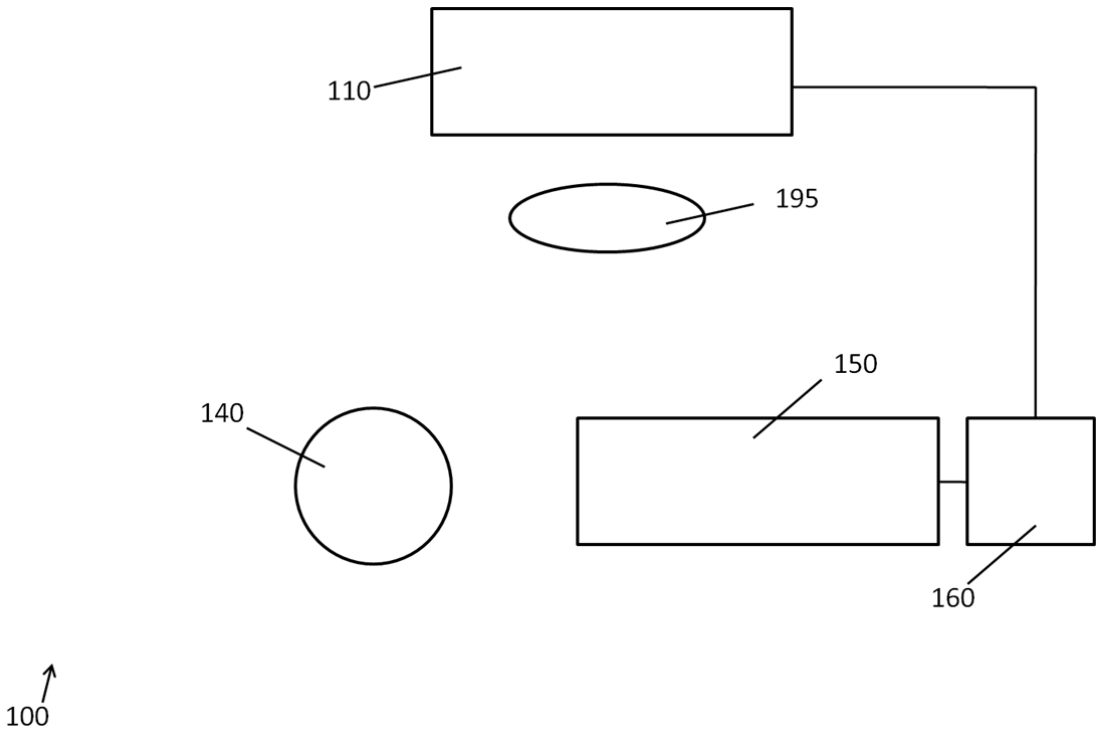

Figure 7

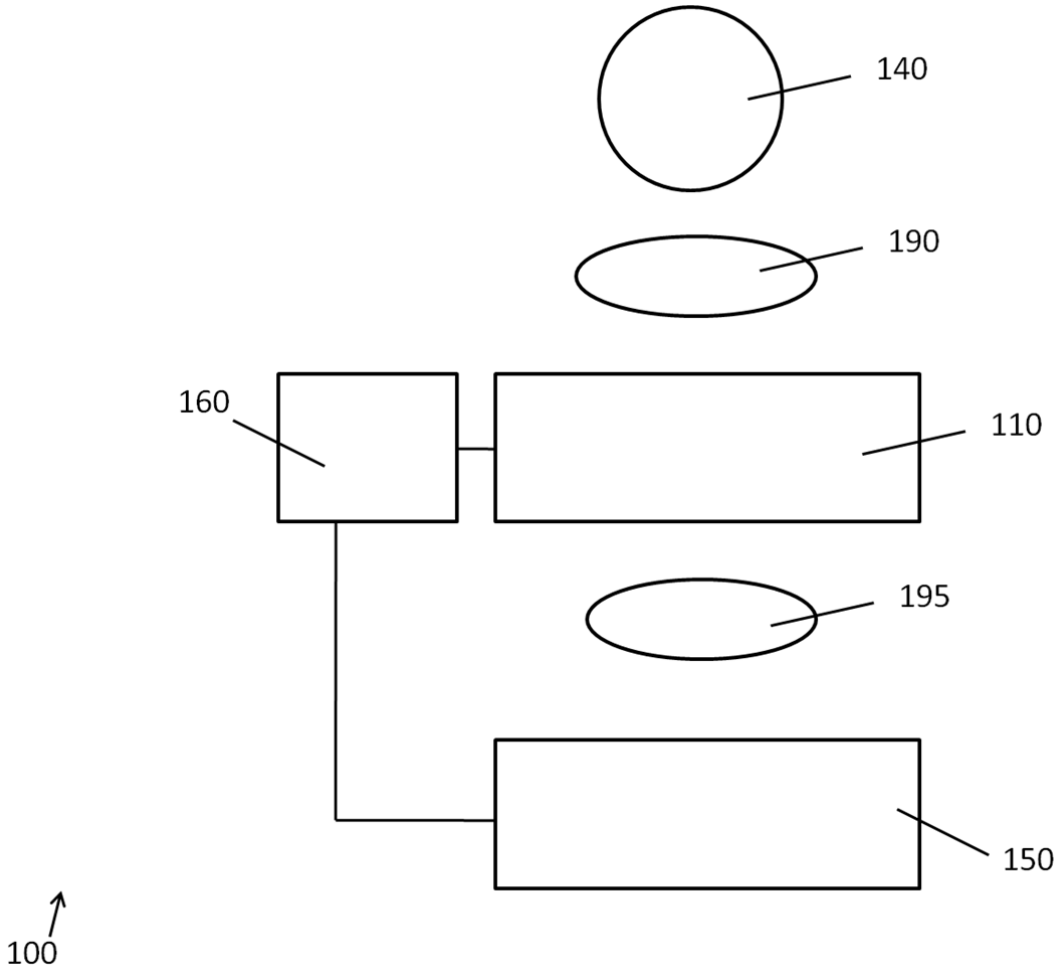

Figure 8

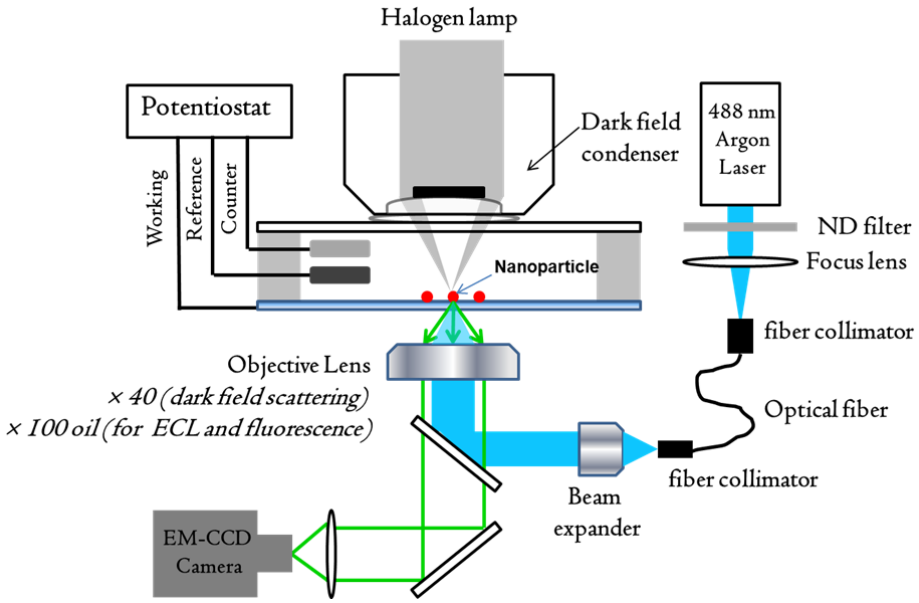
Halogen lamp
Potentiostat
Working
Reference
Counter
Dark field condenser
488 nm Argon Laser
ND filter
Focus lens
Nanoparticle
fiber collimator
Objective Lens
× 40 (dark field scattering)
× 100 oil (for ECL and fluorescence)
Optical fiber
fiber collimator
Beam expander
EM-CCD Camera

Figure 9

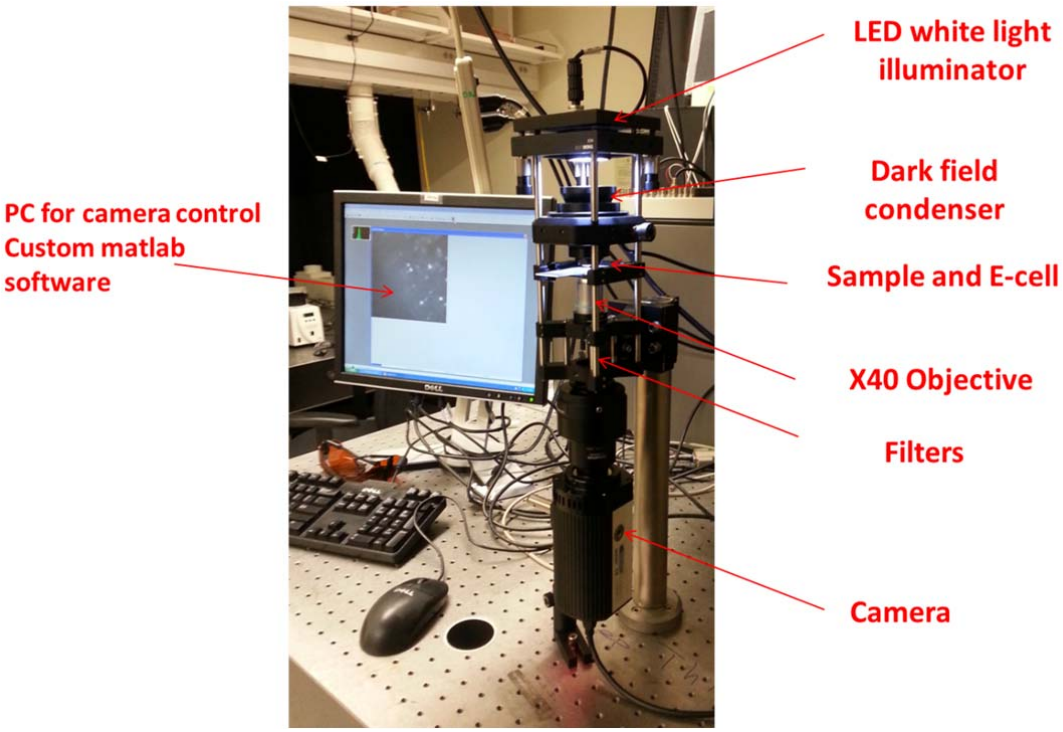
LED white light illuminator
Dark field condenser
PC for camera control
Custom matlab software
Sample and E-cell
X40 Objective
Filters
Camera

Figure 10

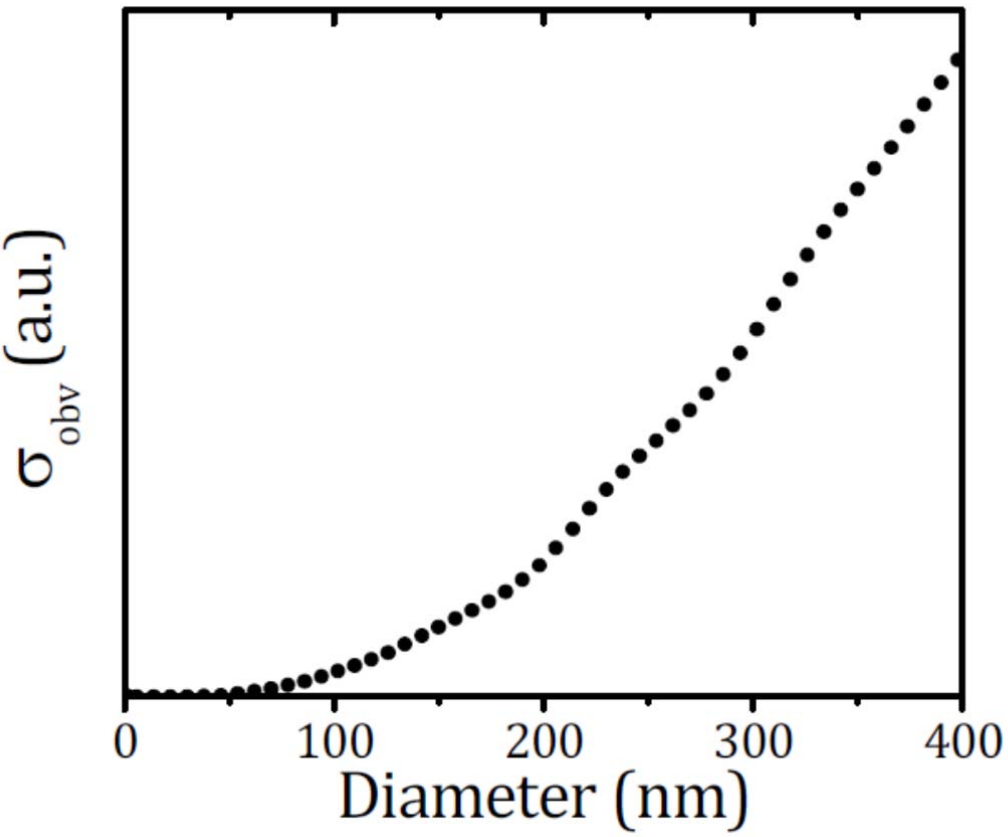

Figure 11

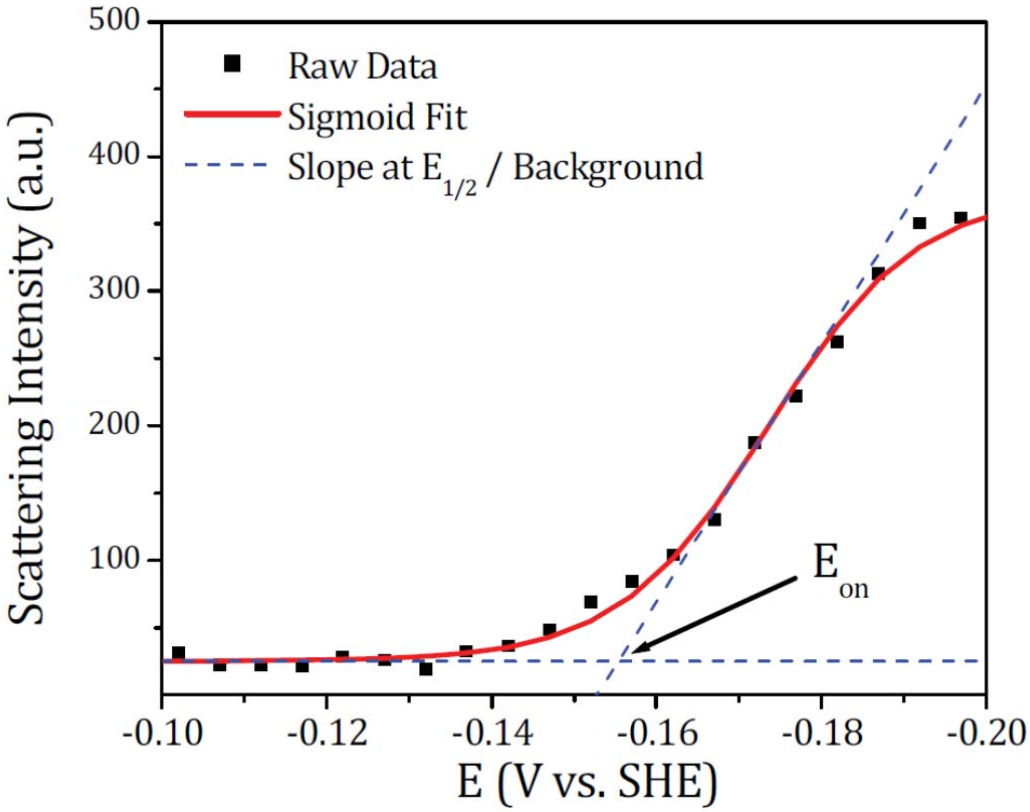
Raw Data
Sigmoid Fit
Slope at E1/2 / Background
Eon
Scattering Intensity (a.u.)
E (V vs. SHE)
500
400
300
200
100
-0.10
-0.12
-0.14
-0.16
-0.18
-0.20

Figure 12

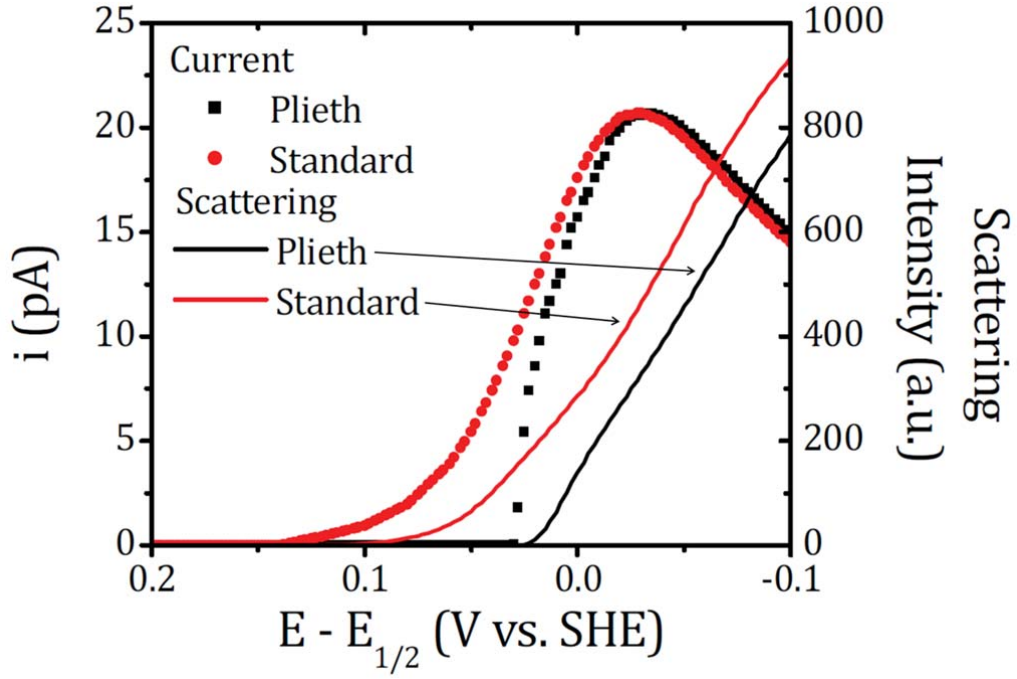
Current
Plieth
Standard
Scattering
Plieth
Standard
i (pA)
Scattering Intensity (a.u.)
E - E1/2 (V vs. SHE)
25
20
15
10
5
0
1000
800
600
400
200
0
0.2
0.1
0.0
-0.1

Figure 13

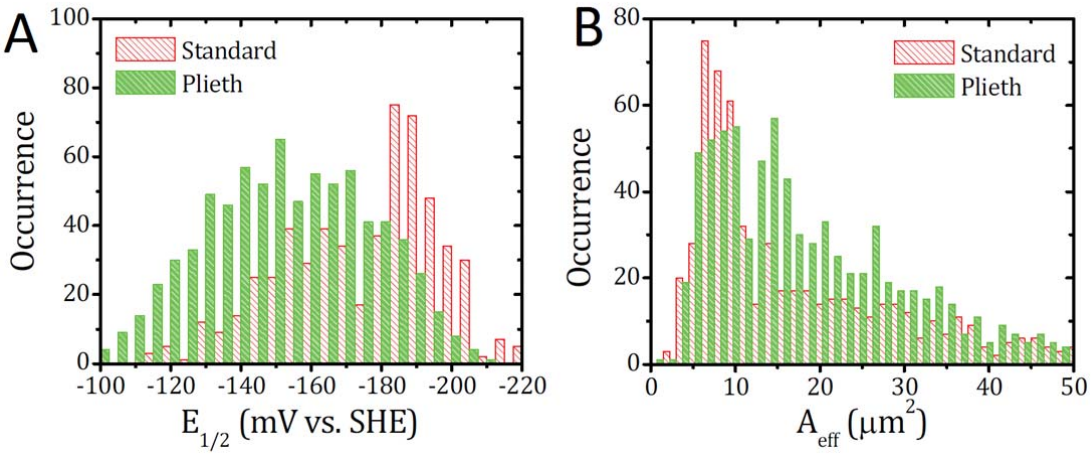
A
Standard
Plieth
Occurrence
100
80
60
40
20
0
-100
-120
-140
-160
-180
-200
-220
E1/2 (mV vs. SHE)
B
Standard
Plieth
Occurrence
80
60
40
20
0
0
10
20
30
40
50
Aeff (μm2)

Figure 14

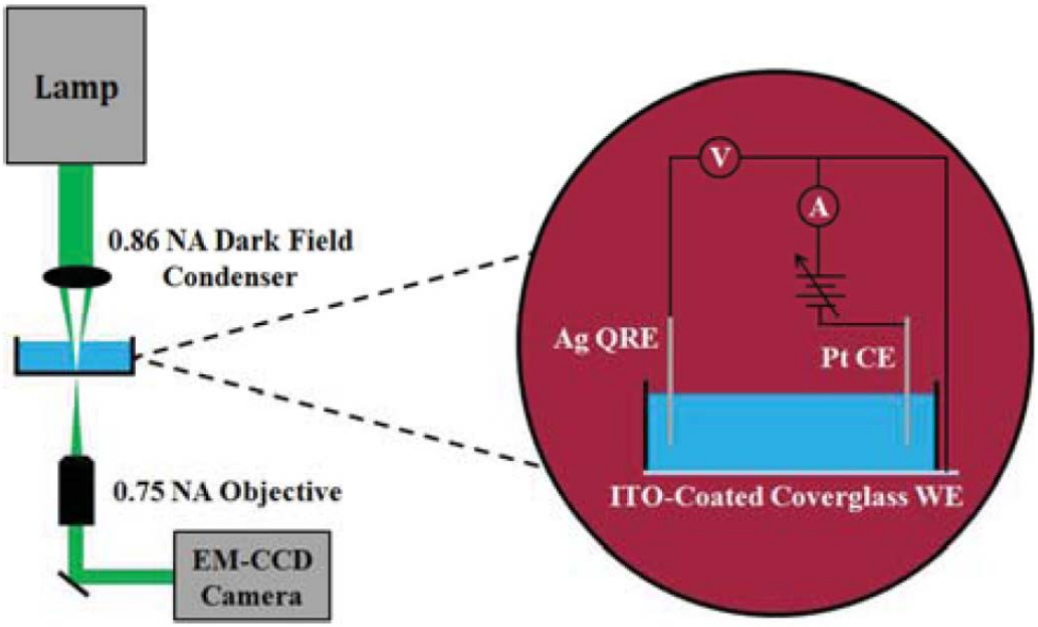
Lamp
0.86 NA Dark Field
Condenser
0.75 NA Objective
EM-CCD
Camera
V
A
Ag QRE
Pt CE
ITO-Coated Coverglass WE

Figure 15

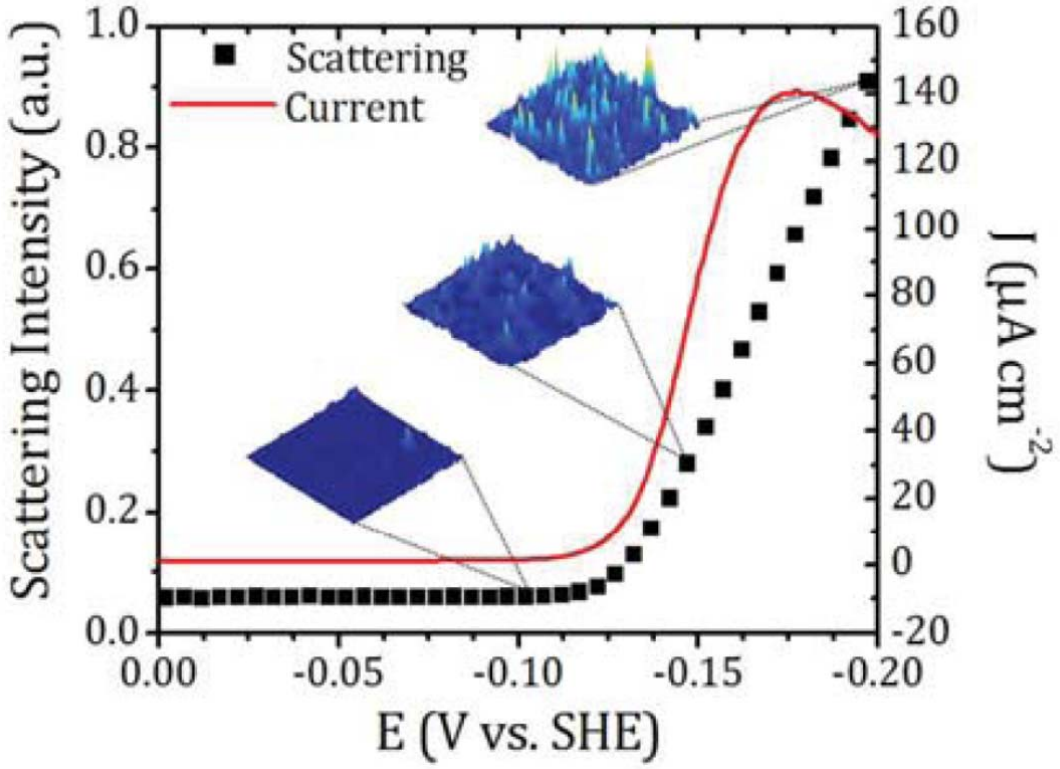
Scattering
Current
Scattering Intensity (a.u.)
J (μA cm-2)
E (V vs. SHE)
1.0
0.8
0.6
0.4
0.2
0.0
160
140
120
100
80
60
40
20
0
-20
0.00
-0.05
-0.10
-0.15
-0.20

Figure 16

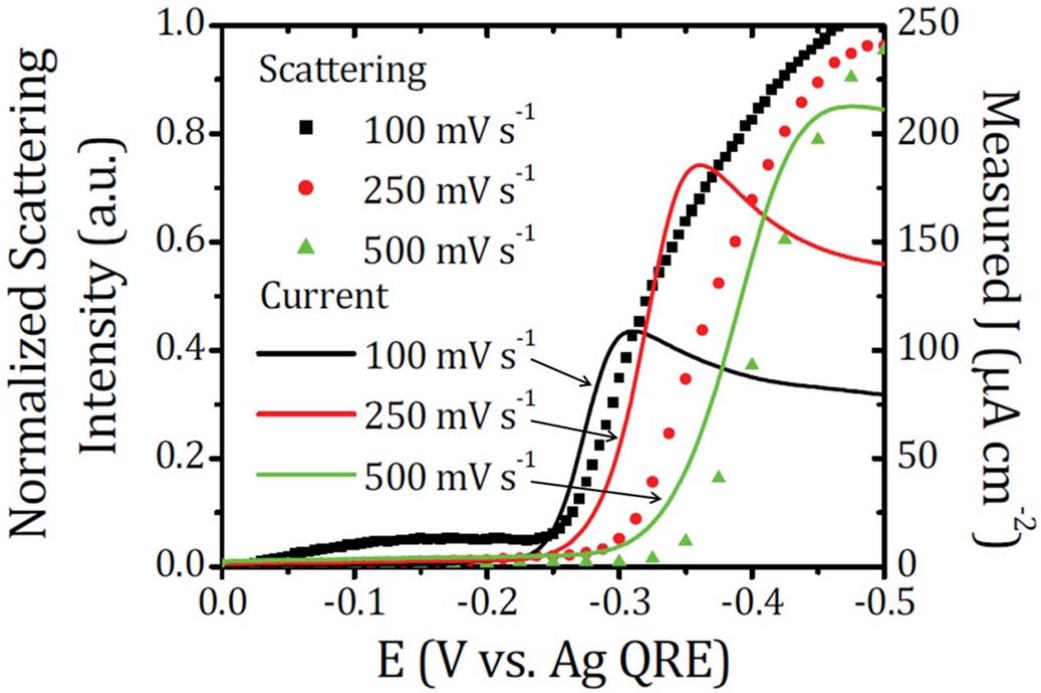
Normalized Scattering Intensity (a.u.)
Measured J (μA cm-2)
E (V vs. Ag QRE)
Scattering
100 mV s-1
250 mV s-1
500 mV s-1
Current
100 mV s-1
250 mV s-1
500 mV s-1
1.0
0.8
0.6
0.4
0.2
0.0
250
200
150
100
50
0
0.0
-0.1
-0.2
-0.3
-0.4
-0.5

Figure 17

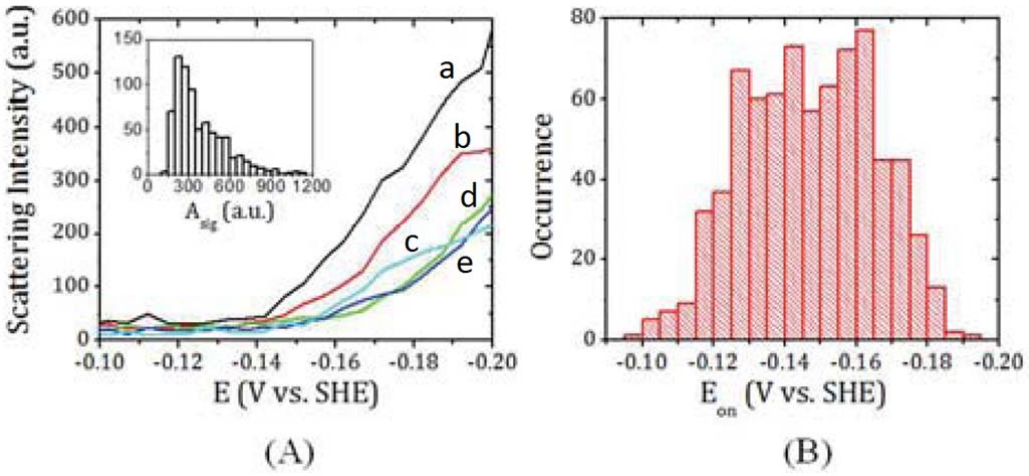
Scattering Intensity (a.u.)
600
500
400
300
200
100
0
150
100
50
0
0 300 600 900 1200
A_sig (a.u.)
a
b
c
d
e
-0.10 -0.12 -0.14 -0.16 -0.18 -0.20
E (V vs. SHE)
(A)
Occurrence
80
60
40
20
0
-0.10 -0.12 -0.14 -0.16 -0.18 -0.20
E_on (V vs. SHE)
(B)

Figure 18

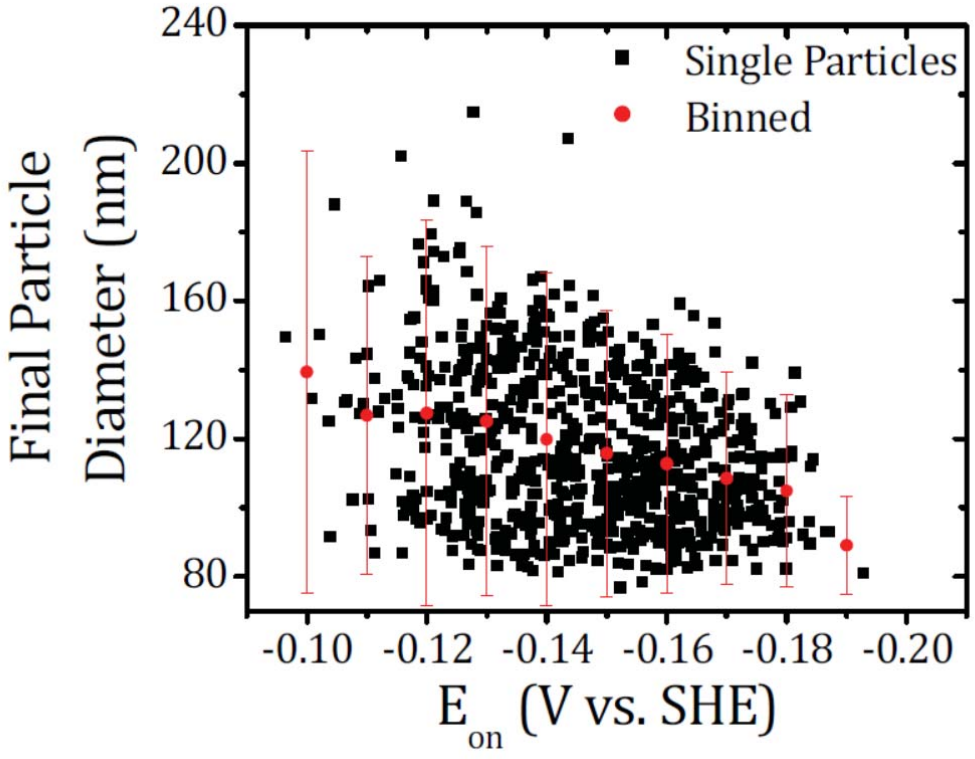
240
200
160
120
80
Final Particle Diameter (nm)
Single Particles
Binned
-0.10
-0.12
-0.14
-0.16
-0.18
-0.20
E on (V vs. SHE)

Figure 19

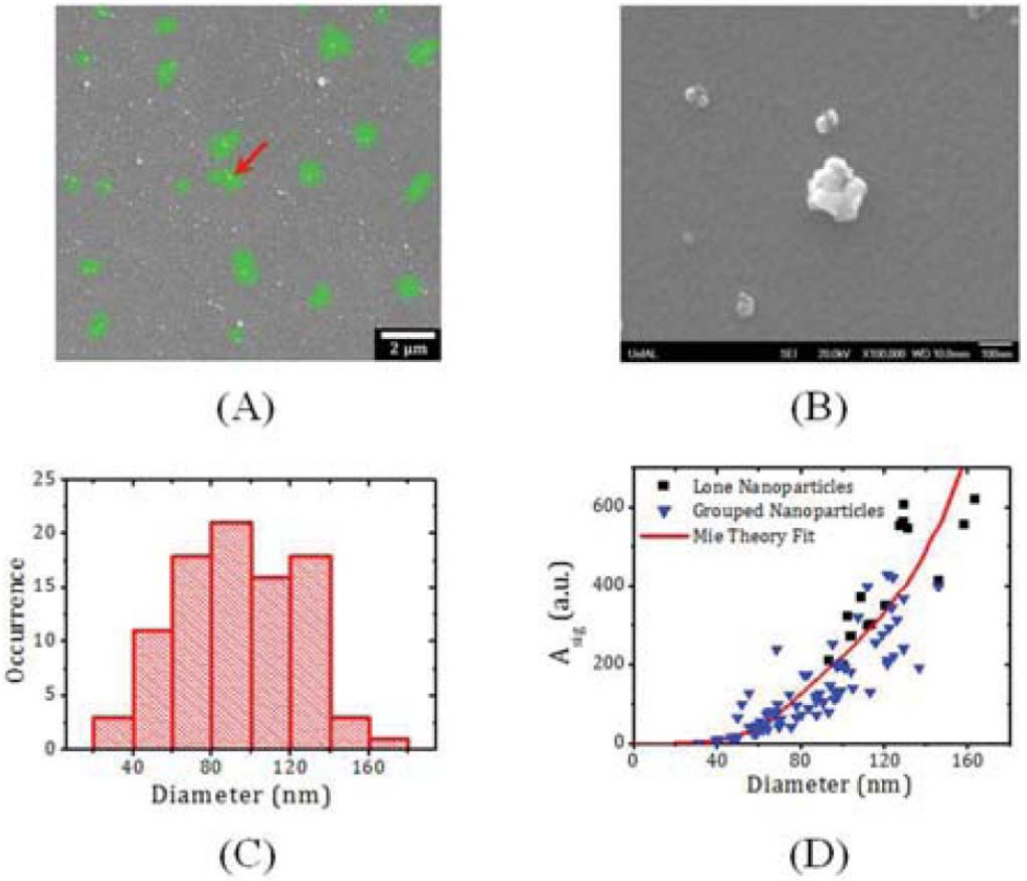
2 μm
(A)
(B)
Occurrence
Diameter (nm)
(C)
Lone Nanoparticles
Grouped Nanoparticles
Mie Theory Fit
A_{sig} (a.u.)
Diameter (nm)
(D)

Figure 20

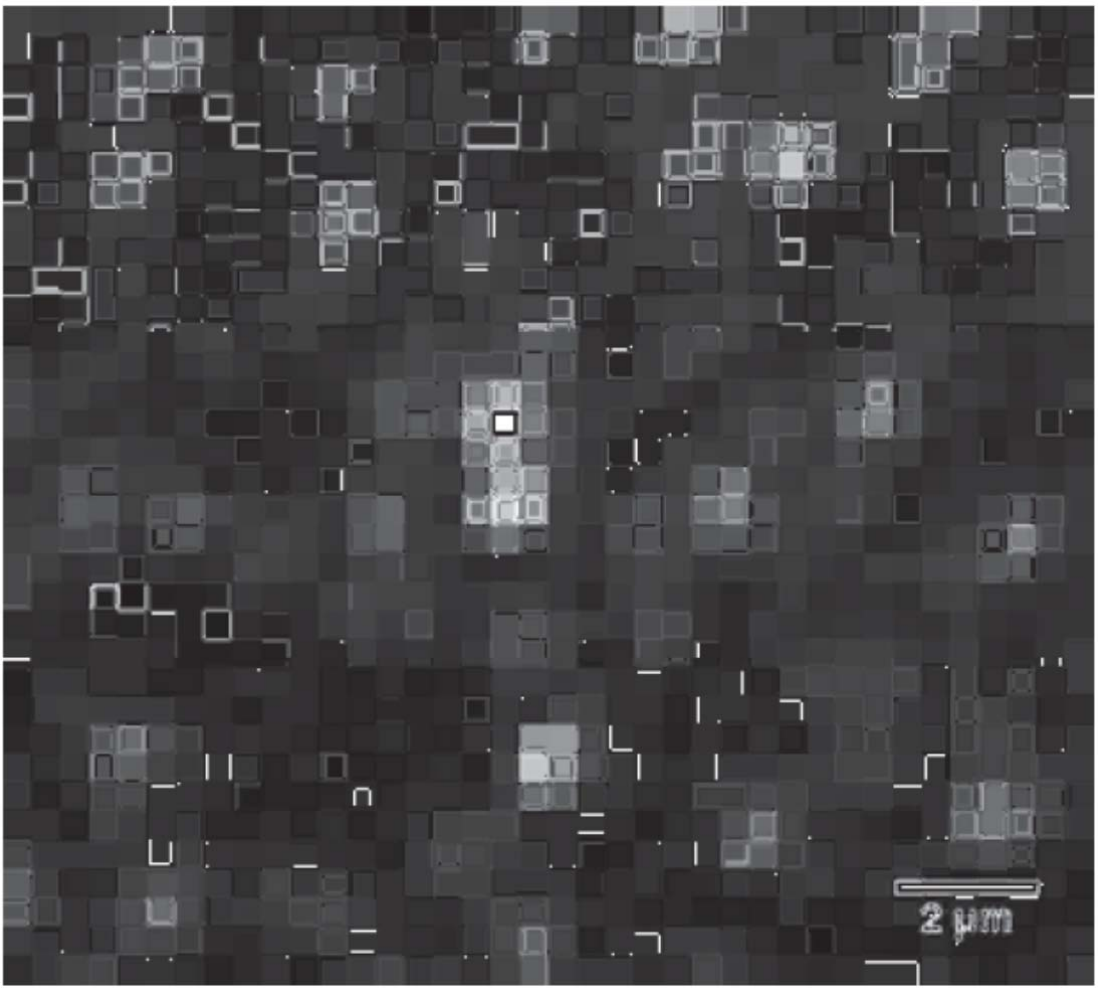

Figure 21

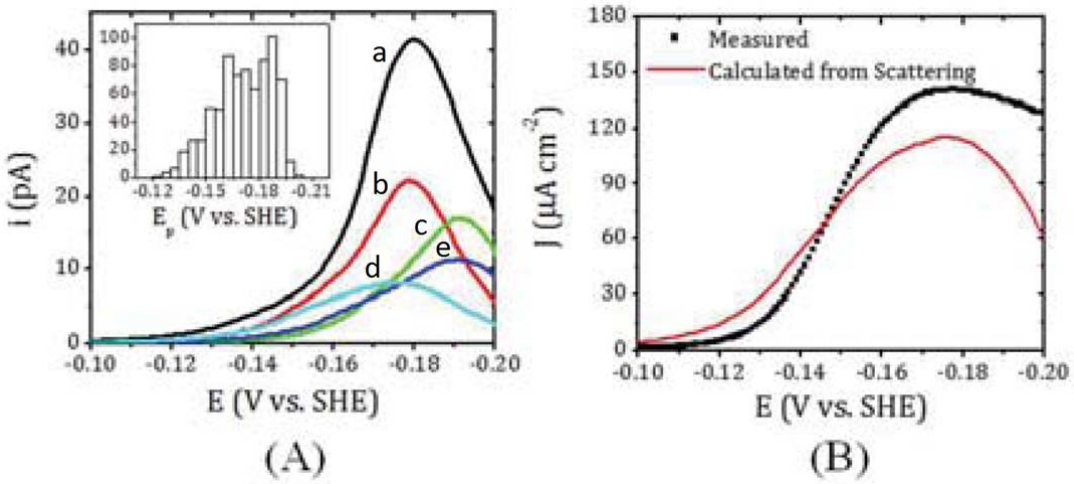
i (pA)
E (V vs. SHE)
(A)
a
b
c
d
e
E_p (V vs. SHE)
J (μA cm^-2)
Measured
Calculated from Scattering
E (V vs. SHE)
(B)

Figure 22

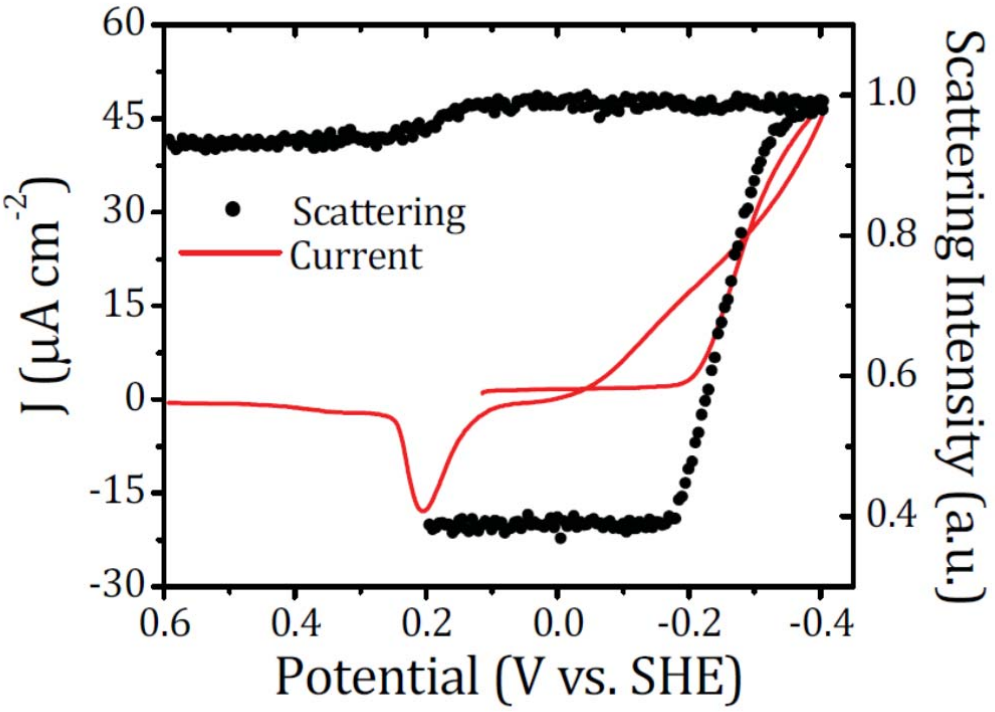
60
45
30
15
0
-15
-30
J (μA cm-2)
Scattering
Current
1.0
0.8
0.6
0.4
Scattering Intensity (a.u.)
0.6
0.4
0.2
0.0
-0.2
-0.4
Potential (V vs. SHE)

Figure 23

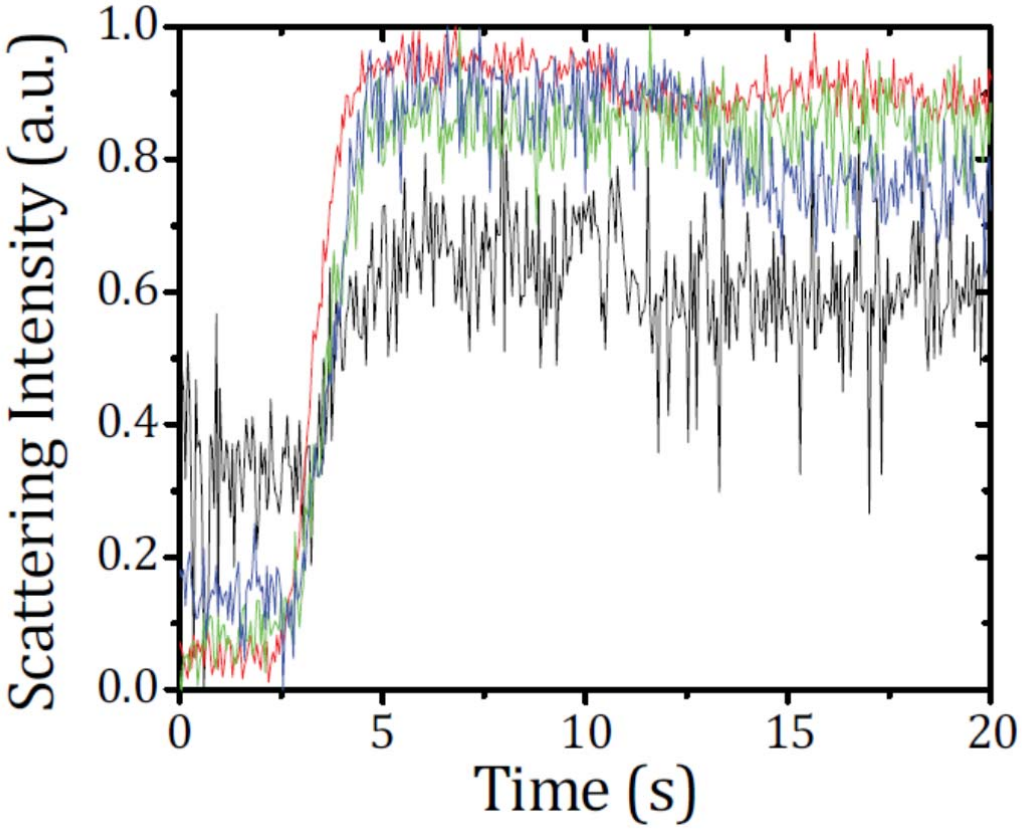

Figure 24

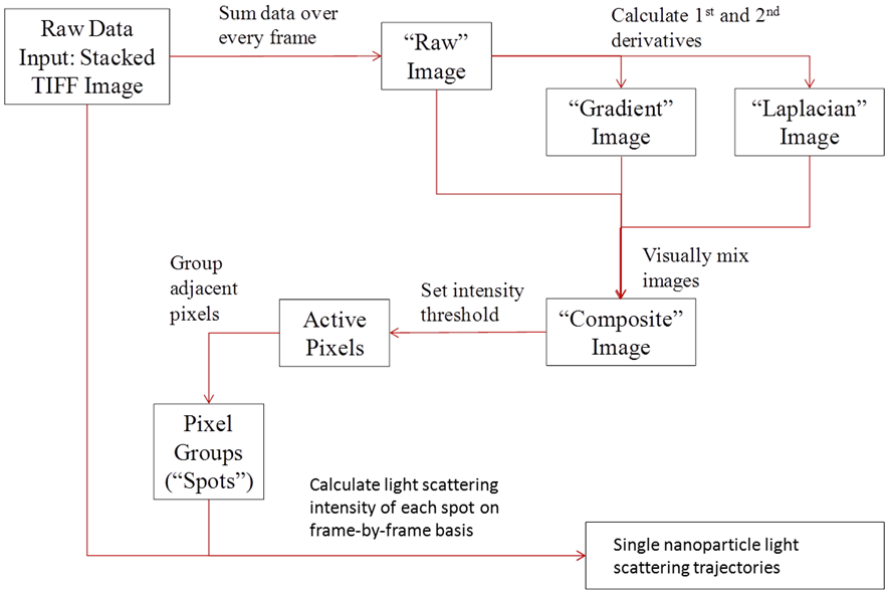
Raw Data Input: Stacked TIFF Image
Sum data over every frame
"Raw" Image
Calculate 1st and 2nd derivatives
"Gradient" Image
"Laplacian" Image
Visually mix images
"Composite" Image
Set intensity threshold
Active Pixels
Group adjacent pixels
Pixel Groups ("Spots")
Calculate light scattering intensity of each spot on frame-by-frame basis
Single nanoparticle light scattering trajectories

Figure 25

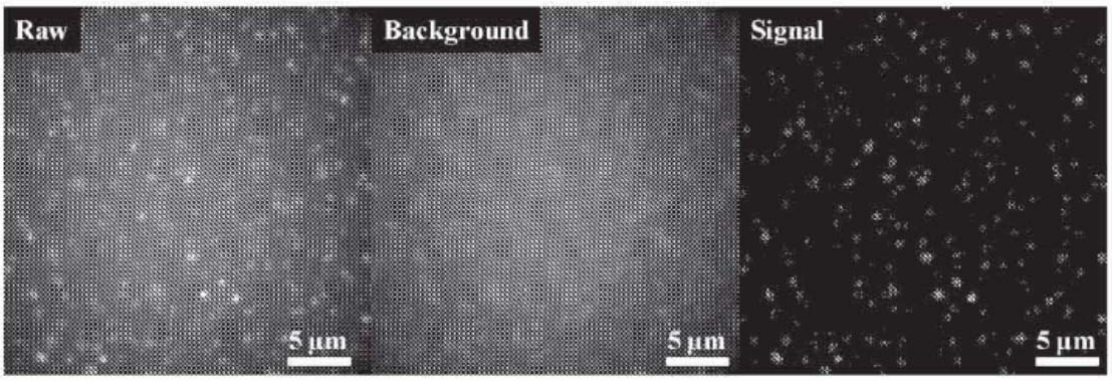

Figure 26

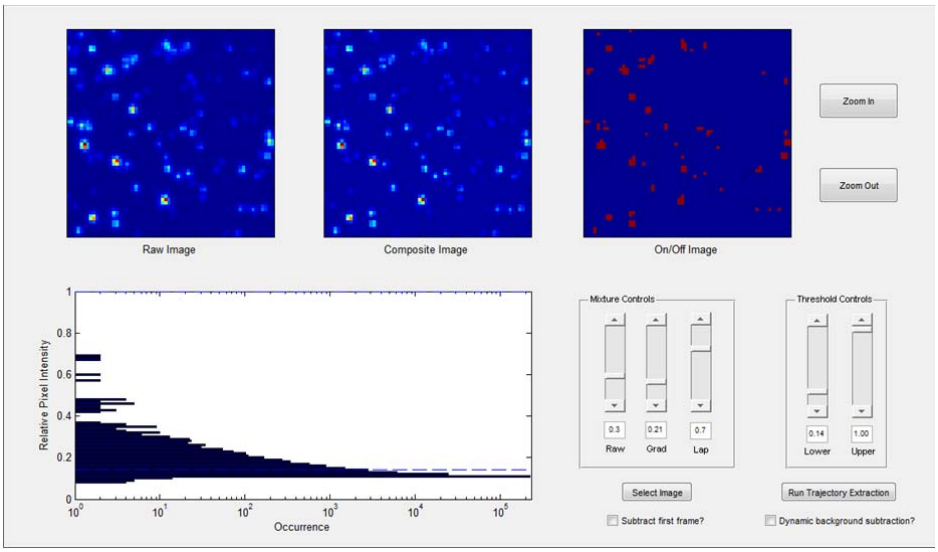
Raw Image
Composite Image
On/Off Image
Zoom In
Zoom Out
Relative Pixel Intensity
Occurrence
Mixture Controls
Raw
Grad
Lap
Threshold Controls
Lower
Upper
Select Image
Run Trajectory Extraction
Subtract first frame?
Dynamic background subtraction?

Figure 27